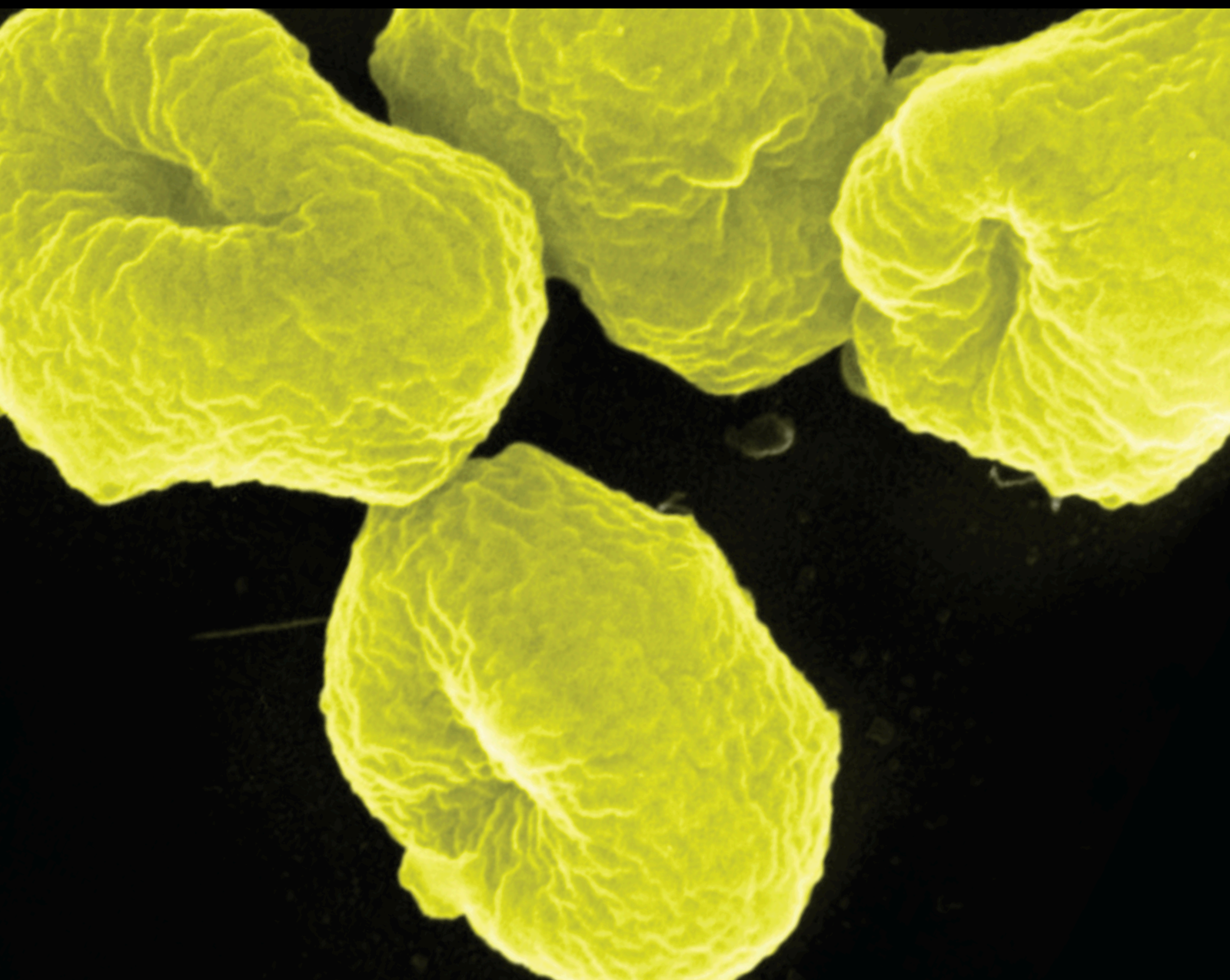


Archaea

Biological Processes for Pollution Control: Current Research and Emerging Technologies 2020

Lead Guest Editor: Jin Li

Guest Editors: Yu Tao, Guangbin Li, Cuijie Feng, Rong Chen, and Ming Hua





**Biological Processes for Pollution Control:
Current Research and Emerging Technologies
2020**

Archaea

**Biological Processes for Pollution
Control: Current Research and
Emerging Technologies 2020**

Lead Guest Editor: Jin Li

Guest Editors: Yu Tao, Guangbin Li, Cuijie Feng,
Rong Chen, and Ming Hua



Copyright © 2021 Hindawi Limited. All rights reserved.


This is a special issue published in "Archaea." All articles are open access articles distributed under the Creative Commons Attribution License, which permits unrestricted use, distribution, and reproduction in any medium, provided the original work is properly cited.

Editorial Board







Sonja-Verena Albers, Germany
Ricardo Amils, Spain
Haruyuki Atomi, Japan
Nils-Kåre Birkeland, Norway
Elizaveta A. Bonch-Osmolovskaya, Russia
Isaac K. O. Cann, USA
Nejat Düzgünes, USA
Michael W. Friedrich, Germany
Toshiaki Fukui, Japan
Dennis W. Grogan, USA
Michael Ibba, USA
Hans-Peter Klenk, United Kingdom
William W. Metcalf, USA
Alla Nozhevnikova, Russia
Frank T. Robb, USA
Francisco Rodriguez-Valera, Spain
Kevin R. Sowers, USA
Stefan Spring, Germany
Antonio Ventosa, Spain
William B. Whitman, USA
Chuanlun Zhang, China

Contents

Biological Processes for Pollution Control: Current Research and Emerging Technologies 2020

Jin Li , Yu Tao, Guangbin Li, Cuijie Feng, Rong Chen, and Ming Hua
Editorial (3 pages), Article ID 9852531, Volume 2021 (2021)





Performance Analysis and Microbial Community Evolution of In Situ Biological Biogas Upgrading with Increasing H₂/CO₂ Ratio

Viola Corbellini , Cuijie Feng , Micol Bellucci , Arianna Catenacci , Tatiana Stella, Anna Espinoza-Tofalos , and Francesca Malpei 
Research Article (15 pages), Article ID 8894455, Volume 2021 (2021)







Flocculation Efficiency and Mechanism of Carbamazepine by Microbial Flocculant Extracted from *Klebsiella pneumoniae* J1

Jie Xing , Nanzhe Song, Xiangwei Chen, Ang Li, and Hongwei Ni 
Research Article (8 pages), Article ID 8811516, Volume 2020 (2020)








Thermophilic Solid-State Anaerobic Digestion of Corn Straw, Cattle Manure, and Vegetable Waste: Effect of Temperature, Total Solid Content, and C/N Ratio

Lianghu Su , Xu Sun, Chenwei Liu, Rongting Ji, Guangyin Zhen , Mei Chen , and Longjiang Zhang 
Research Article (10 pages), Article ID 8841490, Volume 2020 (2020)



Identification and Characterization of a Newly Isolated Chitinase-Producing Strain *Bacillus licheniformis* SSCL-10 for Chitin Degradation

Abirami Sasi , Nagarajan Duraipandiyar , Kannan Marikani , Sugapriya Dhanasekaran , Noura Al-Dayan , and Divya Venugopal 
Research Article (9 pages), Article ID 8844811, Volume 2020 (2020)


A Current Sensing Biosensor for BOD Rapid Measurement

Yiman Liu , Jie Li , Nianxin Wan , Tianyu Fu, Lili Wang , Cong Li , Zhonghui Qie , and Ao Zhu 
Research Article (7 pages), Article ID 8894925, Volume 2020 (2020)

Effects of Sludge Retention Time on the Performance of Anaerobic Ceramic Membrane Bioreactor Treating High-Strength Phenol Wastewater

Chunhua He, Chuanhe Yang, Shoujun Yuan, Zhenhu Hu , and Wei Wang 
Research Article (10 pages), Article ID 8895321, Volume 2020 (2020)



Simulation of a Novel Tubular Microalgae Photobioreactor with Aerated Tangent Inner Tubes: Improvements in Mixing Performance and Flashing-Light Effects

Xuyang Cui, Junhong Yang , Yuanzheng Feng, and Wenwen Zhang
Research Article (16 pages), Article ID 8815263, Volume 2020 (2020)




Response and Adaptation of Microbial Community in a CANON Reactor Exposed to an Extreme Alkaline Shock

Ruili Yang, Wenlong Mao, Xiaojun Wang , Zhaoji Zhang, Junbin Wu, and Shaohua Chen 
Research Article (11 pages), Article ID 8888615, Volume 2020 (2020)


Biosorption Mechanism of Aqueous Pb²⁺, Cd²⁺, and Ni²⁺ Ions on Extracellular Polymeric Substances (EPS)

Di Cui , Chong Tan, Hongna Deng, Xunxue Gu, Shanshan Pi, Ting Chen, Lu Zhou, and Ang Li 
Research Article (9 pages), Article ID 8891543, Volume 2020 (2020)

Integration of Marine Macroalgae (*Chaetomorpha maxima*) with a Moving Bed Bioreactor for Nutrient Removal from Maricultural Wastewater

Xian Li , Yale Deng, Xueying Li, Xiaona Ma , Jinxia Wang , and Jun Li
Research Article (13 pages), Article ID 8848120, Volume 2020 (2020)

Characteristics of Biohydrogen Production and Performance of Hydrogen-Producing Acetogen by Increasing Normal Molasses Wastewater Proportion in Anaerobic Baffled Reactor

Xuejia Gu, Yufeng Wang, Huaibo Li, Ji Li, and Shuo Wang 
Research Article (14 pages), Article ID 8885662, Volume 2020 (2020)

Editorial

Biological Processes for Pollution Control: Current Research and Emerging Technologies 2020

Jin Li ¹, Yu Tao,² Guangbin Li,³ Cuijie Feng,⁴ Rong Chen,⁵ and Ming Hua⁶

¹Qingdao University, Qingdao, China

²Chinese Academy of Sciences, Beijing, China

³University of Maryland, College Park, USA

⁴Polytechnic University of Milan Piazza Leonardo da Vinci, Milan, Italy

⁵Xi'an University of Architecture and Technology, Xi'an, China

⁶Nanjing University, Nanjing, China

Correspondence should be addressed to Jin Li; ljin0532@126.com

Received 19 July 2021; Accepted 19 July 2021; Published 5 November 2021

Copyright © 2021 Jin Li et al. This is an open access article distributed under the Creative Commons Attribution License, which permits unrestricted use, distribution, and reproduction in any medium, provided the original work is properly cited.

With rapid economic growth, aggravated environmental pollution has become a severe issue worldwide [1, 2]. Pollution control and nutrient recovery are imperative for sustainable development and critical for ecosystem and human health [3]. Excessive chemicals and energy have been used to control pollutants, which causes neglected but severe side effects [4].

The biological process is regarded as promising and sustainable [5, 6], developing quickly with exciting breakthroughs in both theory improvement and technology innovation [7]. The bioparts of pollutants are degraded through microbial activities, where complex organic matters are degraded, and nutrients such as nitrogen and phosphorus are removed. Archaea and bacteria are essential in such processes [8, 9]. For example, anaerobic ammonia-oxidizing (anammox) bacteria are responsible for nitrogen removal from both engineered and natural water systems [10, 11].

Aside from pollutant removal, biological processes are integrated with energy production and resource recovery [12]. Archaea and bacteria play essential roles in converting carbon, nitrogen, phosphorus, and other pollutants into energy and valuable chemicals [13, 14]. However, process efficiency and stability issues remain unknown, such as microbiome dynamics, metabolic mechanisms, and identification of novel microorganisms. These investigations will optimize current biological processes and innovate emerging technologies.

Pollutant removal and nutrient recovery are two major themes in this special issue. C. He et al. presented a comprehensive insight into the feasibility and robustness of anaerobic ceramic membrane bioreactors for treating high-strength phenol wastewater [15]. D. Cui et al. investigated the adsorption capacity and mechanism of Pb^{2+} , Cd^{2+} , and Ni^{2+} by the extracellular polymeric substance (EPS) from *Agrobacterium tumefaciens* F2. EPS's potential as a bioadsorbent sheds light on the control of heavy metal pollution [16]. R. Yang et al. studied the response and adaptation of microbial communities to a completely autotrophic nitrogen removal over nitrite (CANON) system exposed to extreme alkaline shocks. This study gave implications for recovering CANON reactors after alkaline shock [17]. J. Xing et al. applied a microbial flocculant extracted from *Klebsiella pneumoniae* J1 to remove carbamazepine in wastewater and domestic sewage. This eco-friendly and highly efficient microbial flocculant is expected for practical applications in carbamazepine removal [18]. For nutrient recovery, X. Gu et al. applied anaerobic baffled reactors for biohydrogen production out of molasses wastewater and analyzed hydrogen-producing acetogen's performance under increasing organic loads [19]. X. Li et al. demonstrated the feasibility of cultivating marine macroalgae (*Chaetomorpha maxim*) in a moving bed bioreactor to remove nitrogen and phosphorus in aquaculture wastewater and produce macroalgae biomass, supplying an effective option to benefit aquaculture systems [20]. A. Sasi

et al. developed a *Bacillus licheniformis* mutant strain that could produce hyperchitinase, which has the excellent potential of recycling and processing chitin waste from crustaceans and shrimp, adding value to the crustacean industry [21]. L. Su et al. applied thermophilic solid-state anaerobic digestion of agricultural wastes, i.e., corn straw, cattle manure, and vegetable waste, and investigated the effects of temperature, total solid content, and C/N ratio [22].

The novel design of techniques is also addressed in the special issue. Y. Liu et al. developed a highly sensitive and rapid method for measuring BOD by establishing a correlation between current and dissolved oxygen. Such a rapid BOD current sensing biosensor method is expected to be used for wastewater monitoring [23]. X. Cui et al. developed a novel tubular photobioreactor with improved potential for microalgal cultivation. The new design can provide a more suitable microenvironment for microalgal cultivation and increase microalgae yield [24].

Given all these advances in biological processes for pollution control and nutrient recovery, what does the future hold for us? The application of biological tools in solving environmental problems has a long history and is broad, covering many underpinning and allied technological areas. We hope that the ten articles that are included in this special issue would supply inspiration to researchers who work in both biological science and environmental engineering.

Conflicts of Interest

I declare that none of the Guest Editors have a conflict of interest.

Jin Li
Yu Tao
Guangbin Li
Cuijie Feng
Rong Chen
Ming Hua

References

- [1] Z. Xie, "China's historical evolution of environmental protection along with the forty years' reform and opening-up," *Environmental Science and Ecotechnology*, vol. 1, article 100001, 2020.
- [2] A. Deletic and H. T. Wang, "Water pollution control for sustainable development," *Engineering*, vol. 5, no. 5, pp. 839–840, 2019.
- [3] Z. M. Liu and P. Espinosa, "Tackling climate change to accelerate sustainable development," *Nature Climate Change*, vol. 9, pp. 494–496, 2019.
- [4] W. Yang, K. Brüggemann, K. D. Seguya et al., "Measuring performance of low impact development practices for the surface runoff management," *Environmental Science and Ecotechnology*, vol. 1, article 100010, 2020.
- [5] A. ter Heijne, "Bioelectrochemistry for flexible control of biological processes," *Environmental Science and Ecotechnology*, vol. 1, p. 100011, 2020.
- [6] M. J. Jin, C. Gunawan, N. Uppugundla, V. Balan, and B. E. Dale, "A novel integrated biological process for cellulosic ethanol production featuring high ethanol productivity, enzyme recycling and yeast cells reuse," *Energy & Environmental Science*, vol. 5, no. 5, pp. 7168–7175, 2012.
- [7] Z. Zhu, Y. Yang, A. Fang et al., "Quorum sensing systems regulate heterotrophic nitrification-aerobic denitrification by changing the activity of nitrogen-cycling enzymes," *Environmental Science and Ecotechnology*, vol. 2, article 100026, 2020.
- [8] Y. Tao, M. E. Ersahin, D. S. M. Ghasimi et al., "Biogas productivity of anaerobic digestion process is governed by a core bacterial microbiota," *Chemical Engineering Journal*, vol. 380, p. 122425, 2020.
- [9] J. De Vrieze, "The next frontier of the anaerobic digestion microbiome: from ecology to process control," *Environmental Science and Ecotechnology*, vol. 3, article 100032, 2020.
- [10] Y. Tao, X. Huang, D. Gao et al., "NanoSIMS reveals unusual enrichment of acetate and propionate by an anammox consortium dominated by *Jettenia asiatica*," *Water Research*, vol. 159, pp. 223–232, 2019.
- [11] J. Li, X. Chen, W. Liu, and Y. Tao, "Biostimulation of a marine anammox bacteria-dominated bioprocess by Co(II) to treat nitrogen-rich, saline wastewater," *Science of The Total Environment*, vol. 749, article 141489, 2020.
- [12] X. Hao et al., "Environmental impacts of resource recovery from wastewater treatment plants," *Water Research*, vol. 160, pp. 268–277, 2019.
- [13] D. Gao, Y. Fu, Y. Tao, W. Wu, R. An, and X. Li, "Current research and development of controlling membrane fouling of MBR," *African Journal of Biotechnology*, vol. 8, pp. 2993–2998, 2009.
- [14] S. Aikawa, A. Joseph, R. Yamada et al., "Direct conversion of spirulina to ethanol without pretreatment or enzymatic hydrolysis processes," *Energy & Environmental Science*, vol. 6, no. 6, pp. 1844–1849, 2013.
- [15] C. He, C. Yang, S. Yuan, Z. Hu, and W. Wang, "Effects of sludge retention time on the performance of anaerobic ceramic membrane bioreactor treating high-strength phenol wastewater," *Archaea*, vol. 2020, Article ID 8895321, 10 pages, 2020.
- [16] D. Cui, C. Tan, H. Deng et al., "Biosorption mechanism of aqueous Pb²⁺, Cd²⁺, and Ni²⁺ ions on extracellular polymeric substances (EPS)," *Archaea*, vol. 2020, Article ID 8891543, 9 pages, 2020.
- [17] R. Yang, W. Mao, X. Wang, Z. Zhang, J. Wu, and S. Chen, "Response and adaptation of microbial community in a CANON reactor exposed to an extreme alkaline shock," *Archaea*, vol. 2020, Article ID 8888615, 11 pages, 2020.
- [18] J. Xing, N. Song, X. Chen, A. Li, and H. Ni, "Flocculation efficiency and mechanism of carbamazepine by microbial flocculant extracted from *Klebsiella pneumoniae* J1," *Archaea*, vol. 2020, Article ID 8811516, 8 pages, 2020.
- [19] X. Gu, Y. Wang, H. Li, J. Li, and S. Wang, "Characteristics of Biohydrogen Production and Performance of Hydrogen-Producing Acetogen by Increasing Normal Molasses Wastewater Proportion in Anaerobic Baffled Reactor," *Archaea*, vol. 2020, Article ID 8885662, 14 pages, 2020.
- [20] X. Li, Y. Deng, X. Li, X. Ma, J. Wang, and J. Li, "Integration of marine macroalgae (*Chaetomorpha maxima*) with a moving bed bioreactor for nutrient removal from maricultural wastewater," *Archaea*, vol. 2020, Article ID 8848120, 13 pages, 2020.
- [21] A. Sasi, N. Duraipandiyam, K. Marikani, S. Dhanasekaran, N. al-Dayam, and D. Venugopal, "Identification and

- characterization of a newly isolated chitinase-producing strain *Bacillus licheniformis* SSCL-10 for chitin degradation,” *Archaea*, vol. 2020, Article ID 8844811, 9 pages, 2020.
- [22] L. Su, X. Sun, C. Liu et al., “Thermophilic solid-state anaerobic digestion of corn straw, cattle manure, and vegetable waste: effect of temperature, total solid content, and C/N ratio,” *Archaea*, vol. 2020, Article ID 8841490, 10 pages, 2020.
- [23] Y. Liu, J. Li, N. Wan et al., “A current sensing biosensor for BOD rapid measurement,” *Archaea*, vol. 2020, Article ID 8894925, 7 pages, 2020.
- [24] X. Cui, J. Yang, Y. Feng, and W. Zhang, “Simulation of a novel tubular microalgae photobioreactor with aerated tangent inner tubes: improvements in mixing performance and flashing-light effects,” *Archaea*, vol. 2020, Article ID 8815263, 16 pages, 2020.

Research Article

Performance Analysis and Microbial Community Evolution of In Situ Biological Biogas Upgrading with Increasing H₂/CO₂ Ratio

Viola Corbellini ¹, Cuijie Feng ¹, Micol Bellucci ¹, Arianna Catenacci ¹, Tatiana Stella,²
Anna Espinoza-Tofalos ² and Francesca Malpei ¹

¹Department of Civil and Environmental Engineering, DICA, Politecnico di Milano, Environmental Section, Piazza L. da Vinci 32, 20133 Milano, Italy

²Department of Earth and Environmental Sciences, DISAT, University of Milano-Bicocca, Research Group of Environmental Microbiology, Piazza della Scienza, 1, 20126 Milano, Italy

Correspondence should be addressed to Viola Corbellini; viola.corbellini@polimi.it

Received 14 May 2020; Revised 27 July 2020; Accepted 15 January 2021; Published 10 February 2021

Academic Editor: Ricardo Amils

Copyright © 2021 Viola Corbellini et al. This is an open access article distributed under the Creative Commons Attribution License, which permits unrestricted use, distribution, and reproduction in any medium, provided the original work is properly cited.

The effect of the amount of hydrogen supplied for the *in situ* biological biogas upgrading was investigated by monitoring the process and evolution of the microbial community. Two parallel reactors, operated at 37°C for 211 days, were continuously fed with sewage sludge at a constant organic loading rate of 1.5 gCOD•(L•d)⁻¹ and hydrogen (H₂). The molar ratio of H₂/CO₂ was progressively increased from 0.5:1 to 7:1 to convert carbon dioxide (CO₂) into biomethane via hydrogenotrophic methanogenesis. Changes in the biogas composition become statistically different above the stoichiometric H₂/CO₂ ratio (4:1). At a H₂/CO₂ ratio of 7:1, the methane content in the biogas reached 90%, without adversely affecting degradation of the organic matter. The possibility of selecting, adapting, and enriching the original biomass with target-oriented microorganisms able to biologically convert CO₂ into methane was verified: high throughput sequencing of 16S rRNA gene revealed that hydrogenotrophic methanogens, belonging to *Methanolinea* and *Methanobacterium* genera, were dominant. Based on the outcomes of this study, further optimization and engineering of this process is feasible and needed as a means to boost energy recovery from sludge treatment.

1. Introduction

Global warming has been proven as the consequence of increased carbon concentration in the atmosphere resulting from greenhouse-gas emissions mainly of carbon dioxide (CO₂) derived from human activities. According to the latest available data [1], China is the greatest producer of CO₂ with 10.9 billion tons of equivalent CO₂ released every year, followed by the USA (5.1 Gt per year) and the European Union (3.2 Gt per year). Among European countries (EU28), Italy is ranked 3rd (0.36 Gt) and 18th worldwide. Accordingly, the imposition of increasingly restrictive limits on municipal wastewater treatment plants (WWTPs), as well as the need to reduce the use of fossil sources, requires plants to become energy self-sufficient [2]. Energy is conventionally regained through biogas production from anaerobic digestion (AD). Biogas, mainly composed of 55-70% CH₄, 30-

45% of CO₂, and other trace gases (nitrogen, oxygen, water, hydrocarbons, ammonia, and siloxanes) [3], can be utilized in combined heat and power engines or, after removal of CO₂ (biogas upgrading) and other impurities, as biomethane. In this last case, the market already offers various chemical/physical upgrading technologies. However, one main drawback lies in simply splitting CO₂ from the biogas flux. Nonetheless, given the considerable challenges in terms of energy/chemical consumption, researchers are investigating alternative solutions [4]. Among these, the biological CO₂ conversion into methane (CH₄) (Equation (1)) is attractive.



It allows the simultaneous reduction of CO₂ and increase of CH₄ yields, towards a more sustainable biogas upgrading technology which converts biogenic CO₂ into an energy

source, with a negative carbon emission footprint in terms of fossil CO₂ [5]. The high biological upgrading requirement of exogenous H₂ to allow CO₂ conversion can be satisfied by exploiting the excess off-peak energy of naturally fluctuating renewables (wind, solar) to sustain the water electrolysis process as power to gas (P2G) [6]. In addition, in a WWTP equipped with sludge AD treatment, the biological biogas upgrading introduces two additional advantages: (i) the O₂ coproduced along with H₂ by water electrolysis could be used in the activated sludge treatment, which requires around 50% of the total WWTP energy needs [2]; (ii) the effluent water from a WWTP could be used as source water for electrolysis, although pretreatment may be needed [7].

The biological CO₂ methanization process is carried out by archaea belonging to the orders of *Methanobacteriales*, *Methanomicrobiales*, and *Methanococcales*, which are classified as hydrogenotrophic methanogens [8]. Hydrogenotrophic methanogens are commonly found in every anaerobic digester playing a significant role in scavenging H₂ in order to maintain a low partial pressure (pH₂ < 10 Pa).

So far, three main applications of this novel upgrading technology were studied at the lab-scale: *in situ*, *ex situ* [9–11], and *hybrid* [12]. In the *in situ*, H₂ is fed into a biogas reactor where it is used with the CO₂ produced by organic substrate degradation. The main drawbacks of the *in situ* system are: (a) accumulation of intermediates due to the increased H₂ partial pressure (pH₂) [13], (b) increase of pH due to a progressive depletion of endogenous dissolved CO₂ [9, 12, 14], and (c) low hydrogen solubility which can limit a homogeneous and efficient distribution of the gas in the liquid phase [13, 15–18].

Regarding the effect on the organic degradation chain, Corbellini et al. [21] tested a novel approach, performed in semibatch bioreactors, consisting in progressively increasing H₂ dosage in order to acclimate and develop a specialized biomass. Few other studies can be found in the literature pertaining *in situ* biogas upgrading treating sewage sludge and specifically focused on the H₂/CO₂ ratio for process optimization [19, 20]. Indeed, it is crucial to obtain a deeper knowledge of the effect of the H₂/CO₂ ratio in shaping a consortium of bacteria and archaea able to steadily and simultaneously maximize CO₂ methanization and degrade the organic substrates.

In this study, the biological *in situ* biogas upgrading was operated in two lab-scale continuous stirred tank reactors (CSTR) working in parallel in order to evaluate the repeatability of the process and of the experimental outcomes: this latter aspect is of importance as it is seldom addressed when testing biological biogas upgrading, and the vast majority of literature reports on single operating reactors. The experimental plan was determined with two main purposes: to investigate the effect of the H₂/CO₂ ratio on the efficiency of biogas upgrading and on the stability of the process and to study the evolution of the specific microbiome in connection with the development of the process at the macroscale. Based on results of this investigation, further knowledge has been gained pertaining to (1) the relationship between the biogas rate produced and the main operational parameters; (2) the H₂/CO₂ ratio up to which the system can be pushed

before encountering instability; (3) the effects of increased H₂/CO₂ ratio on the microbial community, which was analysed at different experimental stages; and (4) the repeatability of the process.

2. Materials and Methods

2.1. Experimental Setup and Design. Two identical lab-scale CSTRs (total volume, $V_{\text{tot}} = 16$ L; working height, $H_w = 31.3$ cm; diameter, $D = 30$ cm; working volume, $V_w = 11$ L), hereafter referred to as R1 and R2, were operated in parallel and daily fed with 0.5 L of a primary and secondary sludge mixture. The organic loading rate referred to the sludge (OLR_{SL}) was 1.5 ± 0.1 gCOD•(L•d)⁻¹ and the hydraulic retention time (HRT) 22 days. The two reactors (Umwelt GmbH) were equipped with peristaltic pumps for sludge loading and discharging and for controlling the pH at 7.4 ± 0.2 by adding acid or basic solutions (0.5 M HCl, 1 M NaOH). H₂ was injected in each reactor with an additional peristaltic pump (Velp Scientifica, Type SP-311/2, Italy) through an aluminium tube ($\varnothing = 6$ mm) sunk at 3/4 of the total sludge height.

Vigorous mixing at 120 rpm was assured by vertical shaft stirrers. External heating jackets maintained the internal temperature at $36.7 \pm 1^\circ\text{C}$. The biogas flow was quantified by a gas meter (RITTER Apparatebau GmbH & Co. KG) and analysed online with a gas analyser (AwiFLEX Cool+, Awite Bioenergie GmbH) for CO₂ (range 0–100%), CH₄ (range 0–100%), and O₂ content (range 0–25%) by pressure and infrared compensation methods, while the H₂S (up to 1500 ppm) was measured by an electrochemical sensor. Hydrogen was analysed, twice per week, using gas chromatography (DANI Master GC) coupled with a flame ionization detector (FID Nukol fused silica). Reactors were operated for a total of 211 days, divided into VIII Periods (Table 1). In Period I (start-up period), both reactors were fed on the sewage sludge mixture only. Then, while maintaining a constant OLR_{SL}, H₂ was progressively fed to reactors at increasing H₂/CO₂ ratios: periods from II to VI were dedicated to the enrichment (H₂/CO₂ from 0.5 up to 4); in Periods VII and VIII, H₂/CO₂ ratios above the stoichiometric value, and equal to 6 and 7, were adopted. Table 1 reports other relevant operating conditions for each period, since the OLR_{tot} is the sum of contributions given by the sewage sludge mixture (OLR_{SL}) and the H₂, both computed on COD basis (conversion factor 8 gCOD•gH₂⁻¹). The length of periods up to the stoichiometric H₂/CO₂ ratio was assumed as in Corbellini et al. [21], where such durations were defined in order to simultaneously achieve a stable response to a perturbation and shorten the start-up time required to adapt the biomass to an increasing H₂ supply.

The amount of H₂ daily dosed in each reactor during Period i (Dose(H₂)_{period, i}) was calculated based on the H₂/CO₂ ratio and on the average rate of CO₂ produced during the ($i-1$)th Period, according to [21]. The daily H₂ amount was supplied by activating the H₂ pump for 20 pulse/day and adjusting the pump speed in order to reach the H₂ amount for each experimental period.

2.2. Inoculum and Feedstock Preparation and Characteristics.

Both the feeding sludge and the inoculum were taken from a

TABLE 1: Operational parameters during experimental periods; in brackets, next to the period number, the H_2/CO_2 ratio adopted.

Period- H_2/CO_2	Duration (d)	Progressive days (begin-end)	OLR _{SL} (g COD·L ⁻¹ ·d ⁻¹)	OLR _{tot} (g COD·L ⁻¹ ·d ⁻¹)
I	97 ^(a)	0-20	1.3 ± 0.6	1.3 ± 0.6
II-0.5	20	21-41	1.5 ± 0.2	1.5 ± 0.1
III-1	7	42-49	1.5 ± 0.1	1.6 ± 0.3
IV-2	8	50-58	1.6 ± 0	1.6 ± 0.4
V-3	8	59-67	1.6 ± 0	1.7 ± 0.2
VI-4	26	68-94	1.4 ± 0.2	1.7 ± 0.3
VII-6	12	95-107	1.5 ± 0.8	1.8 ± 0.8
VIII-7	33	108-141	1.5 ± 0.4	1.9 ± 0.6

^(a)In all figures, only the last 20 days of Period I are shown.

full-scale municipal WWTP located in Bresso (Milan Area, Italy). The feeding sludge ($0.5 L \cdot d^{-1}$) is a mixture of primary and waste activated sludge (WAS), directly taken from the primary settling tank where WAS is recirculated. The inoculum (10 L) was collected from the mesophilic full-scale digester. The sludge mixture was hashed and sieved (2 mm) to prevent clogging of the pump tubes; then, it was stored at $-20^\circ C$ and used after thawing. The main characteristics of the substrates are reported in Table 2. Two biochemical methane potential tests (BMP) were performed on the sludge mixture at the beginning and at the end of the experimentation, in this last case using the reactor effluent as inoculum.

2.3. Monitoring Strategy. Total and volatile solids and total COD were measured every 10 days on the feeding sludge. Total and volatile solids, volatile fatty acids, soluble COD, and alkalinity of the effluent digestate were determined twice a week. Based on the results, two indexes were calculated for each experimental period: (i) the amount of H_2 consumed ($H_{2, eff}$), according to [21], and (ii) the percentage of volatile solids removed in order to monitor the effect of H_2 injection on the organic substrate degradation, according to Equation (2).

$$VS (\%) = \frac{VS_{in} - VS_{out}}{VS_{in}} \cdot 100, \quad (2)$$

where VS_{in} and VS_{out} ($gVS \cdot L^{-1}$) are the volatile solid concentrations in the influent and effluent sludge.

2.4. Analytical Methods. Total and volatile solids (TS, VS) were measured according to Standard Methods 2540 [22]. Alkalinity was measured by titration with H_2SO_4 up to pH 4.3, using an automatic titrator (Hach Lange BIOGAS Titration Manager, USA). Soluble COD (sCOD) was measured using spectrophotometric test kits (DR6000 UV-VIS with RFID by Hach-Lange) after filtration ($0.45 \mu m$). Volatile fatty acid (VFA, acetic, propionic, isobutyric, butyric, isovaleric, and valeric) concentrations were determined according to Standard Methods 5560 [22], using a gas chromatograph (DANI Master GC) coupled with a flame ionization detector. Hereafter, the term TVFA indicates the total concentrations of VFA expressed as equiva-

TABLE 2: Chemical characterization (mean ± standard deviation) of inoculum and sludge mixture used.

Parameters	Sludge mixture	Inoculum
Total solids (TS) ($gTS \cdot kg_{FM}^{-1}$) ^(a)	26 ± 6	20 ± 2
Volatile solids (VS) ($gVS \cdot kg_{FM}^{-1}$)	18 ± 5	12 ± 3
VS/TS (%)	70	59 ± 1
COD _{tot} ($gCOD \cdot kg_{FM}^{-1}$)	12	5.5
TVFA ($mgCOD \cdot L^{-1}$)	1254 ± 130	224
Alkalinity ($mgCaCO_3 \cdot L^{-1}$)	1629 ± 261	5666 ± 148

^(a)FM: fresh matter.

lent COD. Total COD was determined according to Standard Methods 5220 [22]. Biogas composition (CO_2 , CH_4 , H_2 , O_2 , and N_2) was characterized twice a week using gas chromatography (DANI Master GC Analyser equipped with two columns HayeSep Q and Molesieve 5A). The Automatic Methane Potential Test System II (AMPTS II, Bioprocess Control®) was used for BMP determinations. Tests were performed in duplicate, at mesophilic conditions ($35 \pm 0.5^\circ C$) and adopting a substrate to inoculum (S/I) ratio of 0.5 on VS base according to the Italian BMP standard method [23].

2.5. Statistical Analysis. Statistical analyses were carried out using the SPSS v.25 software in order to assess: (i) the repeatability in the operation of the two reactors, R1 and R2, and (ii) the significance of the differences observed between the eight experimental periods. Data distributions were firstly verified, both graphically (results not shown) and numerically. The Kolmogorov-Smirnov and Shapiro-Wilk tests (significance level = 0.05) were used to test variables against normality. As normality conditions were not always satisfied, the nonparametric Mann-Whitney U test and Kruskal-Wallis test (significance level = 0.05) were used to compare the selected dependent variables to the independent categorical variables of interest (reactors or periods).

2.6. Sampling, Amplification of 16S rRNA Gene, Sequencing, and Sequence Analyses. A total of 16 samples were taken from R1 and R2 reactors for high throughput 16S rRNA gene sequencing for microbial community analyses. Sampling points were selected according to the following scheme: one sample was collected at the end of Periods IV (R1-IV and R2-IV) and V (R1-V and R2-V), two during Period VI (R1-VI and R2-VI), one at the end of Period VII (R1-VII and R2-VII), and three in the last Period VIII (R1-VIII_a; R1-VIII_b; R1-VIII_c; R2-VIII_a; R2-VIII_b; R2-VIII_c), as summarized in Figure 1.

Samples were centrifuged (7000 rpm, at $4^\circ C$ for 10 min) to obtain around 2 g of cell pellet. The total microbial DNA was extracted using FastDNA Spin for Soil kit (MP Biomedicals, Solon, USA) according to the manufacturer's protocol. The bacterial V5-V6 hypervariable regions of the 16S rRNA gene were PCR-amplified using 783F and 1046R primers [24, 25], while for the archaeal communities a fragment of the 16S rRNA gene was PCR-amplified using the IA_349F-IA_571R primers [26]. The multiplexed libraries were

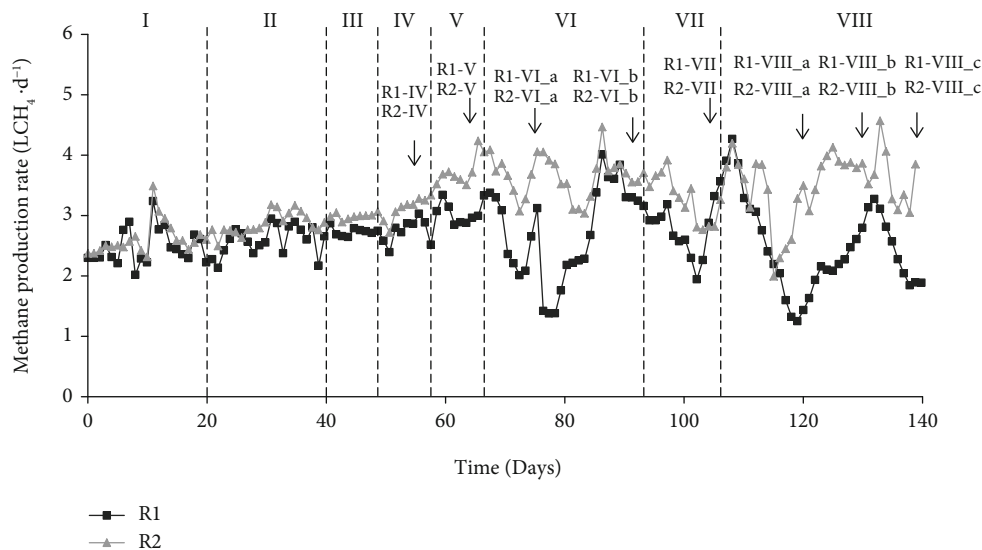


FIGURE 1: Methane rate produced by R1 and R2 reactors during the experiment; arrows indicate DNA extraction sampling points: labels include the name of the reactor sampled (R1 or R2), the experimental period in roman letters, and when needed, a letter to distinguish samples from the same reactor and period (a, b, or c).

prepared using a dual PCR amplification protocol. The bacterial PCR was performed in $2 \times 50 \mu\text{L}$ volume reactions with GoTaq[®] Green Master Mix (Promega Corporation, Madison, WI) and $1 \mu\text{M}$ of each primer, and the cycling conditions were initial denaturation at 98°C for 30 s; 20 cycles at 98°C for 10 s, 47°C for 30 s, and 72°C for 5 s; and a final extension at 72°C for 2 min. The archaeal PCR was performed in $4 \times 25 \mu\text{L}$ volume reactions with Phusion high fidelity polymerase (Thermo Scientific) and $2 \mu\text{M}$ of each primer, and the cycling conditions were initial denaturation at 96°C for 4 min; 10 cycles at 96°C for 30 s, 68°C for 30 s, and 72°C for 25 s; then 30 cycles at 96°C for 30 s, 58°C for 30 s, and 72°C for 25 s; and a final extension at 72°C for 5 min. Amplicons were purified with the Wizard[®] SV Gel and PCR Clean-up System (Promega Corporation, Madison, WI, USA) according to the manufacturer's instructions. After the purification, DNA quality was evaluated spectrophotometrically, and DNA was quantified using Qubit[®] (Life Technologies, Carlsbad, CA). The Illumina Miseq sequencing was carried out at Consorzio per il Centro di Biomedicina Molecolare (Trieste, Italy). Reads from sequencing were de-multiplexed according to the indexes and then quality filtered. Quality-filtered reads were assembled into error-corrected amplicon sequence variants (ASVs) using DADA2 v1.4.0 [27], which represent unique bacterial/archaeal taxa. Assembled ASVs were assigned taxonomy (phylum to species) using the Ribosomal Database Project (RDP).

Rarefaction curves were performed using the PAST3 software. Heat maps were produced with the STAMP software. Nonmetric multidimensional scaling (NMDS) analyses based on Bray-Curtis dissimilarity index were conducted using the vegan packages of R (R version 3.6.0). The discussion of the data is focused on the most abundant bacterial and archaeal genera in the community with relative abundance of at least 0.5% for archaea and >1% for bacteria.

3. Results and Discussion

3.1. Repeatability between Reactor Operation. The repeatability between reactors was statistically tested to assess whether it was reliable to group output data. For this purpose, 5 variables were used: three "gas phase" variables, biogas rate, and its composition (CH_4 and CO_2) and two "liquid phase" variables, alkalinity, and TVFA. They were evaluated either pooling all the data together, independently on the period (case A) or separating testing variables period by period (case B). As for case A, variability in data distributions was found between R1 and R2 if considering biogas rate ($U = 15'727$; asymptotic significance, ASig. < 0.001; mean ranks, MRk: R1 = 103; R2 = 182). Results turned out opposite when testing CH_4 ($U = 1'009$, ASig. = 0.097, MRk: R1 = 55.3; R2 = 45.7) and CO_2 contents ($U = 1'416$, ASig. = 0.252, MRk: R1 = 47.2; R2 = 53.8) as well as alkalinity ($U = 1'148$, ASig. = 0.054, MRk: R1 = 38.3; R2 = 48.7) and TVFA ($U = 387$, ASig. = 0.352, MRk: R1 = 32.6; R2 = 28.4). Although the conditions inside R1 and R2 were found statistically similar, different distributions of data were observed in the biogas rate but displaying statistically comparable gas compositions. This is probably to be ascribed not only to the different microbial communities that developed between the two reactors (see par. 3.5) but also to specific local environmental conditions. After a certain period of H_2 dosing, bioreactors might have improved or conversely limited particular degrading pathways or secretion of specific enzymes. This aspect needs to be further investigated, by adopting a target-oriented experimental plan focused on this purpose. The period by period comparison (case B) between reactors provided more accurate results (see Table S1 in the Supplementary Material): different biogas rate distributions between reactors were observed for all eight periods with significance values well below the 0.05. Conversely, CO_2 and CH_4 content distributions were the

same for R1 and R2 during all periods, except Periods I (exact significance, Sig. = 0.021) and VI (Sig. = 0.008). Results on alkalinity and TVFA confirm what observed testing the entire set of data, from Period I to Period VIII: the chemical conditions inside R1 and R2 were always statistically comparable, except for Periods VI (Sig. = 0.004) and VIII (Sig. = 0.004). It should be noted that Period VI corresponds to the stoichiometric dosage of H₂: starting from this period, significant variability is expected. Based on this statistical analysis, all results obtained are presented and discussed separately for the two reactors, especially with reference to the biogas rate.

3.2. Statistical Significance of Biogas Upgrading. The three “gas phase” variables were statistically tested using the non-parametric, Kruskal-Wallis test to verify the significance of the observed differences between the eight periods (see Table S2 in the Supplementary Material). Significance values were found below 0.001 for all the three variables, then providing strong evidence of a difference between the mean ranks of at least one pair of periods. Following the rejection of Kruskal-Wallis tests, post hoc procedure for pairwise multiple comparisons was performed to identify which pairs were different. Dunn’s pairwise tests were carried out using the Bonferroni correction to adjust the rejection level on the total number of tests (results are summarized in Table S3, Supplementary Materials). This test revealed that, for both reactors, the biogas rate produced during Period I becomes statistically different starting from Period V when approaching the stoichiometric dosage of H₂; then, a different behaviour between R1 and R2 was observed: as for R1, the biogas rate produced during Periods VII (Sig. = 0.109) and VIII (Sig. = 0.878) returned being statistically the same as what was produced during Period I. Conversely, the biogas rates produced during Periods from V to VIII in R2 present strong evidence (Sig. < 0.026) of being statistically different from those produced in both Periods I and II. Similar results were observed for CO₂ and CH₄ content, instead: changes in biogas composition become statistically different from Period II, starting from Period VI (Sig. < 0.043); increasing the H₂/CO₂ ratio above the stoichiometric, however, did not change significantly, from a statistical point of view, the biogas composition.

3.3. Reactor’s Performance

3.3.1. Period I: Pre-H₂ Phase. As shown in Figure S1 in Supplementary Materials, during Period I, initial variability of methane yields was observed in both reactors. However, after 97 days, corresponding to three HRTs, the steady-state was reached in both reactors, and methane yields of 0.26 and 0.28 NLCH₄•gVS⁻¹ for R1 and R2, respectively, resulted being comparable to the BMP values (0.229 ± 0.001 and 0.210 ± 0.002 NLCH₄•gVS⁻¹) measured at the beginning and at the end of the experiment. Table 3 reports the average gaseous flows of methane, carbon dioxide, and hydrogen throughout the periods of the experiment for the two parallel reactors. Since the beginning, higher CO₂ and CH₄ production rates are observed in reactor R2, compared

TABLE 3: Summary of reactors’ gas mass flow (CO₂, CH₄, and H₂) during the experimental periods.

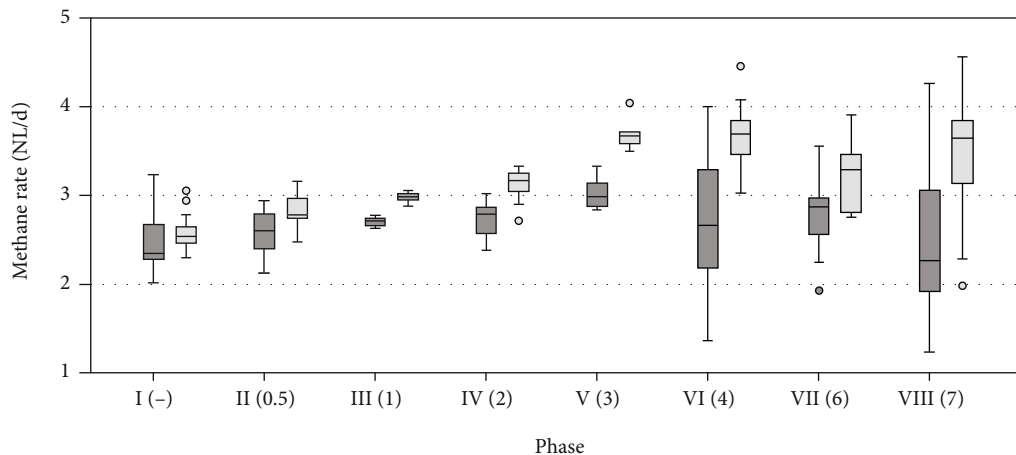
Period–H ₂ /CO ₂	CO ₂ (NmL•d ⁻¹)		CH ₄ (NmL•d ⁻¹)		H ₂ (NmL•d ⁻¹)	
	R1	R2	R1	R2	R1	R2
I	788	894	2597	2772	0	0
II-0.5	955	1054	2813	3137	27	33
III-1	962	1034	2985	3319	42	28
IV-2	953	1094	3161	3612	43	38
V-3	1004	1307	3628	4404	54	65
VI-4	605	1147	3454	4542	203	349
VII-6	575	864	3597	4329	134	229
VIII-7	297	440	3353	4970	235	348

to R1, although similar biogas composition is detected. Such deviation in the biogas rate between R1 and R2 increases during the experiment, despite the same feeding being maintained during all periods: this is probably due to small unintentional changes in the environmental conditions of the two reactors which could have led to different speciation in the microbial community (i.e., alkalinity, nutrients, and VFA, which could, for example, determine the secretion of different specific enzymes). Under normal conditions, such variations result in negligible effects, such as the slightly higher concentrations of unconverted VFA found in R1 up to phase IV. Thereafter, starting to stress the system with H₂ dosing, it is possible that the process turned out to be more sensitive even to small variations, then resulting in more pronounced differences between reactors (see alkalinity and VFA concentrations starting from phase V, when approaching the stoichiometric H₂/CO₂ ratio), which led to the diverse rates of biogas produced reported in Table 3.

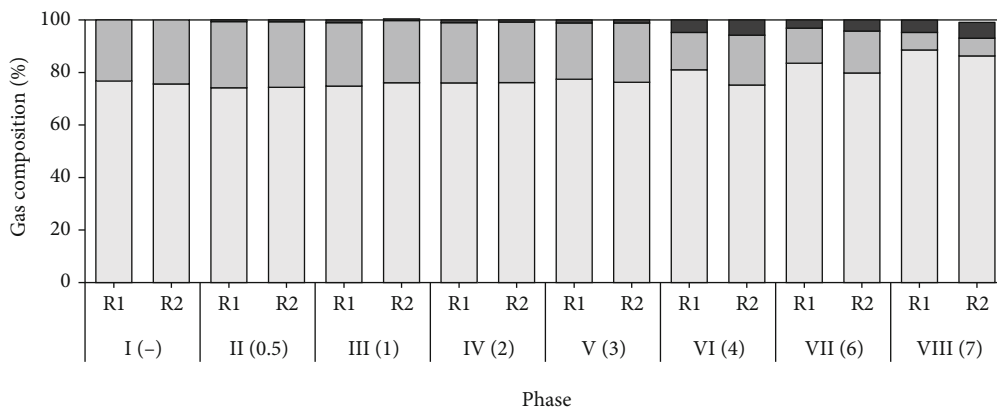
Figure 2 shows, for both reactors, mean values of parameters monitored for each period.

Reactors behaved similarly during Period I, with high methane (76.2%) and low CO₂ (23.8%) contents in the biogas (Figure 2(b)) and comparable alkalinity (Figure 2(c)) and TVFA concentrations (Figure 2(d)), with the acetic acid prevailing.

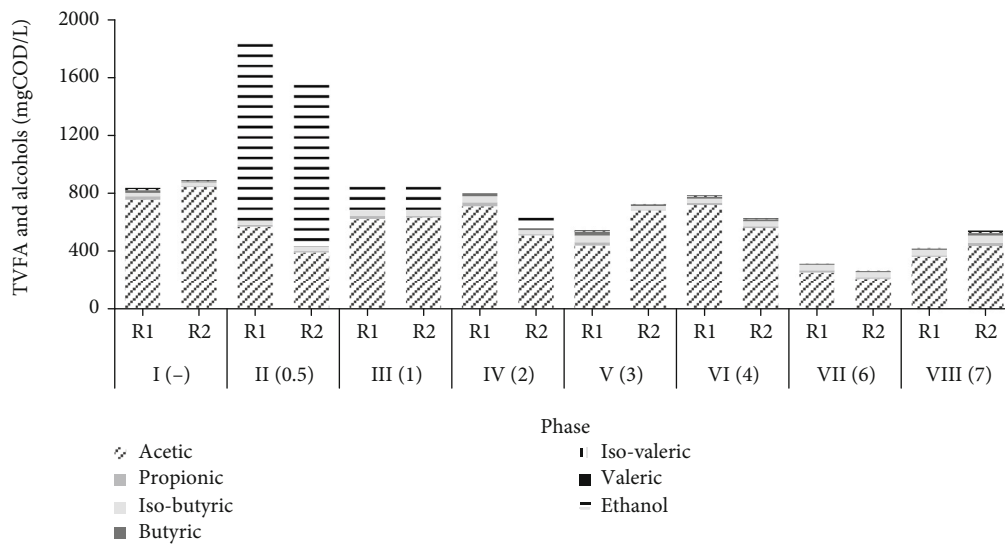
3.3.2. Periods II-VI: Enrichment of the Hydrogenotrophic Methanogens. During Periods II to VI (days 21-94), H₂ was injected by progressively incrementing the dosage. Since very low concentrations were detected in the output gas, it can be concluded that H₂ was completely consumed by the process, while observing a slight increase in the produced methane rate as shown in Figure 2(b). This confirmed that hydrogenotrophic methanogens usually work below their H₂ rate consumption capacity [28], then being able to consume more hydrogen available as soon as they come into contact with it. Furthermore, the anaerobic degradation of the substrate was not affected, and VFAs were easily consumed during the process as no accumulation was observed: biogas production was stable as well as volatile solids degradation, as reported in Table 4. However, as shown in Figure 2(c),



(a)

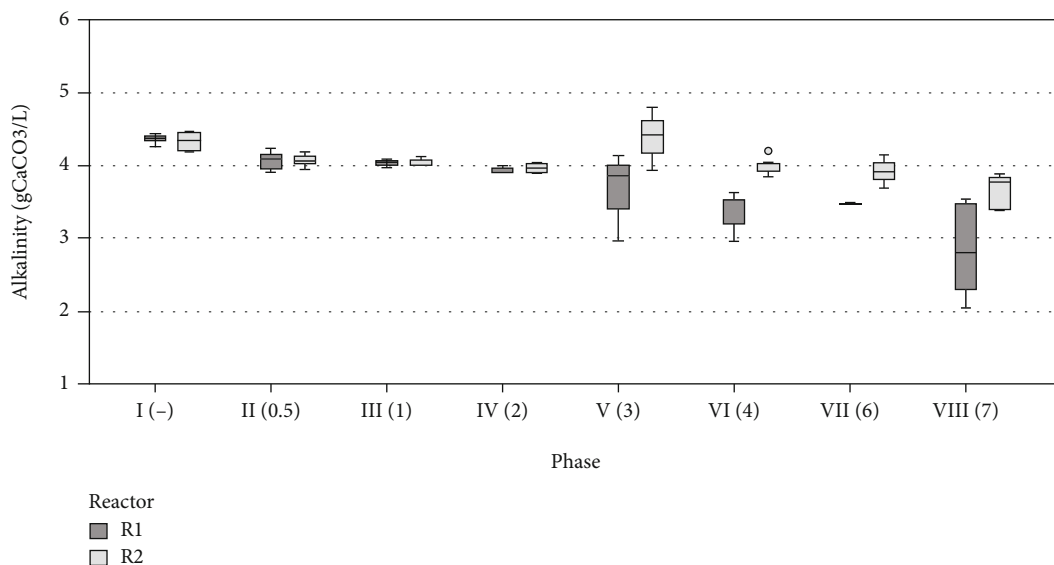


(b)



(c)

FIGURE 2: Continued.



(d)

FIGURE 2: Mean values of parameters measured during each of the eight experimental periods (in brackets the H_2/CO_2 ratio): (a) box plots of methane rate (circles indicate outliers); (b) biogas composition; (c) TVFA composition and alcohols; (d) box plots of alkalinity concentrations (circles indicate outliers).

TABLE 4: Summary of reactor alkalinity and VS removal during the experimental periods.

Period	Reactor	Alkalinity (gCaCO ₃ •L ⁻¹)	VS removal (%)
I	R1	4.36	39%
	R2	4.33	37%
II	R1	4.04	44%
	R2	4.07	42%
III	R1	4.04	39%
	R2	4.01	40%
IV	R1	3.96	45%
	R2	4.02	47%
V	R1	3.99	41%
	R2	4.37	42%
VI	R1	3.36	35%
	R2	4.06	32%
VII	R1	3.48	39%
	R2	3.92	34%
VIII	R1	2.16	37%
	R2	3.63	32%

ethanol peaks of 3.2 and 1.4 gCOD•L⁻¹ in reactors R1 and R2 were reported during Phase II, immediately in response to H_2 injection. To the best of the authors' knowledge, in the recent literature on *in situ* biogas upgrading, ethanol accumulation has not yet been reported. It can probably be ascribed to the regulatory role of H_2 in the normal operation of anaerobic digesters. Ethanol is formed from sugars during the acidogenesis step [29], and it is generally oxidized by syntrophic bacteria and methanogens [30, 31]. Low H_2 concentrations allow thermodynamic degradation

of alcohols and fatty acids by H_2 -producing syntrophic bacteria [30]; thus, the amount of extra H_2 provided to a biomass which is not yet properly acclimatized influenced alcohol oxidation, possibly leading to the ethanol accumulation. Nevertheless, although the H_2 supply was not interrupted, ethanol decreased to 0.2 gCOD•L⁻¹ in both reactors during Period III (H_2/CO_2 1 : 1) and was almost completely depleted in Period IV. This is probably due to an increased activity of H_2 -scavenging microorganisms, which have promptly reduced the exogenous H_2 , then allowing for alcohol degradation.

Furthermore, it is generally reported that around 40% of the total H_2 provided is utilized via homoacetogenesis plus acetoclastic methanogenesis pathways [32]. Despite this, in this study, the acetate concentrations registered were stable in both reactors (0.6 gCOD•L⁻¹ in R1 and 0.4 gCOD•L⁻¹ in R2), which appears to be in contrast with this significant H_2 consumption route.

When reaching the stoichiometric H_2/CO_2 (4 : 1) value in Period VI, high variability in the biogas yield was observed in R1, with a methane production rate varying from 1.5 up to 4 NLCH₄•d⁻¹ (Figure 2(a)). Regardless of the unstable biogas rate, CO₂ content decreased to 14% while CH₄ rose to 81%. R2 behaved differently, having restrained variations of biogas and methane rates (3 up to 4.46 NLCH₄•d⁻¹) but with a lower reduction of CO₂ content (from 23 to 19%) and CH₄ increase (75%) (Figure 2(b)). The authors believe that the lower production of biogas in R1 led to a higher amount of H_2 available for a lower quantity of CO₂ produced, thus allowing for higher CO₂ conversion.

3.3.3. Periods VI-VIII: Overstoichiometric Assessment. In Periods VII and VIII, both reactors were operated at H_2/CO_2 ratio of 6 : 1 and 7 : 1. In the first overstoichiometric period, CO₂ was further converted in order to achieve a CH₄ content of 84% and 80% in R1 and R2, respectively. VFAs

TABLE 5: Summary of literature studies of the in situ biogas upgrading technology associated with H₂ injection.

Substrate	Reactor type	Reactor volume (L)	OLR (gVS·L ⁻¹ ·d ⁻¹)	T (°C)	pH	HRT (d)	H ₂ (LH ₂ ·L ⁻¹ ·d ⁻¹)	H ₂ /CO ₂	H ₂ conversion (%)	CO ₂ removal (%)	CH ₄ (%)	Ref.
Potato starch	UASB	1.4	2.79	55	8.4	7	3.5	4:1	67	76	82	Bassani et al. [48]
Cattle manure	CSTR	0.6	1.85	55	8.3	14	1.8	4:1	>90	N/D	65	Luo et al. [13]
Cattle manure and cheese whey	CSTR	0.6	1.66	55	7.7-7.9	15	1.5-1.7	4:1	N/D	85	75	Luo and Angelidaki [49]
Cattle manure and cheese whey	CSTR	0.6	1.66	55	7.6-8.3	15	0.9-1.8	4:1	N/D	53-91	78-96	Luo and Angelidaki, [16]
Sewage sludge	CSTR	3	1.08	37	8.0	10	0.6-1.3	4:1	96	99	99	Wang et al. [33]
Sewage sludge	Batch	2	0.77	38	7.9-8.4	20	0.3-1.7	2:1-10:1	58-99	43-100	79-92	Agneessens et al. [19]
Sewage sludge	Semicontinuous	2.4	1-1.12	35	7.0-7.4	15	0, 0.62-0.2	1:1-4:1	96-100	13-49	80	Corbellini et al. [21]
Sewage sludge	CSTR	16	1.5	36.7	7.4	22	0.4-5.5	0-7:1	94-99	96.5	90.3	This study

CSTR: continuous stirred tank reactors; HRT: hydraulic retention time; OLR: organic loading rate; UASB: upflow anaerobic sludge blanket.

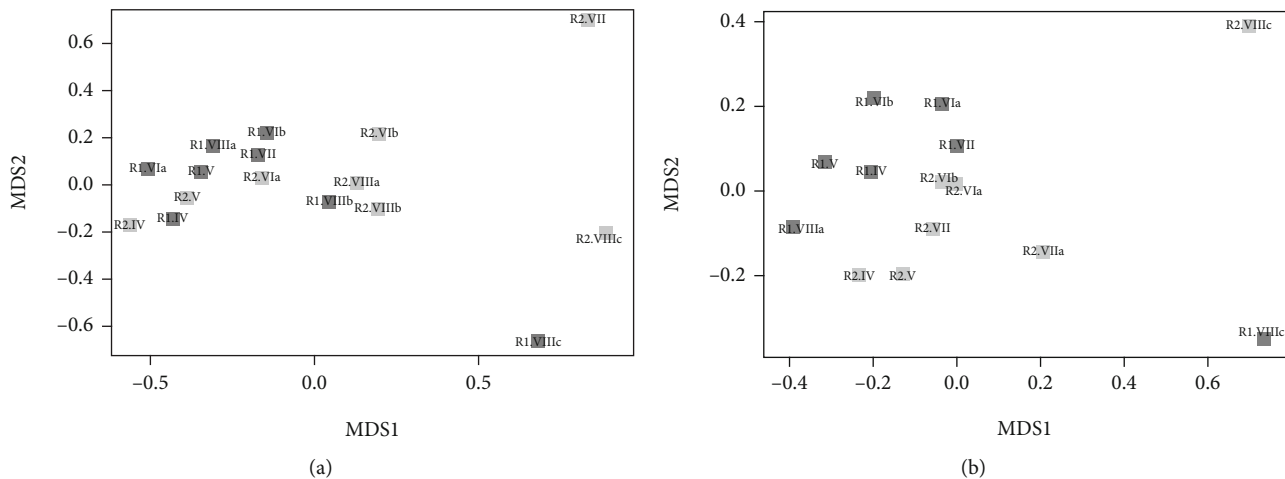


FIGURE 3: Nonmetric multidimensional scaling plots based on Bray–Curtis distances of the bacterial (a) and archaeal (b) communities at ASV level in R1 (light grey) and in R2 (dark grey).

were very low, indicating a stable process. When the H_2/CO_2 ratio was further increased to 7 : 1, both R1 and R2 showed a maximum methane production rate of 4 and 4.5 $NmLCH_4 \cdot d^{-1}$, even though R1 displayed high variability. Furthermore, VFAs and ethanol were almost constant. In this final period, R1 reached the lowest CO_2 content of 4.5% and the maximum CH_4 content of 90.3% (Figure 2(b)). The organic substrate degradation was not negatively affected by exogenous H_2 injections. Indeed, a BMP test on the sludge mixture was carried out (day 137), using as inoculum a mixture of digestates taken from the two reactors. This resulted in $210 \pm 1.5 NmLCH_4 \cdot gVS^{-1}$, a value comparable to $229 \pm 1 NmLCH_4 \cdot gVS^{-1}$ obtained at the beginning of the test using the digestate from the WWTP Bresso as inoculum.

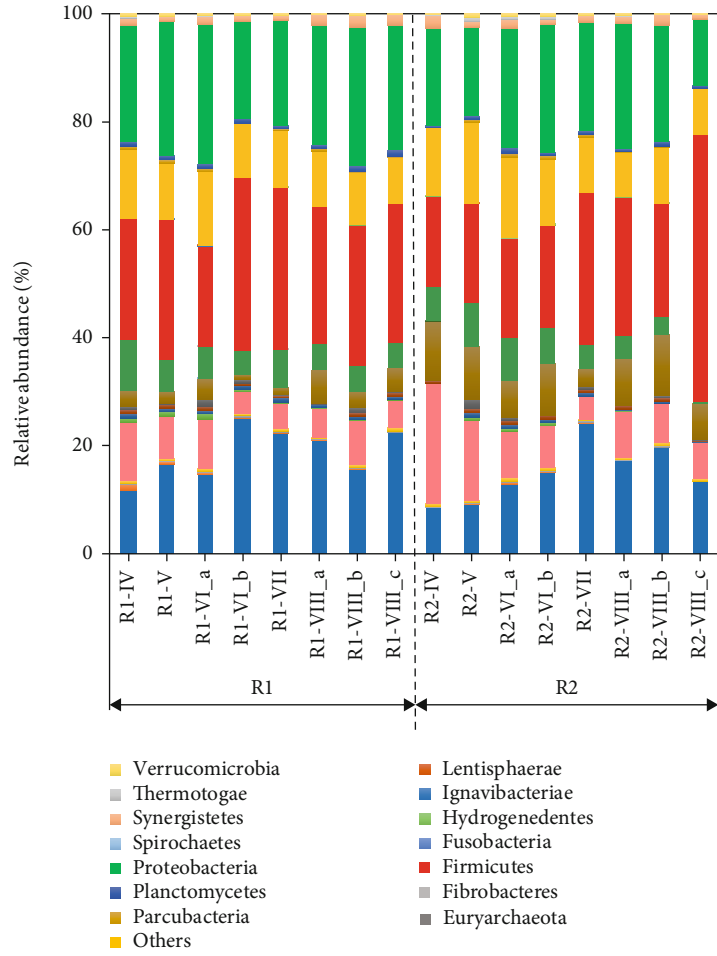
3.3.4. Comparison with Literature. Table 5 summarizes several studies on the *in situ* biogas upgrading by H_2 injection at different operational conditions. It can be seen that few studies pertaining to the *in situ* biogas upgrading process performed at mesophilic conditions with sewage sludge allow a direct comparison with the present work. Wang et al. [33] utilized Synthetic Coke Oven Gas (SCOG 92% H_2 and 8% CO), as hydrogen source injected, with a hollow fibre membrane (HFM) module, into a CSTR applying the stoichiometric biomethanation ratio ($H_2/CO_2 = 4 : 1$). Biogas was completely upgraded (98–99 $CH_4\%$) only when pH value was fixed at 8. Agneessens et al. [19] tested pulse H_2 injections in batch mode with a H_2/CO_2 ratio varied from 2 : 1 to 10 : 1. The ratio 8 : 1 turned out to be the best choice with a final CO_2 content of 11.8%. Later on, in a study performed by Corbellini et al. [21], the H_2/CO_2 ratio was increased from 1 : 1 to a maximum of 4 : 1 in a semicontinuous mode, but the CH_4 fraction reached in the biogas was a maximum 80%. The present study investigated the process with higher volumes (16 L) than all previous studies where the volume adopted was always lower than 3.5 L [49]. The H_2 injection was tested with in a wider range of H_2/CO_2 ratios and in CSTR bioreactors. Moreover, the repeatability of the process was evaluated with two parallel operating reactors, a topic that has never been addressed previously. The effects of the aforementioned

aspects on biological H_2 and CO_2 methanization behaviour are of great importance for practical application with a view towards larger-scale studies.

3.4. Alkalinity Trends over $CO_2\%$. Mean values of alkalinity concentrations in both reactors are reported in Figure 2(d). From Period II, alkalinity was consumed in both reactors along with the progressive increase of the H_2/CO_2 ratio. This evidence is directly related to CO_2 consumption in the liquid phase, in accordance with a previous study [33]. The overall CO_2 reduction, at the end of the experiment, was significantly higher in R1 (-40%) than in R2 (-14%) (Table 4), also confirmed by the lower CO_2 content registered in the output biogas. The buffer capacity of anaerobic digesters is crucial to maintain neutral and stable pH values. For this reason, full-scale applications of the *in situ* upgrading process are limited if the influent organic substrate is not sufficient to restore alkalinity.

3.5. High Throughput 16S rRNA Gene Amplicon Analysis. As shown in Table S4 in Supplementary Materials, a total of 514,295 (bacteria) and 495,983 (archaea) reads were obtained from the 16 samples. All of them, except the archaeal R1-VIII_b and R2-VIII_b, reached a plateau, indicating that the number of ASVs covered the sample richness (Figure S2 in Supplementary Materials). Given not satisfactory archaea sequencing results of R1-VIII_b and R2-VIII_b (only around 200 reads and 5 ASV), these samples were not included for the further analyses. The evolution of the microbial communities over time and with respect to the digesters was performed by NMDS analysis (Figure 3).

For bacteria, distinct clusters could not be observed, while samples collected from the two reactors during the same period are closed to each other suggesting an evolution of the community due to the different operational parameters applied in the different experimental periods. On the contrary, for archaea, two clusters, which contain most of the samples of R1 and R2, could be identified. A neat shift of the community occurred at the end of the operational time



(a)

FIGURE 4: Continued.

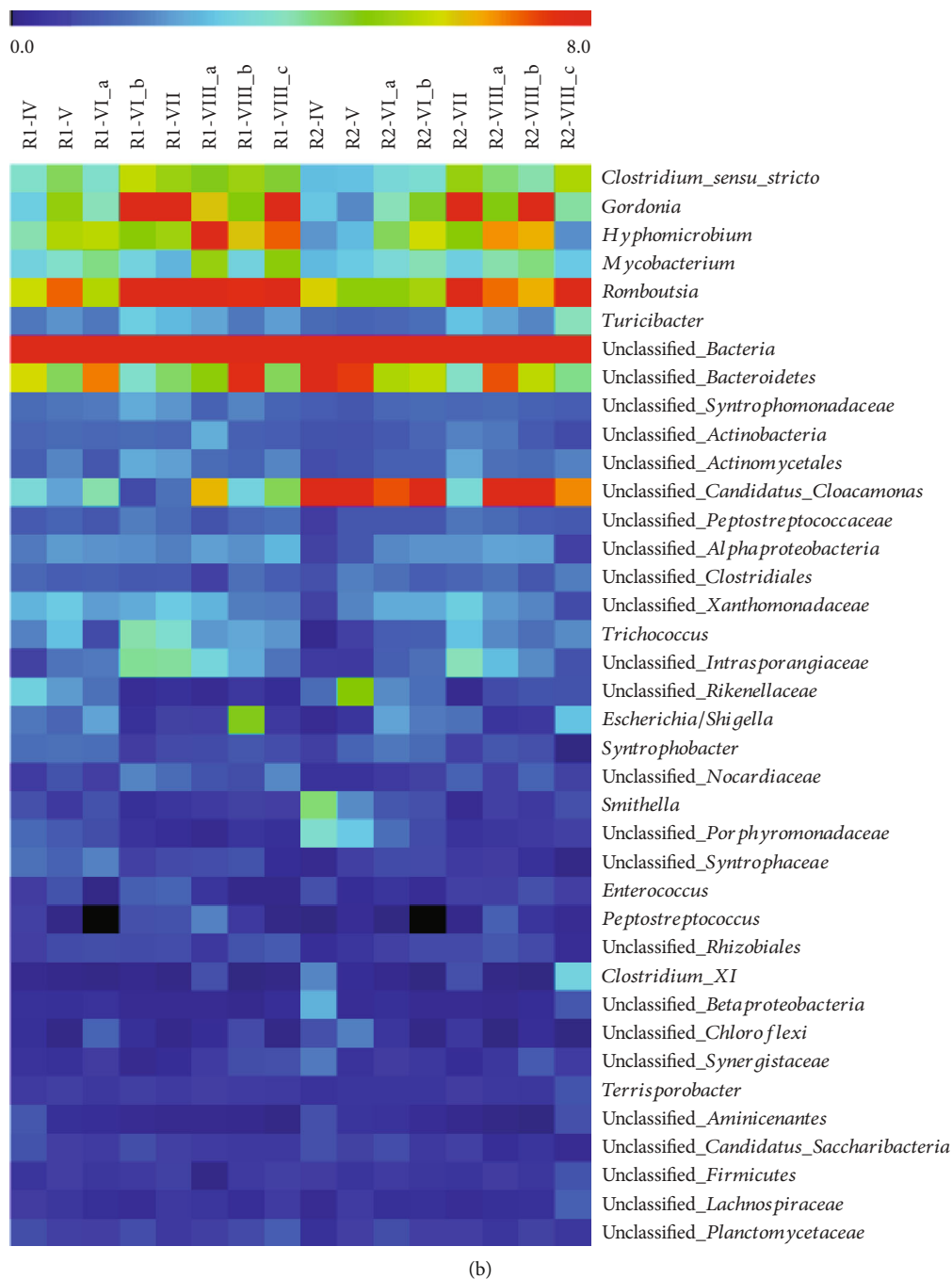
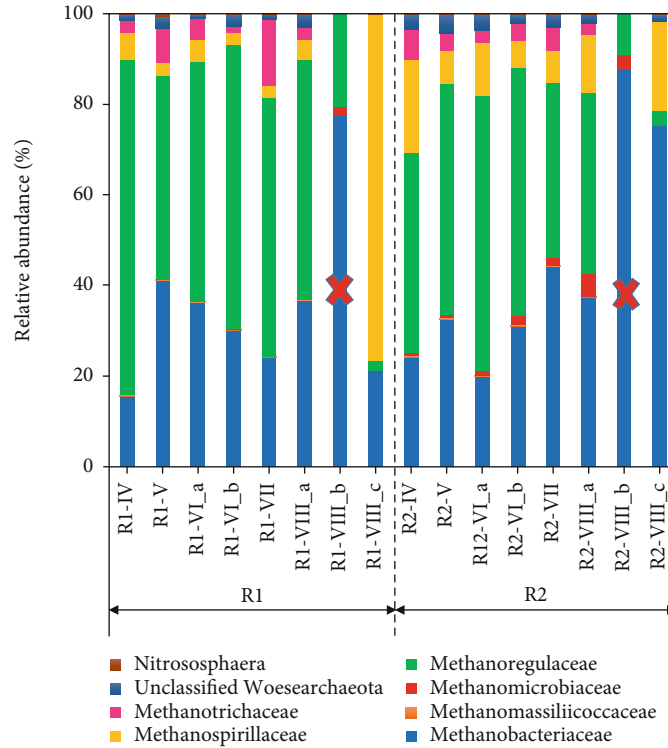


FIGURE 4: (a) Relative abundance of the bacterial phyla of two parallel reactors at several sampling points. (b) Heat maps of relative abundance (>1%) of the most abundant bacterial ASVs of R1 and R2. The scale limit starts from 0 (abundance equal to 1% because of the selection) to 8%. Increasing red colour indicates a higher value of relative species abundance, and blue colour indicates a lower relative abundance.

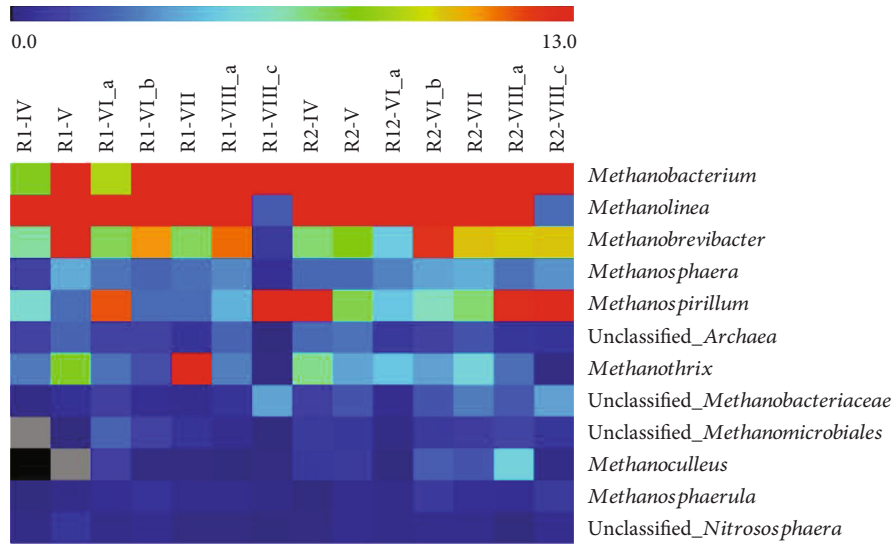
because R1_VIIIc and R2_VIIIc are completely separated from the rest of the samples.

3.5.1. Bacterial Community Composition. The bacterial community consisted of Firmicutes (17%-50%), Proteobacteria (12%-26%), Actinobacteria (9%-25%), and Bacteroidetes (4%-22%), while other phyla, such as Unclassified_bacteria (8%-15%), Cloacimonetes (1% -11%), and Synergistetes (1%-2%), were less abundant (Figure 4(a)). Relative abun-

dances of the bacteria at the genus level are shown in Figure S3 of the Supplementary Materials. As in previous studies, the dominance of Firmicutes and Bacteroidetes in digesters is frequently observed [34], as they are hydrolytic bacteria [33, 35, 36] responsible for the breakdown of polymeric substrates, such as proteins, lipids, and polysaccharides. Proteobacteria, known as acidogenic bacteria, was one of the dominant phyla in this study, in line with previous studies in AD [36, 37]. It can be seen



(a)



(b)

FIGURE 5: (a) Relative abundance of the archaeal community structure on the family level. R1_III b and R2_III b labelled with “X” are without consideration due to unideal archaea sequencing results. (b) Heat maps of relative abundance (>0.5%) of the most abundant archaeal ASVs of R1 and R2.

that the bacteria related to hydrolysis and acidogenesis processes constitute a large proportion, over 60%, of total bacteria [38]. Their proportion rose with the increase in the H_2/CO_2 ratio suggesting that increasing H_2 dosage promoted the development of a microbial consortia enriched with hydrolytic and acidogenic bacteria, which enhanced the methane yield and purity. All further discussions on microbial analysis results were focused only on the most abundant

ASVs with a relative abundance > 1%. 38 ASVs represent the most abundant members in all the samples. The evolution of the most abundant genera detected in the two reactors is represented as heat map at a genus level in Figure 4(b).

Unclassified_Bacteroidetes Romboutsia, *Unclassified_Candidatus_Cloacamonas*, *Hyphomicrobium*, and *Mycobacterium* were found to be the predominant genera in both reactors. *Unclassified_Bacteroidetes*, known to be involved

in the polysaccharide and protein hydrolysis step during the AD process [39], were constantly present with an average of 7% in both reactors during all experimental periods. *Romboutsia*, known as homoacetogens [40], increased its relative abundance constantly from 5% to 9% during the experiment. However, the recorded increases of *Romboutsia* do not seem to be confirmed by the low levels of acetate found during the experimental trial. This is probably due to the faster acetate consumption dynamics of acetoclasts in forming methane, compared to the acetate sampling and measurement intervals. Another most abundant bacterial genus was *Hyphomicrobium*, which increased in both reactors from 3.9% to 7.1% in R1 and 2.1% to 6.4% in R2. Bacteria belonging to this genus are known to cooperate with methanogens (i.e., *Methanosarcina*) in simultaneous denitrification and methanogenesis [41] and the aforementioned *Romboutsia* (from 5.8% up to 8.7% relative abundance) indicating a constant H₂ consumption also by homoacetogenesis. Also, members belonging to *Gordonia* increased in both reactors (from 3% up to 9% in R1 and 3% to 8% in R2). These bacteria are known to be able to degrade environmental pollutants such as polycyclic aromatic hydrocarbons [42] that are normally present in wastewater activated sludge [43].

3.5.2. Archaeal Community Composition. In the archaeal community patterns, two phyla, Euryarchaeota (98%) and Woesearchaeota (1.5%), and 8 families were identified. In Figure 5(a), the most abundant families in all samples are Methanobacteriaceae (16%-75%), Methanoregulaceae (2%-74%), and Methanospirillaceae (3%-76%). According to the heat map at the general level (Figure 5(b)), five genera, i.e., *Methanolinea* (3%-74%), *Methanobacterium* (8%-73%), *Methanobrevibacter* (0-15%), *Methanospirillum* (0-21%), and *Methanotherix* (0-15%), can be considered as the core community displaying more than 90% abundance of each sample and confirming their key role in digesters (relative abundances of the archaea at the genus level are shown in Figure S4 of the Supplementary Materials). It is well known that *Methanolinea*, *Methanobacterium*, *Methanobrevibacter*, and *Methanospirillum* are the most common hydrogenotrophic methanogens [38, 44], for their ability to scavenge H₂ by maintaining a low pH.

Among the archaeal community, *Methanotherix* (also called *Methanosaeata*) with a 100% similarity to *Methanotherix soehngenii* [45, 46] was the only acetoclastic methanogen detected (5.5% in R1 and 4.5% in R2 till VIII_a). Overall, these findings strongly confirmed the dominance of hydrogenotrophic methanogens among the archaeal community in both systems, indicating that the increasing H₂ dosage is an effective way to promote the growth of hydrogenotrophic rather than acetoclastic methanogens.

Something worthy of note was that the hydrogenotrophic methanogens differed during the H₂ dosage periods. More specifically, the most abundant genus *Methanolinea* was present in most samples except R1_VIII_c and R2_VIII_c. The NDMS results showed that most samples clustered together except these two samples. The second most abundant genus was *Methanobacterium*, *Methanobacterium palustre* which is known to utilize H₂/CO₂, for its growth

and/or methane production [47]. Its abundance gradually increased with the increase of the H₂/CO₂ ratio demonstrating its role in the biogas upgrading.

4. Conclusions

The following conclusions can be drawn from the experimentation performed: (i) as already found with other studies [19], the stoichiometric H₂/CO₂ ratio (4:1) is not sufficient to complete the CO₂ conversion to CH₄ and achieve interesting low percentages of carbon dioxide in the biogas; this is also very likely affected by the H₂ injection mode which determine the diffusion of the gas in the liquid phase. Further research is needed in order to optimize the hydrogen gas transfer process; (ii) by increasing the H₂/CO₂ ratio to 7:1, it was possible to efficiently maximize the CO₂ conversion for the production of a biogas mainly composed of methane (max 90.3%); (iii) the sewage sludge degradation was not negatively affected by the incremental supplying of H₂, while a significant alkalinity consumption was observed. In order not to impair the process, it is crucial to ensure that the organic influent is capable of reintegrating the alkalinity consumed; (iv) the efficiency of the process was ensured by the development of a specialized community, composed mainly of *Methanobacterium*, *Methanobrevibacter*, *Methanospirillum* (hydrogenotrophic methanogens), homoacetogens, hydrolytic, and acidogenic bacteria, thanks to the enrichment strategy; (v) during H₂ periods, the two parallel reactors produced different methane rates but displayed similar trends. The results of this experiment are quite robust and repeatable, but further studies focused on this topic are needed in order to assess how the performance of the process, while introducing high concentrations of hydrogen, is susceptible to common small differences normally establishing in anaerobic digesters.

Data Availability

All data used to support the findings of this study are available from the corresponding author upon request.

Conflicts of Interest

The authors declare that there is no conflict of interest regarding the publication of this paper.

Acknowledgments

The authors would like to thank Nadia Margariti and DISAT laboratory (Bicocca University of Milan) for their support in the laboratory activities.

Supplementary Materials

A Supplementary Materials file is provided, including: Table S1: Mann–Whitney test results for comparison between R1 and R2: significance value, total number of samples tested, and mean ranks calculated for the two reactors. Cases where null hypothesis is rejected are highlighted in grey. Table S2: Kruskal–Wallis test results for comparison between phases

of reactors R1 and R2: significance value, total number of samples tested, and test statistic value. Cases where null hypothesis is rejected are highlighted in grey. Table S3: Dunn's pairwise test (Bonferroni correction) for multiple comparisons between phases of reactor R1 and R2: significance value. Cases where null hypothesis is rejected are highlighted in grey. Figure S1: methane yields during the start-up period without H₂ addition, both for reactor R1 and R2. Table S4: read and amplicon sequence variants (ASV) distribution derived from the 16 samples in two parallel CSTR anaerobic digesters. Figure S2: rarefaction curves of the ASV obtained from 16S rRNA gene analysis of the bacterial community of R1 and R2 and (B) archaeal community in parallel anaerobic digestion reactors. Figure S3: relative abundance of the bacteria at the genus level of two parallel reactors at several sampling points. Figure S4: relative abundance of the archaea at the genus level of two parallel reactors at several sampling points. (*Supplementary Materials*)

References

- [1] M. Muntan, D. Guizzardi, E. Schaff, M. Crippa, E. Solazzo, J. Oliver et al., *Fossil CO₂ Emissions of all World Countries - 2018 Report*, Publications Office of the European Union, 2018.
- [2] J. Foley, D. de Haas, K. Hartley, and P. Lant, "Comprehensive life cycle inventories of alternative wastewater treatment systems," *Water Research*, vol. 44, no. 5, pp. 1654–1666, 2010.
- [3] O. W. Awe, Y. Zhao, A. Nzihou, D. P. Minh, and N. Lyczko, "A review of biogas utilisation, purification and upgrading technologies," *Waste and Biomass Valorization*, vol. 8, no. 2, pp. 267–283, 2017.
- [4] R. Muñoz, L. Meier, I. Diaz, and D. Jeison, "A review on the state-of-the-art of physical/chemical and biological technologies for biogas upgrading," *Reviews in Environmental Science and Biotechnology*, vol. 14, no. 4, pp. 727–759, 2015.
- [5] N. Alfaro, M. Fdz-Polanco, F. Fdz-Polanco, and I. Diaz, "Evaluation of process performance, energy consumption and microbiota characterization in a ceramic membrane bioreactor for ex-situ biomethanation of H₂ and CO₂," *Bioresource Technology*, vol. 258, pp. 142–150, 2018.
- [6] G. Guandalini, M. Robinius, T. Grube, S. Campanari, and D. Stolten, "Long-term power-to-gas potential from wind and solar power: a country analysis for Italy," *International Journal of Hydrogen Energy*, vol. 42, no. 19, pp. 13389–13406, 2017.
- [7] M. Carmo, D. L. Fritz, J. Mergel, and D. Stolten, "A comprehensive review on PEM water electrolysis," *International Journal of Hydrogen Energy*, vol. 38, no. 12, pp. 4901–4934, 2013.
- [8] C. Y. Gomec, V. Eroglu, and P. A. Wilderer, "Identifying acetoclastic and hydrogenotrophic methanogens in psychrophilic and mesophilic granular sludges treating synthetic sewage by means of FISH and CSLM," *Journal of Rapid Methods & Automation in Microbiology*, vol. 17, pp. 135–153, 2009.
- [9] G. Luo and I. Angelidaki, "Integrated biogas upgrading and hydrogen utilization in an anaerobic reactor containing enriched hydrogenotrophic methanogenic culture," *Biotechnology and Bioengineering*, vol. 109, no. 11, pp. 2729–2736, 2012.
- [10] I. Bassani, P. G. Kougias, L. Treu, H. Porté, S. Campanaro, and I. Angelidaki, "Optimization of hydrogen dispersion in thermophilic up-flow reactors for ex situ biogas upgrading," *Bioresource Technology*, vol. 234, pp. 310–319, 2017.
- [11] P. G. Kougias, L. Treu, D. P. Benavente, K. Boe, S. Campanaro, and I. Angelidaki, "Ex-situ biogas upgrading and enhancement in different reactor systems," *Bioresource Technology*, vol. 225, pp. 429–437, 2017.
- [12] V. Corbellini, P. G. Kougias, L. Treu, I. Bassani, F. Malpei, and I. Angelidaki, "Hybrid biogas upgrading in a two-stage thermophilic reactor," *Energy Conversion and Management*, vol. 168, pp. 1–10, 2018.
- [13] G. Luo, S. Johansson, K. Boe, L. Xie, Q. Zhou, and I. Angelidaki, "Simultaneous hydrogen utilization and in situ biogas upgrading in an anaerobic reactor," *Biotechnology and Bioengineering*, vol. 109, no. 4, pp. 1088–1094, 2012.
- [14] I. Angelidaki, L. Treu, P. Tsapekos et al., "Biogas upgrading and utilization: current status and perspectives," *Biotechnology Advances*, vol. 36, no. 2, pp. 452–466, 2018.
- [15] L. Rachbauer, G. Voitl, G. Bochmann, and W. Fuchs, "Biological biogas upgrading capacity of a hydrogenotrophic community in a trickle-bed reactor," *Applied Energy*, vol. 180, pp. 483–490, 2016.
- [16] G. Luo and I. Angelidaki, "Hollow fiber membrane based H₂ diffusion for efficient in situ biogas upgrading in an anaerobic reactor," *Applied Microbiology and Biotechnology*, vol. 97, no. 8, pp. 3739–3744, 2013.
- [17] S. Savvas, J. Donnelly, T. Patterson, Z. S. Chong, and S. R. Esteves, "Biological methanation of CO₂ in a novel biofilm plug-flow reactor: a high rate and low parasitic energy process," *Applied Energy*, vol. 202, pp. 238–247, 2017.
- [18] M. Peprah, P. G. Kougias, P. Tsapekos, L. Treu, S. Campanaro, and I. Angelidaki, "Ex-situ biogas upgrading in thermophilic reactors using membranes as gas diffusion devices," in *Abstract from 16th IWA World Conference on Anaerobic Digestion*, pp. 3–5, Delft, Netherlands, 2019.
- [19] L. M. Agneessens, L. D. M. Ottosen, N. V. Voigt et al., "In-situ biogas upgrading with pulse H₂ additions: the relevance of methanogen adaption and inorganic carbon level," *Bioresource Technology*, vol. 233, pp. 256–263, 2017.
- [20] R. Wahid, D. G. Mulat, J. C. Gaby, and S. J. Horn, "Effects of H₂:CO₂ ratio and H₂ supply fluctuation on methane content and microbial community composition during in-situ biological biogas upgrading," *Biotechnology for Biofuels*, vol. 12, no. 1, pp. 1–15, 2019.
- [21] V. Corbellini, A. Catenacci, and F. Malpei, "Hydrogenotrophic biogas upgrading integrated into WWTPs: enrichment strategy," *Water Science and Technology*, vol. 79, no. 4, pp. 759–770, 2019.
- [22] APHA, AWWA, and WEF, *Standard Methods for the Examination of Water and Wastewater, Centinial Addition*, American Public Health Association, American Water Works Association, and Water Environment Federation, 2010.
- [23] CTI - Biogas da fermentazione anaerobica e syngas biogenico, *Metodo per la misura della produzione potenziale di metano da digestione anaerobica ad umido - Matrici in alimentazione*, UNI - Ente Italiano di Normazione, 2018.
- [24] Q. Wang, G. M. Garrity, J. M. Tiedje, and J. R. Cole, "Naïve Bayesian classifier for rapid assignment of rRNA sequences into the new bacterial taxonomy," *Applied and Environmental Microbiology*, vol. 73, no. 16, pp. 5261–5267, 2007.

- [25] J. A. Huber, D. B. M. Welch, H. G. Morrison et al., "Microbial population structures in the deep marine biosphere," *Science*, vol. 318, no. 5847, pp. 97–100, 2007.
- [26] A. L. Gagliano, M. Tagliavia, W. D'Alessandro, A. Franzetti, F. Parello, and P. Quatrini, "So close, so different: geothermal flux shapes divergent soil microbial communities at neighbouring sites," *Geobiology*, vol. 14, no. 2, pp. 150–162, 2016.
- [27] B. J. Callahan, P. J. McMurdie, M. J. Rosen, A. W. Han, A. J. A. Johnson, and S. P. Holmes, "DADA2: high-resolution sample inference from Illumina amplicon data," *Nature Methods*, vol. 13, no. 7, pp. 581–583, 2016.
- [28] T. Kern, J. Theiss, K. Röske, and M. Rother, "Assessment of hydrogen metabolism in commercial anaerobic digesters," *Applied Microbiology and Biotechnology*, vol. 100, no. 10, pp. 4699–4710, 2016.
- [29] B. Demirel and P. Scherer, "The roles of acetotrophic and hydrogenotrophic methanogens during anaerobic conversion of biomass to methane: a review," *Reviews in Environmental Science and Biotechnology*, vol. 7, no. 2, pp. 173–190, 2008.
- [30] R. Conrad, "Contribution of hydrogen to methane production and control of hydrogen concentrations in methanogenic soils and sediments," *FEMS Microbiology Ecology*, vol. 28, no. 3, pp. 193–202, 1999.
- [31] U. Frimmer and F. Widdel, "Oxidation of ethanol by methanogenic bacteria," *Archives of Microbiology*, vol. 152, no. 5, pp. 479–483, 1989.
- [32] R. Liu, X. Hao, and J. Wei, "Function of homoacetogenesis on the heterotrophic methane production with exogenous H₂/CO₂ involved," *Chemical Engineering Journal*, vol. 284, pp. 1196–1203, 2016.
- [33] W. Wang, L. Xie, G. Luo, Q. Zhou, and I. Angelidaki, "Performance and microbial community analysis of the anaerobic reactor with coke oven gas biomethanation and in situ biogas upgrading," *Bioresource Technology*, vol. 146, pp. 234–239, 2013.
- [34] C. Sundberg, W. A. Al-Soud, M. Larsson et al., "454 pyrosequencing analyses of bacterial and archaeal richness in 21 full-scale biogas digesters," *FEMS Microbiology Ecology*, vol. 85, no. 3, pp. 612–626, 2013.
- [35] J. Cardinali-Rezende, R. A. T. P. D. S. Nahat, C. W. G. Moreno et al., "Draft genome sequence of Halomonas sp. HG01, a polyhydroxyalkanoate-accumulating strain isolated from Peru," *Genome Announcements*, vol. 4, no. 1, 2016.
- [36] X. Xie, N. Liu, B. Yang et al., "Comparison of microbial community in hydrolysis acidification reactor depending on different structure dyes by Illumina MiSeq sequencing," *International Biodeterioration and Biodegradation*, vol. 111, pp. 14–21, 2016.
- [37] T. Niu, Z. Zhou, X. Shen et al., "Effects of dissolved oxygen on performance and microbial community structure in a micro-aerobic hydrolysis sludge in situ reduction process," *Water Research*, vol. 90, pp. 369–377, 2016.
- [38] K. Venkiteshwaran, B. Bocher, J. Maki, and D. Zitomer, "Relating anaerobic digestion microbial community and process function: supplementary issue: water microbiology," *Microbiology Insights*, vol. 8s2, 2015.
- [39] I. Bassani, P. G. Kougiass, L. Treu, and I. Angelidaki, "Biogas upgrading via hydrogenotrophic methanogenesis in two-stage continuous stirred tank reactors at mesophilic and thermophilic conditions," *Environmental Science & Technology*, vol. 49, no. 20, pp. 12585–12593, 2015.
- [40] L. M. M. Agneessens, *The Power of the Small: Microbial Conversion of Hydrogen to Methane during Anaerobic Digestion*, [Ph.D. thesis], Aarhus University, 2018.
- [41] A. Fesefeldt, N. C. Holm, and C. G. Gliesche, "Genetic diversity and population dynamics of spp. in a sewage treatment plant and its receiving lake," *Water Science and Technology*, vol. 37, no. 4-5, pp. 113–116, 1998.
- [42] O. Drzyzga, "The strengths and weaknesses of *Gordonia*: a review of an emerging genus with increasing biotechnological potential," *Critical Reviews in Microbiology*, vol. 38, no. 4, pp. 300–316, 2012.
- [43] A. Raheem, V. S. Sikarwar, J. He et al., "Opportunities and challenges in sustainable treatment and resource reuse of sewage sludge: a review," *Chemical Engineering Journal*, vol. 337, pp. 616–641, 2018.
- [44] T. Hori, S. Haruta, Y. Ueno, M. Ishii, and Y. Igarashi, "Dynamic transition of a methanogenic population in response to the concentration of volatile fatty acids in a thermophilic anaerobic digester," *Applied and Environmental Microbiology*, vol. 72, no. 2, pp. 1623–1630, 2006.
- [45] M. S. M. Jetten, A. J. M. Stams, and A. J. B. Zehnder, "Methanogenesis from acetate: a comparison of the acetate metabolism in *Methanotheroxobacterium soehngenii* and *Methanosarcina* spp.," *FEMS Microbiology Letters*, vol. 88, no. 3-4, pp. 181–197, 1992.
- [46] Y. Liu and W. B. Whitman, "Metabolic, phylogenetic, and ecological diversity of the methanogenic archaea," *Annals of the New York Academy of Sciences*, vol. 1125, no. 1, pp. 171–189, 2008.
- [47] G. Zellner, K. Bleicher, E. Braun et al., "Characterization of a new mesophilic, secondary alcohol-utilizing methanogen, *Methanobacterium palustre* spec. nov. from a peat bog," *Archives of Microbiology*, vol. 151, no. 1, pp. 1–9, 1988.
- [48] I. Bassani, P. G. Kougiass, and I. Angelidaki, "In-situ biogas upgrading in thermophilic granular UASB reactor: key factors affecting the hydrogen mass transfer rate," *Bioresource Technology*, vol. 221, pp. 485–491, 2016.
- [49] G. Luo and I. Angelidaki, "Co-digestion of manure and whey for in situ biogas upgrading by the addition of H₂: process performance and microbial insights," *Applied Microbiology and Biotechnology*, vol. 97, pp. 1373–1381, 2013.

Research Article

Flocculation Efficiency and Mechanism of Carbamazepine by Microbial Flocculant Extracted from *Klebsiella pneumoniae* J1

Jie Xing ^{1,2,3}, Nanzhe Song,² Xiangwei Chen,¹ Ang Li,⁴ and Hongwei Ni ³

¹Northeast Forestry University, Harbin 150040, China

²Heilongjiang Provincial Research Academy of Environmental Sciences, Harbin 150056, China

³Institute of Natural Resources and Ecology, HAS, Harbin 150040, China

⁴State Key Laboratory of Urban Water Resource and Environment, School of Environment, Harbin Institute of Technology, Harbin 150090, China

Correspondence should be addressed to Jie Xing; 18686885851@163.com and Hongwei Ni; nihongwei2000@163.com

Received 25 August 2020; Revised 18 September 2020; Accepted 13 October 2020; Published 18 November 2020

Academic Editor: Jin Li

Copyright © 2020 Jie Xing et al. This is an open access article distributed under the Creative Commons Attribution License, which permits unrestricted use, distribution, and reproduction in any medium, provided the original work is properly cited.

The microbial flocculant (MFX) extracted from *Klebsiella pneumoniae* J1 was used to remove carbamazepine in prepared wastewater and domestic sewage. The influence factors and flocculation mechanism were studied. The optimal carbamazepine removal conditions for MFX were pH of 7-8, 7 mL of flocculant, 0.1 mL of coagulant, and 35°C, and the removal rate reached 81.75%. MFX was efficient in the removal of carbamazepine in both domestic sewage (75.03%) and secondary sedimentation tank effluent (69.76%). The pseudo-first-order kinetic equation fitted the adsorption process better than the pseudo-second-order kinetic equation, which suggested that the adsorption was not pure chemical adsorption. The analysis of floc size suggested that the repulsive force between carbamazepine and MFX was weakened under alkaline conditions, which can help the growth and coherence of flocs and increase the carbamazepine removal efficiency. Enough dosage of MFX can generate larger flocs, but excessive dosage of MFX will decrease the carbamazepine removal rate because of increase in electrostatic repulsion. The analysis of 3D-EEM and FTIR suggested that hydroxyl, amino, and carboxyl in MFX played an important role in the removal of carbamazepine. As an eco-friendly and highly efficient microbial flocculant, MFX has potential for practical applications in carbamazepine removal.

1. Introduction

Carbamazepine (CBZ), a typical pharmaceutical and personal care product (PPCP) [1–3], is a medicine for the treatment of epilepsy, depression, glossopharyngeal neuralgia, trigeminal neuralgia, and central partial diabetes insipidus [4]. Toxicological experiments show that the LD50 of carbamazepine is 4205 mg/kg (for rats). Carbamazepine has been detected in sewage treatment stations since 1998, and it has been found that the concentration of carbamazepine in water is higher than that of other PPCPs in recent years [5]. Carbamazepine widely exists in the effluent of urban sewage plants, surface water, and soil. Carbamazepine may eventually enter drinking water and groundwater through environmental migration and transformation [3, 6].

It can be seen from the pollution status of carbamazepine in the environment that carbamazepine widely exists in various environmental media after migration and transformation, and it has good stability and durability, allowing it to exist in the environment for a long time [7, 8]. Therefore, it is urgent to improve the removal efficiency of carbamazepine in the research of PPCP pollutants.

Microbial flocculants (MFX), extracted from microorganisms, widely exist and are nontoxic and eco-friendly [9–11]. There are numerous chemical groups (e.g. hydroxyl, carboxyl, and amino) in MFX, which allow MFX to have good combining capacity with pollutants and have good flocculation efficiency [12–15]. In addition to the removal of turbidity of wastewater, it has been proved that MFX can treat wastewaters that contain heavy metals [16–18] and antibiotics [19–21].

Because there is no secondary pollution of MFX, it is one of the most promising materials to treat wastewater [22].

Until now, most studies on MFX used prepared solution to study the removal efficiency of MFX. Actually, the constituents in actual wastewater are much more complex than those in a prepared solution [23]. There are many other contaminants in actual wastewater, and these contaminants could compete against carbamazepine, which will decrease the carbamazepine removal efficiency by MFX. Therefore, besides prepared solutions, it is also important to conduct experiments on carbamazepine removal in actual wastewater.

In this study, MFX was used to remove carbamazepine from wastewater. The carbamazepine removal efficiency was tested under different conditions (pH, dosage of MFX, dosage of coagulant, and temperature). Considering the practical application of MFX, the carbamazepine removal efficiency by MFX was also studied in domestic sewage and in secondary sedimentation tank effluent. The adsorption kinetics and the mechanism of carbamazepine flocculation were studied.

2. Materials and Methods

2.1. Materials and Reagents. The extraction of MFX from *Klebsiella pneumoniae* J1 (CGMCC No. 6243) was described in our previous work [19]. Briefly, J1 was inoculated and fermented to produce MFX. MFX was extracted by alcohol extraction and was purified by dialysis in ultrapure water. Dried MFX powder was obtained by vacuum freeze drying and stored at 4°C.

Carbamazepine, CaCl₂, and the reagents used to prepare MFX were purchased from Bailingwei Technology Co., Ltd. Ultrapure water (18 MΩ/cm, Milli-Q), and analytical-grade reagents were used in this work.

2.2. Batch Adsorption Experiments. The stock carbamazepine solution (5 mg/L) was prepared by dissolving carbamazepine in ultrapure water and stored at 4°C for later use. The stock carbamazepine solutions were diluted appropriately to obtain the experimental solutions. MFX (1 g/L) and coagulant aid (CaCl₂, 10%) were added to the initial carbamazepine solution (1 mg/L, 1 L). After flocculating and stirring for a period of time, the samples were allowed to stand for 20 min. After adsorption, MFX was separated by 0.45 μm filter membrane and the concentration of carbamazepine was determined by high-performance liquid chromatography (HPLC, Shimadzu, LC-10A (SPD/RID/RFD), Japan). All experimental data were the average of triplicate measurements. The adsorption capacity (q_e , mg/g) of carbamazepine by MFX was calculated as follows:

$$q_e = (C_0 - C_e) \frac{V}{M}, \quad (1)$$

where C_0 and C_e are the initial and equilibrium carbamazepine concentrations (mg/L), respectively, V is the volume of the carbamazepine operating solution (L), and M is the dose of MFX (g).

MFX was also used to adsorb carbamazepine in domestic sewage and sewage from the secondary settling tank from the Harbin Taiping Sewage Treatment Plant. The adsorption process was similar to that of carbamazepine solution. The difference was that the concentration of carbamazepine in the domestic sewage and the sewage from the secondary settling tank was much lower than the prepared carbamazepine solution; therefore, the samples were pretreated via ethyl acetate liquid-liquid extraction. To be specific, the same volume of ethyl acetate was added to the filtered supernatant, the sample was shaken for 10 min, and then, it was allowed to stand for layering. The supernatant liquid was extracted, shaken for 5 min, and then allowed to stand for layering. The supernatant liquid was extracted. After rotary evaporation and nitrogen blowing of the collected upper liquid, it was redissolved with chromatographic grade methanol. The concentration of carbamazepine was measured by high-performance liquid chromatography (HPLC, Waters, USA). Three parallel samples were prepared for each sample. Carbamazepine (20 μg/L) was used as a standard sample to measure the recovery rate of the spiked standard.

2.3. Adsorption Kinetics. The adsorption kinetics of MFX for carbamazepine were discussed using the pseudo-first-order and pseudo-second-order kinetic models. The initial concentration of carbamazepine was at a pH of 7, with CaCl₂ (0.1 mL, 10%) as a coagulant aid. The adsorption times were 5, 10, 15, 20, 30, 40, 50, and 60 min, respectively. The pseudo-first-order and pseudo-second-order kinetic models are displayed in

$$\begin{aligned} \log(q_e - q_t) &= \log(q_e) - \frac{k_1}{2.303}t, \\ \frac{t}{q_t} &= \frac{1}{k_2 q_e^2} + \frac{t}{q_e}, \end{aligned} \quad (2)$$

where q_e and q_t are the equilibrium adsorption capacity and adsorption capacity at a certain moment, respectively (mg/g), t is the adsorption time (min), and k_1 and k_2 are the rate constants of pseudo-first-order and pseudo-second-order kinetic models, respectively.

2.4. Analysis of Mechanisms of Carbamazepine Adsorption on MFX. A granulometer (Malvern MS2000, UK) was used to monitor the growth of different microbial flocculants and to calculate the growth rate of the flocs in the adsorption process. The functional groups were determined by Fourier transform infrared spectroscopy (FTIR, Perkin-Elmer spectrum 100). Three-dimensional fluorescence spectrophotometry (3D-EEM, FP6500, JASCO, Japan) was used to obtain EEM spectra, and the fluorescence response was obtained by scanning the emission spectra from 220 to 650 nm and by varying the excitation wavelength from 220 to 500 nm. Fluorescence quenching, completed by adding carbamazepine into the MFX solution, was used to assess the adsorption characteristics.

3. Results and Discussion

3.1. Factors That Influence the Removal Efficiency of Carbamazepine via MFX. Generally, to evaluate the adsorption capacity of MFX, the removal efficiency of a pollutant needs to be tested under different conditions. In this study, the adsorption performance of carbamazepine by MFX was studied under different conditions by changing the pH, dosage of MFX, dosage of coagulant aid, and temperature, respectively.

3.1.1. pH. The pH value is an important parameter in the adsorption process. The pH not only affects the functional groups of MFX but also affects the surface charge of carbamazepine [24, 25]. The removal rate of carbamazepine by MFX was tested at pH = 5–10, and the results are shown in Figure 1(a). It was obvious that the removal rate of carbamazepine by MFX increased from pH = 5 to pH = 7 and decreased from pH = 7 to pH = 10. MFX showed a poor carbamazepine removal effect under acidic conditions. At pH = 5, the removal rate was only 5.14%. However, the carbamazepine removal rate became better under nonacidic conditions. At pH = 7, MFX had the best carbamazepine removal rate (65.26%), and the removal rate decreased apparently at pH = 9–10. This suggests that both acidic and overly alkaline conditions are not suitable for the removal of carbamazepine by MFX. This was because the change of pH conditions changed the quantity and properties of surface charges of both MFX and carbamazepine, and overly acidic and overly alkaline conditions can weaken the neutralization effect and hinder the aggregation reaction between MFX and carbamazepine [20]. Therefore, the optimal pH range for the removal of carbamazepine by MFX is 7–8.

3.1.2. Dosage of MFX. The dosage of MFX is another important factor that can affect the removal rate of carbamazepine [26]. The removal rate of carbamazepine by MFX was tested after adding a different dosage of MFX, and the results are shown in Figure 1(b). The carbamazepine removal rate increased when the dosage increased from 1 mL to 7 mL but then decreased with the increase of dosage of MFX. MFX performed the best when its dosage was 7 mL and the maximum removal rate was 73.06%. When 9 mL dosage of MFX was added to carbamazepine, the removal rate showed a downward trend. This was because when the dosage of MFX was low, the quantity of MFX was not enough to remove carbamazepine even if MFX reached adsorption saturation. However, when the dosage was too high, the excessive MFX could influence the charge property of the entire system and destroy the balance of charge, which subsequently decreased the carbamazepine removal rate. This result was similar to those in other studies [27].

3.1.3. Dosage of Coagulant Aid. Coagulant aids can improve the flocculation conditions by adjusting the charge property of the system [21]. In this study, CaCl_2 was added as a coagulant aid, and the carbamazepine removal rate of MFX with different dosage of coagulant aid is shown in Figure 1(c). The CaCl_2 dosages of samples 1 to 6 were 0 mL, 0.1 mL, 0.3 mL, 0.5 mL, 1 mL, and 1.5 mL, respectively. It can be seen

that the carbamazepine removal rate by MFX was 54.73% when no coagulant was added, which proves that MFX can remove carbamazepine alone. When the dosage was 0.1 mL, the carbamazepine removal rate increased and reached the maximum removal rate of 77.17%. However, with the increase of CaCl_2 dosage, the carbamazepine removal rate decreased gradually. This was because carbamazepine was removed by MFX through adsorption bridging between macromolecules, and the coagulant aid can strengthen the adsorption bridging by adjusting the charge property of the system. However, excessive dosage of the coagulant aid will introduce excessive positive charges, which bind to the negatively charged adsorption sites in MFX, hindering the connection of carbamazepine and MFX. Therefore, the optimal dosage of coagulant aid needs to be determined by adsorption experiments. In this study, the optimal dosage was 0.1 mL.

3.1.4. Temperature. Temperature is another important factor that can affect the carbamazepine removal efficiency by MFX [26]. Figure 1(d) shows the carbamazepine removal rate by MFX at 15°C, 20°C, 25°C, 30°C, and 35°C, respectively. It can be seen that the removal rate increased as the temperature increased. The removal rate was only 22.06% at 15°C, but increased to 81.75% at 35°C. Generally, an appropriate temperature increase can accelerate the random movement between molecules, which then increase the collision probability among molecules and increase the carbamazepine removal rate by MFX. However, too high of a temperature will lead to the inactivation of MFX, which will decrease the carbamazepine removal rate [28]. In this study, MFX performed the best at 35°C, suggesting MFX was effective even at 35°C.

In summary, the optimal carbamazepine removal conditions for MFX were pH 7–8, 7 mL of flocculant, 0.1 mL of coagulant, and 35°C. The removal rate reached 81.75%.

3.2. Carbamazepine Removal from Domestic Sewage. The above experiments prove that MFX has a good carbamazepine removal efficiency for a prepared carbamazepine solution (1 mg/L). However, the carbamazepine concentration in domestic sewage is usually tens to hundreds of $\mu\text{g/L}$. Moreover, the constituents in domestic sewage are much more complex than a prepared carbamazepine solution [23]. Although domestic sewage contains a large number of suspended solid colloidal particles that are conducive to the formation of flocs, the competition for the adsorption sites on MFX between carbamazepine and other constituents can lead to the decrease of carbamazepine removal rate. Figures 2(a) and 2(b) show the removal rate in domestic sewage and in secondary sedimentation tank effluent. It can be seen that MFX was efficient in the removal of carbamazepine both in domestic sewage (75.03%) and in secondary sedimentation tank effluent (69.76%), which suggested that MFX had a good removal effect on carbamazepine.

3.3. Adsorption Kinetics. Adsorption kinetics is important when studying adsorption mechanism. The kinetics analyzes the effects of adsorption time on the adsorption of pollutants

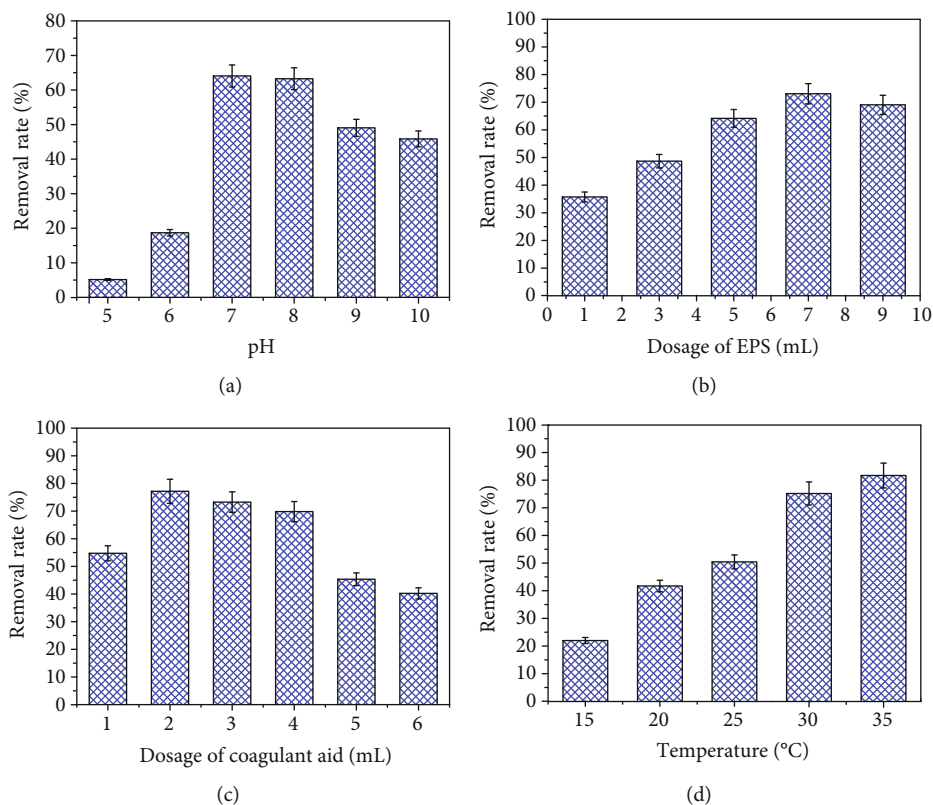


FIGURE 1: Removal efficiency of carbamazepine on MFX at different conditions: (a) pH, (b) dosage of MFX, (c) dosage of coagulant aid, and (d) temperature.

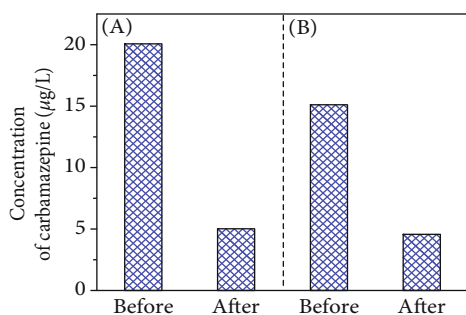


FIGURE 2: Removal efficiency of carbamazepine on MFX: (a) domestic sewage and (b) secondary sedimentation tank effluent.

by describing the adsorption rate and then explores the adsorption mechanism. Usually, the first-order, second-order, pseudo-first-order, and pseudo-second-order kinetic equations are used to analyze the adsorption kinetics. In this study, MFX and carbamazepine were reactants in the adsorption process. Based on the characteristics of MFX and the applicable scope of each kinetic equation, the pseudo-first-order and pseudo-second-order kinetic equations were selected to fit the experimental data in this study.

In the first-order kinetics, the reaction rate is only proportional to the concentration of one reactant, while in the pseudo-first-order kinetics, the reaction rate is related to the concentration of the adsorbent and the adsorbate. When the concentration of one substance is much more than the

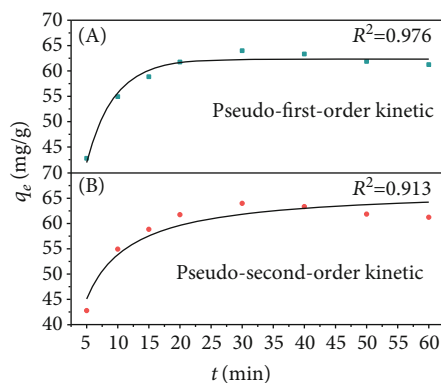


FIGURE 3: The fitting curve of the (a) pseudo-first-order kinetics and (b) pseudo-second-order kinetics.

other, it shows the characteristics of a first-order kinetic reaction [29, 30].

Figures 3(a) and 3(b) show the fitting results of the pseudo-first-order and pseudo-second-order kinetic equations. Table 1 shows the parameters of these kinetic equations. In Figure 3(a), the adsorption reaction reached adsorption equilibrium in 20 min, and the maximum adsorption capacity was 62.32 mg of carbamazepine per gram of MFX. In the actual experiment, the maximum adsorption capacity was 62.99 mg/g and the adsorption time was 30 min, which were consistent with the values predicted by the pseudo-first-order kinetic equation. In Figure 3(b), the

TABLE 1: The parameters of the pseudo-first-order and pseudo-second-order kinetics.

Equation	Experimental q_e (mg/g)	Predicted q_e (mg/g)	k_1	R^2
Pseudo-first-order kinetic	62.99	62.32	-0.22	0.98
Pseudo-second-order kinetic	62.99	66.89	0.0062	0.91

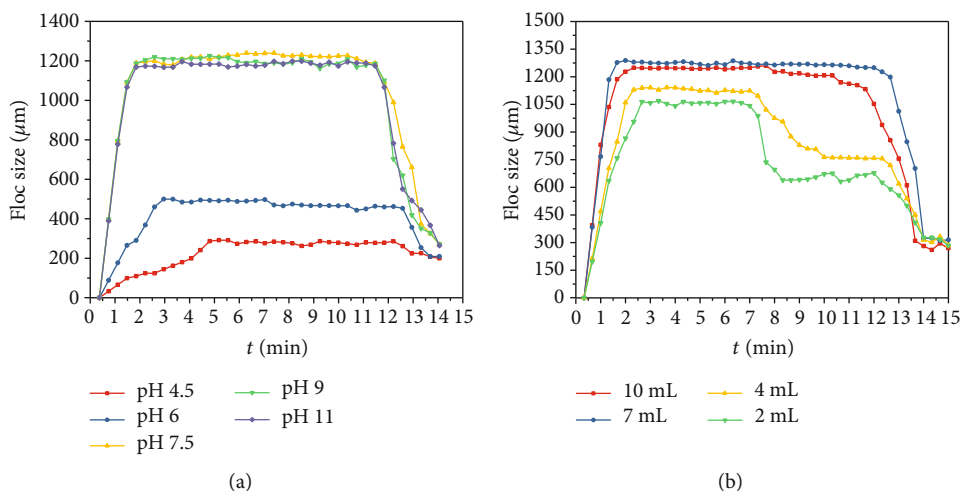


FIGURE 4: The effect of factors on floc formation: (a) pH and (b) dosage of MFX.

predicted adsorption did not reach adsorption equilibrium in 60 min, and the predicted maximum adsorption capacity (66.89 mg/g, 60 min) was more than the actual value. Moreover, the R^2 of the pseudo-first-order kinetic equation is 0.976, which is much higher than the R^2 of the pseudo-second-order kinetic equation. These results suggested that the adsorption of carbamazepine by MFX was more in line with the pseudo-first-order kinetic equation.

According to other studies, the adsorption process described by the first-order kinetic is controlled by substance transport. The pseudo-second-order kinetic simulates the second-order kinetic, which describes a chemical reaction, accompanied by electron sharing or transfer. The adsorption of carbamazepine by the MFX-fitted pseudo-first-order kinetic better than the pseudo-second-order kinetic, which suggested that the adsorption was not pure chemical adsorption [17].

3.4. Mechanisms of Carbamazepine Adsorption on MFX. The preliminary experimental results showed that the pH, dosage of MFX, dosage of coagulant, and temperature can affect the carbamazepine removal rate by MFX. The dosage of MFX and pH were the main factors; therefore, the flocculation morphology was used to further investigate the carbamazepine removal mechanism by MFX. The changes of floc size under different pH values/dosages of MFX at different times are shown in Figure 4. The flocs under different pH conditions showed a similar changing trend in the whole coagulation processes. The floc formation process was slow under acidic condition, and the particle size was relatively small in the stable stage. Moreover, there was no obvious sedimentation at pH = 4.5. The floc formation process was the fastest at

pH = 7.5. When the pH was larger than 7.5, the growth of the flocs was significantly accelerated, the settling velocity of the flocs was fast, and the changes were not obvious as the pH became larger. This was because the surface charge density of MFX and carbamazepine was low under an alkaline condition, which can weaken the repulsive force between carbamazepine and MFX and can help the growth and coherence of flocs [31].

In Figure 4(b), the maximum floc size was the smallest when the dosage of MFX was 2 mL (1064 μm), and the floc size became larger with the increase of MFX dosage. However, when the dosage was 10 mL (1235 μm), the floc size became smaller than that under a dosage of 7 mL (1288 μm). Moreover, the growth of the floc was slower at a low dosage of MFX, and the maintenance time of the stable period was shorter, which was not conducive to the removal of carbamazepine. This was because too low a dosage of MFX cannot provide sufficient adsorption sites for carbamazepine, and the collision probability between MFX and carbamazepine was low. Therefore, enough dosage of MFX can generate larger flocs. However, the dynamic equilibrium period was short with too high dosage of a MFX, because there was a large amount of the same charge with excess MFX, which increased electrostatic repulsion. Similar phenomena have been found in the study of the coagulation of microbial flocculant and kaolin, and this was caused by the adsorption bridging effect.

To investigate whether there was chemical reaction between carbamazepine and MFX, 3D-EEM and FTIR were used to analyze the samples before and after adsorption. Figures 5(a)–5(c) show the EEM of carbamazepine aqueous solution, precipitation after adsorption of carbamazepine by

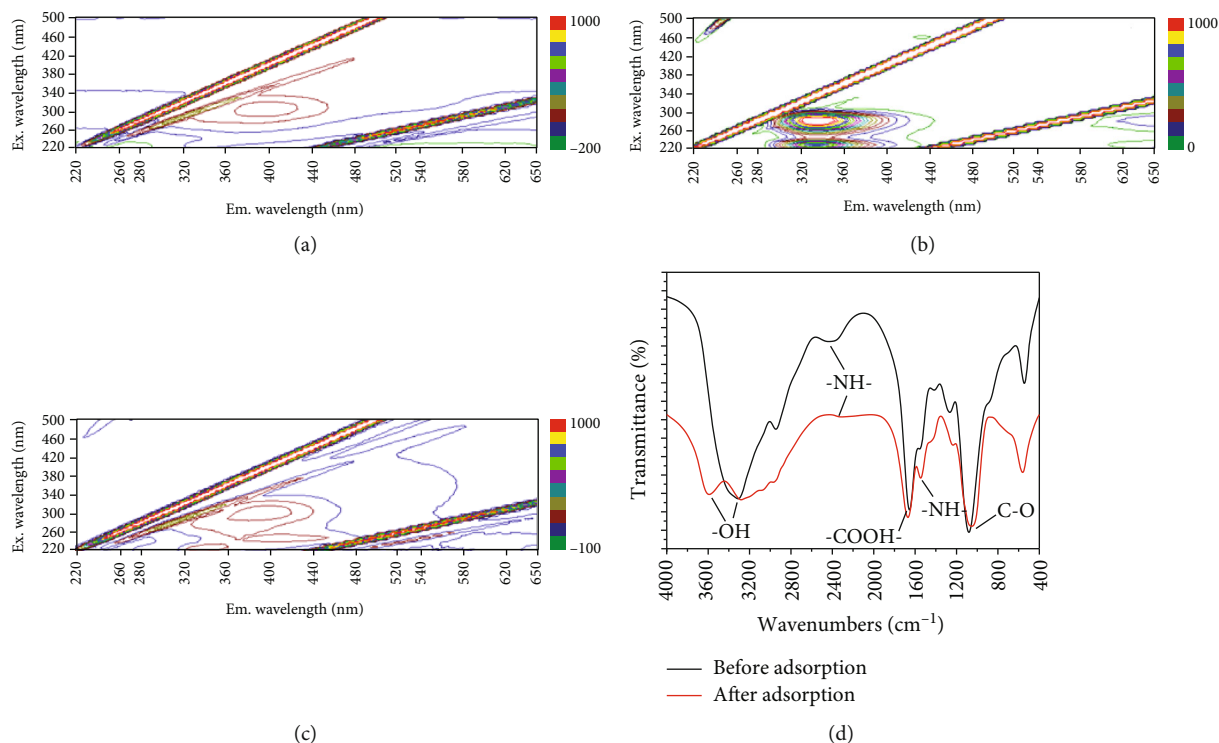


FIGURE 5: EEM of component of MFX adsorbing carbamazepine: (a) carbamazepine aqueous solution, (b) precipitation after adsorption, (c) liquid supernatant after adsorption, and (d) FTIR of MFX before and after carbamazepine.

MFX, and liquid supernatant after adsorption, respectively. In Figure 5(a), it can be seen that the carbamazepine aqueous solution only had an absorption peak at $\lambda_{ex}/\lambda_{em} = (310-320) \text{ nm}/(395-405) \text{ nm}$. This peak belongs to Class I (humic acid-like area), which was caused by typical exogenous organics. In this study, this peak was caused by carbamazepine [32]. In Figure 5(b), the precipitate after adsorption shows two high concentration absorption peaks at $\lambda_{ex}/\lambda_{em} = (270-280) \text{ nm}/(325-335) \text{ nm}$ and $\lambda_{ex}/\lambda_{em} = (225-235) \text{ nm}/(325-335) \text{ nm}$, which are the characteristic peaks of proteins that are the main active components of MFX [20]. No characteristic peak of carbamazepine was found in this spectrum, because carbamazepine has been adsorbed on MFX through intermolecular forces and it was not a free molecule that can be detected. In Figure 5(c), three obvious absorption peaks can be seen in the spectrum of the supernatant after adsorption. The peak at $\lambda_{ex}/\lambda_{em} = (310-320) \text{ nm}/(395-405) \text{ nm}$ is the characteristic peak of carbamazepine. The peak at $\lambda_{ex}/\lambda_{em} = (225-235) \text{ nm}/(325-335) \text{ nm}$ belongs to the tyrosine and benzene ring structure protein related to biological sources, which represent a small amount of the active ingredients of MFX or its derivatives. The peak related to tryptophan at $\lambda_{ex}/\lambda_{em} = (250-280) \text{ nm}/(325-335) \text{ nm}$ disappeared, and a new peak resembling fulvic acid at $\lambda_{ex}/\lambda_{em} = (250-270) \text{ nm}/(410-420) \text{ nm}$ appeared. This peak was a new peak after MFX adsorbed carbamazepine, which suggested that chemical reactions occurred between carbamazepine and the tryptophan-like component on MFX.

To further prove that chemical reactions occurred between carbamazepine and MFX, FTIR was used to analyze MFX before and after adsorption of carbamazepine (Figure 5(d)).

Compared to the FTIR spectrum of MFX before adsorption, there was a new peak in the FTIR spectrum of MFX after adsorption, accompanied by multipeak displacement. The new peak appeared at 3590.22 cm^{-1} , which was the characteristic peak corresponding to hydroxyl. The absorption peak caused by the stretching vibration of associative hydroxyl at 3309.94 cm^{-1} exhibited a redshift to 3291.88 cm^{-1} , and the peak shape became wider. This proved that the hydroxyl played a role in the adsorption of carbamazepine by MFX, and this was achieved by hydrogen bonding. The absorption peak caused by the vibration of amino at 2435.06 cm^{-1} exhibited a redshift to 2321.08 cm^{-1} , and the intensity was significantly weakened. The long and narrow absorption peak at 1654.45 cm^{-1} was a characteristic peak of carboxyl, and this peak exhibited a blueshift to 1669.71 cm^{-1} . The peak at 1549.75 cm^{-1} caused by the bending vibration of amide exhibited a redshift to 1546.45 cm^{-1} , which proved that the active amino in the proteins of MFX participated in the adsorption reaction. The long and narrow absorption peak at 1080.57 cm^{-1} as a typical absorption peak of sugar derivatives included the stretching and vibration of C-O and C-O-C. The peak exhibited a redshift to 1047.34 cm^{-1} after adsorption of carbamazepine. These results proved that the hydroxyl, amino, and carboxyl groups were all involved in the adsorption reaction and played a role together in the removal of carbamazepine by MFX [17].

4. Conclusion

MFX was used to remove carbamazepine. MFX was efficient in the removal of carbamazepine in both domestic sewage

and secondary sedimentation tank effluent. The pseudo-first-order kinetic equation can describe the adsorption process. The adsorption was a compound process that involved physical and chemical adsorption. MFX performed the best under alkaline conditions, because the repulsive force between carbamazepine and MFX was weakened, which can help the growth and coherence of flocs. Enough dosage of MFX can generate larger flocs, but excessive dosage of MFX will decrease the carbamazepine removal efficiency due to the increase of electrostatic repulsion. The hydroxyl, amino, and carboxyl groups in MFX played an important role in the removal of carbamazepine. As a widely existing, non-toxic, and eco-friendly microbial flocculant, MFX has the potential for practical applications in carbamazepine removal from domestic sewage, carbamazepine wastewater, and natural water bodies.

Data Availability

The data that support the findings of this study are available from the corresponding author Jie Xing, upon reasonable request.

Conflicts of Interest

No potential conflict of interest exists in this work; therefore, nothing can affect the objectivity and actions of authors. The conflicts of interest, including direct financial relationships, indirect financial relationships, personal relationships, academic competition, and intellectual passion, are absolutely nonexistent in this work.

Acknowledgments

This work was financially supported by the National Science and Technology Major Project (2014ZX07201-012).

References

- [1] L. Nielsen, P. Zhang, and T. J. Bandosz, "Adsorption of carbamazepine on sludge/fish waste derived adsorbents: effect of surface chemistry and texture," *Chemical Engineering Journal*, vol. 267, pp. 170–181, 2015.
- [2] Y. Gao, G. Yu, K. Liu et al., "Integrated adsorption and visible-light photodegradation of aqueous clofibrate and carbamazepine by a Fe-based metal-organic framework," *Chemical Engineering Journal*, vol. 330, pp. 157–165, 2017.
- [3] L. Nielsen, M. J. Biggs, W. Skinner, and T. J. Bandosz, "The effects of activated carbon surface features on the reactive adsorption of carbamazepine and sulfamethoxazole," *Carbon*, vol. 80, pp. 419–432, 2014.
- [4] S. Jemutai-Kimosop, F. Orata, V. O. Shikuku, V. A. Okello, and Z. M. Getenga, "Insights on adsorption of carbamazepine onto iron oxide modified diatomaceous earth: kinetics, isotherms, thermodynamics, and mechanisms," *Environmental Research*, vol. 180, article 108898, 2020.
- [5] Q. He, J. J. Liang, L. X. Chen et al., "Removal of the environmental pollutant carbamazepine using molecular imprinted adsorbents: molecular simulation, adsorption properties, and mechanisms," *Water Research*, vol. 168, article 115164, 2020.
- [6] X. Gao, Q. Guo, G. Tang, W. Zhu, X. Yang, and Y. Luo, "TBAOH assisted synthesis of ultrathin BiOCl nanosheets with enhanced charge separation efficiency for superior photocatalytic activity in carbamazepine degradation," *Journal of Colloid and Interface Science*, vol. 570, pp. 242–250, 2020.
- [7] J. Chen, D. Zhang, H. Zhang, S. Ghosh, and B. Pan, "Fast and slow adsorption of carbamazepine on biochar as affected by carbon structure and mineral composition," *Sci Total Environ*, vol. 579, pp. 598–605, 2017.
- [8] K. Liu, L. Bai, Y. Shi et al., "Simultaneous disinfection of E. faecalis and degradation of carbamazepine by sulfate radicals: an experimental and modelling study," *Environmental Pollution*, vol. 263, article 114558, 2020.
- [9] A. Li, C. Zhou, Z. Liu et al., "Direct solid-state evidence of H₂-induced partial U(VI) reduction concomitant with adsorption by extracellular polymeric substances (EPS)," *Biotechnology and Bioengineering*, vol. 115, no. 7, pp. 1685–1693, 2018.
- [10] C. Y. Lai, Q. Y. Dong, J. X. Chen et al., "Role of extracellular polymeric substances in a methane based membrane biofilm reactor reducing vanadate," *Environmental Science & Technology*, vol. 52, no. 18, pp. 10680–10688, 2018.
- [11] J. Yang, D. Wu, A. Li et al., "The addition of N-hexanoyl-homoserine lactone to improve the microbial flocculant production of *Agrobacterium tumefaciens* Strain F₂, an exopolysaccharide bioflocculant-producing bacterium," *Applied Biochemistry and Biotechnology*, vol. 179, no. 5, pp. 728–739, 2016.
- [12] D. Cui, C. Tan, H. Deng et al., "Biosorption mechanism of aqueous Pb²⁺, Cd²⁺, and Ni²⁺ ions on extracellular polymeric substances (EPS)," *Archaea*, vol. 2020, Article ID 8891543, 9 pages, 2020.
- [13] J. Yang, L. Zhou, F. Ma et al., "Magnetic nanocomposite microbial extracellular polymeric substances@Fe₃O₄ supported nZVI for Sb(V) reduction and adsorption under aerobic and anaerobic conditions," *Environmental Research*, vol. 189, article 109950, 2020.
- [14] W. Wei, Q. Wang, A. Li et al., "Biosorption of Pb (II) from aqueous solution by extracellular polymeric substances extracted from *Klebsiella* sp. J1: adsorption behavior and mechanism assessment," *Scientific Reports*, vol. 6, no. 1, article 31575, 2016.
- [15] W. Wei, A. Li, J. Yang et al., "Synergetic effects and flocculation behavior of anionic polyacrylamide and extracellular polymeric substrates extracted from *Klebsiella* sp. J1 on improving soluble cadmium removal," *Bioresource Technology*, vol. 175, pp. 34–41, 2015.
- [16] L. Zhou, A. Li, F. Ma, J. Yang, S. Pi, and A. Tang, "Sb(V) reduced to Sb(III) and more easily adsorbed in the form of Sb(OH)₃ by microbial extracellular polymeric substances and core-shell magnetic nanocomposites," *ACS Sustainable Chemistry & Engineering*, vol. 7, no. 11, pp. 10075–10083, 2019.
- [17] W. Wei, A. Li, S. Pi et al., "Synthesis of core-shell magnetic nanocomposite Fe₃O₄@ microbial extracellular polymeric substances for simultaneous redox sorption and recovery of silver ions as silver nanoparticles," *ACS Sustainable Chemistry & Engineering*, vol. 6, no. 1, pp. 749–756, 2017.
- [18] L. Zhou, A. Li, F. Ma et al., "Combining high electron transfer efficiency and oxidation resistance in nZVI with coatings of microbial extracellular polymeric substances to enhance Sb(V) reduction and adsorption," *Chemical Engineering Journal*, vol. 395, article 125168, 2020.
- [19] J. Xing, J. X. Yang, A. Li et al., "Removal efficiency and mechanism of sulfamethoxazole in aqueous solution by

- biofloculant MFx,” *Journal of Analytical Methods in Chemistry*, vol. 2013, Article ID 568614, 8 pages, 2013.
- [20] S. Pi, A. Li, D. Cui et al., “Biosorption behavior and mechanism of sulfonamide antibiotics in aqueous solution on extracellular polymeric substances extracted from *Klebsiella sp. J1*,” *Biore-source Technology*, vol. 272, pp. 346–350, 2019.
- [21] S. Pi, A. Li, W. Wei et al., “Synthesis of a novel magnetic nano-scale biosorbent using extracellular polymeric substances from *Klebsiella sp. J1* for tetracycline adsorption,” *Biore-source Technology*, vol. 245, pp. 471–476, 2017.
- [22] J. Yang, W. Wei, S. Pi et al., “Competitive adsorption of heavy metals by extracellular polymeric substances extracted from *Klebsiella sp. J1*,” *Biore-source Technology*, vol. 196, pp. 533–539, 2015.
- [23] M. Yao, L. Duan, J. Wei, F. Qian, and S. W. Hermanowicz, “Carbamazepine removal from wastewater and the degradation mechanism in a submerged forward osmotic membrane bioreactor,” *Biore-source Technology*, vol. 314, article 123732, 2020.
- [24] J. Huang, Z.-L. Huang, J.-X. Zhou et al., “Enhancement of heavy metals removal by microbial flocculant produced by *Paenibacillus polymyxa* combined with an insufficient hydroxide precipitation,” *Chemical Engineering Journal*, vol. 374, pp. 880–894, 2019.
- [25] D.-Q. Cao, W.-Y. Yang, Z. Wang, and X. D. Hao, “Role of extracellular polymeric substance in adsorption of quinolone antibiotics by microbial cells in excess sludge,” *Chemical Engineering Journal*, vol. 370, pp. 684–694, 2019.
- [26] W. Wei, A. Li, F. Ma et al., “Simultaneous sorption and reduction of Cr(VI) in aquatic system by microbial extracellular polymeric substances from *Klebsiella sp. J1*,” *Journal of Chemical Technology & Biotechnology*, vol. 93, no. 11, pp. 3152–3159, 2018.
- [27] Z. Yang, M. Li, M. Yu et al., “A novel approach for methylene blue removal by calcium dodecyl sulfate enhanced precipitation and microbial flocculant GA1 flocculation,” *Chemical Engineering Journal*, vol. 303, pp. 1–13, 2016.
- [28] P. Sivaperumal, K. Kamala, and R. Rajaram, “Adsorption of cesium ion by marine actinobacterium *Nocardiopsis sp. 13H* and their extracellular polymeric substances (EPS) role in bio-remediation,” *Environmental Science and Pollution Research International*, vol. 25, no. 5, pp. 4254–4267, 2018.
- [29] A. A. Marianou, C. M. Michailof, D. K. Ipsakis et al., “Isomerization of glucose into fructose over natural and synthetic MgO catalysts,” *ACS Sustainable Chemistry & Engineering*, vol. 6, no. 12, pp. 16459–16470, 2018.
- [30] Y. Zhou, Y. S. Lai, E. Eustance, and B. E. Rittmann, “Promoting *Synechocystis sp. PCC 6803* harvesting by cationic surfactants: alkyl-chain length and dose control for the release of extracellular polymeric substances and biomass aggregation,” *ACS Sustainable Chemistry & Engineering*, vol. 7, no. 2, pp. 2127–2133, 2018.
- [31] Y. X. Zhao, B. Y. Gao, H. K. Shon, J. H. Kim, Q. Y. Yue, and Y. Wang, “Floc characteristics of titanium tetrachloride (TiCl_4) compared with aluminum and iron salts in humic acid-kaolin synthetic water treatment,” *Separation and Purification Technology*, vol. 81, no. 3, pp. 332–338, 2011.
- [32] L. Liang, S. Gao, J. Zhu et al., “The enhanced photocatalytic performance toward carbamazepine by nitrogen-doped carbon dots decorated on BiOBr/CeO_2 : mechanism insight and degradation pathways,” *Chemical Engineering Journal*, vol. 391, article 123599, 2020.

Research Article

Thermophilic Solid-State Anaerobic Digestion of Corn Straw, Cattle Manure, and Vegetable Waste: Effect of Temperature, Total Solid Content, and C/N Ratio

Lianghu Su ¹, Xu Sun,^{1,2} Chenwei Liu,¹ Rongting Ji,¹ Guangyin Zhen ³, Mei Chen ¹,
and Longjiang Zhang ¹

¹Nanjing Institute of Environmental Sciences, Ministry of Ecology and Environment, 8 Jiangwangmiao Street, Nanjing 210042, China

²School of Environmental Engineer, Nanjing Institute of Technology, No. 1 Hongjing Road, Nanjing 211167, China

³Shanghai Key Lab for Urban Ecological Processes and Eco-Restoration, School of Ecological and Environmental Sciences, East China Normal University, Dongchuan Road 500, Shanghai 200241, China

Correspondence should be addressed to Mei Chen; chenmei@nies.org and Longjiang Zhang; zlj@nies.org

Received 19 May 2020; Revised 5 October 2020; Accepted 26 October 2020; Published 11 November 2020

Academic Editor: Rong Chen

Copyright © 2020 Lianghu Su et al. This is an open access article distributed under the Creative Commons Attribution License, which permits unrestricted use, distribution, and reproduction in any medium, provided the original work is properly cited.

Thermophilic solid-state anaerobic digestion (SS-AD) of agricultural wastes, i.e., corn straw, cattle manure, and vegetable waste, was carried out in this study. The effects of temperature (40–60°C), initial solid content (ISC, 17.5–32.5%), and C/N ratio (15–32:1) on biogas production were evaluated using a Box-Behnken experimental design (BBD) combined with response surface methodology (RSM). The results showed that optimization of process parameters is important to promote the SS-AD performance. All the factors, including interactive terms (except the ISC), were significant in the quadratic model for biogas production with SS-AD. Among the three operation parameters, the C/N ratio had the largest effect on biogas production, followed by temperature, and a maximum biogas yield of 241.4 mL gVS⁻¹ could be achieved at 47.3°C, ISC = 24.81%, and C/N = 22.35. After 20 d of SS-AD, the microbial community structure under different conditions was characterized by high-throughput sequencing, showing that *Firmicutes*, *Bacteroidetes*, *Chloroflexi*, *Synergistetes*, and *Proteobacteria* dominated the bacterial community, and that *Firmicutes* had a competitive advantage over *Bacteroidetes* at elevated temperatures. The biogas production values and relative abundance of *OPB54* and *Bacteroidia* after 20 d of SS-AD can be fitted well using a quadratic model, implying that *OPB54* and *Bacteroidia* play important roles in the methanogenic metabolism for agricultural waste thermophilic SS-AD.

1. Introduction

China is facing tremendous challenges in managing its massive amount of agricultural waste in rural areas. In 2016, China produced 897 Mt of crop residues, and almost one-quarter of these crop residues were burned in the field after harvest, aggravating the air pollution [1, 2]. With the constant growth of livestock husbandry, the amount of livestock excrement in China increased by 12.8% from 367 to 414 Mt (dry) in 2007–2015, causing grave concerns about the water pollution [3].

Anaerobic digestion is a multistage biological process that, in addition to the treatment and stabilization of

waste, allows the production of biogas as a versatile, renewable energy source and the recovery of residual solid (or liquid) as green fertilizers [4, 5]. Unlike other biomass resources, agricultural wastes are preferred for biogas production due to their large-scale availability and low cost, and they do not directly compete with food or feed production [6]. When compared to those of other treatments, these advantages, together with environmental impacts, make the synergistic utilization of the agricultural organic waste by anaerobic codigestion a promising technology [4].

Compared to liquid anaerobic digestion (L-AD), solid-state anaerobic digestion (SS-AD) operated at a total solid

(TS) content above 15% has much higher volumetric methane productivity, requires less energy for heating and stirring, and generates less wastewater [7, 8]. The resulting residue (called digestate) of SS-AD with a lower moisture content would be favourable for transportation and can be valorized as a fertilizer for land applications [9]. Although there are many obstacles, such as difficulties in feeding and discharging, uneven mass transfer, and acid inhibition [10, 11], SS-AD has still been adopted for lignocellulosic biomass, especially in rural areas of China. In China, L-AD is facing a severe problem in treating anaerobic digester effluent, which has a high concentration of nutrients and low oxygen availability. Direct discharge of effluent to natural waters will deteriorate the water quality, affect aquatic organisms, and lead to biodiversity degradation [12]. The application of effluent to land is difficult due to insufficient storage and transportation facilities and limited land carrying capacity [13]. Further treatment to meet the threshold set by the Chinese standard for irrigation water quality (GB5084-2005) [14], such as $\text{COD} \leq 200 \text{ mg L}^{-1}$, would be economically unfeasible.

SS-AD digesters are usually operated based on empirical knowledge rather than performance optimization [8]. The key parameters (such as moisture content, C/N ratio, and temperature) can be further optimized to achieve a better SS-AD performance. Le Hyaric et al. [15] reported that the initial substrate concentration (ISC) affects all steps of anaerobic digestion. Abbassi-Guendouz et al. [16] showed that an elevated ISC leads to lower methane production and substrate conversion. Fernandez et al. [17] observed that methane production decreased by 17% when the ISC increased from 20% to 30% in a dry mesophilic digester. Improper C/N ratios can result in high total ammonia nitrogen (TAN) release in the digester [18]. Temperature is also an extremely important factor for SS-AD; changes in temperature can alter the activity of enzymes in the microbiome and affect substrate degradation and methanogenesis [11]. It has been reported that for lignocellulosic biomass, thermophilic SS-AD led to a greater reduction in the amount of cellulose and hemicelluloses than mesophilic SS-AD [19]. However, instability is a crucial concern for applying SS-AD under thermophilic conditions [20]. Accumulation of VFAs and decreasing pH values during the start-up phase of thermophilic SS-AD digester failure have been also observed [7, 21].

To the best of our knowledge, the effects of the temperature, total solid content, and C/N ratio involved in the mesophilic SS-AD process of agricultural waste materials have been reported, but the effects of these factors on thermophilic SS-AD are poorly understood. In this study, SS-AD of corn straw, cattle manure, and vegetable waste was investigated under thermophilic conditions (40-60°C). The biogas yield, pH, and TAN concentration were characterized after 20 d of SS-AD. The effects of the temperature, ISC, and C/N ratio on biogas production were evaluated using the Box-Behnken experimental design (BBD) combined with response surface methodology (RSM). Microbial community structures were further characterized after 20 d of SS-AD using high-throughput sequencing.

TABLE 1: Fundamental characteristics of corn straw, cattle manure, and vegetable waste.

Type	C (%)*	N (%)*	C/N	TS (%)	VS (%)	pH
Corn straw	43.36	1.26	34.49	88.16	87.31	6.69
Cattle manure	37.34	2.55	14.67	83.28	78.83	8.56
Vegetable waste	34.37	4.68	7.34	3.42	89.14	7.46

*Total carbon and nitrogen (dry basis) were determined by an elemental CHN analyser (Euro EA3000, Euro Vector, Italy).

2. Materials and Methods

2.1. Substrates and Inoculum. Before use, corn straw was chopped into small pieces (~1-2 cm) using a shredding machine. The cellulose, hemicellulose, and lignin contents of corn straw were 45.79%, 21.90%, and 8.01%, respectively. Cattle manure with a moisture content of 16.72% and a C/N ratio of 14.67 was obtained from a dairy farm near the city of Nanjing (Jiangsu Province, China). Vegetable waste, mainly Chinese cabbage (*Brassica rapa* L. ssp. *pekinensis*), was obtained from a local vegetable market in Nanjing. Inoculated sludge with a total solid (TS) content of 8.31% and VS content of 82.53% was collected from a methanogenic reactor that treats starch wastewater from a wastewater treatment plant (WWTP) in Shanghai, China. To reduce the endogenous gas production, the inoculated sludge was preincubated anaerobically for 7 days. Sixteen bacterial phyla were represented for inoculated sludge, with *Chloroflexi*, *Bacteroidetes*, *Proteobacteria*, and *Firmicutes* being the most abundant phyla, accounting for 33.2%, 14.7%, 11.6%, and 12.1% of the total bacterial sequences, respectively. The fundamental characteristics of corn straw, cattle manure, and vegetable waste are shown in Table 1.

2.2. Experimental Procedure. A three-level-three-factor Box-Behnken design (BBD) was chosen to evaluate the effects and interactive effects of the three independent variables, i.e., temperature (40°C, 50°C, and 60°C), ISC (17.5%, 25.0%, and 32.5%), and C/N ratio (15:1, 23.5:1 and 32:1), as χ^1 , χ^2 , and χ^3 , respectively, on the response variable biogas production (mL gVS^{-1}) during SS-AD. The experiments were designed by Design Expert (Version 8.0.6, Statease, Minneapolis, USA), and the real values of the operating variables are summarized in Table 2. For SS-AD, corn straw, cattle manure, and vegetable waste were rigorously mixed in a mass ratio of 40:10:0.5 (dry wt.) in the laboratory. A 100 g mixed sample with a moisture content of 67.5% (adjusted by distilled water) was used as a mixed substrate. Different doses of distilled water and urea were further added to the mixed substrate to adjust the ISC and C/N ratio. Activated sludge was introduced as inoculum, with a feedstock-to-inoculum ratio (F/I, based on VS) of 3. SS-AD was carried out in 500 mL borosilicate bottles (Wente Experimental Ware, China) with a stainless steel vent pipe (Figure S1) and lasted for 20 d. Bottles were flushed with high-purity N_2 to exclude oxygen and were sealed with a silicone gasket and stopper. The temperature during SS-AD was maintained by a thermostatic water bath (DK-98, Taisite Instrument Co.

TABLE 2: Three-level-three-factor Box–Behnken design for SS-AD of corn straw, cattle manure, and vegetable waste.

Run	χ_1 A:T	χ_2 B:ISC	χ_3 C:C/N	Mixed substrate* (g)	Inoculum [#] (g)	Distilled water (mL)	Urea (g)
1	40	17.5	23.5	100	137.02	86	0.345
2	60	17.5	23.5	100	137.02	86	0.345
3	40	32.5	23.5	100	137.02	0	0.345
4	60	32.5	23.5	100	137.02	0	0.345
5	40	25	15	100	137.02	30	1.091
6	60	25	15	100	137.02	30	1.091
7	40	25	32	100	137.02	30	0.000
8	60	25	32	100	137.02	30	0.000
9	50	17.5	15	100	137.02	86	1.091
10	50	32.5	15	100	137.02	0	1.091
11	50	17.5	32	100	137.02	86	0
12	50	32.5	32	100	137.02	0	0
13	50	25	23.5	100	137.02	30	0.345
14	50	25	23.5	100	137.02	30	0.345
15	50	25	23.5	100	137.02	30	0.345
16	50	25	23.5	100	137.02	30	0.345
17	50	25	23.5	100	137.02	30	0.345

*With a moisture content of 67.5%, the mass ratio of corn straw/cattle manure/vegetable waste = 40 : 10 : 0.5 (dry wt.). [#]The feedstock-to-inoculum ratio (F/I, based on VS) was 3.

TABLE 3: Effect of T, ISC, and C/N ratio on the biogas yield, pH, and TAN concentration after 20 d of SS-AD.

Run	χ_1 A:T	χ_2 B:ISC	χ_3 C:C/N	Biogas yield (mL gVS ⁻¹)	pH	TAN concentration (mg kg ⁻¹)
1	40	17.5	23.5	71.12	8.46	1640.7
2	60	17.5	23.5	147.2	8.67	1807.1
3	40	32.5	23.5	32.60	8.02	2437.1
4	60	32.5	23.5	40.12	8.16	3281.9
5	40	25	15	212.9	8.89	1889.6
6	60	25	15	47.42	8.41	3613.4
7	40	25	32	2.80	7.49	1925.9
8	60	25	32	51.31	8.13	2066.2
9	50	17.5	15	198.1	8.69	2275.4
10	50	32.5	15	130.7	8.85	3367.3
11	50	17.5	32	26.89	6.06	1836.3
12	50	32.5	32	136.5	8.78	2343.7
13	50	25	23.5	261.8	8.67	
14	50	25	23.5	247.1	8.70	
15	50	25	23.5	225.5	8.64	1888.4
16	50	25	23.5	217.9	8.61	
17	50	25	23.5	227.2	8.57	

Ltd., China). An aluminium foil bag (E-switch, Shenyuan Scientific Equipment Co., China) was connected to the gas outlet by a three-way valve (Discofix, B. Braun, Germany) to collect biogas from each bottle. Different parameters, such as pH, TAN, and microbial community, were analyzed

after 20 d of SS-AD. One-way ANOVA was employed to study the primary effects and interactions on biogas production between the parameters selected.

2.3. Analytical Methods. The pH of the digestate was measured by a digital pH meter (Sartorius, Model PB-10, Germany) after shaking for 20 min at 25°C with a liquid-solid ratio of 10:1. The TAN concentration of digestate extracted by ultrapure water was determined by a continuous flow analyser (Skalar San++, Netherlands). To analyze the structure of the microbial communities after 20 d of SS-AD under different operating conditions, 0.5 g of the sample was used for DNA extraction. Total DNA was extracted by a Fast DNA SPIN Kit (BIO 101, Carlsbad, CA, USA) according to the manufacturer's protocol. The V3-V4 region of the 16S rRNA gene was amplified using universal primers 338F (5'-ACT CCT ACG GGA GGC AGC AG-3') and 806R (5'-GGAC TA CHV GGG TWT CTA AT-3'). The amplicons from each sample were sequenced with the Illumina MiSeq platform (Illumina Company, San Diego, CA, USA). Diversity statistics and operational taxonomic unit (OTU) estimators were calculated using mothur software [22]. The coverage of the clone library was calculated based on the formula $C = [1 - (n1/N)] \times 100$, where $n1$ is the number of unique OTUs, and N is the total number of clones in a library.

3. Results and Discussion

3.1. SS-AD Performance. The cumulative biogas volumes with different parameters (ISC, T, and C/N ratio) after 20 d of SS-AD are shown in Table 3. The maximum biogas production of 236 mL gVS⁻¹ was obtained at 50°C, ISC = 25%,

TABLE 4: ANOVA for the quadratic model of SS-AD biogas production.

Source	Sum of squares	df	Mean square	F value	p value	
Model	128108	9	14234	56.10	<0.0001	Significant
χ_1 -T	4315	1	4315	17.01	0.0062	
χ_2 -ISC	687	1	687	2.71	0.1510	
χ_3 -C/N	17263	1	17263	68.04	0.0002	
χ_1, χ_2	1973	1	1973	7.78	0.0316	
χ_1, χ_3	11448	1	11448	45.12	0.0005	
χ_2, χ_3	7833	1	7833	30.87	0.0014	
χ_1^2	54668	1	54668	215.46	<0.0001	
χ_2^2	23310	1	23310	91.87	<0.0001	
χ_3^2	2848	1	2848	11.22	0.0154	
Residual	1522	6	254			
Lack of fit	218	2	109	0.33	0.7338	Not significant
Pure error	1304	4	326			
Cor total	129630	15				

$R^2 = 0.9883$; Adj $R^2 = 0.9706$; Adeq precision = 18.17

and C/N = 23.5. It is noted that the operating parameters at 40°C, ISC = 25%, and C/N = 32 cause digester failure, generating little biogas (2.80 mL gVS⁻¹) during the entire digestion process. According to the three-level-three-factor BBD, the average biogas volume yield was 110.9 mL gVS⁻¹ with 12 different operating parameter settings (excluding failed digester). The results showed that optimizing the process parameters is important to promote the SS-AD performance.

3.2. pH and TAN Concentrations. After 20 d of anaerobic digestion, the NH₄⁺-N concentration of each run was determined. In this study, NH₄⁺-N was derived from cattle manure (N-rich substrates), degradation of nitrogenous organic matter (e.g., proteins and amino acids), and/or conversion of urea by deamination. TAN is a key macronutrient for microbial growth and a buffer to stabilize the pH, while high concentrations of TAN would decrease the methanogen activity and cause anaerobic digestion failure due to ammonia inhibition [23]. Production of excessive ammonia nitrogen is more likely to happen in SS-AD than L-AD due to the higher organic loading and lower water content of the former [24]. As shown in Table 3, the concentration of TAN ranged from 1641-3613 mg kg⁻¹ for all samples after 20 d of anaerobic digestion. It can also be seen that a high TAN concentration was caused by a combination of elevated temperature, high ISC, and low C/N ratio. It is reported that in the L-AD system, the TAN concentration should not reach the range of 1500-3000 mg L⁻¹ to avoid the toxicity of ammonia [25]. Wang et al. [24] showed that a TAN level of 4.3 g kg⁻¹ caused a reduction in the reaction rates and microbial activities for hydrolysis of cellulose and methanogenesis from ace-

tate, and a TAN level of 2.5 g kg⁻¹ decreased the methane yield during SS-AD of corn stover. Therefore, it is believed that the biogas yield from runs 4, 6, and 10 was inhibited due to the excessive TAN levels (greater than 3.0 g kg⁻¹). It seems that the SS-AD failure of run 7 was not caused by the accumulation of VFA (decreasing pH value) or excessive TAN level. The cause for the SS-AD failure of run7 is still unclear. TAN includes both NH₄⁺ and free ammonia (FAN, NH₃). FAN is the main cause of ammonia inhibition because it is membrane permeable [26, 27]. So far, a FAN calculation method has rarely been applied in SS-AD, the digestate of which generally has a higher ionic strength than that in L-AD [23]. FAN inhibition is related to the characteristics of the substrate, pH, process temperature, concentrations of ammonium and ammonia, etc. [28]. Capson-Tojo et al. [4] demonstrated that pH and temperature, rather than the TAN content itself, are the main factors affecting FAN inhibition. Among the high-TAN samples, the biogas yield of run 10, with a higher pH value, was much greater than that of run 4 and run 6. This phenomenon might be related to the higher FAN concentrations at increasing temperatures [23].

3.3. Modeling of SS-AD for Biogas Production. The results in Table 3 were used for multiple regression analysis using the polynomial model equation. This approach enabled the prediction of the optimum degree of biogas production and its corresponding optimum variables. One-way analysis of variance (ANOVA) was employed to test and analyze different models. In this study, the best-fit model found for the biogas production was a quadratic model. The F value of the model was 8.45, with a low p value of 0.0051. However, the F value (0.95) and p value (0.0256) of the lack of fit implied that the prediction for the fit of the model was not good. Further, studentized residual analysis showed that run 2 was an outlier due to its externally studentized residuals being larger than 5. Therefore, the data of run 2 were not included in the following modeling analysis.

The following polynomial quadratic model for biogas production was then adjusted to a better prediction by applying response surface regression (RSREG), as shown in Eq. (1), where χ_1 is the temperature, χ_2 is the ISC, and χ_3 is the C/N ratio.

$$\begin{aligned} \text{Biogas yield (mL gVS}^{-1}\text{)} = & -2215 + 99.96\chi_1 + 38.59\chi_2 - 35.27\chi_3 \\ & + 0.4188\chi_1\chi_2 + 0.6294\chi_1\chi_3 \\ & + 0.6942\chi_2\chi_3 - 1.281\chi_1^2 \\ & - 1.487\chi_2^2 - 0.4046\chi_3^2. \end{aligned} \quad (1)$$

ANOVA was conducted for the response variable, as presented in Table 4. The model F value of 56.10 indicated that the quadratic model was statistically significant for biogas production. The high R^2 coefficient of 0.9883 ensured a satisfactory adjustment of the quadratic model to the experimental data, implying that only 1.17% of biogas production variability could not be explained by the proposed model. The adjusted R -square ($R_{\text{adj}}^2 = 0.9706$) and Adeq-Precision

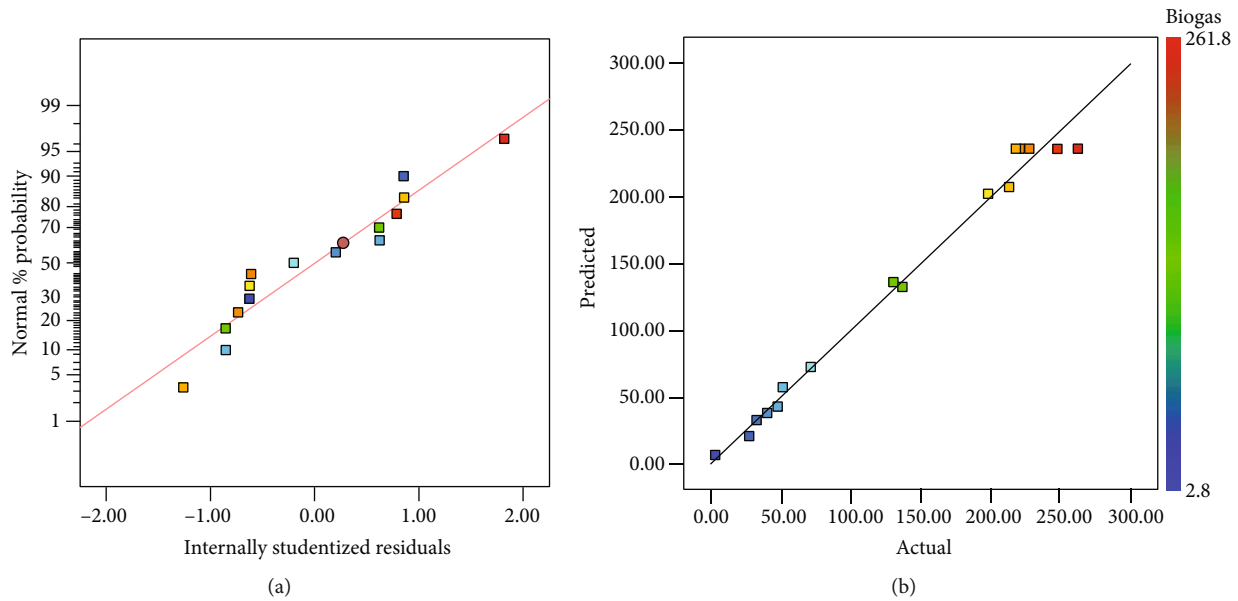


FIGURE 1: Plots of standardized residuals vs. normal % probability for biogas production (a). Actual and predicted values of biogas production (b).

of 18.17 were also high, supporting the high significance of the model. The lack-of-fit F value of 0.33 revealed that the lack of fit was insignificant. Therefore, it is reasonable to believe that the proposed model is reliable for predicting the biogas production of SS-AD.

The significance test for the regression coefficients determined by p values was carried out. The larger the F value of the regression parameter was, the smaller the p values were, indicating that this parameter has a greater impact on biogas production. The corresponding p values showed that all the factors, including interactive terms, were significant model terms, except the ISC (F value = 2.71, p value = 0.1510). Among the three operating parameters, the C/N ratio (F value = 68.04, p value = 0.002) had the largest effect on biogas production, followed by temperature (F value = 17.01, p value = 0.0062).

It is important to check the model adequacy of biogas production for response surface optimization, as the model would give poor or misleading results if not well fit. The normal probability plot indicates whether the residuals follow a normal distribution, in which case the points will follow a straight line [29]. The normality assumption was examined by constructing a plot of standardized residuals vs. the normal % probability. As shown in Figure 1(a), the normal probability plot was approximated well by a straight line, indicating that the response variables did not require transformation, and that there were no apparent abnormality issues [29]. Figure 1(b) shows that the predicted values of the responses from the biogas production model accorded well with the actual values. The distribution of data plots is relatively close to a straight line, indicating reasonably adequate agreement between the actual and predicted values and confirming that the model could be further used to navigate the space defined by BBD.

3.4. Optimization of Biogas Production Operating Parameters. The experimental results were visualized in three-dimensional response surface plots and the corresponding contour plot, which show the simultaneous effect of two independent factors on biogas production, with one variable maintained at its central level. Figure 2(a) illustrates the effects of ISC and T on biogas production at a C/N ratio of 23.5. Noticeable changes in the biogas production by changing each parameter were recorded, and the results showed that both parameters and their interaction are effective [8]. According to Figure 2(a), biogas production showed a significant increasing trend as the ISC increased from 17.5 to 25% and temperature increased from 40 to 50°C; the biogas production then decreased when the ISC and temperature increased beyond those values.

The TS content is responsible for the mass transfer in SS-AD [30]. It is believed that a decreasing TS content might facilitate substrate conversion in SS-AD because metabolism by microorganisms (including hydrolytic bacteria, acidogenic bacteria, acetogenic bacteria, and methanogenic archaea) occurs in the water-soluble phase [31–33]. However, the maximum value of biogas production was not achieved at the lowest ISC (17.5%) in this study. It appears that in this study, the increase in the feed TS content up to 25% has a positive effect on biogas production. Yi et al. [34] showed that biogas production increased as the TS content increased from 5%–20%, and Paritosh et al. [35] reported that increasing the TS content beyond 25% did not result in a significant increase in the methane yield, consistent with our results. Yan et al. [8] reported that biogas production decreased drastically when increasing the ISC from 20 to 35%. This phenomenon suggested that the effect of the TS content on biogas production is related to the specific characteristics of the substrates, the type of inoculum, and the

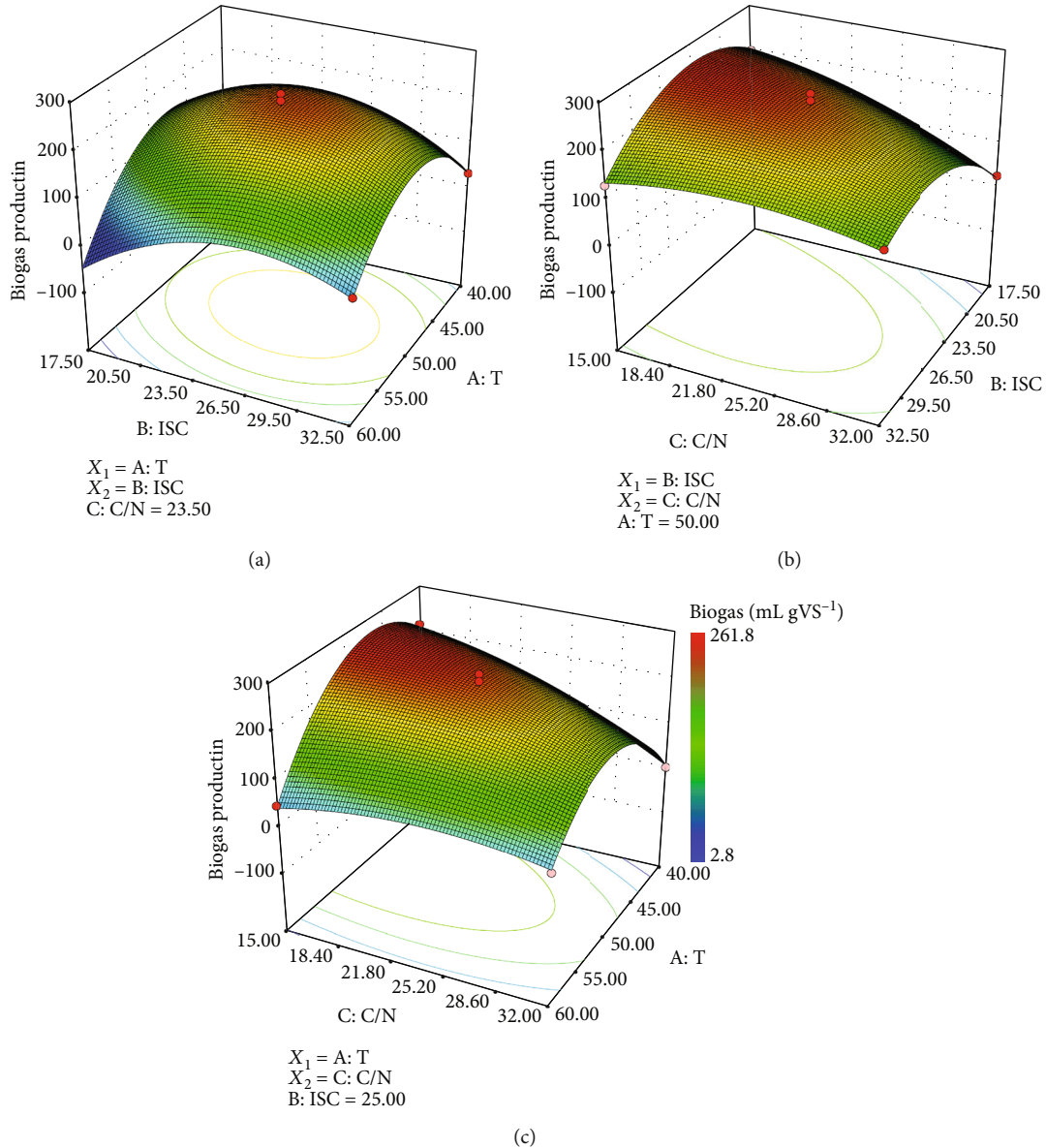


FIGURE 2: Effects of the ISC, T, and C/N ratio on biogas production. (a) Interactive effect of the ISC and T at a C/N ratio of 23.5. (b) Interactive effect of the ISC and C/N ratio at 50°C. (c) Interactive effect of the T and C/N ratio at an ISC of 25%.

interaction of other operating parameters (such as process temperature) [30]. The operating temperature determines the fate of the microbes, which may disturb the overall reaction process. In this study, further increasing the temperature above 50°C exhibited a negative effect on biogas production. It has been reported that thermophilic conditions in SS-AD enhance the hydrolysis of the substrate by stimulating hydrolytic microorganisms, and an excessive process temperature may hamper or inhibit the methanogenesis process due to VFA accumulation [30, 36]. The results from previous studies were consistent with our results.

Figures 2(b) and 2(c) illustrate the effects of the ISC and C/N ratio on biogas production at 50°C and the effects of the T and C/N ratio on biogas production at an ISC of 25%, respectively. It is found that the enhancement of biogas production can be achieved when the ISC increased from

17.5 to 25% at the temperature of 50°C and then decreased gradually after that (Figure 2(b)), showing no difference from the results shown in Figure 2(a). It is also observed that the biogas production decreased when the C/N ratio increased from 15 to 32 at the temperature of 50°C, confirming that a high C/N ratio results in the rapid consumption of nitrogen by methanogens and further results in a lower biogas yield [37]. These results also suggested that the microbial activities for hydrolysis and methanogenesis at 50°C could withstand the inhibition caused by excessive free ammonia production.

3.5. Optimization of SS-AD. The SS-AD parameters were optimized based on the quadratic model using the optimization module of the Design Expert software. The results showed that a maximum biogas production capacity of 265 mL gVS⁻¹ would be achieved with an ISC of 23.4%, T of

TABLE 5: Microbial diversity indices based on 97% identity of 16S rRNA gene sequences.

Sample	Sequences	Observed species	Chao 1	Shannon index	Coverage
S1	27252	777.8	773.74	4.84	99.10%
S2	26466	607.56	641.6	3.8	99.10%
S3	31804	731.53	739.76	4.67	99.10%
S4	16963	636.68	660.15	4.14	99.10%
S5	16877	627.73	609.84	4.31	99.20%
S6	33006	812.68	805.12	4.73	99.00%
S7	20373	615.82	608.88	4.52	99.40%
S8	27445	784.3	671.71	3.87	99.00%
S9	25602	767.25	763.11	4.77	99.10%
S10	24824	709.31	705.33	4.32	99.00%
S11	27304	699.89	712.33	4.75	99.20%
S12	17586	704.69	720.62	4.42	99.10%
S13	24440	680.86	720.56	4.19	99.10%
S14	25193	621.92	623.55	4.17	99.20%

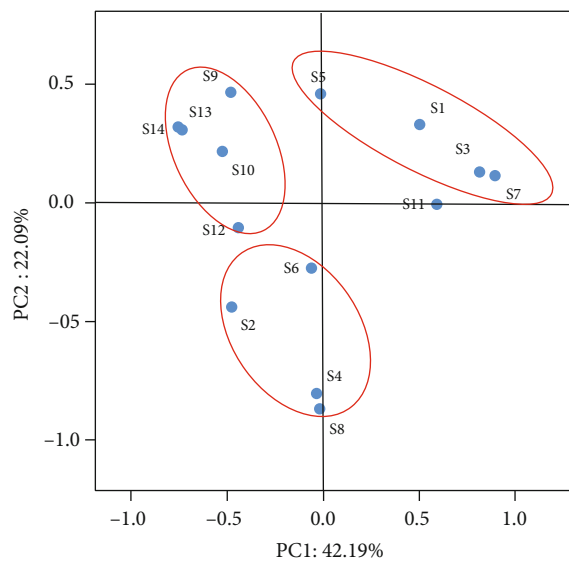


FIGURE 3: PCoA plot comparing bacterial communities from different 20 d SS-AD samples.

47.7°C, and C/N ratio of 17.2, without considering other factors. It is noteworthy that the optimized C/N ratio is relatively low, indicating that considerable extra urea or other nitrogen sources should be added during the SS-AD process, which would increase the operating cost. Moreover, a low C/N ratio might hinder the composting of the digestate of SS-AD [38]. Torres-Climent et al. reported that a C/N ratio of 28-31 showed the most rapid temperature increase during composting of the solid phase of digestate [39]. Additionally, a relatively lower temperature would be desired for SS-AD because of the stability and lower heating energy costs. Therefore, a goal was set to maximize biogas production and the C/N ratio while minimizing the process temperature. Concretely, for optimization, the importance of temperature

and the C/N ratio were considered important (+), and biogas production was considered the most important (+++++). The results indicated that a biogas productivity of 241.4 mL.gVS⁻¹ would be achieved at 47.3°C, ISC = 24.81%, and C/N = 22.35. As the optimized parameters, i.e., ISC, C/N ratio, and T, are close to the parameters designed in this study, a verification experiment of SS-AD was not further carried out.

3.6. Comparison of the Community Diversity of Bacteria.

After 20 d, the bacterial communities in SS-AD samples from run 1 to run 14 were further characterized by amplicon sequencing of 16S rRNA genes. As shown in Table 5, different high-quality sequences ranging from 16,877 to 33,006 per sample were obtained. All of the sequences were aligned and clustered to calculate the operational taxonomic units (OTUs) based on 97% sequence identity, resulting in 1105 OTUs at a sequencing depth of 16000 reads per sample and coverage of 99.0-99.4%. These results showed that the Chao 1 estimator of richness and Shannon diversity index of the microbial community at 60°C (except S6) were lower than those at 50°C, indicating that the microbial communities at 50°C were generally more complex than those at 60°C. The differences in microbial communities among SS-AD samples were also described by principal coordinate analysis (PCoA), as shown in Figure 3. The first two axes of the PCoA explained 42.19% and 22.09% of the variance, respectively, or collectively 64.28% of the variance. This analysis also showed a distinct community structure among SS-AD samples that can be separated into three groups based on incubation temperatures (i.e., 40, 50, and 60°C), except S11, which had excessive acidification (Figure 4).

Ten major phyla, represented by more than 1% of the total bacterial sequence of each phylum, were found for the SS-AD samples. This result is not surprising because distinct differences in the relative abundance of these phyla were observed with various operating parameters. *Firmicutes* and *Bacteroidetes* have been repeatedly reported as the main phyla in different anaerobic digesters [40]. In this study, *Firmicutes* sequences indicated that it was the most predominant phylum at temperatures of 50°C and 60°C, accounting for 65-90% of the total bacterial sequences; the percentages of *Firmicutes* sequences in the SS-AD samples were 37.5-60% at 40°C, except for S7 (27%). *Bacteroidetes* was the second most prevalent phylum at 40°C (18.62-28.37%, except for S7), but it only represented 0.76-12.21% of the total bacterial sequences at 50 and 60°C. These observations of a higher abundance of *Firmicutes* and a lower abundance of *Bacteroidetes* at the process temperatures of 50-60°C compared with 40°C are consistent with the results from previous studies [41, 42], indicating a competitive advantage of *Firmicutes* over *Bacteroidetes* at elevated temperatures [40]. For the phylum *Thermotogae*, the percentage of sequences at 60°C (2.07-5.45%) is much higher than that at other temperatures (0.15-1.29%), except for S12 (2.85%). Due to the SS-AD failure, the major bacterial phyla of S7 were dramatically different from those of other samples at 40°C (Figure 4(a)), containing a lower percentage of *Firmicutes* sequences and *Bacteroidetes* sequences and a much higher percentage of *Proteobacteria* sequences. It also noted that S11, with excessive acidification, contained a higher percentage of

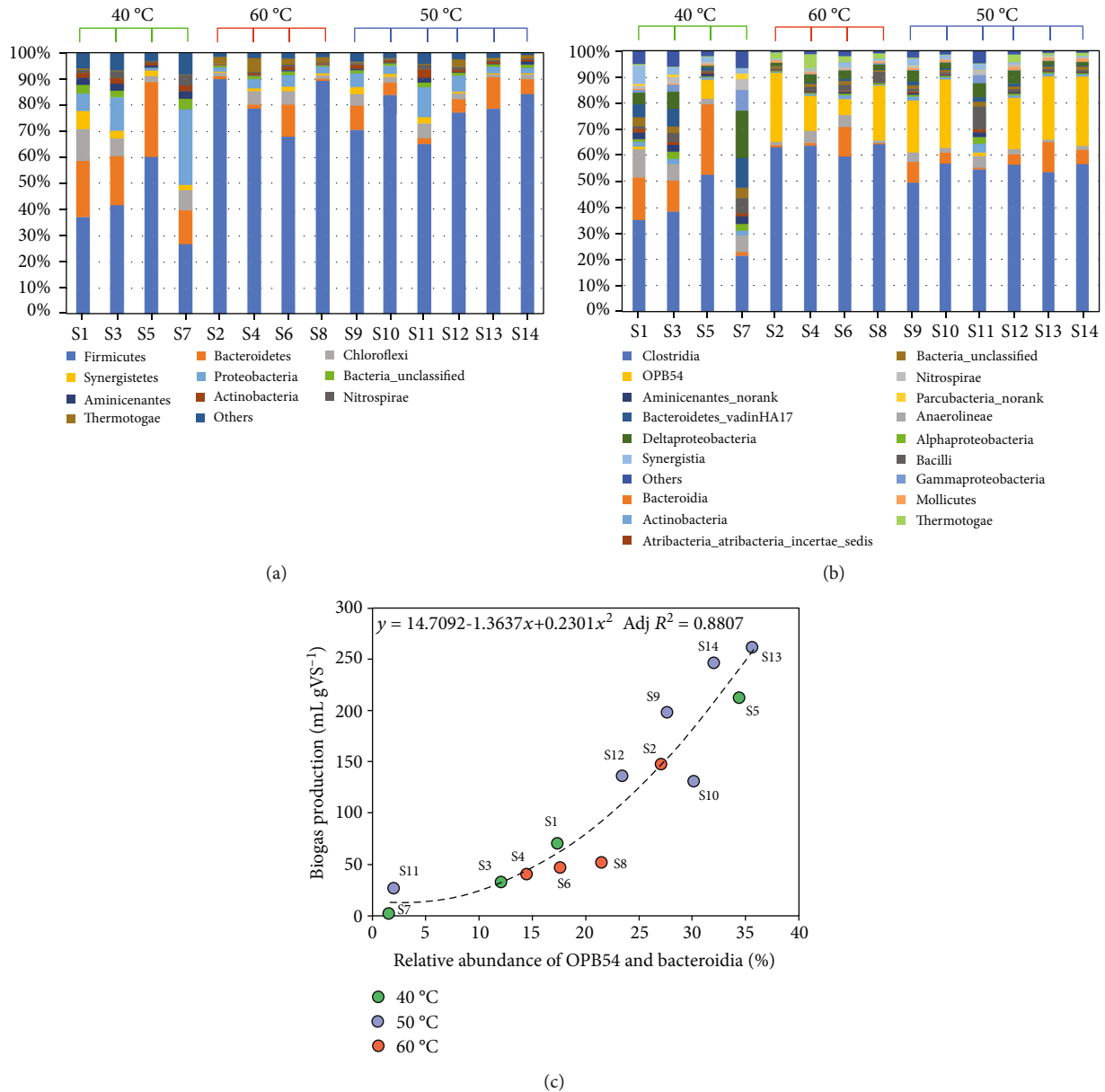


FIGURE 4: Major bacterial phyla (each represented by >1% total sequences in at least one sample) (a), relative abundance (% of the total bacterial sequences in each sample) of the major OTUs (b), and relationship between biogas production and relative abundance of *OPB54* and *Bacteroidia* (c) after 20 d of SS-AD.

Proteobacteria, *Aminicenantes*, *Actinobacteria*, and *Nitrospirae* sequences and a lower percentage of *Firmicutes* sequences than the other samples at 50°C.

A total of 18 classes were identified for SS-AD samples that harboured $\geq 1\%$ of the reads in one or more of the sequences, while *Clostridia*, *Bacteroidia*, *Anaerolineae*, and *OPB54* were the primary communities (Figure 4(b)). Among them, the class *Clostridia* has been associated with hydrolysis, acidogenesis, and acetogenesis steps [40]. *OPB54* was previously identified in an enrichment culture of lignocellulosic biomass and was the most abundant anaerobic syntrophic acetate-oxidizing genus in biogas digesters fed with high levels of acetate [43, 44]. The difference between the S13 and S14 samples, which have identical operating parameters,

was quite small at the class level, where *OPB54_norank* in the phylum *Firmicutes* was the most dominant genus (Figure S2). It is worth noting that the biogas production values and relative abundances of *OPB54* and *Bacteroidia* after 20 d of SS-AD can be fitted well using a quadratic model (Figure 4(c)), with $\text{Adj } R^2 = 0.8807$, implying that *OPB54* and *Bacteroidia* play important roles in the methanogenic metabolism for agriculture waste thermophilic SS-AD.

4. Conclusion

Optimizing the process parameters, i.e., temperature (40–60°C), initial solid content (17.5–32.5%), and C/N ratio (15–

32:1), is important to promote the thermophilic SS-AD performance of the agriculture waste. All the factors, including interactive terms (except the ISC), were significant in the quadratic model for biogas production. Among the three operating parameters, the C/N ratio had the largest effect on biogas production, followed by temperature, and the maximum biogas yield of 241.4 mL gVS⁻¹ could be achieved at 47.3°C, ISC = 24.81%, and C/N = 22.35. After 20 d of SS-AD, PCoA showed a distinct community structure that could be separated into three groups based on incubation temperatures, except for the SS-AD sample with excessive acidification. The biogas production values and relative abundance of *OPB54* and *Bacteroidia* after 20 d of SS-AD can be fitted well using a quadratic model, implying that *OPB54* and *Bacteroidia* play important roles in the methanogenic metabolism.

Data Availability

The data used to support the findings of this study are available from the corresponding author upon request.

Disclosure

The funding sources had no role in the study design, data collection, and analysis, decision to publish, or preparation of the manuscript.

Conflicts of Interest

There are no conflicts to declare.

Acknowledgments

The authors wish to thank the Basal Research Fund of Central Public-interest Scientific Institution of Nanjing Institute of Environmental Sciences, Ministry of Ecology and Environment (No. GYZX190203 and No. 20160301), the Distinguished Professor in Universities of Shanghai (Oriental Scholar, No. TP2017041), and the National Key Research and Development Program of China (2016YFD0800601).

Supplementary Materials

Figure S1: SS-AD reactor used in this study. Figure S2: major bacterial genera (a list of the 50 most abundant genera) after 20 d of SS-AD. (*Supplementary materials*)

References

- [1] J. Chen, Y. Gong, S. Wang, B. Guan, J. Balkovic, and F. Kraxner, "To burn or retain crop residues on croplands? An integrated analysis of crop residue management in China," *Science of The Total Environment*, vol. 662, pp. 141–150, 2019.
- [2] Y. R. Fang, Y. Wu, and G. H. Xie, "Crop residue utilizations and potential for bioethanol production in China," *Renewable and Sustainable Energy Reviews*, vol. 113, article 109288, 2019.
- [3] W. Bao, Y. Yang, T. Fu, and G. H. Xie, "Estimation of livestock excrement and its biogas production potential in China," *Journal of Cleaner Production*, vol. 229, pp. 1158–1166, 2019.
- [4] G. Capson-Tojo, R. Moscoviz, S. Astals, Á. Robles, and J. P. Steyer, "Unraveling the literature chaos around free ammonia inhibition in anaerobic digestion," *Renewable and Sustainable Energy Reviews*, vol. 117, article 109487, 2020.
- [5] Z.-B. Yue, W.-W. Li, and H.-Q. Yu, "Application of rumen microorganisms for anaerobic bioconversion of lignocellulosic biomass," *Bioresource Technology*, vol. 128, pp. 738–744, 2013.
- [6] M. R. Riazi and D. Chiaramonti, *Biofuels Production and Processing Technology*, CRC Press, 2017.
- [7] E. Rouches, R. Escudí, E. Latrille, and H. Carrère, "Solid-state anaerobic digestion of wheat straw: impact of S/I ratio and pilot-scale fungal pretreatment," *Waste Management*, vol. 85, pp. 464–476, 2019.
- [8] Z. Yan, Z. Song, D. Li, Y. Yuan, X. Liu, and T. Zheng, "The effects of initial substrate concentration, C/N ratio, and temperature on solid-state anaerobic digestion from composting rice straw," *Bioresource Technology*, vol. 177, pp. 266–273, 2015.
- [9] X. Ge, F. Xu, and Y. Li, "Solid-state anaerobic digestion of lignocellulosic biomass: recent progress and perspectives," *Biore-source Technology*, vol. 205, pp. 239–249, 2016.
- [10] Y. Li, S. Y. Park, and J. Zhu, "Solid-state anaerobic digestion for methane production from organic waste," *Renewable and Sustainable Energy Reviews*, vol. 15, no. 1, pp. 821–826, 2011.
- [11] Y. Liu, J. Fang, X. Tong et al., "Change to biogas production in solid-state anaerobic digestion using rice straw as substrates at different temperatures," *Bioresource Technology*, vol. 293, article 122066, 2019.
- [12] T. Pincam, H. Brix, and A. Jampeetong, "Treatment of anaerobic digester effluent using *Acorus calamus*: effects on plant growth and tissue composition," *Plants*, vol. 7, no. 2, p. 36, 2018.
- [13] Q. Shui, H. Dong, Z. Zhu, and H. Huang, "Present status of biogas effluent treatment technology research and application (in Chinese)," *Journal of Agricultural Science and Technology*, vol. 13, pp. 83–87, 2011.
- [14] SEPA, *Standards for Irrigation Water Quality of China*, Beijing, China, 2005.
- [15] R. Le Hyaric, H. Benbelkacem, J. Bollon, R. Bayard, R. Escudie, and P. Buffiere, "Influence of moisture content on the specific methanogenic activity of dry mesophilic municipal solid waste digestate," *Journal of Chemical Technology and Biotechnology*, vol. 87, no. 7, pp. 1032–1035, 2012.
- [16] A. Abbassi-Guendouz, D. Brockmann, E. Trably et al., "Total solids content drives high solid anaerobic digestion via mass transfer limitation," *Bioresource Technology*, vol. 111, pp. 55–61, 2012.
- [17] J. Fernandez, M. Perez, and L. I. Romero, "Effect of substrate concentration on dry mesophilic anaerobic digestion of organic fraction of municipal solid waste (OFMSW)," *Biore-source Technology*, vol. 99, no. 14, pp. 6075–6080, 2008.
- [18] X. Wang, X. Lu, F. Li, and G. Yang, "Effects of temperature and carbon-nitrogen (C/N) ratio on the performance of anaerobic co-digestion of dairy manure, chicken manure and rice straw: focusing on ammonia inhibition," *PLoS One*, vol. 9, no. 5, article e97265, 2014.
- [19] J. Fernández-Rodríguez, M. Pérez, and L. I. Romero, "Comparison of mesophilic and thermophilic dry anaerobic digestion of OFMSW: kinetic analysis," *Chemical Engineering Journal*, vol. 232, pp. 59–64, 2013.
- [20] S. Steudler, A. Werner, and J. J. Cheng, *Solid State Fermentation Research and Industrial Applications*, Springer International Publishing, 2019.

- [21] D. Brown and Y. Li, "Solid state anaerobic co-digestion of yard waste and food waste for biogas production," *Bioresource Technology*, vol. 127, pp. 275–280, 2013.
- [22] P. D. Schloss, S. L. Westcott, T. Ryabin et al., "Introducing mothur: open-source, platform-independent, community-supported software for describing and comparing microbial communities," *Applied and Environmental Microbiology*, vol. 75, no. 23, pp. 7537–7541, 2009.
- [23] R. Rajagopal, D. I. Massé, and G. Singh, "A critical review on inhibition of anaerobic digestion process by excess ammonia," *Bioresource Technology*, vol. 143, pp. 632–641, 2013.
- [24] Z. Wang, F. Xu, and Y. Li, "Effects of total ammonia nitrogen concentration on solid-state anaerobic digestion of corn stover," *Bioresource Technology*, vol. 144, pp. 281–287, 2013.
- [25] G. Bitton, *Wastewater Microbiology*, John Wiley & Sons Inc., Hoboken, NJ, USA, 2005.
- [26] T. Müller, B. Walter, A. Wirtz, and A. Burkovski, "Ammonium toxicity in bacteria," *Current Microbiology*, vol. 52, no. 5, pp. 400–406, 2006.
- [27] T. Sayara and A. Sánchez, "A review on anaerobic digestion of Lignocellulosic wastes: pretreatments and operational conditions," *Applied Sciences*, vol. 9, no. 21, article 4655, 2019.
- [28] O. Yenigün and B. Demirel, "Ammonia inhibition in anaerobic digestion: a review," *Process Biochemistry*, vol. 48, no. 5–6, pp. 901–911, 2013.
- [29] Z. Guangyin and Z. Youcai, "Enhanced sewage sludge dewaterability by chemical conditioning," in *Pollution Control and Resource Recovery for Sewage Sludge*, Z. Guangyin and Z. Youcai, Eds., pp. 13–99, Butterworth-Heinemann, 2017.
- [30] J. Bollon, H. Benbelkacem, R. Gourdon, and P. Buffière, "Measurement of diffusion coefficients in dry anaerobic digestion media," *Chemical Engineering Science*, vol. 89, pp. 115–119, 2013.
- [31] X. Li, X. Dai, J. Takahashi et al., "New insight into chemical changes of dissolved organic matter during anaerobic digestion of dewatered sewage sludge using EEM-PARAFAC and two-dimensional FTIR correlation spectroscopy," *Bioresource Technology*, vol. 159, pp. 412–420, 2014.
- [32] S. Shakeri Yekta, M. Gonsior, P. Schmitt-Kopplin, and B. H. Svensson, "Characterization of dissolved organic matter in full scale continuous stirred tank biogas reactors using ultrahigh resolution mass spectrometry: a qualitative overview," *Environmental Science & Technology*, vol. 46, no. 22, pp. 12711–12719, 2012.
- [33] M. Xing, X. Li, J. Yang, Z. Huang, and Y. Lu, "Changes in the chemical characteristics of water-extracted organic matter from vermicomposting of sewage sludge and cow dung," *Journal of Hazardous Materials*, vol. 205–206, pp. 24–31, 2012.
- [34] J. Yi, B. Dong, J. Jin, and X. Dai, "Effect of increasing total solids contents on anaerobic digestion of food waste under mesophilic conditions: performance and microbial characteristics analysis," *PLoS One*, vol. 9, no. 7, article e102548, 2014.
- [35] K. Paritosh, N. Pareek, A. Chawade, and V. Vivekanand, "Prioritization of solid concentration and temperature for solid state anaerobic digestion of pearl millet straw employing multi-criteria assessment tool," *Scientific Reports*, vol. 9, no. 1, article 11902, 2019.
- [36] J. Shi, Z. Wang, J. A. Stiverson, Z. Yu, and Y. Li, "Reactor performance and microbial community dynamics during solid-state anaerobic digestion of corn stover at mesophilic and thermophilic conditions," *Bioresource Technology*, vol. 136, pp. 574–581, 2013.
- [37] V. Marchioro, R. L. R. Steinmetz, A. C. do Amaral, T. C. Gaspareto, H. Treichel, and A. Kunz, "Poultry litter solid state anaerobic digestion: effect of digestate recirculation intervals and substrate/inoculum ratios on process efficiency," *Frontiers in Sustainable Food Systems*, vol. 2, 2018.
- [38] M. A. Bustamante, A. P. Restrepo, J. A. Alburquerque et al., "Recycling of anaerobic digestates by composting: effect of the bulking agent used," *Journal of Cleaner Production*, vol. 47, pp. 61–69, 2013.
- [39] A. Torres-Climent, J. Martin-Mata, F. Marhuenda-Egea et al., "Composting of the solid phase of digestate from biogas production: optimization of the moisture, C/N ratio, and pH conditions," *Communications in Soil Science and Plant Analysis*, vol. 46, Supplement 1, pp. 197–207, 2015.
- [40] D. G. Mulat, S. G. Huerta, D. Kalyani, and S. J. Horn, "Enhancing methane production from lignocellulosic biomass by combined steam-explosion pretreatment and bioaugmentation with cellulolytic bacterium *Caldicellulosiruptor bescii*," *Biotechnology for Biofuels*, vol. 11, no. 1, p. 19, 2018.
- [41] Y. F. Li, M. C. Nelson, P. H. Chen, J. Graf, Y. Li, and Z. Yu, "Comparison of the microbial communities in solid-state anaerobic digestion (SS-AD) reactors operated at mesophilic and thermophilic temperatures," *Applied Microbiology and Biotechnology*, vol. 99, no. 2, pp. 969–980, 2015.
- [42] L. Sun, P. B. Pope, V. G. H. Eijsink, and A. Schnürer, "Characterization of microbial community structure during continuous anaerobic digestion of straw and cow manure," *Microbial Biotechnology*, vol. 8, no. 5, pp. 815–827, 2015.
- [43] L. Hao, F. Lü, L. Mazéas et al., "Stable isotope probing of acetate fed anaerobic batch incubations shows a partial resistance of acetoclastic methanogenesis catalyzed by *Methanosarcina* to sudden increase of ammonia level," *Water Research*, vol. 69, pp. 90–99, 2015.
- [44] M. T. Wong, W. Wang, M. Lacourt, M. Couturier, E. A. Edwards, and E. R. Master, "Substrate-driven convergence of the microbial community in lignocellulose-amended enrichments of gut microflora from the Canadian beaver (*Castor canadensis*) and north American moose (*Alces americanus*)," *Frontiers in Microbiology*, vol. 7, p. 961, 2016.

Research Article

Identification and Characterization of a Newly Isolated Chitinase-Producing Strain *Bacillus licheniformis* SSCL-10 for Chitin Degradation

Abirami Sasi ¹, Nagarajan Duraipandiyan ², Kannan Marikani ³,
Sugapriya Dhanasekaran ⁴, Noura Al-Dayyan ⁵ and Divya Venugopal ⁴

¹Department of Microbiology, Kamaraj College, Thoothukudi, India

²Department of Zoology, Kamaraj College, Thoothukudi, India

³Department of Zoology, V.H.N.S.N.College (Autonomous), Virudhunagar626001, TN, India

⁴Department of Medical Lab Sciences, College of Applied Medical Sciences, Prince Sattam Bin Abdulaziz University, Wadi ad-Dawasir Campus, Saudi Arabia

⁵Department of Medical Lab Sciences, College of Applied Medical Sciences, Prince Sattam Bin Abdulaziz University, Al Kharj, Saudi Arabia

Correspondence should be addressed to Sugapriya Dhanasekaran; sughaphd@yahoo.com

Received 22 July 2020; Revised 9 September 2020; Accepted 15 October 2020; Published 9 November 2020

Academic Editor: Yu Tao

Copyright © 2020 Abirami Sasi et al. This is an open access article distributed under the Creative Commons Attribution License, which permits unrestricted use, distribution, and reproduction in any medium, provided the original work is properly cited.

Chitinases or chitinolytic enzymes have different applications in the field of medicine, agriculture, and industry. The present study is aimed at developing an effective hyperchitinase-producing mutant strain of novel *Bacillus licheniformis*. A simple and rapid methodology was used for screening potential chitinolytic microbiota by chemical mutagenesis with ethylmethane sulfonate and irradiation with UV. There were 16 mutant strains exhibiting chitinase activity. Out of the chitinase-producing strains, the strain with maximum chitinase activity was selected, the protein was partially purified by SDS-PAGE, and the strain was identified as *Bacillus licheniformis* (SSCL-10) with the highest specific activity of 3.4 U/mL. The induced mutation model has been successfully implemented in the mutant EMS-13 (20.2 U/mL) that produces 5-6-fold higher yield of chitinase, whereas the mutant UV-11 (13.3 U/mL) has 3-4-fold greater chitinase activity compared to the wild strain. The partially purified chitinase has a molecular weight of 66 kDa. The wild strain (SSCL-10) was identified as *Bacillus licheniformis* using 16S rRNA sequence analysis. This study explores the potential applications of hyperchitinase-producing bacteria in recycling and processing chitin wastes from crustaceans and shrimp, thereby adding value to the crustacean industry.

1. Introduction

Shrimp production in India was estimated to be 700,000 tons in 2019, with the state of Tamil Nadu being one of the main producers. The seafood industry makes a significant contribution to the global food supply providing an essential source of protein. The commercialization of this aquaculture has generated economic profits while the wastes produced by these industries have had an adverse effect on the ecosystem [1, 2]. The global fish production is estimated to rise from 154 million tons in 2011 to 186 million tons in 2030 [3].

Approximately 5% of shrimp wastes are processed into flours and extracts which form a base for animal feed [4]. Shrimp wastes consist of 40% chitin, a polysaccharide made up of N-acetylglucosamine units [5] and a significant primary resource for the source of bioactive molecules [6].

Chitin is degraded most frequently by the chemical pathway to generate oligosaccharides. However, this involves adverse consequences such as processing costs and harmful effects on the ecosystem with the use of highly corrosive chemical reagents [7, 8]. On the other hand, the biotechnological pathway is an ecofriendly approach [9] where

chitinases (glycosyl-hydrolase proteins) play an important role in cleaving the β -1,4 bonds of the N-acetylglucosamine units resulting in chitin degradation [10].

Most of the common bacteria and fungi microbiota synthesize chitinolytic enzymes, and some unknown species effectively decompose this chitin polymer. Researchers have reported that marine environments are the principal source of chitinase-synthesizing microorganisms, mostly bacterial species [11] out of which only 4% of the strains are classified [12]. Among the genera that are identified as chitinase producers from the marine ecosystem include *Bacillus*, *Aeromonas*, *Serratia*, *Enterobacter*, *Erwinia*, *Chromobacterium*, *Flavobacterium*, *Arthrobacter*, and *Vibrio* [13]. Several other bacterial species that have been investigated for the production of chitinolytic enzymes are *Streptococcus*, *Clostridium*, and *Eubacterium* genera that were isolated from whale wastes [14]; *Bacillus licheniformis* from the liquid waste of the food industry [15]; *Streptomyces* and *Serratia* from the residues of crustaceans [16]; and *Bacillus amyloliquefaciens* and *Acinetobacter johnsonii* from shrimp residues [17]. Chitinase producers are rarely isolated from aquatic ecosystems as compared to terrestrial environments, as they are aerobic [12]. Screening for chitinase producers has become an important area for many researchers to help pave the way for degradation of shrimp residues in an economically feasible and ecofriendly manner. Therefore, the present investigation focused to isolate a chitinase-producing strain and to identify it using 16S rRNA sequencing. A mutant strain producing hyperchitinase was developed.

2. Materials and Methods

2.1. Organism, Media, and Culture Conditions. The strain *Bacillus licheniformis* (SSCL-10) that had been isolated from seafood industrial waste (shrimp shell dumping area) of Thoothukudi, India, and identified at the microbiology laboratory, V.H.N.S.N (autonomous), Virudhunagar, TN, India, has been used in this study. The culture conditions, optimal temperature, pH, and colloidal chitin concentration were followed according to an earlier report by Abirami et al. [7]. Chitin decomposing and antifungal properties have been identified and published [7, 18].

2.1.1. Preparation of Colloidal Chitin and Colloidal Chitin Agar (CCA) Plates. Colloidal chitin was prepared according to [19]. Briefly, 5 g chitin powder (GRM1356-100G Himedia, India) was added slowly to 60 L of (10 N HCl) concentrated HCl with continuous stirring at 4°C overnight. This mixture was added to 50% of 500 mL ice-cold ethanol at 25°C with continuous and vigorous stirring at 200 rpm overnight in the rotary shaker. After centrifugation at 10,000 rpm for 20 minutes, the precipitate was collected and washed with sterile distilled water until became neutral (pH 7.0). Collected colloidal chitin was freeze dried and stored at 4°C until use. The colloidal chitin agar plates were prepared according to our earlier report [7] by mixing 5 g of colloidal chitin with mineral salts (KH_2PO_4 0.7 g, K_2HPO_4 0.3 g, $\text{MgSO}_4 \cdot 5\text{H}_2\text{O}$ 0.5 g, $\text{FeSO}_4 \cdot 7\text{H}_2\text{O}$ 0.001 g, ZnSO_4 0.001 g, MnCl_2 0.001 g, and agar 20 g for 1 L with pH 8).

2.1.2. Primary Screening of Chitin-Degrading Bacteria. Primary screening was performed by spot inoculating all the chitin-degrading bacterial isolates on CCA using toothpick heads of 2 mm diameter and incubated at room temperature. The zone of clearance due to chitin hydrolysis was recorded up to 5 days. The bacterial isolates producing clear zone over 5 mm alone were selected and subjected to secondary screening.

2.2. Determination of Specific Chitinolytic Activity. Chitinase activity was measured according to the method of Vyas and Deshpande [20]. Briefly, colloidal chitin was used as the substrate to measure chitinase activity. Enzyme solution (0.5 mL) was added to 1.0 mL of substrate solution (0.5% suspension of the colloidal chitin in a phosphate buffer (50 mM, pH 7.0)) incubated at 37°C for 15 minutes. After centrifugation, the supernatant was measured for reducing sugars by the dinitrosalicylic acid method and N-acetyl glucosamine was used as a standard [21]. One unit of chitinase activity was defined as the amount of enzyme required to liberate 1 μmol of N-acetyl- D-glucosamine equivalent at 50°C h⁻¹.

2.3. Determination of Shrimp Shell Degradation Using Chitinolytic Microorganisms. The biodegradation potential of *Bacillus licheniformis* (SSCL-10) was determined on shrimp shells. Briefly, the selected *Bacillus licheniformis* (SSCL-10) were grown in 0.5% colloidal chitin containing nutrient broth as inoculum. Fifty microliter of bacterial inoculum (0.5 OD) was inoculated to 1 g of shrimp shells in 5 mL minimal medium (pH 7) at 40°C in 100 rpm rotary shaker for 6 and 12 days. After incubation, based on the shrimp shell-degrading efficacy, the *Bacillus licheniformis* (SSCL-10) was selected for mutagenesis and maintained on nutrient agar slants for further studies.

2.4. Molecular Identification and Phylogenetic Tree Construction

2.4.1. PCR Amplification. Molecular identification was done by 16S rRNA analysis. Briefly, high yield of chitinase producer *Bacillus licheniformis* (SSCL-10) reported in our earlier studies [7] was selected for the study. Bacterial genomic DNA of *Bacillus licheniformis* (SSCL-10) was extracted using the Insta Gene TM Matrix (Bio-Rad, cat-no. 7326030), according to the manufacturers' instruction. Then, a 16S rRNA subunit gene fragment was amplified by using 16S rRNA universal primers 27F (5'-AGAGTTTGATCMTGG CTCAG-3') and the reverse primer 1492R (5'-TACGGYTACCTTGTTAC GACTT-3') [22] using MJ Research Peltier Thermal Cycler (Marshall Scientific, USA). PCR was performed in a 30 μL reaction mixture (20 ng genomic DNA) under the following cycling conditions: 95°C for 2 min, followed by 35 cycles of 95°C for 1 min, 55°C for 1 min, and 72°C for 1 min, with a final incubation at 72°C for 10 min.

2.4.2. 16S rRNA Gene Sequencing. The PCR product was detected using agarose gel electrophoresis and extracted using the Genei® Gel Extraction Kit (Bangalore Genei, India). Cycle sequencing was performed with the help of ABI3730xl DNA Analyzer with a BigDye Terminator Cycle

Sequencing Kit v.3.1 (Applied Biosystems, Carlsbad, CA, USA). The primers 518F (5'-CCAGCAGCCGCGGTAA TACG-3') and 800R (5'-TACCAGGGTATCTAATCC-3') were used for the sequencing reactions. The short sequence of the 16S rRNA gene was compiled using SeqMan (DNASTAR Inc.). The newly generated sequences were deposited in GenBank.

2.4.3. Phylogenetic Analysis. To analyse the closest phylogenetic classification for the chitinase producer, the sequenced 16S rRNA genes were compared with BLAST (<https://blast.ncbi.nlm.nih.gov/Blast.cgi>) using the NCBI blast similarity search tool. The phylogenetic analysis of our sequence with the closely related sequence from the blast results was performed followed by multiple sequence alignment. The program MUSCLE 3.7 was used for multiple alignments of sequences [23]. The aligned sequences were cured using Gblocks 0.91b to eliminate poorly aligned positions and divergent regions (removes alignment noise) [24]. Finally, Phylml 3.0 aLRT program was used for phylogenetic analysis and HKY85 as the substitution model which is shown to be at least as accurate as other existing phylogeny programs using simulated data and the order of magnitude being faster. Tree Dyn 198.3 program was used for tree rendering [25].

2.5. UV Mutagenesis of *Bacillus licheniformis*. UV mutagenesis protocol was followed according to Vaidya et al. [26] with modifications. The wild-type *Bacillus licheniformis* (SSCL-10) was inoculated in nutrient broth and incubated at 37°C for 24 hours. One microlitre culture was exposed to short UV light wavelength (280 nm) from a distance of 60 cm (Philips TUV 30 W, G3018, Holland) with different time intervals (0, 2, 4, 6, 8, and 10 minutes) in an open glass petridish under dark conditions to protect from photoreactivation. Then, the culture was serially diluted on CCA plates and mutant strains were isolated from a low ratio of UV survivors. Mutants were screened and selected by observing higher zone of clearance (CZ) to colony size (CS) ratio and chitinase activity.

2.6. Chemical Mutagenesis of *Bacillus licheniformis*. Mutations were induced chemically by ethylmethane sulphonate (EMS) according to the method of Vaidya et al. [26] with modifications. The UV mutant strain was further mutated chemically by EMS to observe the effect on hyperchitinase production. The *Bacillus licheniformis* (SSCL-10) (UV-11) was inoculated in nutrient broth and incubated at 37°C for 24 hours. After incubation, the pellet was collected from 1 mL of culture medium and washed twice with sterile 0.1 M Tris-HCl buffer (pH 7.5) and suspended in equal volume of 0.1 M Tris-HCl buffer (pH 7.5). The pellet was collected and resuspended in half the volume of 0.1 M Tris-HCl buffer (pH 7.5). Cells were collected in 0.1 mL aliquots and kept on ice. A total of 50 µg/mL of EMS was added to each tube and placed in a shaker water bath at 37°C for 30 minutes. The cells were washed and suspended in 1 mL with 0.1 M Tris-HCl buffer (pH 7.5), and the mutated sample was grown for 24 h. The induced mutants were serially diluted and plated on CCA plates. Mutants were screened and

selected by observing for higher zone of clearance (CZ) to colony size (CS) ratio and chitinase activity.

2.7. Screening and Isolation of Hyperchitinase-Producing Mutant. After the mutagenesis process, the CCA plates were incubated at room temperature and examined up to 5 days for the zone of clearance (chitin hydrolysis). The colony size (CS) as well as the zone of clearance (CZ) was measured, and the CZ/CS ratios were measured and compared with the wild type. Higher CZ/CS colonies were subcultured on chitin agar slants and simultaneously inoculated into 100 mL nutrient broth containing 1% colloidal chitin and incubated at 30°C on a rotary shaker at 100 rpm for 48 h. The culture filtrate was collected and measured for chitinase activity.

2.8. Partial Purification of Chitinase. The crude enzyme was partially purified from the culture supernatant (wild, UV mutant, and EMS mutant strains) using 65% saturated ammonium sulfate (SAS) precipitation at 4°C in stirring according to the method of Akeed et al. [27]. Precipitation was done by centrifuging at 11,500 x g for 10 min at 4°C. The precipitate was resuspended in equal volume of sodium-acetate buffer (pH 6), and the protein concentration was estimated [28]. The isolate with the highest chitinase activity was purified on 12% polyacrylamide gel electrophoresis and stained using 0.5% Coomassie Brilliant Blue R250 (Sigma). A protein marker was also electrophoresed for size determination.

2.9. Statistical Analysis. Analysis of variance (ANOVA) was performed and the means were compared using Tukey tests ($p < 0.05$) on the specific chitinolytic activity using the SPSS 18.0 statistical software.

3. Results

3.1. Screening of the Wild-Type Strain. Our earlier study reported that the 16 bacterial strains isolated from shrimp residues expressed different hydrolysis halo sizes (zone of clearance over 5 mm in colloidal chitin agar medium) [8]. From these isolates, *Bacillus licheniformis* (SSCL-10) produced the highest chitinase activity that was used as the wild type (KCCD 201018) and compared with the mutant producers (Fig. S2). The SSCL-10 was catalogued in the institution collection of Kamaraj College Culture Depository (KCCD 201018). Similarly, the mutant strains, UV-11 and EMS-13 were catalogued with the numbers KCCD 201807 and KCCD 201812, respectively.

The colony morphology of strain *Bacillus licheniformis* (SSCL-10) shows white, circular and convex shape with full borders and smooth texture. Microscopic examination showed rod-shaped, motile vegetative cells and endospore forming that was confirmed to belong to the *Bacillus* group (Fig. S3). The *Bacillus licheniformis* (SSCL-10) showed enzyme activity of 3.4 U/mL on the 4th day of incubation (Figure 1). Based on our previous study [8], the optimum concentration of colloidal chitin (1%), temperature 40°C, and pH 7 were used in this study for growth of both wild and mutant strains for the chitinase production.

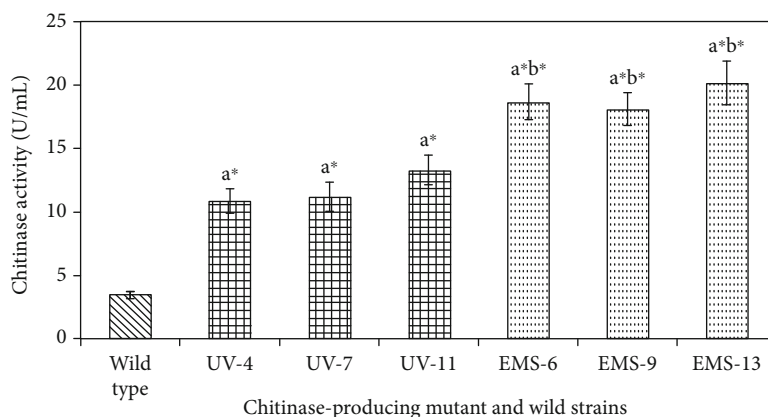


FIGURE 1: Specific chitinolytic activity of *Bacillus licheniformis* SSCL-10 wild type along with maximum chitinolytic activity of three mutants of UV and EMS strains. Values with a*b* are significantly ($p < 0.05$) higher activity. a*: wild type compared with UV and EMS mutant. b⁶: UV compared with EMS mutant.

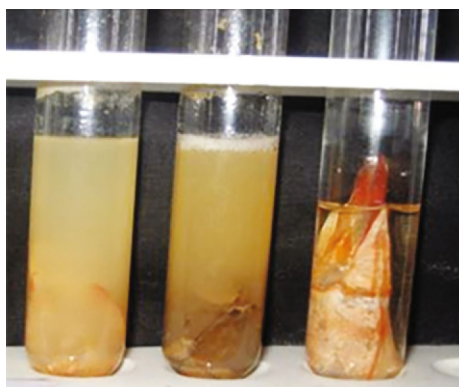


FIGURE 2: Shrimp shell degradation effects by partial purified chitinase enzyme produced by wild strains of *B. licheniformis* (SSCL-10). (1) Shrimp shells alone without *Bacillus licheniformis* (SSCL-10). (2) Shrimp shells with *Bacillus licheniformis* SSCL10 for 6 days. (3) Shrimp shells with *Bacillus licheniformis* SSCL10 for 12 days.

Figure 2 revealed the biodegradation of shrimp shells after 6 and 12 days in a time-dependent manner observed visually. Twelve days effectively degrades the exoskeleton of shrimp shell compared to 6 days.

3.2. UV Mutagenesis. *Bacillus licheniformis* (SSCL-10) was mutated by UV and the survivors were plated on CCA plates to measure zone of clearance (CZ) to colony size (CS). Mutant hyperchitinase-producing strains were identified and isolated at different time intervals. The percentage survivors decreased in a dose-dependent manner at various time intervals (0, 2, 4, 6, 8, and 10 minutes) (Figure 3(a)). Thirteen mutants, which showed a high CZ/CS ratio, were examined for the production of chitinase with zones of clearance ranging from 15 to 19 mm in colloidal chitin agar medium. Mutant UV-11 was found to produce 13.3 U/mL (Table 1) of chitinase that was significantly higher ($p < 0.05$) than the wild type (3.4 U/mL) (Figure 1).

3.3. EMS Mutagenesis. *Bacillus licheniformis* (SSCL-10) mutant UV-11 was further mutated with EMS and the

decrease in survivors was dose dependent (0-7 μg) measured spectrophotometrically (Figure 3(b)). Sixteen mutants showing higher CZ/CS ratio were examined for the production of chitinase that gave zones of clearance ranging from 19 to 27 mm in a colloidal chitin agar medium. Mutant EMS 13 was found to produce the highest amount of chitinase of 20.2 U/mL (Table 1) that was significantly higher ($p < 0.05$) than the wild type (3.4 U/mL) and mutant UV-11 (13.3 U/mL) (Figure 1). The hyperchitinase yield of the mutant EMS-13 was measured and found to be stable by subculturing consecutively on CCA slants for over 6 months.

3.4. Specific Chitinolytic Activity. Figure 1 shows the analysis of chitinolytic activity among three significant mutant chitinase producers ($p < 0.05$) that have different chitinolytic capacities as compared to the wild strain. In the increasing order of specific activity, the wild *Bacillus licheniformis* (SSCL-10) produced the lowest followed by the mutant UV-11 and the highest was produced by the mutant EMS 13. The results of specific chitinase activity with the selected strains ranged from 3.4 U/mL to 20.4 U/mL of protein (Table 1) (Fig. S4). In addition, a strong association was found between the observed chitinase activity and the hydrolytic zone formation observed in each strain.

3.5. Phylogenetic Analysis. Compared with the database sequences, the 16S rRNA from the SSCL-10 isolate showed 97% similarity with *Bacillus licheniformis* that was recorded in the NCBI database (Bank ID SUB2051105; Gene Bank Accession No. KY063593; identified organism *Bacillus licheniformis*) (Table S1-S2). The program Tree Dyn 198.3 was used for phylogenetic tree rendering (Table S3). Figure 4 shows tree rendering results of *Bacillus licheniformis* (SSCL-10). The alignment and phylogenetic analysis of 16S rRNA sequences of different *Bacillus* species strongly suggested species status of the bacterial strain (SSCL-10) (Fig. S7) and confirmed the classification and identification of the isolated bacterial strains as *Bacillus licheniformis*.

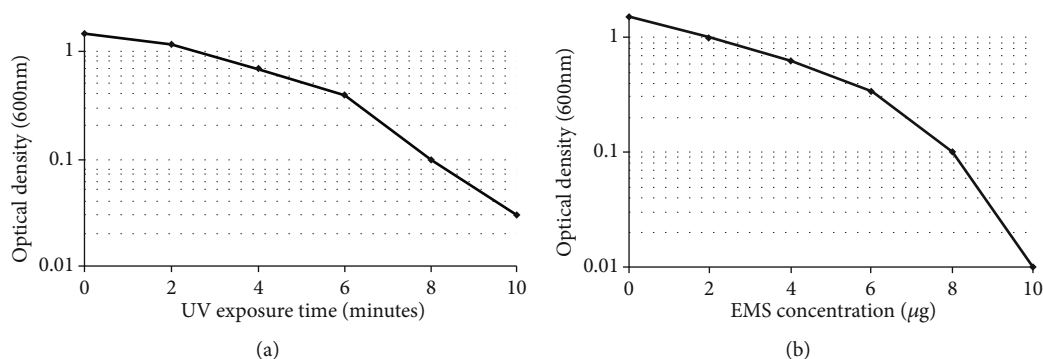


FIGURE 3: Survival curve of mutagenesis. (a) UV survival curve of *Bacillus licheniformis* SSCL-10. (b) EMS survival curve of *Bacillus licheniformis* SSCL-10 UV-11.

TABLE 1: Ratio of zone of clearance (CZ)/size of colony (CS) and chitinase activity of *Bacillus licheniformis* SSCL-10 wild type, maximum CZ/CS of three mutants of UV and EMS strains were selected for chitinase production.

S. no.	Bacterial isolate	CZ/CS (after 48 h)	Chitinase activity (units/mL ⁻¹)
1	Wild-type strain	13-14	3.40 ± 0.31
2	UV mutant 4	16-17	10.8 ± 0.98
3	UV mutant 7	16-17	11.2 ± 1.14
4	UV mutant 11	18-19	13.3 ± 1.21
5	EMS mutant 6	22-23	18.7 ± 1.42
6	EMS mutant 9	22-23	18.1 ± 1.30
7	EMS mutant 13	24-25	20.2 ± 1.72

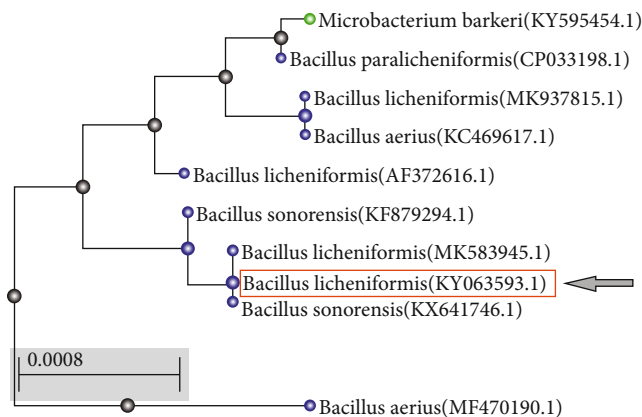


FIGURE 4: Phylogenetic tree of the selected strain *Bacillus licheniformis* SSCL-10 from other bacterial taxa.

3.6. Chitinase Purification. The chitinase (Chi-66) was partially purified by 65% saturated ammonium sulfate (SAS) precipitation at 4°C. SDS-PAGE of the denatured partially purified chitinase identified the molecular weight near 66 kDa (Figure 5). Based on the equivalent amount of total protein loaded for all the strains, the precipitate of the wild type showed a thin, small band; the UV mutant strain revealed a medium size band; and the EMS mutant strain showed a thick band indicating the increasing degree of yield of chitinase (Fig. S5-S6). The EMS mutant chitinase-

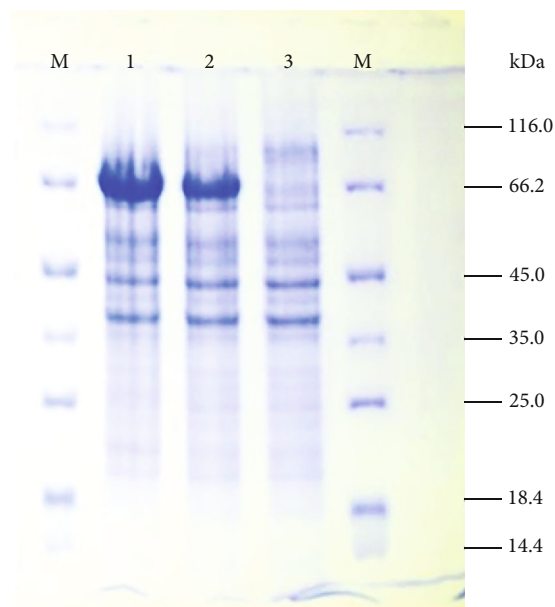


FIGURE 5: SDS-PAGE analysis for partial purification of chitinase from *Bacillus licheniformis* (SSCL-10). M: Marker, 1: cell extract fraction of wild-type strain, 2: cell extract fraction of UV mutant 11, 3: cell extract fraction of EMS-13.

producing strain effectively produces the highest level of chitinase compared to UV mutant and wild type.

4. Discussion

Chitinase has recently been successfully isolated and characterized from *Bacillus* species [29–31]. However, it is necessary to produce high yield of chitinases to fulfill the essential needs for the sustenance of the ecosystem. The present research reports the isolation, molecular identification, and induced mutagenesis of high yielding wild strain of *Bacillus licheniformis* with chitinolytic activity from shrimp wastes. Our previous study reported chitinase-producing isolates, its characterization, and optimal growth factors such as temperature, pH, nutrient composition of the culture medium with colloidal chitin concentration, chitinase production, and its activity from different marine sources [7]. The chitinolytic activity was indicated by the presence of a zone of clearance given by the isolates. Earlier studies

demonstrated that the presence of halo (zone of clearance) requires a long incubation period of 5 to 6 days [32]. Presence of Gram-negative isolates is common in the marine environment, especially in crustaceans and shrimp wastes that can cause diseases in marine organisms. Our earlier studies observed that chitinase produced by *Bacillus licheniformis* (SSCL-10) degrades exoskeleton of cockroach effectively [7]. Similarly, a present study also proved that the enzyme produced by *Bacillus licheniformis* (SSCL-10) effectively degrades shrimp shell wastes. Our results revealed that *Bacillus licheniformis* (SSCL-10) is a potential organism to be used as a biocontrol agent and improve ecofriendly environment.

Compared to Gram-positive bacteria, 90% of the diversity of Gram-negative bacteria in marine ecosystems has traits that enhance survival of these organisms in extreme temperature, tolerance and rapid adaptation to nutrient deficiencies, and high salt concentration [33, 34]. The chitinase activity of the mutated strains of UV-11 and EMS-13 showed values greater than earlier reports [27] with a maximum specific enzymatic activity of 14.2 U/mL in a strain of *Bacillus licheniformis* B307. On the other hand, our wild strain of *Bacillus licheniformis* SSCL-10 showed chitinolytic activity values of 3.4 U/mL, which is lower than the mutant values compared in this study and reported in our earlier studies [7]. Dai et al. [35] reported that *Bacillus* spp. Hu1 showed chitinase activity of 11.1 U/mg of protein in crude extract, whereas *B. licheniformis* LHH100 showed chitinase activity of 494.5 U/mg of protein reported by Laribi-Habchi et al. [15].

In addition to normal production of chitinase, we designed mutant strains for increased chitinase activity by inducing UV and EMS mutation. This method was applied in an earlier study with *Alcaligenes xylosoxydans*, which enhances the chitinase production 2-3-fold higher [26]. Our study is the first report of hyperchitinase activity in *Bacillus licheniformis* induced chemically (EMS) and by UV radiation. Furthermore, the UV mutant *Bacillus licheniformis* SSCL-10 UV-11 enhanced chitinase production 3-4-fold higher than the wild type. Further, chitinase production was enhanced by mutagenizing the UV mutant (UV-11) with EMS (EMS-13) with a specific activity of 20.4 U/mL. Thus, UV and chemical mutation induced higher yield of chitinase from the wild-type *Bacillus licheniformis* SSCL-10 by 5-6-fold. Others have reported twofold enhanced chitinase production in *Serratia marcescens* QMB 1466 [36] and in *Pseudomonas stutzeri* YPL-M26 with N-methyl-N'-nitro-N-nitrosoguanidine (NTG) mutagenesis [37]. The partially purified chitinase was identified as a 66 kDa (Figure 5) molecular weight protein by SDS-PAGE. Researchers have isolated and purified chitinase produced by *Bacillus* spp. with a range of 36, 42, 53, 59, 62, 66, 72, 76, and 89 kDa [38-40]. Chitinases have been isolated from other microorganisms with molecular weights falling in the same range. An endochitinase of 66 kDa was isolated and cloned from *Serratia proteamaculans* [41]. Another study found that four chitinases with molecular weights of 92, 82, 70, and 55 kDa secreted by *Aeromonas caviae* CB101 were encoded by a single gene *chi1* [42]. The proteins were different truncations of

the same *Chi1* protein possibly due to posttranslational proteolytic cleavage that forms the chitinase processing. However, the role of such processing is uncertain. Most of the chitinolytic bacteria studied have multiple chitinases that function synergistically for chitin degradation. Further elucidation of the chitinase structure from our study will highlight the similarities and differences with other chitinases and indicate possibly the presence of multiple truncations of the same protein. Our previous study reported that the isolated chitinase enzyme tested as important biocontrol agents against selected phytofungus pathogens viz. *Fusarium solani*, *Rhizoctonia solani*, *Fusarium oxysporum*, and *Aspergillus* spp. [18].

Bacillus licheniformis, a part of the subtilis group, is commonly found in soil and bird feathers. In birds, it is involved in feather degradability and impacts molting and color patterns. In humans, these commonly cause food poisoning and are a contaminant of dairy products, raw milk, vegetables, cooked meats, and processed baby foods. Since this bacterium produces and secretes hydrolytic enzymes, it has the ability to degrade many substrates. This degradability feature has captured the interest for potential applications in biotechnology [18, 43]. The fermented bird feathers are turned into nutritious livestock feed. It also produces an alkaline protease, which is in turn used in laundry detergent as it can remove proteinaceous dirt from clothes at lower temperatures. It is used as a biopesticide as it possesses antifungal activity [17, 44]. This has probiotic potential when used along with *B. subtilis* that promotes better immune function. *B. licheniformis* has a significant role to play in the bioconversion of chitin, one of the major wastes of the crustacean industry. Chitin is difficult to biodegrade that poses an environmental problem which can be alleviated by chitinases. Chitinases is responsible for the bioconversion of chitin to pharmacologically active products such as N-acetyl glucosamine and chito-oligosaccharides. These derivatives can eventually contribute to a sustainable environment and further downstream applications. The characterization and sequencing of *Bacillus licheniformis* could represent a biotechnological alternative to manipulate nonpathogenic microorganisms capable of decomposing chitin in marine ecosystem and for feasible industrial applications.

5. Conclusions

Chitinolytic potential was identified and isolated in *Bacillus licheniformis* (SSCL-10) from shrimp wastes. Our result revealed that *Bacillus licheniformis* (SSCL-10) was a potential organism to be used as a biocontrol agent and improve the ecofriendly environment. Mutagenesis was induced in the isolated wild strain to enhance the production of chitinase. Extracellular chitinase was partially purified, and the size of the purified enzyme was around 66 kDa. The chitinase yield was enhanced 6-7-fold in the mutant strains as compared to the wild strain. Sequencing of 16S rRNA of the isolated wild chitinase producer determined that it belongs to the species *Bacillus licheniformis*, and the sequence was recorded in the NCBI database (Bank ID SUB2051105; Gene Bank Accession No. KY063593; identified organism *Bacillus*

licheniformis). The strain with the hyperchitinolytic capacity was mutant EMS-13, with a specific activity of 20.4 U/mL. The EMS-induced mutant strain from *Bacillus licheniformis* SSCL-10, EMS-13, was identified as a highest yielding chitinase producer that can find potential applications in biocontrol, pharmaceuticals, and biotechnological sectors (Fig. S1). Furthermore, future studies that include molecular analysis of the chitinase structure can help in drawing comparisons with other characterized chitinases. This will also help in studying further the possibility of a chitin-degradation system available in *Bacillus* and the presence of multiple chitinases or truncated forms of the same protein. Due to its high degradability feature, industrial applications for using this enzyme can be explored. Hyperchitinase mutants can be investigated for bioconversion of chitinous wastes at commercial level. Further, its biocontrol on pathogenic fungi can be employed for disease control among commercially important crops thereby minimizing the use of pesticides and its negative effects on crops and human health.

Data Availability

All data used in this study available as Supplementary Material for this article can be found online.

Additional Points

Highlights. (1) A chitinase producer was isolated and identified by 16S rRNA gene sequencing as *B. licheniformis*. (2) Mutagenesis by EMS and UV induced increased hyperchitinase production as compared to the wild chitinase production. (3) Chitinase was partially purified and determined as a 66 kDa protein. (4) This study offers an effective industrial-grade strategy for hyperchitinase production that can bioprocess nondegradable chitin wastes from environmental crustaceans and shrimp residues.

Conflicts of Interest

The authors declare no conflict of interest.

Authors' Contributions

AS, ND, KM, and SD did the concept and design of the study, data acquisition, and supervision of the study. NAD, DV, and AS did the literature search. AS, KM, and ND did the manuscript preparation critical review. AS, ND, SD, KM, DV, and NAD did the final revision of the manuscript.

Acknowledgments

The authors are thankful to the Deanship of Scientific Research, Prince Sattam bin Abdulaziz University, for supporting this work. The authors express heartfelt thanks to our team for their timely assistance and SD is personally grateful to Mr. Muthamil Selvan for his understanding, full-hearted support, and encouragement.

Supplementary Materials

Figure 1: chitinolytic producers were isolated and identified from soil containing shrimp wastes. The isolate *Bacillus licheniformis* (SSCL-10) was tested for shrimp degradation properties and mutagenesis. Molecular typing of 16S rRNA sequence revealed the phylogenetic lineage of *Bacillus licheniformis* (SSCL-10). The wild strain was mutated with UV, and high-yielding chitinase producer (UV-11) was selected for EMS mutation and compared the chitinase production between wild and mutant strains. Extracellular chitinase was partially purified and the size of the purified enzyme was determined around 66 kDa. Our result indicated the potential of the organism as a biocontrol agent that can aid in improving an ecofriendly environment. Figure 2: primary screening and isolation of chitinase-degrading organism in colloidal chitin agar. Figure 3: morphology of wild strain *B. licheniformis* SSCL-10. Figure 4: chitinase activity of wild and mutant strains. Figure 5: HPLC of partially purified chitinase enzyme produced by *Bacillus licheniformis* (SSCL-10). Figure 6: partial purification of SDS-PAGE (original). Table 1: analysis report of B1 (B1_contig_1 report). Table 2: blast N report of B1. Table 3: parameters used for constructing the phylogenetic tree. (*Supplementary Materials*)

References

- [1] P. Chávez-Crooker and J. Obreque-Contreras, "Bioremediation of aquaculture wastes," *Current opinion in Biotechnology*, vol. 21, no. 3, pp. 313–317, 2010.
- [2] X. Biao and Y. Kaijin, "Shrimp farming in China: operating characteristics, environmental impact and perspectives," *Ocean and Coastal Management*, vol. 50, no. 7, pp. 538–550, 2007.
- [3] M. Kobayashi, S. Msangi, M. Batka, S. Vannuccini, M. M. Dey, and J. L. Anderson, "Fish to 2030: the role and opportunity for aquaculture," *Aquaculture economics & management*, vol. 19, no. 3, pp. 282–300, 2015.
- [4] V. L. Pachapur, K. Guemiza, T. Rouissi, S. J. Sarma, and S. K. Brar, "Novel biological and chemical methods of chitin extraction from crustacean waste using saline water," *Journal of Chemical Technology and Biotechnology*, vol. 91, no. 8, pp. 2331–2339, 2016.
- [5] I. Younes and M. Rinaudo, "Chitin and chitosan preparation from marine sources. Structure, properties and applications," *Marine Drugs*, vol. 13, no. 3, pp. 1133–1174, 2015.
- [6] X. Gao, X. Chen, J. Zhang, W. Guo, F. Jin, and N. Yan, "Transformation of chitin and waste shrimp shells into acetic acid and pyrrole," *ACS Sustainable Chemistry & Engineering*, vol. 4, no. 7, pp. 3912–3920, 2016.
- [7] S. Abirami, K. Yogalsakshmi, P. A. S. Raja, and M. Kananan, "Screening and identification of chitin degrading bacteria from shrimpshell waste dumping soil environment and its media optimization for chitinase enzyme production," *World Journal of Pharmaceutical Sciences*, vol. 5, pp. 743–757, 2016.
- [8] S. Kaur and G. S. Dhillon, "Recent trends in biological extraction of chitin from marine shell wastes: a review," *Critical Reviews in Biotechnology*, vol. 35, no. 1, pp. 44–61, 2015.
- [9] J. Pal, V. H. Om, M. V. Kumar, M. S. Kumar, D. Roy, and J. Kumar, "Biological method of chitin extraction from shrimp waste an eco-friendly low cost technology and its advanced

- application,” *International Journal of Fisheries and Aquatic Studies*, vol. 1, no. 6, pp. 104–107, 2014.
- [10] F. Deeba, S. H. Abdullah, M. Irfan, and Q. J. Iqbal, “Chitinase production in organisms: a review,” *Punjab University Journal of Zoology*, vol. 31, no. 1, pp. 101–106, 2016.
- [11] S. Paulsen, B. Andersen, L. Gram, and H. Machado, “Biological potential of chitinolytic marine bacteria,” *Marine Drugs*, vol. 14, no. 12, 2016.
- [12] B. M. Swiontek and W. Donderski, “Chitinolytic bacteria in two lakes of different trophic status,” *Polish Journal of Ecology*, vol. 54, pp. 295–301, 2006.
- [13] P. C. Souza, C. B. Almeida, R. R. Colwell, and G. N. Rivera, “The importance of chitin in the marine environment,” *Marine Biotechnology*, vol. 13, no. 5, pp. 823–830, 2011.
- [14] A. M. Olsen, S. A. Blix, T. H. A. Utsi, W. Sørmo, and D. S. Mathiesen, “Chitinolytic bacteria in the minke whale forestomach,” *Canadian Journal of Microbiology*, vol. 46, no. 1, pp. 85–94, 1999.
- [15] H. Laribi-Habchi, A. Bouanane-Darenfed, N. Drouiche, A. Pauss, and N. Mameri, “Purification, characterization, and molecular cloning of an extracellular chitinase from *Bacillus licheniformis* strain LHH100 isolated from wastewater samples in Algeria,” *International Journal of Biological Macromolecules*, vol. 72, pp. 1117–1128, 2015.
- [16] Á. Castro, A. Álvarez, E. Machado, M. Mendoza, R. Gómez, and P. García, *Characterization of an extracellular chitinase produced by Serratia sp. BIOMI-363706 using colloidal chitin as substrate*, vol. 77, no. 2, 2011, Revista. de. la Sociedad, Química. Del. Perú., 2011.
- [17] I. N. Setia and P. Suharjo, “Chitinolytic assay and identification of bacteria isolated from shrimp waste based on 16S rDNA sequences,” *Advances in Microbiology*, vol. 5, no. 7, pp. 541–548, 2015.
- [18] S. Abirami, J. Ronald, M. Kannan, and A. J. Singh, “Bioconversion of shrimp shell waste by *Bacillus licheniformis* for the production of antifungal chitinase enzyme,” *Research Journal of Pharmaceutical, Biological and Chemical Sciences*, vol. 3, pp. 789–796, 2012.
- [19] V. Shanmugaiyah, N. Mathivanan, N. Balasubramanian, and P. T. Manoharan, “Optimization of cultural conditions for production of chitinase by *Bacillus laterosporous* MML2270 isolated from rice rhizosphere soil,” *African Journal of Biotechnology*, vol. 7, no. 15, pp. 2562–2568, 2008.
- [20] P. Vyas and M. V. Deshpande, “Chitinase production by *Myrothecium verrucaria* and its significance for fungal mycelia degradation,” *The Journal of General and Applied Microbiology*, vol. 35, no. 5, pp. 343–350, 1989.
- [21] T. Imoto and K. Yagishita, “Chitin coated cellulose as an adsorbent of lysozyme-like enzymes preparation and properties,” *Agricultural and Biological Chemistry*, vol. 37, no. 3, pp. 465–470, 1973.
- [22] W. G. Weisburg, S. M. Barns, D. A. Pelletier, and D. J. Lane, “16S ribosomal DNA amplification for phylogenetic study,” *Journal of Bacteriology*, vol. 173, no. 2, pp. 697–703, 1991.
- [23] R. C. Edgar, “MUSCLE: multiple sequence alignment with high accuracy and high throughput,” *Nucleic Acids Research*, vol. 32, no. 5, pp. 1792–1797, 2004.
- [24] G. Talavera and J. Castresana, “Improvement of phylogenies after removing divergent and ambiguously aligned blocks from protein sequence alignments,” *Systematic Biology*, vol. 56, no. 4, pp. 564–577, 2007.
- [25] A. Dereeper, V. Guignon, G. Blanc et al., “Phylogeny. fr: robust phylogenetic analysis for the non-specialist,” *Nucleic Acids Research*, vol. 36, Supplement 2, pp. W465–W469, 2008.
- [26] R. J. Vaidya, S. L. Macmil, P. R. Vyas, and H. S. Chhatpar, “The novel method for isolating chitinolytic bacteria and its application in screening for hyperchitinase producing mutant of *Alcaligenes xylosoxydans*,” *Letters in Applied Microbiology*, vol. 36, no. 3, pp. 129–134, 2003.
- [27] Y. Akeed, F. Atrash, and W. Naffaa, “Partial purification and characterization of chitinase produced by *Bacillus licheniformis* B307,” *Heliyon*, vol. 6, no. 5, article e03858, 2020.
- [28] M. M. Bradford, “A rapid and sensitive method for the quantitation of microgram quantities of protein utilizing the principle of protein-dye binding,” *Analytical Biochemistry*, vol. 72, no. 1-2, pp. 248–254, 1976.
- [29] N. Khan, P. Martínez-Hidalgo, T. A. Ice et al., “Antifungal activity of *Bacillus* species against *Fusarium* and analysis of the potential mechanisms used in biocontrol,” *Frontiers in Microbiology*, vol. 9, article 2363, 2018.
- [30] D. Wang, A. Li, H. Han, T. Liu, and Q. Yang, “A potent chitinase from *Bacillus subtilis* for the efficient bioconversion of chitin-containing wastes,” *International journal of biological macromolecules*, vol. 116, pp. 863–868, 2018.
- [31] E. A. Veliz, P. Martínez-Hidalgo, A. M. Hirsch, 1 Department of Molecular Cell and Developmental Biology, Molecular Biology Institute, University of California, Los Angeles, 90095-1606, USA, and 2 Departamento de Microbiología y Genética, Universidad de Salamanca, Salamanca, Spain, “Chitinase-producing bacteria and their role in biocontrol,” *AIMS Microbiology*, vol. 3, no. 3, pp. 689–705, 2017.
- [32] M. R. Cody, “Distribution of chitinase and chitobiase in *Bacillus*,” *Current Microbiology*, vol. 19, no. 4, pp. 201–205, 1989.
- [33] S. Das, P. S. Lyla, and S. A. Khan, “Marine microbial diversity and ecology: importance and future perspectives,” *Current Science*, vol. 90, no. 10, pp. 1325–1335, 2006.
- [34] A. Nocker, E. J. Lepo, and A. R. Snyder, “Influence of an oyster reef on development of the microbial heterotrophic community of an estuarine biofilm,” *Applied and Environmental Microbiology*, vol. 70, no. 11, pp. 6834–6845, 2004.
- [35] H. D. Dai, L. W. Hu, R. G. Huang, and W. Li, “Purification and characterization of a novel extracellular chitinase from thermophilic *Bacillus* sp. Hu1,” *african Journal of biotechnology*, vol. 10, no. 13, pp. 2476–2485, 2011.
- [36] J. D. Reid and D. M. Ogrzydziak, “Chitinase-overproducing mutant of *Serratia marcescens*,” *Applied and Environmental Microbiology*, vol. 41, no. 3, pp. 664–669, 1981.
- [37] H. S. Lim, Y. S. Kim, and S. D. Kim, “*Pseudomonas stutzeri* YPL-1 genetic transformation and antifungal mechanism against *Fusarium solani*, an agent of plant root rot,” *Applied and Environmental Microbiology*, vol. 57, no. 2, pp. 510–516, 1991.
- [38] S. Kudan and R. Pichyangkura, “Purification and characterization of thermostable chitinase from *Bacillus licheniformis* SK-1,” *Applied and Environmental Microbiology*, vol. 157, no. 1, pp. 23–35, 2009.
- [39] D. Liu, J. Cai, C. C. Xie, C. Liu, and Y. H. Chen, “Purification and partial characterization of a 36-kDa chitinase from *Bacillus thuringiensis* subsp. *colmeri*, and its biocontrol potential,” *Enzyme and Microbial Technology*, vol. 46, no. 3-4, pp. 252–256, 2010.

- [40] L. A. Trachuk, L. P. Revina, T. M. Shemyakina, G. G. Chestukhina, and V. M. Stepanov, "Chitinases of *Bacillus licheniformis* B-6839: isolation and properties," *Canadian Journal of Microbiology*, vol. 42, no. 4, pp. 307–315, 1996.
- [41] M. A. Mehmood, X. Xiao, F. Y. Hafeez, Y. Gai, and F. Wang, "Purification and characterization of a chitinase from *Serratia proteamaculans*," *World Journal of Microbiology and Biotechnology*, vol. 25, no. 11, pp. 1955–1961, 2009.
- [42] M. A. Mehmood, Y. Gai, Q. Zhuang, F. Wang, X. Xiao, and F. Wang, "*Aeromonas caviae* CB101 contains four chitinases encoded by a single gene *chi1*," *Molecular biotechnology*, vol. 44, no. 3, pp. 213–220, 2010.
- [43] S. L. Wang, T. Y. Lin, Y. H. Yen, H. F. Liao, and Y. J. Chen, "Bioconversion of shellfish chitin wastes for the production of *Bacillus subtilis* W-118 chitinase," *Carbohydrate Research*, vol. 341, no. 15, pp. 2507–2515, 2006.
- [44] S. Sharma, S. Kumar, A. Khajuria, P. Ohri, R. Kaur, and R. Kaur, "Biocontrol potential of chitinases produced by newly isolated *Chitinophaga* sp. S167," *World Journal of Microbiology and Biotechnology*, vol. 36, no. 6, 2020.

Research Article

A Current Sensing Biosensor for BOD Rapid Measurement

Yiman Liu ¹, Jie Li ^{1,2}, Nianxin Wan ³, Tianyu Fu,¹ Lili Wang ¹, Cong Li ¹,
Zhonghui Qie ¹ and Ao Zhu ¹

¹School of Environmental and Municipal Engineering, Qingdao University of Technology, Qingdao, 266033, China

²Laboratory for Marine Geology, Pilot National Laboratory for Marine Science and Technology, Qingdao, China

³Jihongtan Reservoir Management Station, Shandong Water Diversion Project Operation and Maintenance Center, Qingdao 266111, China

Correspondence should be addressed to Jie Li; jli@qut.edu.cn

Received 12 June 2020; Revised 8 September 2020; Accepted 7 October 2020; Published 26 October 2020

Academic Editor: Jin Li

Copyright © 2020 Yiman Liu et al. This is an open access article distributed under the Creative Commons Attribution License, which permits unrestricted use, distribution, and reproduction in any medium, provided the original work is properly cited.

In order to improve the practicality of the rapid biochemical oxygen demand (BOD) method, a highly sensitive rapid detection method for BOD that is based on establishing the correlation between current and dissolved oxygen (DO) was developed. In this experiment, *Bacillus subtilis* was used as the test microorganism, and the embedding method was used to achieve quantitative fixation of microorganisms, which could increase the content of microorganisms and prolong the service life of the biological element. The conductivity (COND) probe is used as a sensing element, so that the testing value can be read every second. In the program, the moving average method is used to process the collected data so that the value can be read every minute. National standard samples were detected to test the accuracy and stability of the method. The results showed that relative error and analytical standard deviations were less than 5%. Different polluted water was tested to evaluate its application range. The results showed that relative error was less than 5%. The results of the method are consistent with the results of the wastewater sample obtained by the BOD₅ standard method. The proposed rapid BOD current sensing biosensor method should be promising in practical application of wastewater monitoring.

1. Introduction

Biochemical oxygen demand (BOD) is a widely used index for estimating the level of water pollution by organic compounds [1]. BOD can provide useful information for biological and environmental impact assessment and has been the most preferred method for environmental applications [2–5]. The standard BOD₅ method described by APHA (1998) is the most widely used method for measuring biodegradable organic levels in waters and wastewaters [6, 7]. However, the classical BOD₅ method is unsuitable for rapid detection and online applications [4, 8].

In order to get the BOD values within minutes, the development of a new detection method has become a very attractive option. To date, tremendous efforts have been devoted to developing new BOD detection methods to reduce assay time and simplify procedures to meet the requirements of end users [4, 7, 9–26], such as (i) biosensors based on biolumines-

cent bacteria, (ii) biosensors with redox mediators, (iii) microbial fuel cell (MFC) biosensor, (iv) biosensors with entrapped microorganisms, and (v) biosensors based on the bioreactor/chemist at technology [2, 5]. Among them, because of the complexity and low precision of the bioluminescence reaction, the two former technologies show the least potential in practical applications [5, 20, 22, 23, 27, 28]. Currently, the most widely adopted approach is the type of biosensor method based on the respiration rate [5, 26]. In addition, MCF has become the mostly studied method. The main issues in the development of new detection methods involve time-consuming preparation procedures [4, 12, 26], longer incubation or activation or measurement times [4, 12, 26, 29, 30], rigorous maintenance [26, 31], online applications [26, 32], and complex analysis systems [26, 33]. Although MFCs can generate stable current under constant condition, the pollution of toxic substances in MFCs usually reduces the current by affecting microorganisms [34, 35].

Membrane-type BOD sensors also have other problems, such as membrane fouling, nonportability, and insufficient online design [23, 36, 37]. Because the traditional BOD rapid monitor has a complicated pipeline system, it is difficult to clean. Residual biofilms inevitably exist in the pipeline, which will eventually affect the test results. Besides, the analytical performance of many existing rapid BOD methods is usually severely affected by the sample matrix. The measured analysis signal is highly dependent on the sample matrix, showing the inherent limitations of a narrow range of application, as well as defects in the repeatability and reliability of real sample analysis [4, 9, 12, 26, 38]. In addition, the traditional microbial immobilization technology used in rapid detection is difficult to quantify the immobilization of microbial cells. In the actual detection, the change in the number of microorganisms affects the detection results. In fact, the rapid BOD sensor achieved rapid monitoring at the expense of sacrificing unique advantages of the BOD₅ method [4, 12, 26]. China advocates defining standard water quality less than 10 mg L⁻¹ BOD. In order to assess such a low BOD value, building an accurate BOD monitoring system has become an important factor for monitoring the water quality [39]. The development of a new BOD method that can achieve rapidity (the inherent advantage of fast BOD sensors), solve the shortcomings of the traditional biofilm method, and maintain the widespread application of the BOD₅ method is of an important practical issue and scientifically challenging.

In this study, we aimed to develop a simple and accurate BOD monitoring method, which can be used for real-time detection and online monitoring. According to the traditional fast monitoring method, BOD can be calculated from the reduction of DO based on the output signal of the DO sensor and the correlation between the concentration of the target substrate and BOD [40, 41]. Based on this principle, we have studied the monitoring objects and determined the method of evaluating BOD by detecting changes in electrical signals. With this detection method, the complex piping system in the instrument can be removed, the complicated cleaning work can be reduced, and the instrument volume can be greatly reduced. This method can improve the sensitivity and stability of monitoring to a certain extent and can reduce the influence caused by the unstable substrate matrix and monitoring signal. In addition, in this method, an embedding technique is used to quantify and immobilize microorganisms. The polymer matrix used to fix microbial cells makes microbial spherical particles an identification element for biodegradable organic matter, which can reduce the impact of problems such as biofilm clogging on monitoring.

2. Experimental

2.1. Method. Based on the principle of the standard detection method, the detection time is greatly shortened and the operation process is simplified. Immobilized microbial cell particles are used as reaction elements, which can realize the full mixing and reaction of microbes and water samples. In the closed reaction vessel, microorganisms decompose organic matter and consume oxygen, which results in a decrease in

the concentration of DO in the water; at the same time, the value of COND will change. This study explored the reaction relationship between COND and DO, and multiple relationship curves were established. In the actual detection process, BOD can be accurately detected by detecting the change of COND in the sample and performing relevant calculations. In addition, in order to adapt to different testing requirements, this study determined a variety of testing modes.

Because the COND value can be detected every second, in principle, this method can detect the BOD value once per second. In order to ensure the accuracy and stability of the detection, the moving average calculation method is executed during the calculation process, so the BOD value can be obtained every minute.

2.2. Control System. First, the conductivity signal is collected by the COND probe (COND value can be detected every second). After that, the signal is collected to the transmitter through the MODBUS protocol, and the transmitter transmits the signal to the controller by the 4-20 mA signal. The controller performs moving average processing on the conductivity signal, and the data is displayed once every minute after the moving average processing. After reaching the specified running time (manual setting), the test results and reaction time will be output for the data processing and comparison.

2.3. Materials and Tools. PVA (polyvinyl alcohol), sodium alginate, xanthan gum, NaCl, glucose, and glutamic acid were purchased from Beijing Chemical Reagents Company. Unless otherwise indicated, all reagents used in this study were laboratory-grade materials, and all solutions were prepared with high-purity deionized (Milli-Q) water.

The BOD standard solution (136.4 mg glucose and 136.4 mg glutamic acid are dried at 103°C for 2 hours, dissolved, and diluted to 100 mL, GGA) was prepared according to the standard method. This solution in this study has a known BOD value of 2000 ± 160 mg L⁻¹. And lower concentration BOD solution was prepared by appropriate dilution with deionized water.

Phosphate buffer solution (PBS, 5 mM, pH 7.0) was prepared in accordance with standard methods using diluting samples and activating and washing microbial spherical particles.

Based on theoretical principles, an experimental R&D platform and a simple prototype have been produced. The R&D platform is used for curve research and correction.

The prototype is used for water sample monitoring. The structure diagram of the prototype is shown in Figure 1, and the appearance of the prototype is shown in Figure 2.

2.4. Immobilized Microbial Cell Particles. *Bacillus subtilis* used in the experiment was isolated from the water sample of the aeration basin of the Shandong Taian Wastewater Treatment Plant and stored at 4°C. Physiological saline solution with a mass and volume fraction of 0.8% was prepared and transferred to an Erlenmeyer flask for sterilization.

The microbial consortium was harvested and washed twice with physiological saline solution by centrifugation

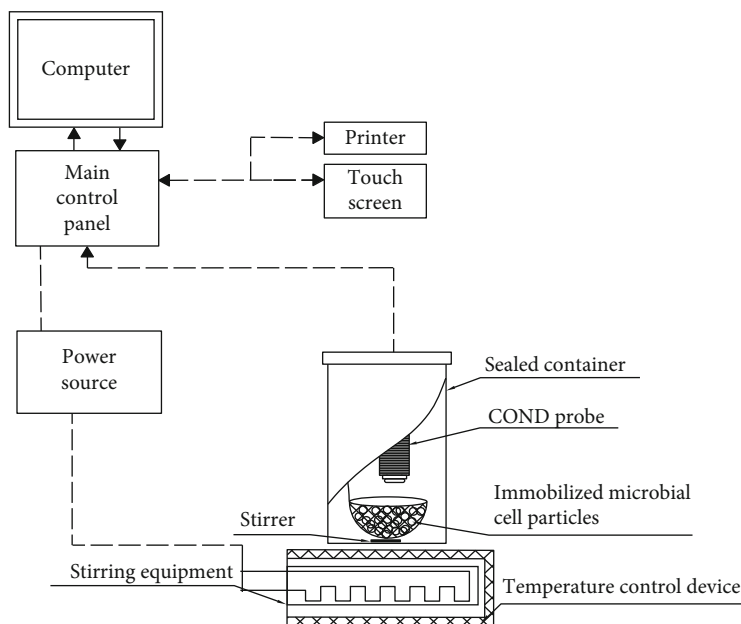


FIGURE 1: Schematic diagram of the current sensing biosensor for BOD.



FIGURE 2: The appearance of the prototype.

(6000 rpm for 10 min) at room temperature. The supernatant liquid was then discarded, and the remaining sediment was quantified by weight for construction of microbial spherical particles. Polyvinyl alcohol, sodium alginate, and xanthan gum in a mass ratio of 1:1:2 (PVA mass is 2 g) were dissolved in 30 mL of deionized water and then cooled to 40°C, then mixed thoroughly with 1 gram microbial consortium (the concentration of cell is about 3.0×10^9 cells g^{-1}).

The resulting mixture was placed in a sterilization mold and cooled to form spherical beads. The pellets were washed with physiological saline, then dried at 4°C for 24 hours, and stored at 4°C before use.

2.5. Determination of the Relationship Curve. The BOD standard solution as the experimental object was prepared according to the standard method. The BOD standard solu-

tion with a certain concentration, KCl electrolyte solution, and microorganism-embedded particles were added to the closed reaction container for full reaction. The temperature and stirring frequency remain unchanged during the reaction. During the process, the COND and DO values in the solution were detected and recorded. There are three concentration ranges of high ($800+ \text{mg L}^{-1}$), medium ($400\text{-}800 \text{mg L}^{-1}$), and low ($400\text{-}mg \text{L}^{-1}$), and each concentration range is divided into different concentration gradients to conduct exploration experiments, and each group of experiments carries out multiple sets of repeated experiments. High-fitting curves were selected for the verification test.

The concentration gradient was subdivided within the detection range of each curve. The corresponding concentration standard sample is detected, and the test is repeated multiple times. Then, the deviation degree of each relationship curve is detected, and the curve coefficient is calibrated.

2.6. Measurement Procedures. A COND probe (DJS-1D, Shanghai, China) purchased from Shanghai Yidian Scientific Instrument Co., Ltd. was used as the transducer, which was plugged in the center of the reactor. The microbial spherical particles are placed in the reactor, and electromagnetic stirring is used to ensure that they fully react with the water sample. A temperature control system was placed at the bottom of the reactor which was used to control the reaction temperature to 25°C.

Before measurement, about 500 mL of 0.005 mol L^{-1} PBS was poured into the activation box. Then, about 2 g glucose and 0.5 g glutamic acid were added to the PBS solution which was used to provide nutrients to the microorganisms in the microbial spherical particles. The amount of microbial spherical particles used in one test is about 5 g. Then, the activation box needed to be covered, and the temperature of the

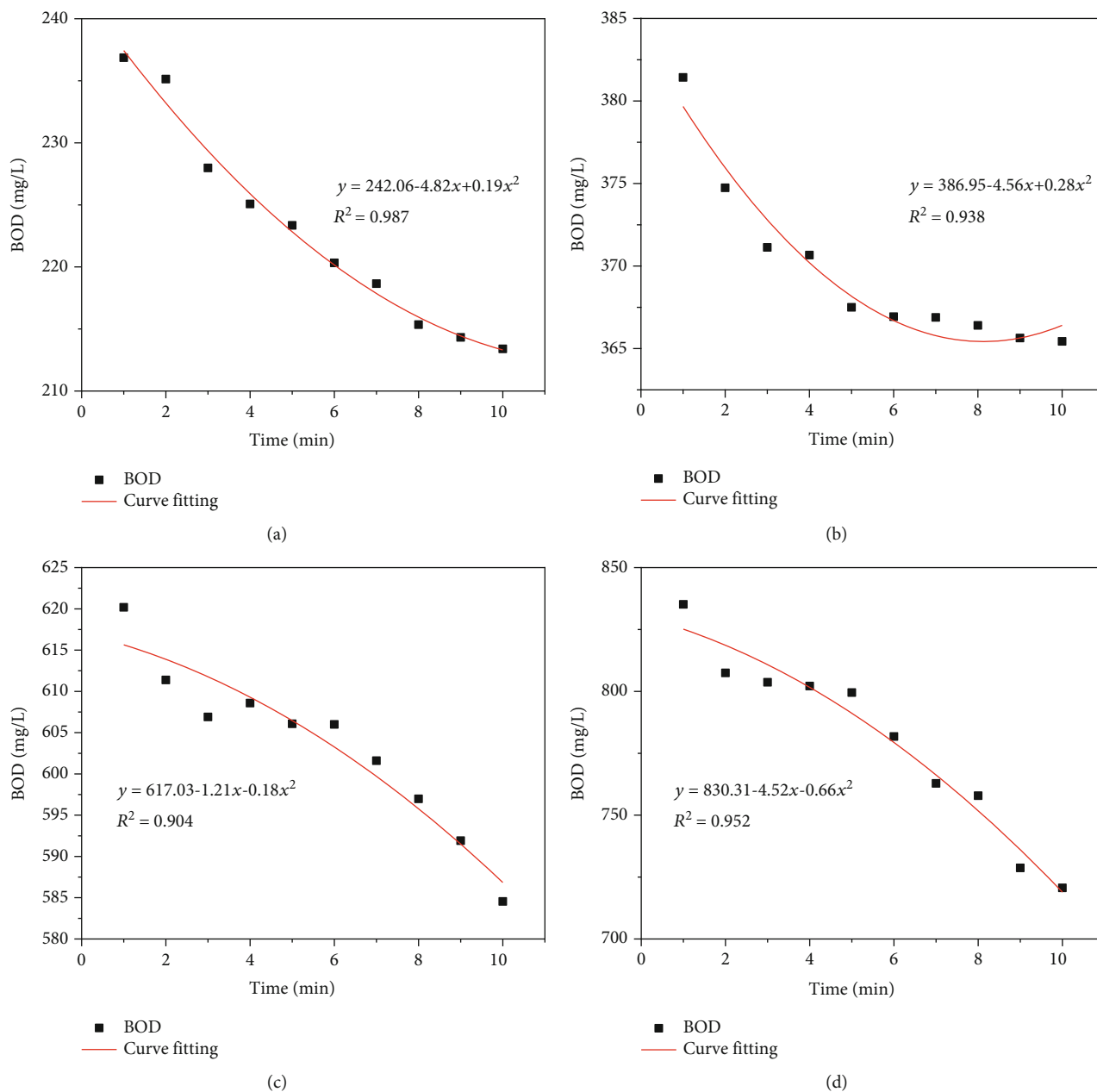


FIGURE 3: Testing results of glucose-glutonic acid solution: (a) 200 mg L⁻¹; (b) 400 mg L⁻¹; (c) 600 mg L⁻¹; (d) 800 mg L⁻¹.

activation box needed to be controlled at about 35°C (suitable for microbial growth) for 48 hours.

BOD standard solution was used to regulate the BOD sensor. The probe needs to be washed with deionized water before each monitoring. The measurement of the conventional BOD₅ value was carried out by the standard method [6, 7]. In order to analyze the accuracy and stability of this monitoring method, the monitoring results obtained by this monitoring method need to be compared with the results obtained by the BOD₅ method.

3. Results and Discussion

3.1. GGA Standard Solution. In order to carry out preliminary tests on the stability and accuracy of the method,

continuous tests were conducted on the different concentrations of GGA standard solution in the laboratory. This experiment was conducted on the original R&D platform. This experiment sets the concentration gradient to 200. A total of four samples with different concentrations were selected for testing. Six consecutive experiments were conducted on samples with concentrations of 200 mg L⁻¹ and 400 mg L⁻¹, respectively. Three consecutive experiments were carried out on samples with concentrations of 600 mg L⁻¹ and 800 mg L⁻¹. Due to the unstable initial reaction, the experimental data discarded the continuous data for the first 5 minutes and recorded the continuous monitoring data for 6-16 minutes. The average value of 6 sets (or 3 sets) of data corresponding to each minute is obtained. The results are shown in Figure 3. The average

TABLE 1: The results of GGA standard solution.

Standard sample guaranteed value	Average BOD (mg L^{-1})	Relative mean deviation (%)	Maximum relative deviation (%)	Error (%)
200 ± 16	223.0	3.0	6.2	11.5
400 ± 32	369.4	1.0	3.3	-7.6
600 ± 48	603.4	1.3	2.8	0.6
800 ± 64	778.0	3.8	7.1	-2.5

TABLE 2: The results of standard sample BOD mass concentration.

Sample no.	Average BOD (mg L^{-1})		Error (%)
	Prototype measured value	Standard sample guaranteed value	
1	169.5	170.0	-0.3
2	106.8	107 ± 9	-0.8
3	10.2	10.5 ± 2.4	-2.5
4	598.3	600 ± 49.7	-0.3
5	997.8	1050 ± 87	-0.2

TABLE 3: The results of continuous monitoring.

Experiment no.	BOD (mg L^{-1})	
	Influent	Effluent
1	1140.2	130.1
2	1089.5	141.1
3	1020.4	125.8
4	1001.9	119.6
5	1067.5	120.1
6	1123.2	128.1
Average	1073.8	127.5

TABLE 4: The results of typical samples.

Sample	Average BOD (mg L^{-1})		Error (%)
	Prototype	BOD ₅	
Domestic sewage	98.3	101.3	-3.0
Printing and dyeing wastewater	99.1	109.7	9.7
Gray water	73.9	75.1	-1.5
Industrial wastewater	248.3	261.4	-5.0

BOD values, deviation, and error values are shown in Table 1.

Due to some accidental errors in solution preparation and dilution, the relative deviation of different batches of experiments will be different, and the single data deviation phenomenon that occurs accidentally in multiple sets of experiments cannot be excluded. The experimental data is

evenly distributed, and the data fit is high, indicating that the detection method has good stability.

The error of the test result of the sample with a concentration of 200 mg L^{-1} is relatively large. The error value of the test results of other concentration samples is within the allowable range (relative error $\leq 8\%$). The average deviation value also indicates that the test has better stability. In the subsequent prototype production, the curve correction work was carried out, basically solving the problem of large error in the detection results of the low concentration in this part.

3.2. Repeatability and Deviation. The repeatability is an important parameter that can be used to indicate the precision of the prototype. The same sample is tested under the same conditions, and the error is performed to analyze the precision of the prototype. In this experiment, five standard samples with different mass concentrations were selected for detection in each applicable range, and each concentration sample was subjected to 6 repeated tests. The average values are shown in Table 2.

The analysis of the experimental data and the significance test show that the measured value of the prototype is not significantly different from the guaranteed value of the standard sample ($p < 0.105$), and the relative error is less than 5%, indicating that the detection method has high test accuracy.

3.3. Stability. The stability indicates the stability of the prototype which is used to detect water samples continuously. In this test, the influent and effluent water samples of a sewage treatment plant were detected 6 times within 2 days. The prototype was set to standby except working time. The results are shown in Table 3.

The measurement results show that the average deviation of the prototype is 4.7% for the inlet water sample and 5.7% for the effluent water. The results suggest that the prototype was stable during the practical application.

3.4. Actual Detection. The ultimate purpose of testing various performances of the prototype is to explore the feasibility of the prototype for the detection of actual wastewater samples. In this experiment, in order to verify the feasibility of this method for testing actual water samples, *Bacillus subtilis* was used to make microbial particles to test several typical actual water samples. Each water sample was tested three times, and the average value was taken. At the same time, the BOD₅ standard method was used to detect each water sample, and the test results were compared with the prototype test results.

The significance test indicated that the BOD mass concentration value measured by the prototype was not significantly different from the BOD₅ standard method ($p < 0.105$). Taking the test results of the BOD₅ standard method as the standard, the deviations of the test values of the prototype are all less than 5%. It is proved that this method and the BOD₅ standard method have a good correlation with the test values of actual water samples. It shows that the prototype has accurate detection results for a variety of wastewater and meets the standard requirements. It can be concluded from Table 4 that the BOD values of the prototype are lower

than the BOD values of the BOD₅ standard method. Because the BOD₅ standard method has a long reaction time, the microorganism can degrade most of the biodegradable organic compounds in the water sample, while the microorganism in the current sensing biosensor method can only quickly degrade some organics that are easily degraded in the water sample. Therefore, the test results of the same water sample by the current sensing BOD₅ standard method are not exactly the same. Table 4 indicates that there is a large error between the test results of the BOD₅ standard method and the current sensing biosensor method of the printing and dyeing wastewater. The reason for the result may be that the printing and dyeing wastewater contains more heavy metal ions and has a certain toxic effect on the immobilized microbial cell particles.

4. Conclusion

This method improves the traditional rapid monitoring instruments, reduces the complicated piping system, and optimizes the immobilization method of microorganisms. This method does not require elution. Compared with the traditional biofilm method, it can achieve quantitative immobilization of microorganisms, which can increase the number of fixed microorganisms by several orders of magnitude and control the number of the microbial cell particles used in the detection. Therefore, this method was more accurate and effective for BOD measurement which can greatly shorten the reaction time and simplify the operation steps. The test results of actual water samples show that BOD values of this method are consistent with the BOD values of the BOD₅ standard method (error < 5%). The results of this study indicated that this method can meet the requirement of BOD rapid measurement. Toxicants such as heavy metal ions and organic toxicants have toxic effects on *Bacillus subtilis*; therefore, antitoxic strains need to be selected for detecting specific wastewater. It provides a general direction for the follow-up of this research, that is, the use of mixed strains, and precise control of the proportion of various strains, to expand the detection range and improve the stability of the detection.

Data Availability

All data generated or analyzed during this study are included in this published article and its supplementary information files.

Conflicts of Interest

The authors declare that they have no conflicts of interest.

Authors' Contributions

Yiman Liu and Jie Li have contributed equally to this work.

References

- [1] S. Niyomdech, W. Limbut, A. Numnuam, P. Asawatreratanakul, P. Kanatharana, and P. Thavarungkul, "A novel BOD biosensor based on entrapped activated sludge in a porous chitosan-albumin cryogel incorporated with graphene and methylene blue," *Sensors and Actuators B-chemical*, vol. 241, pp. 473–481, 2017.
- [2] S. Jouanneau, L. Recoules, M. J. Durand et al., "Methods for assessing biochemical oxygen demand (BOD): a review," *Water Research*, vol. 49, pp. 62–82, 2014.
- [3] K. Morris, K. Catterall, H. Zhao, N. Pasco, and R. John, "Ferricyanide mediated biochemical oxygen demand - development of a rapid biochemical oxygen demand assay," *Analytica Chimica Acta*, vol. 442, no. 1, pp. 129–139, 2001.
- [4] C. Liu, H. Zhao, L. Zhong et al., "A biofilm reactor-based approach for rapid on-line determination of biodegradable organic pollutants," *Biosensors & Bioelectronics*, vol. 34, no. 1, pp. 77–82, 2012.
- [5] T. T. P. Pham, P. Nguyen, T. T. Nguyen, and H. T. L. Duong, "Self-build packed-bed bioreactor for rapid and effective BOD estimation," *Environmental Science and Pollution Research*, vol. 26, no. 25, pp. 25656–25667, 2019.
- [6] APHA, *Standard methods for the examination of water and wastewater*, American Public Health Association, Washington D.C., 20th Ed edition, 1998.
- [7] J. Wang, Y. Zhang, Y. Wang, R. Xu, Z. Sun, and Z. Jie, "An innovative reactor-type biosensor for BOD rapid measurement," *Biosensors & Bioelectronics*, vol. 25, no. 7, pp. 1705–1709, 2010.
- [8] S. Zhang, H. Zhao, D. Jiang, and R. John, "Photoelectrochemical determination of chemical oxygen demand based on an exhaustive degradation model in a thin-layer cell," *Analytica Chimica Acta*, vol. 514, no. 1, pp. 89–97, 2004.
- [9] C. Liu, C. Ma, D. Yu et al., "Immobilized multi-species based biosensor for rapid biochemical oxygen demand measurement," *Biosensors and Bioelectronics*, vol. 26, no. 5, pp. 2074–2079, 2011.
- [10] J. Jianbo and D. Shaojun, "The progress of microbial biosensors for biochemical oxygen demand," *Chinese Journal of Analytical Chemistry*, vol. 31, no. 6, pp. 742–748, 2003.
- [11] K. Catterall, K. Morris, C. Gladman, H. Zhao, N. Pasco, and R. John, "The use of microorganisms with broad range substrate utilisation for the ferricyanide-mediated rapid determination of biochemical oxygen demand," *Talanta*, vol. 55, no. 6, pp. 1187–1194, 2001.
- [12] K. Catterall, H. Zhao, N. Pasco, and R. John, "Development of a rapid ferricyanide-mediated assay for biochemical oxygen demand using a mixed microbial consortium," *Analytical Chemistry*, vol. 75, no. 11, pp. 2584–2590, 2003.
- [13] C. Preininger, I. Klimant, and O. S. Wolfbeis, "Optical fiber sensor for biological oxygen demand," *Analytical Chemistry*, vol. 66, no. 11, pp. 1841–1846, 2002.
- [14] A. Kumlanghan, P. Kanatharana, P. Asawatreratanakul, B. Mattiasson, and P. Thavarungkul, "Microbial BOD sensor for monitoring treatment of wastewater from a rubber latex industry," *Enzyme & Microbial Technology*, vol. 42, no. 6, pp. 483–491, 2008.
- [15] I. S. Chang, J. K. Jang, G. C. Gil et al., "Continuous determination of biochemical oxygen demand using microbial fuel cell type biosensor," *Biosensors & Bioelectronics*, vol. 19, no. 6, pp. 607–613, 2004.
- [16] C. Chan, M. Lehmann, K. Chan et al., "Designing an amperometric thick-film microbial BOD sensor," *Biosensors & Bioelectronics*, vol. 15, no. 7-8, pp. 343–353, 2000.

- [17] G. J. Chee, Y. Nomura, K. Ikebukuro, and I. Karube, "Development of photocatalytic biosensor for the evaluation of biochemical oxygen demand," *Biosensors & Bioelectronics*, vol. 21, no. 1, pp. 67–73, 2005.
- [18] H. Pang, N. Kwok, P. Chan, C. Yeung, W. Lo, and K. Wong, "High-throughput determination of biochemical oxygen demand (BOD) by a microplate-based biosensor," *Environmental Science & Technology*, vol. 41, no. 11, pp. 4038–4044, 2007.
- [19] L. Lin, L. L. Xiao, S. Huang et al., "Novel BOD optical fiber biosensor based on co-immobilized microorganisms in ormosils matrix," *Biosensors & Bioelectronics*, vol. 21, no. 9, pp. 1703–1709, 2006.
- [20] T. Sakaguchi, Y. Morioka, M. Yamasaki et al., "Rapid and onsite BOD sensing system using luminous bacterial cells-immobilized chip," *Biosensors & Bioelectronics*, vol. 22, no. 7, pp. 1345–1350, 2007.
- [21] N. Kwok, S. Dong, W. Lo, and K. Wong, "An optical biosensor for multi-sample determination of biochemical oxygen demand (BOD)," *Sensors and Actuators B-chemical*, vol. 110, no. 2, pp. 289–298, 2005.
- [22] H. Nakamura, Y. Abe, R. Koizumi et al., "A chemiluminescence biochemical oxygen demand measuring method," *Analytica Chimica Acta*, vol. 602, no. 1, pp. 94–100, 2007.
- [23] H. Nakamura, K. Suzuki, H. Ishikuro et al., "A new BOD estimation method employing a double-mediator system by ferricyanide and menadione using the eukaryote *Saccharomyces cerevisiae*," *Talanta*, vol. 72, no. 1, pp. 210–216, 2007.
- [24] H. Chen, T. Ye, B. Qiu, G. Chen, and X. Chen, "A novel approach based on ferricyanide-mediator immobilized in an ion-exchangeable biosensing film for the determination of biochemical oxygen demand," *Analytica Chimica Acta*, vol. 612, no. 1, pp. 75–82, 2008.
- [25] J. Liu and B. Mattiasson, "Microbial BOD sensors for wastewater analysis," *Water Research*, vol. 36, no. 15, pp. 3786–3802, 2002.
- [26] C. Liu, H. Zhao, S. Gao et al., "A reagent-free tubular biofilm reactor for on-line determination of biochemical oxygen demand," *Biosensors & Bioelectronics*, vol. 45, pp. 213–218, 2013.
- [27] T. Sakaguchi, K. Kitagawa, T. Ando et al., "A rapid BOD sensing system using luminescent recombinants of *Escherichia coli*," *Biosensors & Bioelectronics*, vol. 19, no. 2, pp. 115–121, 2003.
- [28] A. S. Zaitseva, V. A. Arlyapov, N. Y. Yudina, S. V. Alferov, and A. N. Reshetilov, "Use of one- and two-mediator systems for developing a BOD biosensor based on the yeast *Debaryomyces hansenii*," *Enzyme and Microbial Technology*, vol. 98, pp. 43–51, 2017.
- [29] T. C. Tan and E. W. C. Lim, "Thermally killed cells of complex microbial culture for biosensor measurement of BOD of wastewater," *Sensors and Actuators B Chemical*, vol. 107, no. 2, pp. 546–551, 2005.
- [30] I. S. Chang, H. Moon, J. K. Jang, and B. H. Kim, "Improvement of a microbial fuel cell performance as a BOD sensor using respiratory inhibitors," *Biosensors & Bioelectronics*, vol. 20, no. 9, pp. 1856–1859, 2005.
- [31] P. Namour, N. Jaffrezic-Renault, and P. Namour, "Sensors for measuring biodegradable and total organic matter in water," *Trends in Analytical Chemistry*, vol. 29, no. 8, pp. 848–857, 2010.
- [32] N. Pasco, K. Baronian, C. Jeffries, and J. Hay, "Biochemical mediator demand – a novel rapid alternative for measuring biochemical oxygen demand," *Applied Microbiology and Biotechnology*, vol. 53, no. 5, pp. 613–618, 2000.
- [33] R. Iranpour and M. Zermenio, "Online biochemical oxygen demand monitoring for wastewater process control–full-scale studies at Los Angeles Glendale wastewater plant, California," *Water Environment Research*, vol. 80, no. 4, pp. 298–307, 2008.
- [34] M. Kim, M. Sik Hyun, G. M. Gadd, and H. Joo Kim, "A novel biomonitoring system using microbial fuel cells," *Journal of Environmental Monitoring*, vol. 9, no. 12, pp. 1323–1328, 2007.
- [35] N. E. Stein, H. V. M. Hamelers, and C. N. J. Buisman, "Stabilizing the baseline current of a microbial fuel cell-based biosensor through overpotential control under non-toxic conditions," *Bioelectrochemistry*, vol. 78, no. 1, pp. 87–91, 2010.
- [36] L. Cheng, S. B. Quek, and R. Cord-Ruwisch, "Hexacyanoferrate-adapted biofilm enables the development of a microbial fuel cell biosensor to detect trace levels of assimilable organic carbon (AOC) in oxygenated seawater," *Biotechnology & Bioengineering*, vol. 111, no. 12, pp. 2412–2420, 2014.
- [37] B. H. Kim, I. S. Chang, G. Cheol Gil, H. S. Park, and H. J. Kim, "Novel BOD (biological oxygen demand) sensor using mediator-less microbial fuel cell," *Biotechnology Letters*, vol. 25, no. 7, pp. 541–545, 2003.
- [38] J. Liu, L. Björnsson, and B. Mattiasson, "Immobilised activated sludge based biosensor for biochemical oxygen demand measurement," *Biosensors & Bioelectronics*, vol. 14, no. 12, pp. 883–893, 2000.
- [39] J. Hu, Y. Li, G. Gao, and S. Xia, "A mediated BOD biosensor based on immobilized *B. subtilis* on three-dimensional porous graphene-polypyrrole composite," *Sensors*, vol. 17, no. 11, p. 2594, 2017.
- [40] I. Karube, T. Matsunaga, S. Mitsuda, and S. Suzuki, "Microbial electrode BOD sensors," *Biotechnology & Bioengineering*, vol. 19, no. 10, pp. 1535–1547, 1977.
- [41] M. Raud, M. Tutt, E. Jögi, and T. Kikas, "BOD biosensors for pulp and paper industry wastewater analysis," *Environmental Science & Pollution Research*, vol. 19, no. 7, pp. 3039–3045, 2012.

Research Article

Effects of Sludge Retention Time on the Performance of Anaerobic Ceramic Membrane Bioreactor Treating High-Strength Phenol Wastewater

Chunhua He,^{1,2} Chuanhe Yang,^{1,2} Shoujun Yuan,^{1,2} Zhenhu Hu ^{1,2} and Wei Wang ^{1,2}

¹Department of Municipal Engineering, School of Civil Engineering, Hefei University of Technology, Hefei 230009, China

²Anhui Provincial Engineering Laboratory for Rural Water Environment and Resources, Hefei 230009, China

Correspondence should be addressed to Zhenhu Hu; zhhu@hfut.edu.cn and Wei Wang; wang_wei@hfut.edu.cn

Received 25 April 2020; Revised 29 May 2020; Accepted 5 June 2020; Published 1 August 2020

Academic Editor: Cuijie Feng

Copyright © 2020 Chunhua He et al. This is an open access article distributed under the Creative Commons Attribution License, which permits unrestricted use, distribution, and reproduction in any medium, provided the original work is properly cited.

Anaerobic ceramic membrane bioreactor (AnCMBR) is an attractive alternative for the treatment of high-strength phenol wastewater, but the effects of sludge retention time (SRT) on the performance and membrane fouling are still unclear. The results indicated that the AnCMBR was successfully employed to treat high-strength wastewater containing 5 g phenol L⁻¹. The removal efficiencies of phenol and chemical oxygen demand (COD) reached over 99.5% and 99%, respectively, with long SRT and short SRT. SRT had no obvious effect on the performance of the AnCMBR treating high-strength phenol wastewater with long time operation. The strong performance robustness of AnCMBR benefited from the enrichment of hydrogenotrophic methanogens and syntrophic phenol-degrading bacteria. However, the decline of SRT led to a more severe membrane fouling in the AnCMBR, which was caused by the small size of sludge flocs and high concentration of protein in the biopolymers. Therefore, this work presented a comprehensive insight to the feasibility and robustness of the AnCMBR for treating high-strength phenol wastewater.

1. Introduction

Many coal industrial liquid effluents, such as coking and coal gasification, contain a very high concentration of phenolic compounds [1, 2]. For example, the concentration of phenolic compounds in coal gasification wastewater varies from 4.5 to 7.5 g L⁻¹ [3]. Although both the anaerobic and aerobic processes were used to treat the phenolic wastewater, the anaerobic process was a more attractive alternative because of its advantages of low operation cost and energy resource recovery [4, 5]. It is a challenge for anaerobic process to treat high-strength phenol wastewater, since the anaerobic sludge is difficult to be granulated and easy to escape from the bioreactor under strong toxicity condition [6].

Anaerobic membrane bioreactor (AnMBR) is a promising alternative for the treatment of industrial wastewaters. AnMBR with combination of anaerobic digestion and membrane separation endows some advantages, such as high

sludge concentration, low sludge yield, and excellent removal capacity [7, 8]. Therefore, the AnMBR can be used to treat the high-strength phenol wastewater, because sufficient amount of biomass remained in the reactor which could overcome the slow hydrolysis rate of phenol [9]. However, membrane fouling is one of the biggest obstacles which limited the application of AnMBR in wastewater treatment [10, 11]. A feasible alternative to alleviate membrane fouling was to use the ceramic membranes as a replacement of polymeric membranes due to their higher membrane hydrophilicity [12, 13]. Ceramic membrane filtration operated better than polymeric membrane in terms of lower fouling rate, stronger performance robustness against chemical exposure, and higher mechanical strength [14]. It provided a possibility for the treatment of high-strength phenol wastewater using ceramic membranes in the anaerobic reactor. However, the corresponding operational parameter and its effects on the anaerobic ceramic

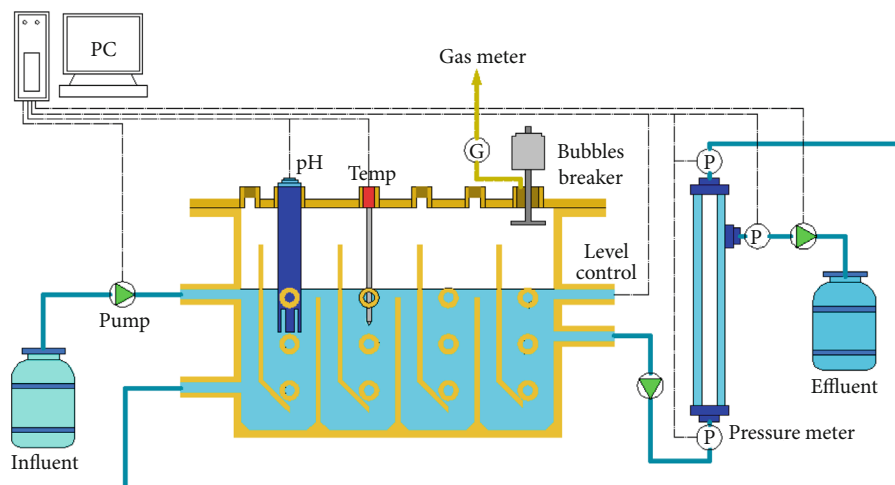


FIGURE 1: The schematic diagram of the AnCMBR.

membrane bioreactor (AnCMBR) treating high-strength phenol wastewater are still unclear.

As known, the sludge retention time (SRT) is a feasible operational parameter of bioreactor which directly affects treatment performance and membrane fouling [15]. Nevertheless, the views of previous studies on the SRT effect on the treatment performance and the membrane fouling were contradictory. It was widely considered that better digestion efficiency and effluent quality and higher methane yield could be achieved at the longer SRT [16]. However, the effects of SRT on the membrane fouling of the AnMBR treating different wastewater were different. Han et al. found that the longer SRT resulted in more serious membrane fouling because the sludge particles were more severely deposited on the membrane surface and extracellular polymeric substances (EPS) of sludge would be increased at longer SRT [17]. But, Estrada-Arriaga and Mijaylova found that a lower SRT and hydraulic retention time (HRT) caused more serious membrane fouling when the MBR was operated with treating estrogen-containing wastewater [18]. Therefore, the effect of SRT on the robustness performance of AnCMBR should be explored which was practically significant for the treatment of high-strength phenol wastewater.

The objectives of this study were to examine the influence of SRTs on the performance robustness of AnCMBR treating high-strength phenol wastewater. The effect of SRTs on the transmembrane pressure (TMP) of AnCMBR was presented. Moreover, the soluble microbial products (SMP), EPS, the particle size distribution (PSD), and microbial community structure of sludge at different SRTs were investigated.

2. Materials and Methods

2.1. Experimental Setup and Synthetic Wastewater. The schematic diagram of the AnCMBR is shown in Figure 1 and the details were described in a previous study [19]. The volume of the reactor was 6.2 L with a hydraulic retention time of 2 days. The whole experiment could be divided into two phases (phase I and II), and the longer SRT was controlled at 233 days at phase I and the shorter SRT was controlled at 61 days

at phase II. Before this study, the inoculation sludge was acclimated to phenolic wastewater ($5000 \text{ mg phenol L}^{-1}$) for about one month. The mixed liquor suspended solids (MLSS) and mixed liquor volatile suspended solids (MLVSS) concentrations of the inoculum was 18.53 g L^{-1} and 12.90 g L^{-1} , respectively. The wastewater consisted of phenol (5000 mg L^{-1}) and sodium acetate (2770 mg L^{-1}), which contributed to the total COD concentration of around 14000 mg L^{-1} . Additionally, the macronutrients, micronutrients, yeast extract, and a phosphate buffer solution were also added, and their concentration and composition were referred to a previous study [19].

2.2. Effects of SRTs on the Transmembrane Pressure (TMP) of AnCMBR. The transmembrane pressure (TMP) was detected in real time by the pressure sensors, and the LabVIEW software was used for recording the data. The fouled membrane in the AnCMBR was physically and chemically cleaned at the end of phases I and II. The physical cleaning was applied by scrubbing cake layer from the membrane surface using tap water. After that, the chemical cleaning was conducted to remove irreversible fouling by soaking the membrane in NaClO solution (0.5%) for 4 hours and followed by flushing with tap water [20].

2.3. Effects of SRTs on SMP and EPS of Sludge. At the end of every phase, the sludge samples were collected for the analyses of SMP and EPS. The sample supernatant was used to analyze the concentration of SMP, which was obtained after centrifugation with 9000 r min^{-1} for 15 min and filtration with $0.45 \mu\text{m}$ filter. The cation exchange resin (CER) technique was adopted to extract EPS [21]. The concentrations of carbohydrates and protein were measured by phenol-sulphuric acid method [22] and a modified version of the Lowry method [23], respectively. The concentrations of carbohydrates and protein were detected by a spectrophotometer at absorbance of $\text{OD}_{490 \text{ nm}}$ and $\text{OD}_{750 \text{ nm}}$.

2.4. Effects of SRTs on Microbial Community Structure. At the end of every phase, the sludge samples were collected for the

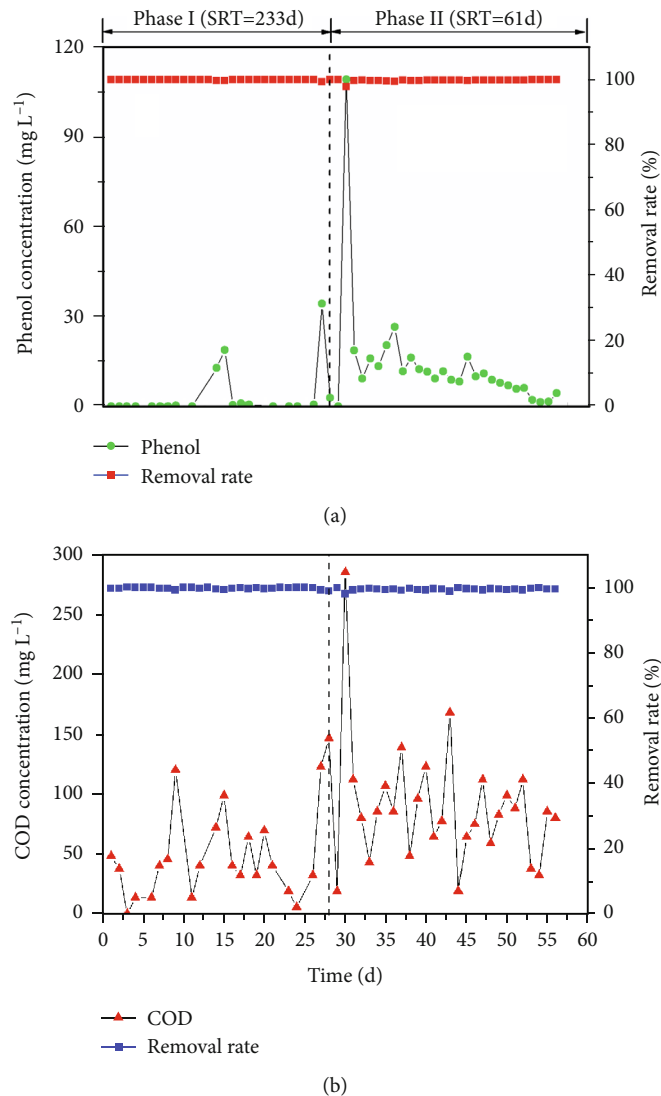


FIGURE 2: Treatment performance of AnCMBR treating high-strength phenol-containing wastewater with different SRTs (phase I: SRT, 233 days; phase II: SRT, 61 days).

analysis of microbial community structure. A bacterial genomic extraction kit (E.Z.N.A. Mag-Bind Soil DNA Kit, OMEGA) was employed to extract DNA from the sludge samples, and the agarose gel electrophoresis was used to check the integrity of DNA. The primers of 341F (5'-CCTACGGG NGGCWGCAG-3')/805R (5'-GACTACHVGGGTATCTA ATCC-3') were selected for amplifying of bacterial populations, and the primers of 340F (5'-CCCTAYGGGGYG-CASCAG-3')/1000R (5'-GGCCATGCACYWCYTCTC-3') were employed for amplifying of *archaea* populations. After PCR reaction, DNA purification, and quantification, the sludge samples were sequenced by Illumina MiSeq platform (Illumina, Inc., San Diego, CA, USA). The above analytical procedures were conducted by Shanghai Sangon Biological Engineering Technology and Services Co., Ltd. The analysis of sequence data was operated as the previous literature [24].

2.5. Other Analytical Methods. The concentration of phenol was determined by high-performance liquid chromatography (1260 Infinity, Agilent, USA) with a mobile phase of 50% acetonitrile. A laser granularity distribution analyzer (Malvern Instruments, MS-2000) was used to analyze the particle size distribution (PSD) of sludge samples. The concentrations of COD, MLSS, and MLVSS were measured according to the standard methods [25].

3. Results and Discussion

3.1. Effects of SRTs on the Treatment Performance of AnCMBR Treating High-Strength Phenol Wastewater. Figure 2 shows the treatment performance of AnCMBR treating high-strength phenol wastewater at two different SRTs. According to Figure 2(a), when the SRT was 233 days in phase I, the phenol concentration was not detected in the

effluent. Subsequently, the SRT was decreased to 61 days in phase II, and the effluent became worse in the first five days in which the phenol concentration was about 85.3-138.7 mg L⁻¹. The treatment performance gradually normalized, and the removal efficiency of phenol was about 99.8%. As shown in Figure 2(b), the removal efficiency of COD remained around 99.8% and 99.4% with longer SRT and shorter SRT, respectively. An obvious fluctuation of effluent was also observed when SRT was decreased at the early stage of phase II (shorter SRT) in which the COD concentration in the effluent was higher to 285.33 mg L⁻¹. Accompanied with the running, the effluent COD concentration declined to lower than 100 mg L⁻¹. The results suggested that the AnCMBR had strong performance robustness for treating high-strength phenol wastewater. Due to the shock loading of high-strength phenol, the UASB reactor was very difficult to acquire a strong performance robustness [26]. Previous literature demonstrated that 2000 mg L⁻¹ of phenol caused a remarkable inhibitory effect on the phenol degraders and methanogens in the saline UASB reactor [24]. When anaerobic bacteria were exposed to high concentration of phenol precipitately, the conversion of phenol to methane was blocked, resulting in the accumulation of phenol in the effluent [24]. The AnMBR was particularly suitable for high-strength wastewater due to its long SRT and sufficient amount of biomass, thus facilitating higher organic loading and performance stability [27, 28]. For the high-strength phenol wastewater, the slow-growing phenol degraders and methanogens could be enriched in the AnCMBR. The well-cultivated phenol degraders and methanogens in the AnCMBR should play a key role to remain high metabolic activity under extremely high concentration of phenol. Therefore, the specialized anaerobic microorganisms might be strengthened in the AnCMBR under the extremely high concentration of phenol. As calculated, phenol loading rate of sludge was correspondingly enhanced from 0.2 (longer SRT) to 0.275 (shorter SRT) g phenol g⁻¹ MLVSS d⁻¹, and it was much higher than the reported values [24, 29]. The strong performance robustness of AnCMBR treating high-strength phenol wastewater was mainly attributed to the efficient microbial community [30, 31]. As shown in Figure 2, it was also presented that the worse treatment performance and the obvious fluctuation of effluent were observed at the early stage of SRT decreasing. The worse performance with shorter SRT might contribute to the decrease of sludge concentration and the shift of microbial community structure in the AnMBR [30]. The bacteria and archaea communities gradually adapted the high-strength phenol condition and then the treatment performance was recovered [31]. Therefore, the AnCMBR was a promising alternative to treat high-strength phenol wastewater.

3.2. Effects of SRTs on the Transmembrane Pressure (TMP) of AnCMBR. Figure 3 shows the TMP variation of AnCMBR at the two different SRTs. It could be found that the TMP values of shorter SRT increased faster than that of longer SRT. Despite the initial TMPs were 28.40 and 28.05 kPa with two different SRTs, but it took 28 and 16 days to reach a TMP of 45 kPa with longer SRT (phase I) and shorter SRT

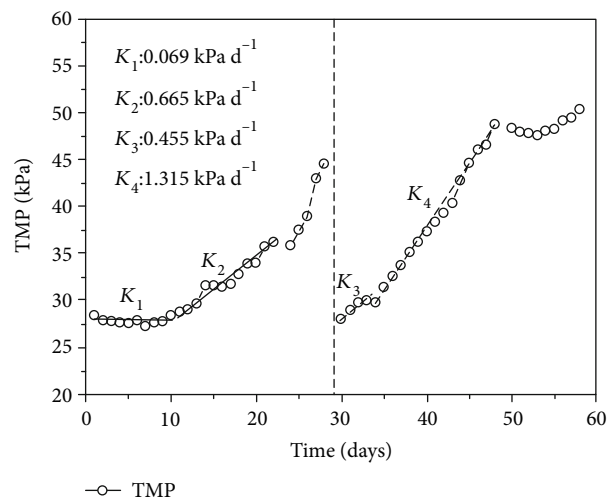


FIGURE 3: The effect of SRTs on the TMP variations of AnCMBR.

(phase II), respectively. The TMP profiles were composed of two phases: horizontal and exponential increase [12, 32]. At the horizontal increase phase, the ascending rate was 0.069 kPa d⁻¹ with the duration of 12 days at phase I (longer SRT), while the increasing rate was up to 0.455 kPa d⁻¹ with the duration of only 4 days at phase II (shorter SRT). The horizontal increase of TMP might result from the gradually accumulated organic macromolecules, microorganisms, and soluble compounds on the membrane surface, which did not significantly reduce the membrane flux [33]. At the exponential increase phase, the slopes of TMP profiles were 0.665 and 1.315 kPa d⁻¹ at phases I and II, respectively. The exponential increase of TMP chiefly ascribed to the plugged membrane pores by the microbial products and thick cake layer on the membrane surface, which aggrandized the fouled membrane areas so that the membrane flux rose sharply [34]. It indicated that both the horizontal and exponential increase rates of TMP with shorter SRT were higher than that of longer SRT and the results were different from the previous study. Jeison and van Lier found that membrane fouling was accelerated by the high sludge concentration in the AnMBR with long SRT [35]. Huang et al. explored the role of SRTs on the performance of submerged AnMBR for domestic wastewater treatment and observed that smaller particle size and less particle flocculation which resulted from lower concentrations of protein and carbohydrate in EPS accelerated the fouling development at longer SRT [33]. However, Huang et al. reported that the higher concentration of SMP at a shorter SRT also significantly affected membrane fouling [36]. In this study, the shorter SRT caused the more severe membrane fouling in AnCMBR with treating high-strength phenol wastewater. The reason might be related to the change of microbial products (e.g., EPS and SMP) and the particle size of sludge under the extreme high-strength phenol condition.

3.3. Effects of SRTs on the Soluble Microbial Products (SMP) and the Extracellular Polymeric Substances (EPS) of Sludge. Figure 4 shows the SMP and EPS composition at the two

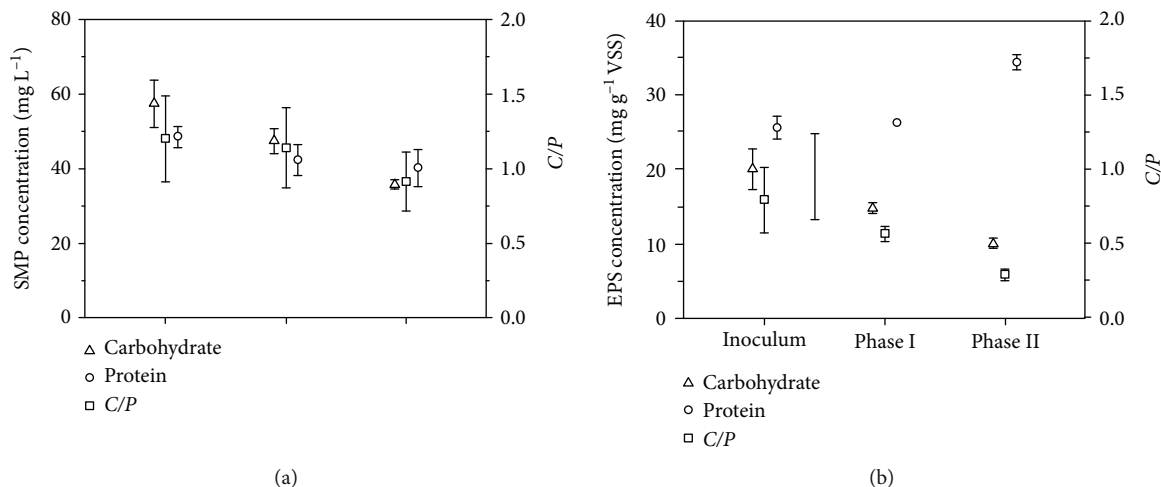


FIGURE 4: The effects of SRT on the SMP and EPS composition of sludge. (a) SMP compositions with two different SRTs. (b) EPS compositions with two different SRTs (phase I: SRT, 233 days; phase II: SRT, 61 days; C/P: mass concentration ratio of carbohydrate to protein).

different SRTs. SMP and EPS which mainly contain proteins and carbohydrates were reported to play important roles in the membrane fouling [33]. As shown in Figure 4(a), the proteins of SMP declined from 42.3 ± 4.1 to 40.0 ± 4.9 mg L⁻¹ with SRT shortening, and the carbohydrates of SMP also declined from 47.3 ± 3.4 to 35.7 ± 1.2 mg L⁻¹. The result indicated that SMP which included proteins and carbohydrates decreased with shorter SRT. Furthermore, the ratio of carbohydrates to protein (C/P) of SMP significantly decreased with a shorter SRT, which attributed to the remarkable decline of carbohydrate concentration and the little decrease of protein concentration in the SMP. This result was consistent with the previous study which reported that the microorganisms metabolized more actively and resulted in more organic compounds degraded and less SMP remained with a shorter SRT [33]. Our findings indicated that the severe membrane fouling with the shorter SRT was not caused by the SMP variation.

Figure 4(b) shows the variation of EPS concentration at the two different SRTs. Similar to the SMP, a significant decline of carbohydrates and C/P ratios were found in EPS with the decrease of SRT. However, the concentration of protein in EPS increased from 26.3 ± 0.4 to 34.4 ± 1.0 mg g⁻¹ VSS⁻¹ with the enhancement of phenol loading. The results indicated that the increase of phenol loading facilitated the production of protein in EPS. It was known that EPS which was generated by bacterium and enveloped the cells against the stress conditions [37]. As the phenol loading increased with shorter SRT, the microbial communities faced more toxic condition; hence, the protein of EPS increased greatly. The result was consistent with the previous study in which the protein concentration of EPS raised with the increase of phenol concentration in the anaerobic reactor [38]. EPS played an important role in the degradation of phenol, which was absorbed firstly and further be degraded by the relevant enzymes in EPS [39]. Therefore, the increase of protein concentration in EPS was closely related to the treatment performance of the AnCMBR.

In addition, the protein and carbohydrates were the main components of SMP and EPS, but the carbohydrates could be considered hydrophilic, while many proteins had hydrophobic properties [40]. The decrease of C/P ratio resulted in a decrease in the negative charge of the sludge surface, thereby increasing the surface hydrophobicity. Lee et al. reported that hydrophobicity of sludge was connected with adhesion forces [41]. Furthermore, the hydrophobic foulants could cause greater adhesion to hydrophobic membranes [42]. Hence, the increase of protein concentration in EPS might be responsible for the increasing adhesion forces and exponential increase in membrane fouling at the shorter SRT.

3.4. Effects of SRTs on the Particle Size Distribution (PSD) of Sludge. The PSD of sludge in the AnCMBR at the two different SRTs is shown in Figure 5. The results suggested that the shorter SRT caused a descending trend of floc size. The curve of PSD exhibited two independent peaks with longer SRTs. The average particle size of larger sludge flocs was 1300 μ m with longer SRT, but it was almost not observed with shorter SRT. Furthermore, the particle size of small sludge flocs decreased from 12.0 to 8.6 μ m with SRT of 61 days. The large size sludge flocs were disintegrated, which was caused by the increase of phenol loading with shorter SRT. Han et al. reported that the microenvironmental characteristics in different sizes of flocs influenced the bacterial diversity and distribution of functional microbes, thereby the size distribution of sludge flocs played an important role in the removal of pollutants [43]. The decrease of floc size suggested that the microbial community structure might shift to the one with higher mass transfer efficiency and stronger tolerance to the environment. Similarly, the proportion of small size anaerobic granular sludge increased by the increase of phenol loading, corresponding with the shifts in the dominant microbial community [38]. Therefore, the decrease of floc size might be a favorable feedback responding to the shift of community structure and the enrichment of phenol degraders under extremely high-strength phenol wastewater.

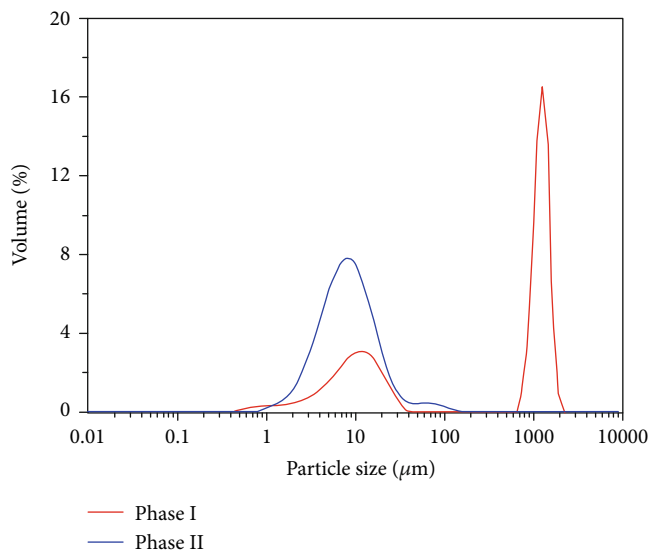


FIGURE 5: The effect of SRT on the particle size distribution of sludge (phase I: SRT, 233 days; phase II: SRT, 61 days).

As discussed in the previous section, the increase of phenol loading would lead to the decrease of carbohydrate concentration in EPS which was responsible for both adhesion and cohesion interactions between sludge cells [44]. In order to adapt to the change of environment, the sludge flocs tended to be smaller to enhancing mass transfer, enabling the system to adapt the change of OLR and achieving a higher organic removal rate [45]. In addition, the shear stress induced by biogas sparging in the reactor also brought about the decrease of particle size [19]. However, the small sludge flocs would induce denser biocake in the membrane surface. Although ceramic membranes had lower fouling propensity than polymeric membranes due to the weaker bonding between the foulants and membranes [46, 47], the small sludge flocs could plug the membrane pores easily, thereby sharply reducing the duration of horizontal increase of TMP with a shorter SRT. Therefore, higher concentration of protein in EPS and smaller particle size which were caused by a shorter SRT were the two main factors for more severe membrane fouling.

3.5. Effects of SRTs on the Change of Microbial Community Structure. Figure 6(a) shows the relative abundances of the major bacteria at genus level with the two different SRTs. With a longer SRT, the dominant bacterial genera were *Levilinea* (30.257%), *Syntrophorhabdus* (20.23%), *Mesotoga* (7.95%), *Ornatilinea* (5.22%), *Leptolinea* (3.59%), *Longilinea* (3.05%), *Thermovirga* (2.34%), *Syntrophus* (2.21%), and *Clostridium III* (1.30%), adding up to approximately 76.15% of relative abundances of all classified sequences. After switching to a shorter SRT, the dominant bacterial genera were *Levilinea* (11.13%), *Syntrophorhabdus* (21.53%), *Mesotoga* (10.56%), *Ornatilinea* (2.56%), *Leptolinea* (3.10%), *Longilinea* (1.49%), *Thermovirga* (4.90%), *Syntrophus* (5.64%), and *Clostridium III* (3.01%). The highest abundance of *Levilinea* significantly declined as the SRT decreased, which might result from the increase of phenol loading with a shorter SRT. In line with

the previous study, the relative abundance of *Levilinea* witnessed a drop with the increase of phenol loading in the UASB reactor. *Levilinea* was an anaerobic bacteria, which could convert amino acids and sugars into hydrogen and acetic and lactic acids [48]. Meanwhile, the relative abundances of other genera such as *Ornatilinea*, *Leptolinea*, and *Longilinea* decreased with shorter SRT. Contrary, the increase of *Thermovirga* and *Mesotoga* presented stronger tolerance to the increase of phenol loading. The former was able to ferment proteinous substrates, some single amino acids and organic acids and could be enriched with the enhancement of phenol loading [49]. The latter, which belonged to phylum *Thermotogae* and preferred to dwelling in the high salt and mesophilic conditions, could degrade fatty acids and play an essential ecological role in the ecosystems contaminated by aromatic compounds [50, 51]. Genus *Syntrophorhabdus*, which belonged to the class *Deltaproteobacteria*, was the subdominant group of phase I [52]. The role of *Syntrophorhabdus* was identified to convert phenol to benzoate and further to H_2 and acetate in the syntrophic consortium with a hydrogenotrophic methanogen [53]. It indicated that *Syntrophorhabdus* had a stronger endurance toward the increase of phenol loading than genus *Levilinea* at an extremely high concentration of phenol. *Syntrophus* was one of the faster growing strain, which was reported to have a relatively high abundance in anaerobic treatment of phenolic wastewater [54] and could transform benzoate into acetate and H_2/CO_2 [55]. Previous study reported that syntrophic bacteria such as *Syntrophus* and *Syntrophorhabdus* could work solely to convert phenol to acetate [56]. Hence, the two syntrophic bacteria were the dominant phenol degraders for successfully treating extremely high-strength phenol wastewater. Although the removal of phenol was not affected by the decreased SRT, the community structure of phenol degraders was changed, corresponding with *Syntrophorhabdus* and *Syntrophus* exhibiting a strong robustness. However, these slow-growing syntrophic bacteria, which played an important role in degrading phenol under the extremely high concentration of phenol, were easily washed out in the conventional anaerobic reactors. But the increase of *Syntrophorhabdus* and *Syntrophus* with shorter SRT presented an advantage of AnCMBR holding a sufficient amount of biomass in the reactor [39]. Therefore, it indicated that the enrichment of syntrophic phenol-degrading bacteria in the AnCMBR ensured efficient phenol removal and strong performance robustness at an extremely high concentration of phenol.

Figure 6(b) shows the effect of SRT on the relative abundances of archaea at genus level. The results indicated that the change of SRT had no obvious effect on archaea. The dominant populations were *Methanotherix*, *Methanosphaerula*, and *Methanolinea*, and the relative abundances of archaea with two different SRTs were similar. As known, *Methanotherix* was affiliated to acetoclastic methanogens [57] and its relative abundances slightly increased from 78.55% to 79.81% when SRT declined from 233 days to 61 days. A previous study presented that *Methanotherix* was the dominant archaea on the surface of granules for treating complex phenolic wastewater in UASB reactors [58]. The findings indicated that acetoclastic methanogenesis was the

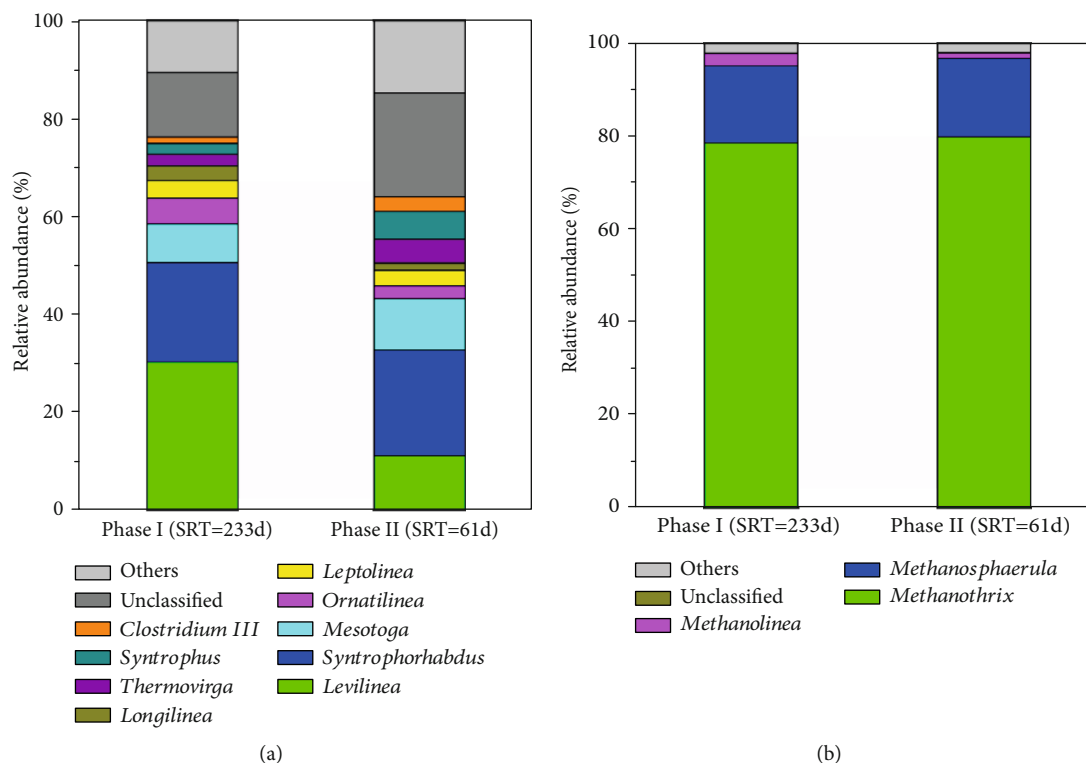


FIGURE 6: The relative abundance of bacteria and archaea at genus level with different SRTs (a) bacteria, (b) archaea. “Other” represents all classified taxa that were <1% in all samples.

main methane production way. Despite the increase of phenol loading rate, the relative abundances of *Methanospaerula* and *Methanolinea* which all belonged to hydrogenotrophic methanogen were not dramatically changed with shorter SRTs [59]. The result indicated that the hydrogenotrophic methanogens were stable in AnCMBR, in spite of high-strength phenol condition. The hydrogenotrophic methanogens played an important role in the conversion of phenol to methane, which could make the benzoate degradation reaction thermodynamically favorable [54]. Due to the enhancement of phenol loading with shorter SRT, the phenol degraders would shift to syntrophic phenol-degrading bacteria with stronger endurance to high-strength phenol condition, but this shift required the assistance from hydrogenotrophic methanogens. Poirier et al. found that the ratio of methane production via the hydrogenotrophic pathway was gradually increased along with the increase of phenol stress, which indicated that hydrogenotrophic methanogen also held strong endurance to extremely high concentration of phenol [31]. Therefore, the hydrogenotrophic methanogens and syntrophic phenol-degrading bacteria should play an important role in the degradation of high-strength of phenol. Although the phenol loading rate increased with a shorter SRT, the syntrophic bacteria such as *Syntrophus* and *Syntrophorhabdus* were enriched and hydrogenotrophic methanogens were kept stable in the AnCMBR. The AnCMBR provided a strong robustness pathway for anaerobic treatment of high-strength phenol wastewater.

4. Conclusion

Based on the experimental results, the main conclusions were drawn as follows:

- (1) The AnCMBR achieved satisfactory treatment performance with phenol concentration of 5 g L^{-1} although phenol loading rate of sludge was increased from 0.2 to $0.275 \text{ g phenol g}^{-1} \text{ MLVSS d}^{-1}$
- (2) Severe membrane fouling emerged in the AnCMBR at a shorter SRT, resulting from the increase of protein concentration in EPS and the decline of floc size
- (3) With the increase of phenol loading at a shorter SRT, the enrichment of syntrophic phenol-degrading bacteria and the stability of hydrogenotrophic methanogens might be the main reason of the strong performance robustness of AnCMBR treating high-strength phenol wastewater

Data Availability

The data used to support the findings of this study are available from the corresponding author upon request.

Conflicts of Interest

The author(s) declare(s) that they have no conflicts of interest.

Authors' Contributions

Chunhua He and Chuanhe Yang are co-first authors.

Acknowledgments

This work was supported by the Project of National Key Research and Development Program of China (No. 2019YFC0408502), National Science Foundation of China (51878232), and Fundamental Research Funds for the Central Universities of China (JZ2019YYPY0018).

References

- [1] M. Bajaj, C. Gallert, and J. Winter, "Treatment of phenolic wastewater in an anaerobic fixed bed reactor (AFBR)–Recovery after shock loading," *Journal of Hazardous Materials*, vol. 162, no. 2-3, pp. 1330–1339, 2009.
- [2] W. Wang, H. Han, M. Yuan, H. Li, F. Fang, and K. Wang, "Treatment of coal gasification wastewater by a two-continuous UASB system with step-feed for COD and phenols removal," *Bioresource Technology*, vol. 102, no. 9, pp. 5454–5460, 2011.
- [3] Z. Yu, Y. Chen, D. Feng, and Y. Qian, "Process development, simulation, and industrial implementation of a new coal-gasification wastewater treatment installation for phenol and Ammonia removal," *Industrial & Engineering Chemistry Research*, vol. 49, no. 6, pp. 2874–2881, 2010.
- [4] W. Wang and H. Han, "Recovery strategies for tackling the impact of phenolic compounds in a UASB reactor treating coal gasification wastewater," *Bioresource Technology*, vol. 103, no. 1, pp. 95–100, 2012.
- [5] W. Yan, F. Sun, J. Liu, and Y. Zhou, "Enhanced anaerobic phenol degradation by conductive materials via EPS and microbial community alteration," *Chemical Engineering Journal*, vol. 352, pp. 1–9, 2018.
- [6] F. Rosenkranz, L. Cabrol, M. Carballa et al., "Relationship between phenol degradation efficiency and microbial community structure in an anaerobic SBR," *Water Research*, vol. 47, no. 17, pp. 6739–6749, 2013.
- [7] G. Skouteris, D. Hermosilla, P. López, C. Negro, and Á. Blanco, "Anaerobic membrane bioreactors for wastewater treatment: a review," *Chemical Engineering Journal*, vol. 198–199, pp. 138–148, 2012.
- [8] A. L. Smith, L. B. Stadler, N. G. Love, S. J. Skerlos, and L. Raskin, "Perspectives on anaerobic membrane bioreactor treatment of domestic wastewater: a critical review," *Bioresource Technology*, vol. 122, pp. 149–159, 2012.
- [9] S. Wang, C. Ma, C. Pang, Z. Hu, and W. Wang, "Membrane fouling and performance of anaerobic ceramic membrane bioreactor treating phenol- and quinoline-containing wastewater: granular activated carbon vs polyaluminum chloride," *Environmental Science and Pollution Research*, vol. 26, pp. 34167–34176, 2019.
- [10] M. Remy, V. Potier, H. Temmink, and W. Rulkens, "Why low powdered activated carbon addition reduces membrane fouling in MBRs," *Water Research*, vol. 44, no. 3, pp. 861–867, 2010.
- [11] H. Lin, W. Peng, M. Zhang, J. Chen, H. Hong, and Y. Zhang, "A review on anaerobic membrane bioreactors: applications, membrane fouling and future perspectives," *Desalination*, vol. 314, pp. 169–188, 2013.
- [12] X. Yue, Y. K. Koh, and H. Y. Ng, "Effects of dissolved organic matters (DOMs) on membrane fouling in anaerobic ceramic membrane bioreactors (AnCMBRs) treating domestic wastewater," *Water Research*, vol. 86, pp. 96–107, 2015.
- [13] X. Yue, Y. K. Koh, and H. Y. Ng, "Treatment of domestic wastewater with an anaerobic ceramic membrane bioreactor (AnCMBR)," *Water Science and Technology*, vol. 72, no. 12, pp. 2301–2307, 2015.
- [14] B. Hofs, J. Ogier, D. Vries, E. F. Beerendonk, and E. R. Cornelissen, "Comparison of ceramic and polymeric membrane permeability and fouling using surface water," *Separation and Purification Technology*, vol. 79, no. 3, pp. 365–374, 2011.
- [15] X. Wang, Y. Chen, B. Yuan, X. Li, and Y. Ren, "Impacts of sludge retention time on sludge characteristics and membrane fouling in a submerged osmotic membrane bioreactor," *Bioresource Technology*, vol. 161, pp. 340–347, 2014.
- [16] R. K. Dereli, F. P. van der Zee, B. Heffernan, A. Grelot, and J. B. van Lier, "Effect of sludge retention time on the biological performance of anaerobic membrane bioreactors treating corn-to-ethanol thin stillage with high lipid content," *Water Research*, vol. 49, pp. 453–464, 2014.
- [17] S.-S. Han, T.-H. Bae, G.-G. Jang, and T.-M. Tak, "Influence of sludge retention time on membrane fouling and bioactivities in membrane bioreactor system," *Process Biochemistry*, vol. 40, no. 7, pp. 2393–2400, 2005.
- [18] E. B. Estrada-Arriaga and P. N. Mijaylova, "Influence of operational parameters (sludge retention time and hydraulic residence time) on the removal of estrogens by membrane bioreactor," *Environmental Science and Pollution Research International*, vol. 18, no. 7, pp. 1121–1128, 2011.
- [19] W. Wang, S. Wang, X. Ren, Z. Hu, and S. Yuan, "Rapid establishment of phenol- and quinoline-degrading consortia driven by the scoured cake layer in an anaerobic baffled ceramic membrane bioreactor," *Environmental Science and Pollution Research*, vol. 24, no. 33, pp. 26125–26135, 2017.
- [20] Z. Wang, F. Meng, X. He, Z. Zhou, L. N. Huang, and S. Liang, "Optimisation and performance of NaClO-assisted maintenance cleaning for fouling control in membrane bioreactors," *Water Research*, vol. 53, pp. 1–11, 2014.
- [21] B. Frølund, R. Palmgren, K. Keiding, and P. H. Nielsen, "Extraction of extracellular polymers from activated sludge using a cation exchange resin," *Water Research*, vol. 30, no. 8, pp. 1749–1758, 1996.
- [22] T. Masuko, A. Minami, N. Iwasaki, T. Majima, S. Nishimura, and Y. C. Lee, "Carbohydrate analysis by a phenol-sulfuric acid method in microplate format," *Analytical Biochemistry*, vol. 339, no. 1, pp. 69–72, 2005.
- [23] R. Komsa-Penkova, R. Spirova, and B. Bechev, "Modification of Lowry's method for collagen concentration measurement," *Journal of Biochemical and Biophysical Methods*, vol. 32, no. 1, pp. 33–43, 1996.
- [24] W. Wang, B. Wu, S. Pan, K. Yang, Z. Hu, and S. Yuan, "Performance robustness of the UASB reactors treating saline phenolic wastewater and analysis of microbial community structure," *Journal of Hazardous Materials*, vol. 331, pp. 21–27, 2017.
- [25] APHA, *Standard Methods for the Examination of Water and Wastewater*, American Water Works Association, Washington, DC, 21st edition, 2012.
- [26] D. E. Belostotskiy, E. E. Ziganshina, M. Siniagina, E. A. Boulygina, V. A. Miluykov, and A. M. Ziganshin, "Impact

- of the substrate loading regime and phosphoric acid supplementation on performance of biogas reactors and microbial community dynamics during anaerobic digestion of chicken wastes,” *Bioresource Technology*, vol. 193, pp. 42–52, 2015.
- [27] L. Yin, Z. Kaisong, B. Rune, L. Chunming, and L. Haining, “Membrane installation for enhanced up-flow anaerobic sludge blanket (UASB) performance,” *Journal of Bioscience and Bioengineering*, vol. 116, pp. 357–361, 2013.
- [28] M. Kanai, V. Ferre, S. Wakahara, T. Yamamoto, and M. Moro, “A novel combination of methane fermentation and MBR - Kubota submerged anaerobic membrane bioreactor process,” *Desalination*, vol. 250, pp. 964–967, 2009.
- [29] W. Wang, K. Yang, J. M. Sierra, X. Zhang, S. Yuan, and Z. Hu, “Potential impact of methyl isobutyl ketone (MIBK) on phenols degradation in an UASB reactor and its degradation properties,” *Journal of Hazardous Materials*, vol. 333, pp. 73–79, 2017.
- [30] A. Yurtsever, B. Calimlioglu, and E. Sahinkaya, “Impact of SRT on the efficiency and microbial community of sequential anaerobic and aerobic membrane bioreactors for the treatment of textile industry wastewater,” *Chemical Engineering Journal*, vol. 314, pp. 378–387, 2017.
- [31] S. Poirier, A. Bize, C. Bureau, T. Bouchez, and O. Chapleur, “Community shifts within anaerobic digestion microbiota facing phenol inhibition: towards early warning microbial indicators?,” *Water Research*, vol. 100, pp. 296–305, 2016.
- [32] Y. Tian and X. Su, “Relation between the stability of activated sludge flocs and membrane fouling in MBR: under different SRTs,” *Bioresource Technology*, vol. 118, pp. 477–482, 2012.
- [33] Z. Huang, S. L. Ong, and H. Y. Ng, “Submerged anaerobic membrane bioreactor for low-strength wastewater treatment: effect of HRT and SRT on treatment performance and membrane fouling,” *Water Research*, vol. 45, no. 2, pp. 705–713, 2011.
- [34] J. Zhang, H. C. Chua, J. Zhou, and A. G. Fane, “Factors affecting the membrane performance in submerged membrane bioreactors,” *Journal of Membrane Science*, vol. 284, no. 1-2, pp. 54–66, 2006.
- [35] D. Jeison and J. B. van Lier, “Cake layer formation in anaerobic submerged membrane bioreactors (AnSMBR) for wastewater treatment,” *Journal of Membrane Science*, vol. 284, no. 1-2, pp. 227–236, 2006.
- [36] Z. Huang, S. L. Ong, and H. Y. Ng, “Performance of submerged anaerobic membrane bioreactor at different SRTs for domestic wastewater treatment,” *Journal of Biotechnology*, vol. 164, no. 1, pp. 82–90, 2013.
- [37] J. Song, Y. Zhou, and C. Wu, “The activated sludge metabolic characteristics changing sole carbon source from readily biodegradable acetate to toxic phenol,” *Water Science and Technology*, vol. 73, pp. 2324–2331, 2016.
- [38] Y. Li, S. Tabassum, C. Chu, and Z. Zhang, “Inhibitory effect of high phenol concentration in treating coal gasification wastewater in anaerobic biofilter,” *Journal of Environmental Sciences (China)*, vol. 64, pp. 207–215, 2018.
- [39] L. F. Ren, R. Chen, X. Zhang, J. Shao, and Y. He, “Phenol biodegradation and microbial community dynamics in extractive membrane bioreactor (EMBR) for phenol-laden saline wastewater,” *Bioresource Technology*, vol. 244, Part 1, pp. 1121–1128, 2017.
- [40] F. Jorand, F. Boué-Bigne, J. C. Block, and V. Urbain, “Hydrophobic/hydrophilic properties of activated sludge exopolymeric substances,” *Water Science and Technology*, vol. 37, no. 4-5, pp. 307–315, 1998.
- [41] W. Lee, S. Kang, and H. Shin, “Sludge characteristics and their contribution to microfiltration in submerged membrane bioreactors,” *Journal of Membrane Science*, vol. 216, no. 1-2, pp. 217–227, 2003.
- [42] A. Charfi, A. N. Ben, and J. Harmand, “Analysis of fouling mechanisms in anaerobic membrane bioreactors,” *Water Research*, vol. 46, p. 2637, 2012.
- [43] Y. Han, J. Liu, X. Guo, and L. Li, “Micro-environment characteristics and microbial communities in activated sludge flocs of different particle size,” *Bioresource Technology*, vol. 124, pp. 252–258, 2012.
- [44] J. Ray, T. Shinnick, and R. Lerner, “A mutation altering the function of a carbohydrate binding protein blocks cell-cell cohesion in developing *Dictyostelium discoideum*,” *Nature*, vol. 279, no. 5710, pp. 215–221, 1979.
- [45] X. Huang, P. Gui, and Y. Qian, “Effect of sludge retention time on microbial behaviour in a submerged membrane bioreactor,” *Process Biochemistry*, vol. 36, no. 10, pp. 1001–1006, 2001.
- [46] S. J. Lee, M. Dilaver, P. K. Park, and J. H. Kim, “Comparative analysis of fouling characteristics of ceramic and polymeric microfiltration membranes using filtration models,” *Journal of Membrane Science*, vol. 432, pp. 97–105, 2013.
- [47] A. Murić, I. Petrinić, and M. L. Christensen, “Comparison of ceramic and polymeric ultrafiltration membranes for treating wastewater from metalworking industry,” *Chemical Engineering Journal*, vol. 255, pp. 403–410, 2014.
- [48] Y. Maspolim, Y. Zhou, C. Guo, K. Xiao, and W. J. Ng, “The effect of pH on solubilization of organic matter and microbial community structures in sludge fermentation,” *Bioresource Technology*, vol. 190, pp. 289–298, 2015.
- [49] H. Dahle and N. K. Birkeland, “*Thermovirga lienii* gen. nov., sp. nov., a novel moderately thermophilic, anaerobic, amino-acid-degrading bacterium isolated from a North Sea oil well,” *International Journal Of Systematic And Evolutionary Microbiology*, vol. 56, no. 7, pp. 1539–1545, 2006.
- [50] B. H. Tuo, J. B. Yan, B. A. Fan, Z. H. Yang, and J. Z. Liu, “Biodegradation characteristics and bioaugmentation potential of a novel quinoline-degrading strain of *Bacillus* sp. isolated from petroleum-contaminated soil,” *Bioresource Technology*, vol. 107, pp. 55–60, 2012.
- [51] W. Ben Hania, R. Ghodbane, A. Postec et al., “Cultivation of the first mesophilic representative (“mesotoga”) within the order *Thermotogales*,” *Systematic and Applied Microbiology*, vol. 34, no. 8, pp. 581–585, 2011.
- [52] Y. L. Qiu, S. Hanada, A. Ohashi, H. Harada, Y. Kamagata, and Y. Sekiguchi, “*Syntrophorhabdus aromaticivorans* gen. nov., sp. nov., the first cultured anaerobe capable of degrading phenol to acetate in obligate syntrophic associations with a hydrogenotrophic methanogen,” *Applied and Environmental Microbiology*, vol. 74, pp. 2051–2058, 2008.
- [53] J.-G. Na, M.-K. Lee, Y.-M. Yun, C. Moon, M.-S. Kim, and D.-H. Kim, “Microbial community analysis of anaerobic granules in phenol-degrading UASB by next generation sequencing,” *Biochemical Engineering Journal*, vol. 112, pp. 241–248, 2016.
- [54] L. Alibardi, N. Bernava, R. Cossu, and A. Spagni, “Anaerobic dynamic membrane bioreactor for wastewater treatment at ambient temperature,” *Chemical Engineering Journal*, vol. 284, pp. 130–138, 2016.

- [55] H. H. Fang, Y. Liu, S. Z. Ke, and T. Zhang, "Anaerobic degradation of phenol in wastewater at ambient temperature," *Water Science and Technology*, vol. 49, no. 1, pp. 95–102, 2004.
- [56] C. L. Chen, J. H. Wu, I. C. Tseng, T. M. Liang, and W. T. Liu, "Characterization of active microbes in a full-scale anaerobic fluidized bed reactor treating phenolic wastewater," *Microbes and Environments*, vol. 24, no. 2, pp. 144–153, 2009.
- [57] D. Wang, Y. Han, H. Han, K. Li, and C. Xu, "Enhanced treatment of Fischer-Tropsch wastewater using up-flow anaerobic sludge blanket system coupled with micro-electrolysis cell: a pilot scale study," *Bioresource Technology*, vol. 238, pp. 333–342, 2017.
- [58] A. Ramakrishnan and S. K. Gupta, "Effect of hydraulic retention time on the biodegradation of complex phenolic mixture from simulated coal wastewater in hybrid UASB reactors," *Journal of Hazardous Materials*, vol. 153, no. 1-2, pp. 843–851, 2008.
- [59] D. Wang, W. Ma, H. Han, K. Li, and X. Hao, "Enhanced treatment of Fischer-Tropsch (F-T) wastewater by novel anaerobic biofilm system with scrap zero valent iron (SZVI) assisted," *Biochemical Engineering Journal*, vol. 117, pp. 66–76, 2017.

Research Article

Simulation of a Novel Tubular Microalgae Photobioreactor with Aerated Tangent Inner Tubes: Improvements in Mixing Performance and Flashing-Light Effects

Xuyang Cui,^{1,2} Junhong Yang ,^{1,2} Yuanzheng Feng,^{1,2} and Wenwen Zhang^{1,2}

¹Key Laboratory of Efficient Utilization of Low and Medium Grade Energy, MOE, Tianjin University, Tianjin 300350, China

²School of Mechanical Engineering, Tianjin University, Tianjin 300350, China

Correspondence should be addressed to Junhong Yang; yangjunhong@tju.edu.cn

Received 7 April 2020; Revised 5 June 2020; Accepted 13 June 2020; Published 10 July 2020

Academic Editor: Yu Tao

Copyright © 2020 Xuyang Cui et al. This is an open access article distributed under the Creative Commons Attribution License, which permits unrestricted use, distribution, and reproduction in any medium, provided the original work is properly cited.

At present, large-scale and high-efficiency microalgal cultivation is the key to realizing the technology for carbon capture and storage (CCS) and bioresource recovery. Meanwhile, tubular photobioreactors (PBRs) have great potential for microalgal cultivation due to their high productivity. To improve the mixing performance and flashing-light effect, a novel tube PBR with the inner tube tangential to the outer tube was developed, whose radial aeration pores are situated along the length of the inner tube. The direction of aeration, aeration rate, light/dark cycle period (L/D), light-time ratio, average turbulent kinetic energy (TKE), and degree of synergy between the velocity and direction of the light field in the PBR were optimized by a computational fluid dynamics (CFD) simulation and field synergy theory. The results show that a downwards aeration direction of 30° and an aeration rate of 0.7 vvm are the most conducive to reducing the dead zone and improving the light/dark cycle frequency. Compared to the concentric double-tube PBR, the light/dark cycle frequency and light time of the tangent double-tube PBR increased by 78.2% and 36.2% to 1.8 Hz and 47.8%, respectively, and the TKE was enhanced by 48.1% from 54 to 80 cm²·s⁻². Meanwhile, field synergy theory can be extended and applied to the design of tubular microalgae PBRs, and the average synergy of the light and velocity gradients across the cross-section increased by 38% to 0.69. The tangential inner tube aeration structure generated symmetrical vertical vortices between the light and dark areas in the PBR, which significantly improved the mixing performance and flashing-light effect. This novel design can provide a more suitable microenvironment for microalgal cultivation and is promising for bioresource recovery applications and improving the yield of microalgae.

1. Introduction

Microalgae are considered to be one of the most promising technologies for carbon capture and storage (CCS) and have been identified as a superior feedstock for biodiesel production [1, 2]. Microalgae are also important biological resources for recycling. However, the low biomass productivity of microalgal cultivation systems is a bottleneck in commercial production, which leads to the high cost of microalgae biofuels [3]. Before this situation can be reversed, a significant improvement in volumetric productivity is required [4]. This goal will require improved microalgae genetic engineering and microalgae process engineering [5]. However, compared to other engineering processes, it is difficult to achieve break-

throughs in genetic engineering. Therefore, it is very important to improve the cultivation system related to mass and radiation energy transfer, nutrient absorption, and growth rate [6]. Focusing on high efficiency and large-scale microalgal cultivation, tubular photobioreactors (PBRs) are considered one of the most suitable culture systems. However, their weak mass transfer, wall growth, photoinhibition, and photolimitations have limited their development [7]. Several tube-based photobioreactors (PBRs) have been designed for microalgal cultivation, but the experimental characterization of the flow field in PBR is difficult and costly [8]. The development of computational fluid dynamics (CFD) has facilitated the study of hydrodynamic performance and the structural design of tubular PBRs [1].

Tubular PBRs have great potential for microalgal cultivation due to their high productivity compared with open ponds [9]. CFD has been widely used in flow field simulations of tubular PBR to optimize the mixing of the culture medium. Azizi et al. [10] studied a new type of tubular PBR with an embedded static mixer via CFD simulation and showed that the mixing conditions and fluid dynamics in the proposed PBR were better than those in the traditional PBR. Later, Qin and Wu [11] studied tubular PBR with a 4-unit Kenics mixer and a 1-unit Kenics mixer using CFD, thereby confirming two methods for increasing the efficiency of the light/dark cycle frequency. Gómez-Pérez et al. [12] studied the effect of wall turbulence promoters (that is, the profile of the inner tube PBR wall) and found that the wall turbulence promoters offer better mixing behavior than standard PBRs at flow velocities of 0.2–0.25 m/s, although the energy uptake is 60–80% lower. Based on this study, Lei et al. [13] developed a new type of tubular PBR with spiral ribs, which has good mixing performance and flashing-light effects. In addition, Wu et al. [14] studied the flow dynamics of a spiral tube by CFD and showed stable Dean vortex motion along the axial coordinates, although there was no vortex in the tubular section. The mixing performance of a spiral tube PBR is much better than that of a tubular PBR. Perner-Nochta and Posten [15] subsequently focused on a tubular PBR using a static mixer for spiral tube PBRs, applying CFD and trajectory analysis to examine the scale-down/-scale-up effects. Gómez-Pérez et al. [16] discussed four types of twisted tubular PBRs by CFD simulation and provided an important contribution towards constructing an efficient tubular PBR. Meanwhile, Ye et al. [8] simulated a novel type of continuous lantern-shaped PBR (LDT) that can generate a vortex flow field and enhance the mass transfer in a microalgal solution, similar to the effect of twisting a tubular PBR.

In addition, Su et al. [17] studied PBRs; they designed a destabilized mixing bar using CFD, and the results show that the vertical speed along the light path caused by the mixing bar helped achieve homogenous mixing of the culture medium, thereby improving the photosynthetic efficiency of the algal cells. Pruvost et al. [18] designed a ring-shaped PBR that can accurately control the light and provide very effective mixing, especially along the light gradient of the culture. Pruvost et al. [19] proposed an attenuated ring-shaped vortex flow caused by the tangential inlet, which increased the displacement of the microalgae along the light gradient. Similarly, Sato et al. [20] invented three novel closed PBRs that used aeration to mix, including a parabola, a pipe, and a diamond. The simulation results show that the parabola has advantages in mass transfer and that the pipe is the best performer for *Chaetoceros calcitrans* cultivation (1.8 times higher performance than that of the control dome). Therefore, mixing along the light gradient can improve the efficiency of photosynthesis, which is the main principle of new PBR designs. Moreover, Cheng et al. [1] proposed using a tangential jet that generates a large clockwise vertical vortex and several secondary vortices in a novel jet-charged tangential swirl plate PBR (JTSP); this method can significantly reduce the dead zone and increase the light/dark cycle frequency. According to a report by Guo et al. [21], in 1998,

the field synergy principle was proposed to improve the convective heat transfer rate by analyzing the boundary layer heat transfer mechanism. The effects depended on the synergy level of the velocity and the thermal flow field, as well as the synergy angle between the velocity and the thermal gradient [22]. Under the same speed and temperature boundary conditions, the higher the level of synergy is, the higher the heat transfer intensity [23]. Based on the similarities between heat and mass transfer, Chen et al. [24] derived mathematical synergy equations for mass transfer and used them to optimize the mass transfer of a photocatalytic oxidation reactor. In general, light and mixing are very important for microalgal cultivation. Mixing along the direction of light is conducive to the transmission of light but also to the mixing of the gas phase (CO_2), liquid phase (culture medium), and solid phase (microalgae cells), thereby producing a suitable flow environment and flashing-light effect, which are beneficial to microalgal cultivation [1]. However, few works have reported the synergy between the light field and flow field of the tubular PBR used for microalgal cultivation.

In this work, we propose a novel tangent double tube with radial aeration pores along the length of the inner tube, in which the inner tube is tangential to the outer tube in order to strengthen the synergy between the light and velocity gradients. The direction of aeration, the aeration rate, the light/dark cycle period (L/D), the light-time ratio, the average turbulent kinetic energy (TKE), and the degree of synergy between the velocity and the direction of the light field in the PBR were analyzed by computational fluid dynamics (CFD) and the field synergy principle.

2. Design and Numerical Models of a Novel PBR

2.1. Development of a Novel PBR. In our previous study [25], we illustrated the initial concept of a novel double-tube PBR (see Figure 1(a)), which included a concentric double tube with aeration pores along the tube length. Previous research results indicate that the concentric double-tube PBR proposed in this previous work can help facilitate efficient microalgal cultivation. As shown in Figure 1(a), microalgae are cultivated in the annular space between the outer tube and the inner tube and are aerated through a series of radial pores installed along the length of the inner tube, which can provide air and mix the cultures.

As shown in Figures 1(b) and 1(c), the new tangent double-tube PBR in this work can reduce the volume of the dark areas, thereby increasing the proportion of the light and dark areas. Fernández et al. [26] discussed the light distribution of the tube and found that under normal outdoor conditions, the tube had almost no dark areas and a diameter of 0.06 m. Provided the zone that has a light path less than 60 mm is a light zone, the light/dark ratio for the tangent with an outer tube of 200 mm diameter and an inner tube of 80 mm diameter is 0.648 and increases by 31.4% compared to 0.493 for a tube of the same size. To some extent, increasing the proportion of light and dark areas is beneficial for microalgal cultivation. Barbosa et al. [27] studied the effects of cycle time (10–100 s) and light fraction (0.1–1) on the growth rate and biomass yield of *Dunaliella tertiolecta* in

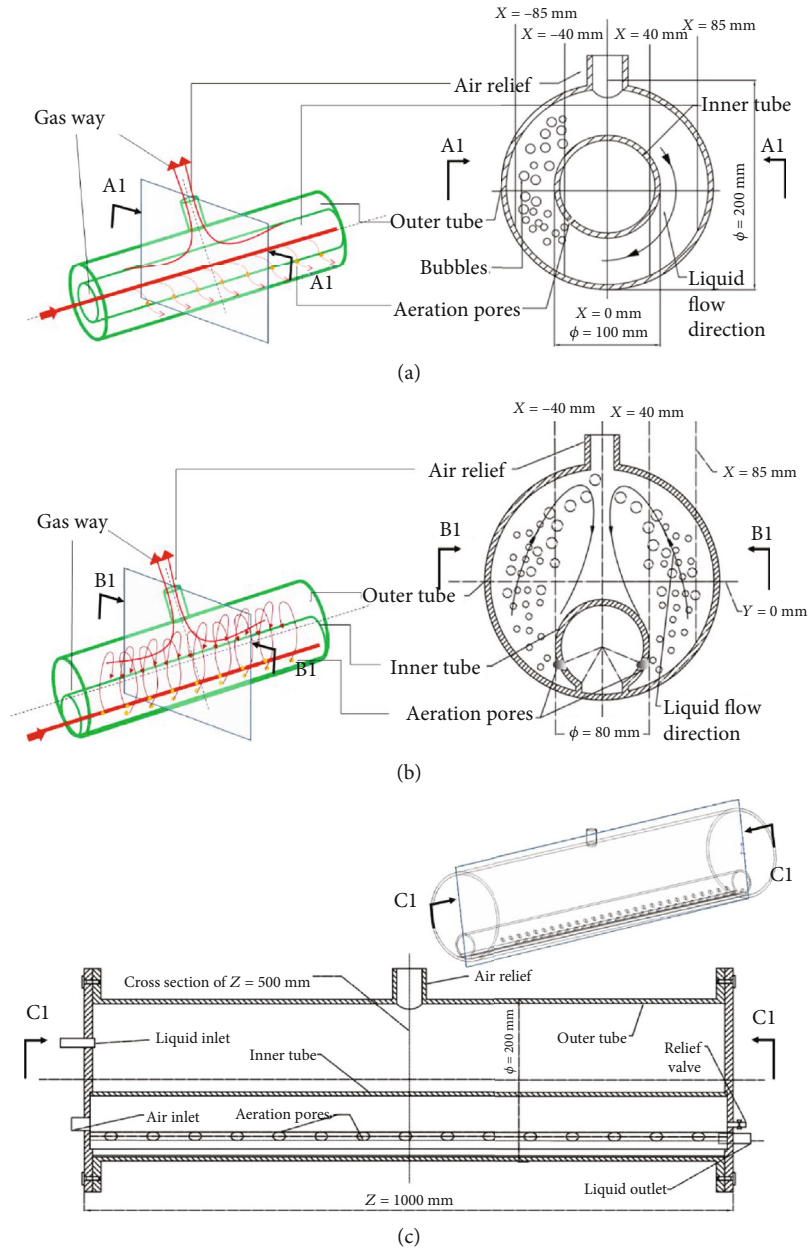


FIGURE 1: Conceptual structures for a novel double-tube photobioreactor (PBR). (a) The concentric double-tube PBR in our previous work; (b, c) the novel tangent double-tube PBR in this work.

airlift reactors, and the results show that an increase in the light fraction, for a constant medium cycle time, led to an increase in the biomass yield and growth rate. In addition, compared with the vortex attenuation flow caused by coaxial inlets [28], this new aeration method is expected to reduce the attenuation of the vortex flow along the length of the tube, thereby obtaining better performance.

As shown in Figure 1(b), a 60° arc was removed at the bottom of the inner tube, and the inner and outer tubes were connected by a glass panel to alleviate algae stuck to the wall near the corner. As shown in Figure 1, the origin is located at the axis of the outer tube, the x -axis direction extends from the origin to the top of the outer tube (illuminated area), and the y -axis direction extends from the origin to the right

side of the outer tube. As presented by Sato et al. [20], the parabola reactor (modified from a conventional panel by removing the corners) had an acute angle to alleviate the algae stuck to the wall near the corner. Aeration resulted in the two symmetric rows of pores located on the inner tube producing a parabolic flow, which resulted in high mixing efficiency of the algae, nutrients, and dissolved gas. Similarly, the simulation results of Sato et al. [20] showed that algae, nutrients, and dissolved gases mix best in a parabola. Notably, the parabola proposed by Sato et al. is different from the structure shown in Figure 1(a), and it is not an annular volume. In addition, the cultivation effect of microalgae in the annular space ventilated by the outer circular tube is the best [29], likely because of the annular space of the circular

tube and the radial aeration caused by a series of pores. Therefore, these tangential double tubes seem to be better in microalgal cultivation.

2.2. Theoretical Model and CFD Simulation

2.2.1. The Synergy Principle for Microalgal Cultivation. The synergy between the velocity of the fluid particles in the laminar flow field and the temperature gradient can be calculated using Equation (1). If the direction of the fluid velocity is closer to the direction of the heat flow, the effect of convective heat transfer in the laminar flow will be better [24, 30]:

$$\alpha = \arccos \left[\frac{(\vec{U} \cdot \nabla T)}{(|\vec{U}| \cdot |\nabla T|)} \right]. \quad (1)$$

Considering that the heat flux in the PBR is almost constant, and the direction of the light under the artificial light source is also constant, the synergy between the light field and the flow field can be calculated as Equation (2), where I is the illumination intensity and \vec{U} is the flow velocity. The angle between the velocity field and the light direction indicates the degree of synergy. When the angle α is 90° , the degree of coordination is the worst. When α is 180° or 0° , the degree of synergy is optimal. Here, the absolute value of $|\cos \alpha|$ is used to analyze the synergy. The $|\cos \alpha|$ value is 1, so the degree of synergy is the best.

$$|\cos \alpha| = \left| \frac{(\vec{\text{gard}}I \cdot \vec{U})}{(|\vec{U}| \cdot |\vec{\text{gard}}I|)} \right|. \quad (2)$$

2.2.2. Numerical Mathematics Models. The Eulerian–Eulerian two-flow model and the standard k - ε turbulence model were used to simulate the hydrodynamic characteristics of the flow in the novel PBRs. The slurry of the freshwater green algae *C. vulgaris* displayed Newtonian behavior for biomass concentrations from 0.5 to 60 kg·m⁻³, with an increase in viscosity from 1 to 1.6 m·s⁻¹. The slurry of *Nannochloris* sp. and *Phaeodactylum tricornutum* gave similar results, which are also similar to the physical properties of water. Thus, a two-phase flow of air-water was adopted during the simulation [31]. Moreover, the UDF was used to analyze the $|\cos \alpha|$ curve.

(1) Euler–Euler Two-Phase Model. The continuity equation was calculated as

$$\frac{\partial}{\partial t} (r_q \rho_q) + \nabla (r_q \rho_q \vec{U}_q) = 0 \quad (q = 1, g), \quad (3)$$

where t , r_q , ρ_q , and \vec{U}_q are the time, volume fraction, density, and velocity vector of phase q , respectively.

The momentum equation is provided in

$$\begin{aligned} \frac{\partial}{\partial t} (r_q \rho_q \vec{U}_q) + \nabla [r_q (\rho_q \vec{U}_q \vec{U}_q)] \\ = -r_q \nabla p_q + r_q \rho_q (\vec{F}_q + \vec{F}_{\text{lift},q}) \\ + \nabla \left[r_q \mu_q \left(\nabla \vec{U}_q + (\nabla \vec{U}_q)^T \right) \right] \quad (q = 1, g), \end{aligned} \quad (4)$$

where p_q , \vec{F}_q , $\vec{F}_{\text{lift},q}$, and μ_q are the partial pressure, body force, lift force, and dynamic coefficient of the viscosity of phase q , respectively. The superscript T indicates the turbulent term [32]. Microalgae growth needs constant temperature, so this project could be simplified to the mass transfer of a two-phase flow without heat transfer.

(2) Turbulence Model. The turbulence in the continuous phase (nutrient) is captured using the standard k - ε model. The standard k - ε equation was summarized from the experimental phenomena based on the semiempirical transport equation of the turbulence energy (k) and turbulent dissipation rate (ε) [31].

The transport equation of the turbulence energy was calculated using

$$\begin{aligned} \frac{\partial}{\partial t} (r_q \rho_q k_q) + \nabla [r_q \rho_q k_q \vec{U}_q] = \nabla \left(\frac{r_q \mu_{q,t}}{\sigma_k} \cdot \nabla k_q \right) + r_q G_{k,q} \\ + \prod_{k,g} r_q \rho_q - r_q \rho_q \varepsilon_q. \end{aligned} \quad (5)$$

Next, the transport equation of the turbulent dissipation rate was calculated via

$$\begin{aligned} \frac{\partial}{\partial t} (r_q \rho_q \varepsilon_q) + \nabla [r_q \rho_q \varepsilon_q \vec{U}_q] = \nabla \left(\frac{r_q \mu_{q,t}}{\sigma_\varepsilon} \cdot \nabla \varepsilon_q \right) + \frac{r_q \varepsilon_q}{k_q} (C_{1\varepsilon} G_{k,q}) \\ - \frac{C_{2\varepsilon} r_q \rho_q \varepsilon_q^2}{k_q} + \prod_{\varepsilon,g} r_q \rho_q. \end{aligned} \quad (6)$$

The turbulence kinetic energy, $G_{k,q}$, results from the average velocity gradient. $\Pi_{k,q}$ and $\Pi_{\varepsilon,q}$ describe the impact of the dispersed phase on the continuous phase. $\mu_{q,t}$ is the turbulence viscosity coefficient, and $\mu_{q,t}$ was calculated using

$$\mu_{q,t} = \frac{C_\mu \rho_q k_q^2}{\varepsilon_q}, \quad (7)$$

where $C_{1\varepsilon}$, $C_{2\varepsilon}$, and C_μ are the model constants fixed at 1.44, 1.92, and 0.09, respectively, and the turbulent Prandtl numbers σ_k and σ_ε were set as 1.0 and 1.3, respectively.

2.2.3. Initial Boundary Conditions of Simulation. The inlet conditions were set based on the gas-liquid two-phase velocity inlet. The aeration pores in the tangent structure were

located on the two sides, while the pores in the concentric structure were placed on only one side and canted downwards by 45° ($x < 0$). The aeration rates were set to 0.3, 0.7, and 1 vvm, and these PBRs were initially filled with water. The outlet conditions were set based on the pressure-outlet boundary, and the walls were all set without slip boundary conditions. Meanwhile, the angle of light incidence was simplified as 90° .

The calculation step length was 0.1 s to conduct unsteady calculations, and the convergence residual was 10^{-4} . The three-dimensional meshes of the novel PBRs were designed with the ANSYS ICEM CFD 12.1 software (64 bits). Due to the cylinder structures in the tangent double tube, the computational domain was dispersed through the unstructured grid. The grids of the tangent double tube were 340 thousand, while the grids of the concentric double tube were 870 thousand. The grid independence experiment showed that when the grid number was greater than the previous grid number, the difference in the calculation results was not obvious. Four positions of $x = \pm 40$ mm and $x = \pm 85$ mm were chosen to monitor and analyze the data. The data of $|\cos \alpha|$ were calculated via UDF (User-Defined Function) to assess the extent of the synergy between the light direction and the velocity vector.

2.2.4. Calculation of the Light/Dark Cycle Period. During this simulation, spherical particles are used to represent the algal cells with a number (n) of 20, a diameter (d) of $10 \mu\text{m}$, and a density (ρ) of $1000 \text{ kg}\cdot\text{m}^{-3}$, and their positions are recorded every 0.1 s. The maximum particle tracking time is set to 60 s. The discrete random walk model is used to simulate the motion of the particles in the PBRs [8]. The particles are affected by the drag force (F_D) and pressure gradient force (F_p), which are shown in [33]

$$F_D = \frac{1}{8} \pi \rho_d d^2 C_D |\vec{v}_f - \vec{v}_d| \left(\vec{v}_f - \vec{v}_d \right), \quad (8)$$

$$F_p = \frac{\pi d^3 \rho_{df} d \vec{v}_f}{6 dt}, \quad (9)$$

where \vec{v}_f is the velocity vector and \vec{v}_d is the particle velocity vector. Subscripts p and f denoted the particle and the fluid, respectively. The value of C_D is 0.44, which is the drag coefficient required to compute the drag force.

According to the previous experimental work [25], the light zone of the double-tube PBR is $0.04 < y < 50$ mm, and the dark zone is $-50 \text{ mm} < y < 0.04$ mm. Thus, the boundaries of the light zones and the dark zone were set as lines, where $y = 0$ mm. According to Yang et al. [34] and Ye et al. [8], the time during which the algal cells pass through the light/dark interface twice can be defined as a light/dark cycle period (T) consisting of light time (t_l) and dark time (t_d), and the average light/dark cycle period of the whole population can be calculated via

$$T = \lim_{n \rightarrow \infty} \left(\frac{1}{n} \cdot \sum_{i=1}^n (t_l + t_d) \right). \quad (10)$$

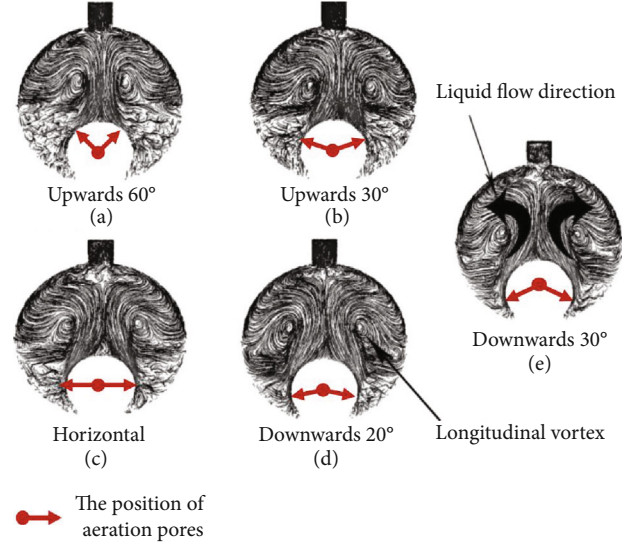


FIGURE 2: Flow fields of the novel tangent double-tube under different aeration directions at $z = 500$ mm.

The light/dark cycle frequency (f) and the light-time ratio (φ) were calculated using

$$f = \frac{1}{T}, \quad (11)$$

$$\varphi = \lim_{n \rightarrow \infty} \left(\frac{1}{n} \cdot \sum_{i=1}^n \left(\frac{t_l}{t_l + t_d} \right) \right). \quad (12)$$

3. Results and Discussion

3.1. Effect of the Aeration Direction on the Performance of the Novel PBRs. In order to optimize the aeration direction, the flow field of the tangent double-tube PBR was simulated, and the values of the radial velocity (V_r) and $|\cos \alpha|$ were calculated. Based on an aeration rate of 0.3 vvm, the cross-sectional flow field characteristics at five different aeration directions ($z = 500$ mm) were analyzed. The path lines of different aeration directions in the cross-section of $z = 500$ mm are shown in Figures 2(a)–2(e), and the longitudinal vortices were generated. Compared to the five parts in Figures 2(a)–2(e), for the structure with upwards and horizontal aeration directions, the flow in the dark area is sparse and disordered, resulting in a poor mixing effect in the dark area. The poor mixing effect in the dark area not only hinders the complete dissolution and mixing of carbon dioxide and nutrients but also causes cell sedimentation [1].

However, in the downwards direction, the flow lines in the dark area are inerratic. Wu et al. [14] proposed using spiral tube PBRs, which can produce strong swirling motions near the wall; ultimately, no vortices were formed in the middle sections of these spiral tube PBRs. Compared to the spiral tube PBRs, the longitudinal vortices produced by the tangent double tube were clearer, especially for the downwards aerations. This phenomenon possible occurs because the main stream flows in the axial direction, and the spiral structure has little effect on the radial disturbance.

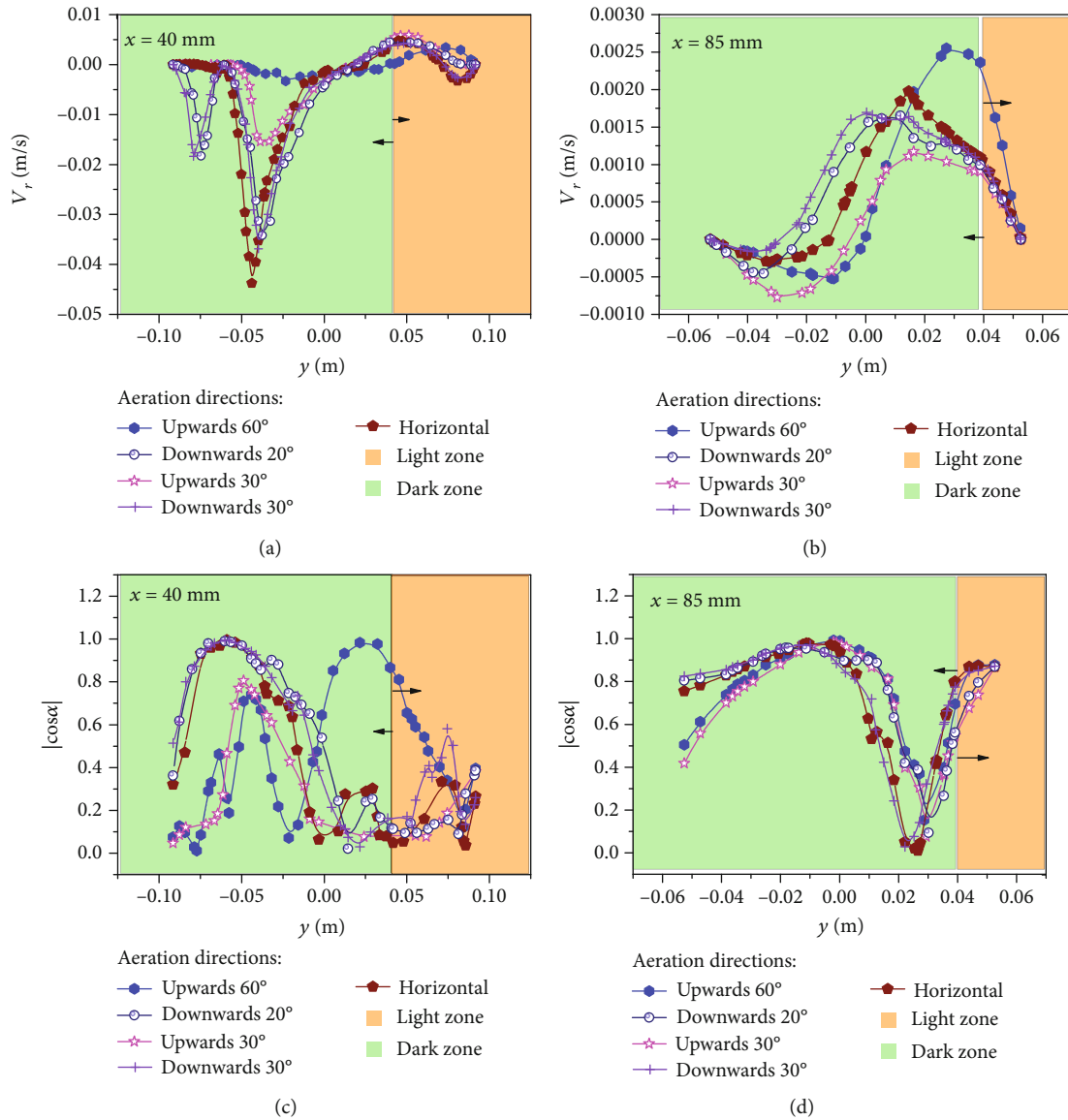


FIGURE 3: The V_r and $|\cos \alpha|$ curves of the line $x = 40$ mm (a, c) and 85 mm (b, d) at aeration flow rates of 0.3 vvm under different aeration directions: upwards 60°, upwards 30°, horizontal, downwards 20°, and downwards 30°.

In addition, the vortices with greater energy and velocity drive the microalgae to shuttle continuously between the light and dark zones, which is beneficial for the photosynthesis of microalgae [1]. The analysis of photocatalytic oxidation reactors in the plate type showed that the generation of multiple longitudinal vortex flows effectively enhanced the mass transfer [24]. Thus, downwards aeration offers more opportunities for microalgae to obtain sufficient mixing in the dark area and was conducive to improving the mass transfer performance and flashing-light effect of the PBRs, thereby creating favorable conditions for the growth of microalgae.

The microalgal growth rate was directly related to the velocity in the PBRs, which determined the mixing performance of the PBRs [35]. Figures 3(a)–3(d) show the relationship between V_r and $|\cos \alpha|$ at $x = 40$ mm (around the aeration pores)/85 mm (around the wall) under different aer-

ation directions. In Figure 3(a), for the upwards and horizontal aerations, the V_r value of the area below the tangent point of the double tube at the $x = 40$ mm line is close to 0 m/s, which indicates that the microalgae cells are likely to experience cell sedimentation here. Creswell note that when the velocity is around 0 m/s, microalgae will experience sedimentation, so the dead zone should be avoided as much as possible ($V_r = 0$ m/s) [6]. At the same time, for the new PBRs with downwards aeration, the velocity gradient distribution was large, and two peaks appeared in the dark area. This phenomenon indicates that downwards aeration can significantly improve the mixing effect. Wang et al. [32] found that the presence of a velocity gradient between the dark and light areas could allow algal cells to more effectively swim between the dark and light areas. For the novel PBRs proposed in this study, the streamline curves of all aeration directions in the

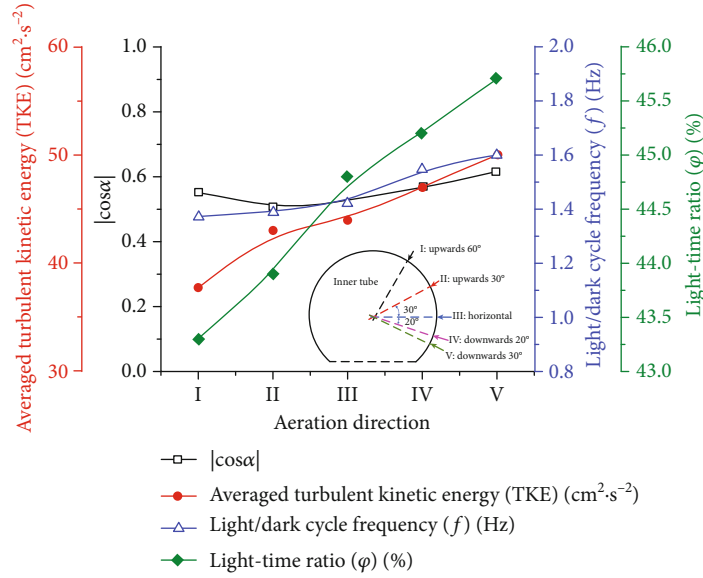


FIGURE 4: The average $|\cos \alpha|$, average turbulent kinetic energy (TKE), light/dark cycle frequency (f), and light-time ratio (ϕ) at aeration flow rates of 0.3 vvm under different aeration directions.

light area are similar and have small values. Further, as can be seen in Figure 2, the flow area in the light area may be larger than that in the dark area. As shown in Figure 3(b), the value of V_r at the line of $x = 85$ mm is one order of magnitude smaller than the value of V_r at the line of $x = 40$ mm. This phenomenon may be due to anchorage dependence, similar to that reported by Haut et al. [36]. For all aeration directions, the enhancement of mass transfer near the wall of the PBRs was very weak, so attention should be paid to the periphery of the wall. In the area of $y < 0.01$ m, the V_r value of the PBR with downwards aeration of 30° was greater than that of the other PBRs. That is to say, aeration oriented 30° downwards achieved flow disturbance in the dark area, thereby reducing the mass boundary layer. In the area of $y > 0.01$ m, the PBR with aeration 60° upwards had the largest V_r value, making it the most suitable for mixing in the light area. However, in the dark area with aeration oriented upwards at 60° , the V_r value was lower. In addition, Gris et al. [37] showed that mixing along the light direction can improve light reception and mass transfer and produce a flashing-light effect, which may be beneficial for microalgal cultivation.

According to Equations (1) and (2), the angle between the velocity field and the light direction represents the degree of coordination. As shown in Figure 3(c), in the area below $y = 0$ m, the $|\cos \alpha|$ value of the upwardly aerated PBRs is similar. However, for the $|\cos \alpha|$ at $y = 0$ m, the PBR with 60° upwards aeration has a higher $|\cos \alpha|$ value than the PBR with 30° upwards aeration. Under horizontal and downwards aeration conditions, the peak of $|\cos \alpha|$ is close to 1 in the dark area, which is greater than the peak value under upwards aeration conditions. However, in the light zone, the value of the $|\cos \alpha|$ of the PBR with 60° upwards aeration is the largest. By comparing the average $|\cos \alpha|$ values in the PBRs of all aeration directions, the following relationship is

obtained: $|\cos \alpha|_{\text{upwards } 30^\circ} < |\cos \alpha|_{\text{upwards } 60^\circ} < |\cos \alpha|_{\text{horizontal}} < |\cos \alpha|_{\text{downwards } 20^\circ} < |\cos \alpha|_{\text{downwards } 30^\circ}$. Therefore, the average $|\cos \alpha|$ value of 0.521 was the largest under 30° downwards aeration. In Figure 3(d), at $x = 85$ mm, the $|\cos \alpha|$ values of the PBRs with aeration structures of 20° and 30° downwards are greater than the $|\cos \alpha|$ values of the other PBRs. At the same time, as shown in Figure 4, under 30° downwards aeration, the average value of $|\cos \alpha|$ at $x = 85$ mm is the largest and reached 0.711. The maximum value is reached when the structure is aerated 30° downwards (0.616).

The TKE value reflects the mixing performance of a PBR. Many studies have shown that the higher the TKE is, the better the mixing performance of the PBR [10, 38, 39]. Figure 4 shows a relationship curve of the averaged turbulent kinetic energy (TKE) in different aeration directions. In Figure 4, the TKE of 30° downwards aeration is the greatest, increasing by approximately 35% to $50 \text{ cm}^2\cdot\text{s}^{-2}$ compared to the TKE of 60° upwards aeration [10]. A higher TKE value indicates more effective mixing of the mass, which is associated with a more suitable environmental for microalgal growth [35]. In Figure 2, it can be seen that the inner tube with aeration can form multiple longitudinal vortices in the PBRs. The 30° downwards aeration structure can achieve a notably better mixing process, thereby greatly increasing the radial velocity of the microalgal solution and the TKE value.

In addition, as shown in Figure 4, when the aeration rate is 0.3 vvm, the light/dark cycle frequency and light-time ratio increase as the aeration direction rotates clockwise from top to bottom. The maximum light/dark cycle frequency and time ratios are achieved at 1.6 Hz and 46%, respectively, under the structure with 30° downwards aeration. The minimum light/dark cycle frequency and light-time ratio are achieved at 1.45 Hz and 44%, respectively, under the structure with 60° upwards aeration. In Figure 2, the structure

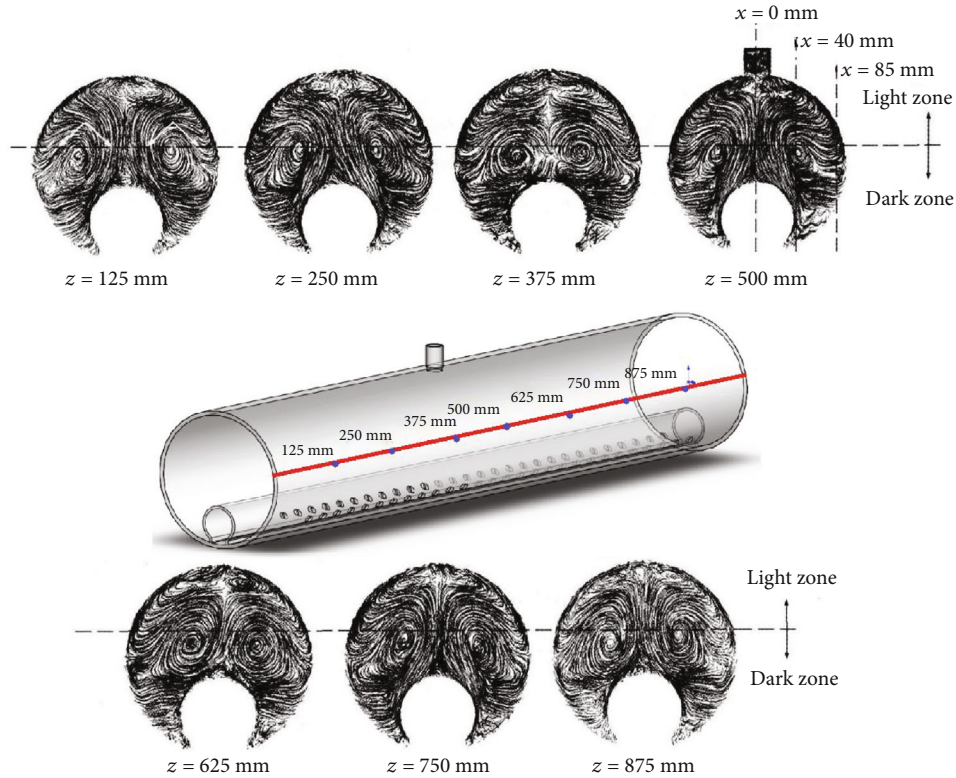


FIGURE 5: The flow characteristics of each section in the axial direction of the novel PBR under 30° downwards aeration.

with 60° upwards aeration provides less disturbance to the radial flow of microalgae solution than the structure with 30° downwards aeration. The structure with upwards aeration produces cell sedimentation in the lower dead zone, which results in disordered flow in the dark zone and insufficient radial velocity to push the microalgae cells back to the light zone. Meanwhile, the structure with upwards aeration produces a current in the longitudinal vortices of the light area. Although this phenomenon can increase the time the algal cells stay in the light area, it does not improve the flashing-light effect. According to previous research [8], increasing the flashing-light effect can effectively increase the photosynthesis of the algal cells. The structure with 30° downwards aeration enabled the longitudinal vortices to be located at the boundary between the light and dark zones, thus providing sufficient kinetic energy for the algal cells to swim between the light and dark zones. These phenomena provide a reasonable explanation for the optimal light/dark cycle frequency and the optimal light-time ratio between the light and dark areas caused by the 30° downwards aeration structure shown in Figure 4. In other words, adjusting the direction of the inner tube aeration can enhance the flashing-light effect of microalgae cells and can enhance the dissolution and diffusion of CO₂ and improve the mixing of the nutrients. According to the above comparisons, the performance of the PBR can be comprehensively evaluated based on the average $|\cos \alpha|$, the average turbulent kinetic energy (TKE), the light/dark cycle frequency (f), and the light-time ratio (φ). The 30° downwards aeration structure optimized the synergy and achieved the greatest mixing

along the light direction, thereby improving the flashing-light effect and mass transfer and helping create the best microenvironment for algal cells.

Figure 5 presents the flow characteristics of each section in the axial direction of the novel PBR based on CFD. When the downwards aeration direction is 30°, longitudinal vortices are generated in each section of the PBR, and small vortices are present in the light zone. The main longitudinal vortices, with high energy and velocity, not only prevent the microalgae from sinking but also push the microalgae cells between the light and dark areas. In addition, small vortices in the light region at the top of the PBR facilitate full dissolution and gas- (CO₂-) liquid (nutrient) mixing. Compared with the work of Cheng et al. [1] on plate PBRs, the main vortices generated here by the jet flow in the plate PBRs are beneficial to gas-liquid mixing, while the secondary vortices push the microalgae between the light and dark regions. However, these vortices have similar functions that improve mass transfer performance and the flashing-light effect of the PBR and promote the growth of microalgae. Taking the cross-section of $z = 250$ mm as an example, the vortex structure is symmetrically distributed on the left and right sides, and the streamline distribution in the dark zone shows that the gas-liquid two-phase flow significantly improved the mixing degree of the dark zone and was conducive to the swimming of algal cells toward the light zone. With constant CO₂ gas in the outer tube, the energy of the main vortex is constantly replenished to maintain and reciprocate the vortex motion. Although some sections at 125 mm, 375 mm, 625 mm, and 875 mm do not have aeration pores,

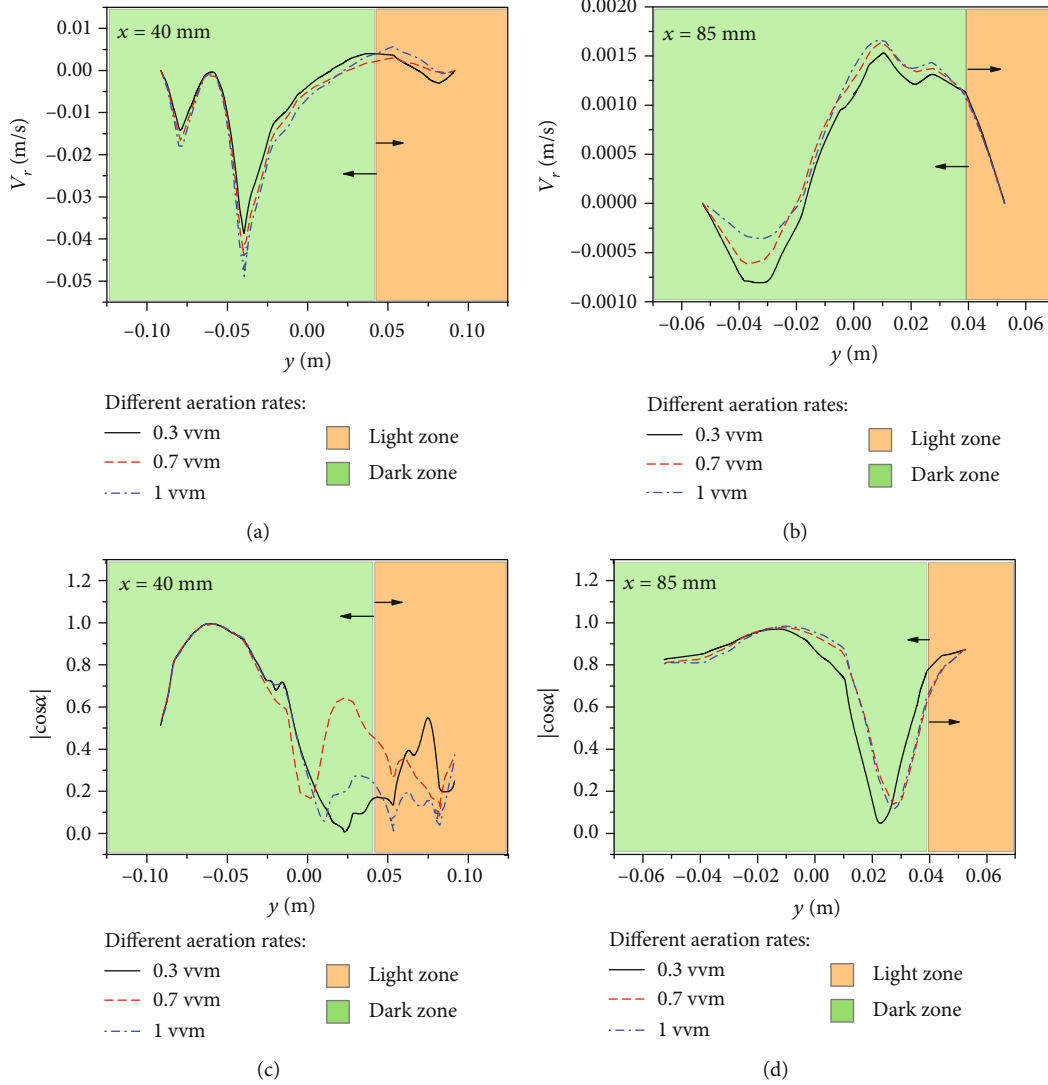


FIGURE 6: The V_r and $|\cos \alpha|$ curves of the lines $x = 40$ mm (a, c) and 85 mm (b, d) at aeration flow rates of 0.3 , 0.7 , and 1.0 vvm based on 30° downwards aeration.

longitudinal vortices are still formed due to the flow around the surrounding aeration.

3.2. Effect of Aeration Rates on the Performance of the Novel PBRs. According to the above results, 30° downwards aeration was most beneficial to optimize the $|\cos \alpha|$ and achieve higher mixing in the dark zones. Next, based on 30° downwards aeration, three aeration rates of 0.3 vvm, 0.7 vvm, and 1 vvm were compared to obtain the optimal aeration rate. Figure 6 shows the curves of V_r and $|\cos \alpha|$ for $x = 40$ mm and $x = 85$ mm under different aeration rates.

In Figure 6(a), the V_r at $x = 40$ mm slightly increases as the aeration rate increases. The peaks of V_r for 0.3 vvm, 0.7 vvm, and 1 vvm are 0.0393 m/s, 0.045 m/s, and 0.049 m/s, respectively. As shown in Figure 6(b), the V_r at $x = 85$ mm under the three aeration rates is one order smaller than that at $x = 40$ mm. Meanwhile, the V_r increases as the aeration rate increases at $y < -0.01$ m, while in other areas, the V_r value remains almost the same. As shown in

Figure 6(c), at $x = 40$ mm, the three curves of $|\cos \alpha|$ almost coincide, and the peak value is able to reach 0.996 at the bottom of the PBR. At the top of the dark area ($0 < y < 0.04$ m), under an aeration rate of 0.7 vvm, the synergistic effect is higher than that under other aeration rates and reaches a peak of 0.646 . In the light zones, the $|\cos \alpha|$ values are low. The value of $|\cos \alpha|$ under 0.3 vvm is the largest, while the value of $|\cos \alpha|$ under 1 vvm is the smallest. Meanwhile, the average $|\cos \alpha|$ value is the largest (0.603) at 0.7 vvm. In Figure 6(d), in the dark zones at $y < 0.03$ m, all the values of $|\cos \alpha|$ are close to 1 . This gives the following relation: $|\cos \alpha|_{0.3} < |\cos \alpha|_{1.0} \approx |\cos \alpha|_{0.7}$.

In Figure 6, the maximum value of the cross-sectional average $|\cos \alpha|$ is the largest under 0.7 vvm. Finally, as shown in Figure 7, an aeration rate of 0.7 vvm is more conducive to synergy between the velocity field and the direction of light. The radial velocities at different aeration rates are not significantly different. The average $|\cos \alpha|$ value for 0.7 vvm ($|\cos \alpha|_{0.7}$) is 0.69 , which means that an aeration rate

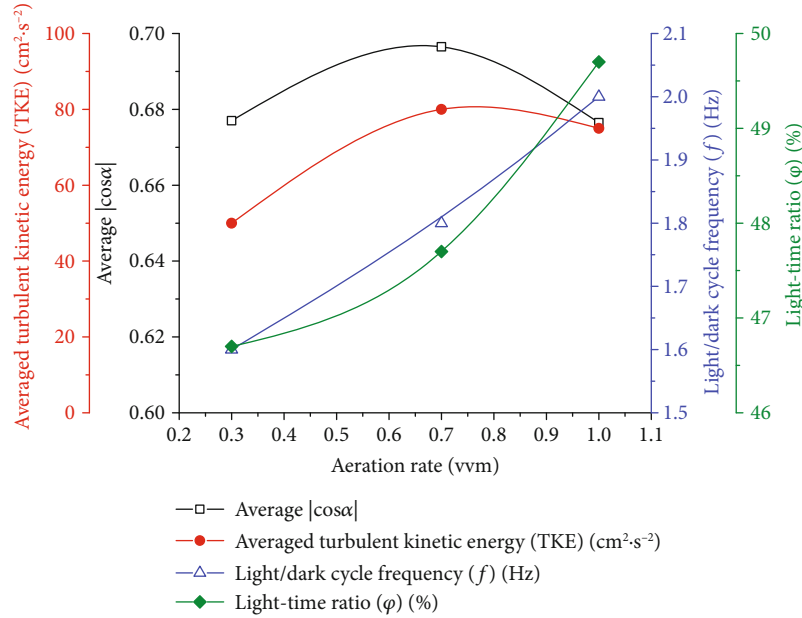


FIGURE 7: The average $|\cos \alpha|$, average turbulent kinetic energy (TKE), light/dark cycle frequency (f), and light-time ratio (ϕ) at different aeration flow rates of 0.3 vvm, 0.7 vvm, and 1 vvm based on 30° downwards aeration.

of 0.7 vvm is more conducive to synergy, as well as most conducive to mass transfer and light reception.

Figure 7 shows the effect of different aeration rates on the light/dark cycle frequency and light-time ratio of microalgae cells under the structure with downwards aeration of 30° . In algal cultivation, the flashing-light effect reflects the periodic exposure of algae to light and dark areas or rapid movement between light and dark areas. At an aeration rate of 0.3 vvm, the minimum light/dark cycle frequency and light-time rate were obtained as 1.65 Hz and 47.1%, respectively. When the aeration rate was 1.0 vvm, the maximum light/dark cycle frequency and light-time rate were 2.1 Hz and 49.1%, respectively. The structure with 30° downwards aeration enables the longitudinal vortices to be located at the boundary between the light and dark zones, thereby providing sufficient kinetic energy for algal cells to swim between the light and dark zones. When the aeration rate increased from 0.3 to 1.0 vvm, sufficient kinetic energy was given to the fluid; moreover, the presence of vortices and the enhancement of radial flow improved the mixing of the cell between the light and dark zones, thereby shortening the L/D cycle of microalgae cells. In addition, as shown in Figure 7, as the aeration volume increases, the TKE of the tangential PBR achieves its maximum value. When the aeration rate increases from 0.7 to 1.0 vvm, the value of TKE increases from 51 to $80 \text{ cm}^2\cdot\text{s}^{-2}$. The vortex was ultimately the main disturbing force in the PBR. With an increase in the aeration rate, more kinetic energy was injected into the culture solution, which promoted the formation of a vortex [35, 39]. However, when the aeration rate was too high, the existence of a large number of bubbles prevented mixing of the gas-liquid phase to some extent. This phenomenon is similar to the study of jet aerated PBR by Cheng et al. [1]. Thus, combined with the degree of synergy, excessive gas content in the medium is not always

conductive to the mixing of the solution along the light direction [8]. Therefore, when the aeration rate increased from 0.7 to 1.0 vvm, the values of TKE and $|\cos \alpha|$ decreased by 4% and 6%, respectively. That is, when the aeration rate was 0.7 vvm, the TKE value was higher, and the mixing performance of the PBR was better. In short, although the light/dark cycle frequency (f) and the light-time ratio (ϕ) were best when the aeration rate was 1 vvm, the mixing performance was inferior to that at 0.7 vvm. Moreover, when the aeration rate was 0.7 vvm, the flashing-light effect was already satisfactory. Therefore, an aeration rate of 0.7 vvm is an effective choice for this novel PBR.

According to the above comparisons, the performance of the PBR can be comprehensively evaluated based on the average $|\cos \alpha|$, average turbulent kinetic energy (TKE), light/dark cycle frequency (f), and light-time ratio (ϕ). A downwards aeration direction of 30° and an aeration rate of 0.7 vvm were the most conducive to reducing the dead zone and improving the light/dark cycle frequency, which improved the flashing-light effect and mass transfer and helped create a more suitable microenvironment for algal cells.

3.3. Performance Comparison of Tangent Double-Tube PBRs with Concentric Double-Tube PBRs. To better understand the advantages of tangent double-tube PBRs in this work, These PBRs were compared with the simulation result of the concentric double-tube PBR presented in Figure 1(a). For the concentric double-tube PBRs, the inner and outer tubes are coaxial, and aeration is accomplished via one row of pores located on the inner-tube [25]. The flow in the tangent double-tube PBR is symmetrical. However, the flow field is distributed differently on both sides of the concentric PBR because the aeration is located on only one side ($x < 0$).

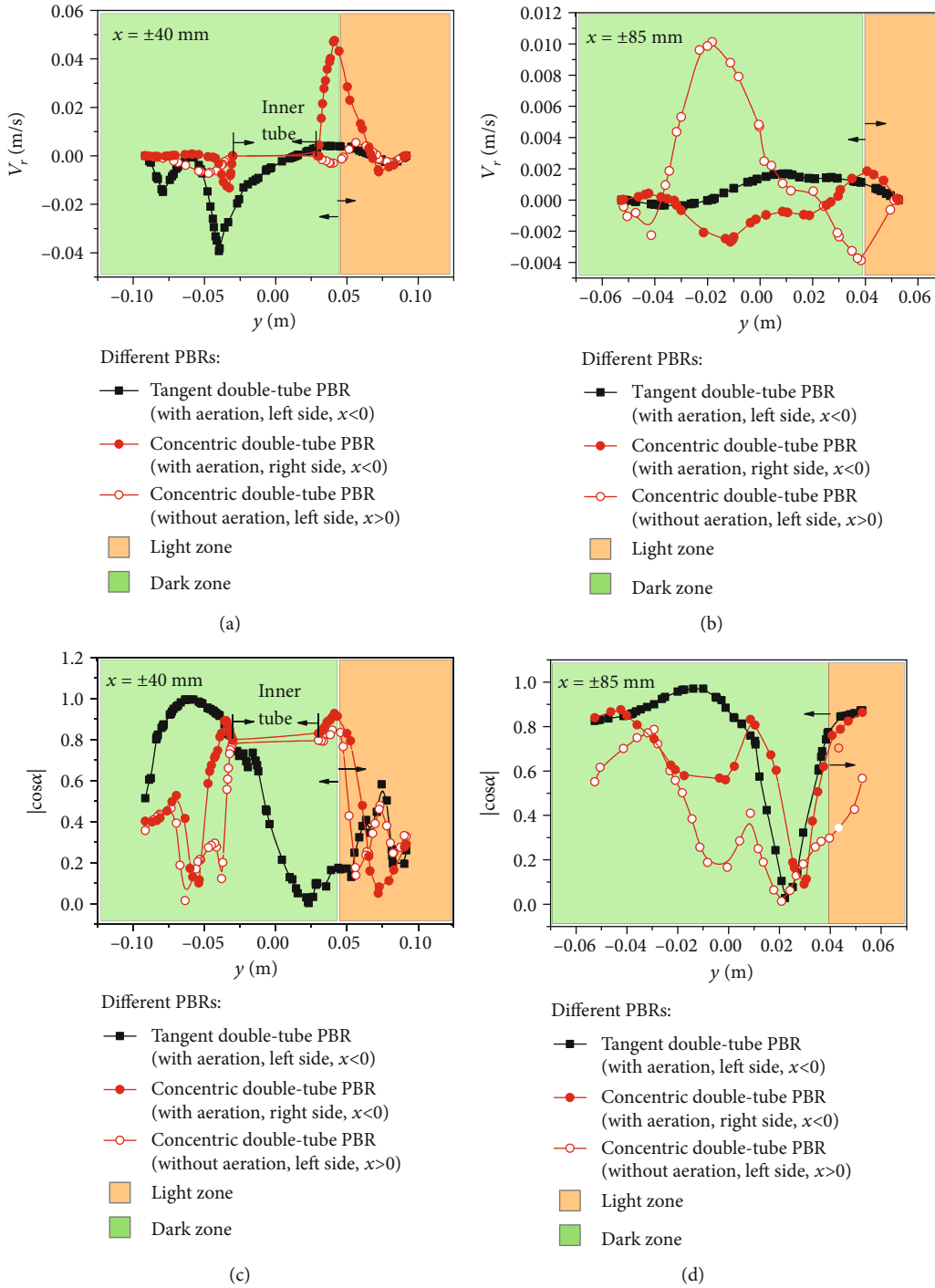


FIGURE 8: The V_r and $|\cos \alpha|$ curves of the lines $x = \pm 40$ mm and $x = \pm 85$ mm in the tangent and concentric double-tube PBRs.

Therefore, during the analysis, four lines of $x = \pm 40$ mm and $x = \pm 85$ mm from the concentric PBR were selected. The curves of V_r and $|\cos \alpha|$ in the two PBRs are presented in Figures 8(a)–8(d).

As shown in Figure 8(a), in the dark area, the V_r value of the tangent double-tube PBR is higher with two peak velocities, while at $x = 40$ mm, the V_r value of the concentric double-tube PBR is very low. However, in the light zones of $x = -40$ mm, a peak appeared in the V_r of the concentric

double-tube PBR, reaching its maximum ($0.047 \text{ m}\cdot\text{s}^{-1}$). These data demonstrate that the comprehensive mixing effect was better in the tangent double-tube PBR. As shown in Figure 8(b), the V_r for the line at $x = 85$ mm in the two PBRs was one order lower than that for the line at $x = 40$ mm. However, the V_r of the concentric structure was larger near the wall, which indicates that enhancing the flow disturbance near the wall is an important consideration for improving the tangent double-tube PBR. This phenomenon seems to be due

TABLE 1: Comparison of performance of the different tubular photobioreactors (PBRs).

PBR characteristics	$ \cos \alpha $	TKE ($\text{cm}^2 \cdot \text{s}^{-2}$)	f (Hz)	φ (%)	Reference
Tangent double-tube PBRs	0.69	80	1.8	47.8	This work
Concentric double-tube PBRs	0.5	54	1.01	35.1	This work
Serial lantern-shaped draft tube PBRs	—	26.6	0.476	32.9	[8]
Novel static mixers inside the tubular PBR	—	23	—	—	[10]
Successive and independent arrangement of Kenics mixer units in tubular PBRs	—	—	0.59-0.64	—	[11]
Tubular PBRs with spiral ribs	—	—	1.0-1.4 Hz	—	[13]
Twisted tubular photobioreactor	—	—	0.9-4.0	—	[16]
A draft-tube airlift PBR for <i>Botryococcus braunii</i>	—	32-74	0.7 ± 0.02	—	[38]

“—” means “not calculated in the literature”.

to the dispersion of power caused by the aeration on both sides. A comparison of the radial velocity showed that the tangent double-tube PBR offers better mixing performance, but the tangent double-tube PBR provides weaker interference on the boundary layer than the concentric double-tube PBR.

As shown in Figure 8(c), in the dark zones of $x = \pm 40$ mm, the $|\cos \alpha|$ value of the tangent double-tube PBR is larger than that of the concentric double-tube PBR, which shows that the synergy of the tangent double-tube PBR was better in the dark zones. However, in the light zones of $0.04 \text{ m} < y < 0.06 \text{ m}$, the $|\cos \alpha|$ value of the concentric double-tube PBR is higher, while in the light zones of $y > 0.06 \text{ m}$, the $|\cos \alpha|$ of the concentric double-tube PBR is lower. This phenomenon might be due to wall interference from the inner tube. In the light zones of $0.04 \text{ m} < y < 0.06 \text{ m}$, the flow field of the concentric double-tube PBR was disturbed by the inner tube wall surface, and the fluid velocity near the boundary layer was reduced to make it suitable for the growth of microalgae. Compared to the tangent double-tube PBR at the same position, the flow velocity of the tangent double-tube PBR at $0.04 \text{ m} < y < 0.06 \text{ m}$ is higher than that of the concentric PBR due to the lack of inner wall interference. Therefore, the $|\cos \alpha|$ value of the concentric double-tube PBR was temporarily higher than the $|\cos \alpha|$ value of the tangent double-tube PBR. When the fluid in the concentric PBR was far away from the surface of the inner tube wall, the boundary layer effect disappeared, as the excessive fluid velocity was no longer a component suitable for the environment. Moreover, the $|\cos \alpha|$ value of the concentric double-tube PBR decreased.

As shown in Figure 8(d), on the line at $x = \pm 85$ mm, in most areas, the $|\cos \alpha|$ value of the tangent double-tube PBR is greater than the $|\cos \alpha|$ value of the concentric double-tube PBR. For the range of $0.005 \text{ m} < y < 0.028 \text{ m}$ on the line at $x = -85$ mm, the $|\cos \alpha|$ value of the concentric double-tube PBR was slightly larger. In Table 1, the average $|\cos \alpha|$ value of the tangent double-tube PBR is 0.649, which is greater than the average $|\cos \alpha|$ value (0.508) of the concentric double-tube PBR at 0.3 vvm. Therefore, the synergy extent of the tangent double-tube PBR was better and more beneficial to mass transfer. Through the comparisons of V_r and $|\cos \alpha|$ above, the flow disturbance of the dark zones in the tangent double-tube PBR and the synergy between the light direction and velocity field were both shown to be

better, but the flow disturbance near the wall is the key position for optimizing the tangential double-tube PBR structure.

In this work, concentric double-tube PBRs and tangent double-tube PBRs were used as the simulation objects, and the flow characteristics and flashing-light effect of the tangent double-tube PBRs and the concentric double-tube PBRs were investigated using the hydrodynamics method. It is well known that a variety of tube PBRs have been designed for microalgae cultures [1] and that experimental characterization of the flow field in a PBR is difficult and expensive [8]. Therefore, computational fluid dynamics (CFD) is a significant, popular, and reliable method for measuring the internal performance of a tube PBR [16].

In our previous work [25], a concentric double-tube structure was manufactured and studied experimentally in the laboratory. The potential of use of a concentric double-tube PBR for microalgae cultures was verified through microalgae culture experiments. In particular, the concentric double-tube PBR was more amenable to the growth of microalgae. The experimental data showed that the biomass yield of the concentric double-tube PBR increased by at least 43.6% to 107.4% compared to the common tubular PBR. At the same time, field synergy theory combined with the concentric double-tube PBR simulation mode was applied to the design of tubular microalgae PBRs. The light and velocity gradients for the cross-section of the synergy degree were higher on average ($|\cos \alpha| = 0.5$) for the concentric double-tube PBR experimental results (which provides a theoretical explanation), and the simulation results show that, for PBRs, a TKE value up to $54 \text{ cm}^2 \cdot \text{s}^{-2}$ is superior to other values. During the 15-day culture process, the pH value of the concentric double-tube PBR changed from 7.5 to 9.0, while that of the common PBR changed from 7.5 to 8.8. The dissolved oxygen concentration of the PBR fluctuated between 6.0 and $7.0 \text{ mg} \cdot \text{L}^{-1}$, while that of the common PBR fluctuated between 6.6 and $10.2 \text{ mg} \cdot \text{L}^{-1}$. These experimental and simulated data show that the mixing performance of the concentric double-tube PBR was obviously better than that of the common PBR. In other words, the experimental results verify the reliability of the two-tube model. In this paper, the simulated models of the tangent double-tube PBR were developed based on a concentric double-tube PBR model and a physical model with high similarity. The simulation

results show that, compared to the concentric double-tube PBR, the light/dark cycle frequency and light time of the tangent double-tube PBR increased by 78.2% and 36.2% to 1.8 Hz and 47.8%, respectively, and the TKE was enhanced by 48.1%, from 54 to 80 $\text{cm}^2\cdot\text{s}^{-2}$. The average synergy of the light and velocity gradients on the cross-section increased by 38% to 0.69. In general, the models of the tangent double-tube PBR and the concentric double-tube PBR established in this work are reliable, and the tangent double-tube PBR has greater potential than the concentric double-tube PBR. In other words, the tangent double-tube PBR is a more attractive and functional choice for microalgae cultures.

3.4. Performance Comparison with Other Tubular PBRs. As shown in Table 1, we compared the PBR proposed in this paper to other novel tubular PBRs proposed in recent studies. The TKE value is a key parameter for the mixing performance of a PBR. Compared to the concentric double-tube PBR, the TKE value of the tangent double-tube PBR increased by nearly 48.1%. Xu et al. [38] proposed a draft-tube airlift PBR for *Botryococcus braunii*, whose TKE value increased from 32 to 74 $\text{cm}^2\cdot\text{s}^{-2}$ by optimizing its internal structure. Azizi et al. [10] also found that after a static mixer was embedded in the tubular PBR, the mixing conditions and hydrodynamic performance in the PBR were better than those of a traditional PBR, and the TKE value was able to reach 23 $\text{cm}^2\cdot\text{s}^{-2}$, which is basically consistent with the tubular PBR research results of Ye et al. [8] using a four-cell Kenics mixer and a one-cell Kenics mixer (TKE = 26.6 $\text{cm}^2\cdot\text{s}^{-2}$). Moreover, these studies were mainly designed to adjust the physical locations to improve the mixing performance of a culture solution. The novel PBRs proposed in this work adopted a tangential inner tube aeration structure, which generated symmetrical vertical vortices between the light and dark zones of the PBR. These novel structures promoted the mixing performance of the solution and significantly increased the TKE value (up to 80 $\text{cm}^2\cdot\text{s}^{-2}$). The research focus of this study was similar to that of Cheng et al. [1], who improved mixing performance by using jet flow in a plate PBR, increasing the TKE by about 35.5%. In this work, compared to adding a static mixer or a draft tube, using an adjustable aeration method more effectively improved the mixing performance (or TKE value) of the culture medium. In other words, the tangent double-tube PBR offered better mixing performance and was more suitable for microalgae growth.

As shown in Table 1, the performance of the tangent double-tube PBR is superior to that of the concentric double-tube PBR in terms of its light/dark cycle frequency and light-time rate. In particular, the f of the tangent tube PBR is 1.8 times higher than that of the concentric double-tube PBR. This is mainly because the tangent double-tube PBR generated vortices between the light zone and the dark zone, which reduced the dead zone of the PBR and allowed the microalgae cells to effectively swim between the light zone and the dark zone. According to previous studies, the light/dark cycle frequency and light-

time rate of tubular PBR have been widely explored [8, 13, 16]. Ye et al. [8] proposed a serial lantern-shaped draft tube PBR that could effectively improve the flashing-light effect of PBRs. Similar to the study by Azizi et al. [10], adding static mixers, such as Kenics mixer units, can also improve the mixing performance of a PBR. However, these methods did not generate obvious vortices in the culture medium, and improvement of the light/dark cycle frequency and light-time rate was limited. Gómez-Pérez et al. [16] developed a spiral PBR that could generate an obvious eddy current in the culture solution, which significantly improved the light/dark cycle frequency of the PBR, reaching as high as 0.9 Hz, similar to the concentric double-tube PBR. Next, Lei et al. [13] designed a novel tubular PBR with spiral ribs with a maximum light-dark cycle of 1.4 Hz, which is higher than that proposed by Gómez-Pérez et al. [16] and the concentric double-tube PBR but lower than the tangent double-tube PBR (1.8 Hz). According to Cheng et al. [1, 8], a suitable velocity flow field and mixing ability can provide an appropriate growth microenvironment for microalgae. Uniform velocity distribution can facilitate the uniform distribution of microalgae in the PBR, thereby minimizing aggregation or precipitation and promoting the penetration and uniform distribution of light, which will promote the growth of microalgae. At the same time, the complex vortex flow field in the tangential double-tube PBR, especially the velocity component along the light penetration direction, caused the microalgae to move back and forth between the light and dark zone solutions, an activity more conducive to photosynthesis (see Figure 2).

According to our previous studies [25], the concentric double-tube PBR formed large dead zones in the dark zone, causing the microalgae cells to remain in the dark zone for a long period of time. Therefore, in a concentric double-tube PBR, it is difficult for these microalgae cells to swim upwards to obtain light. Consequently, the light/dark cycle frequency and light-time ratio of the tangent double-tube PBR were much higher than those of the concentric double-tube PBR. The existing experiments showed that under some cultivation conditions, the volume production rate of *Chlorella vulgaris* in the concentric double tube increased by 137.50% compared to that in the tubular PBR [25]. When the aeration direction was located 30° downwards and the aeration rate was 0.7 vvm, compared to the concentric double-tube PBR, the tangent double-tube PBR of the light/dark cycle frequency and light-time ratio increased by 78.2% and 36.2% to 1.8 Hz and 47.8%, respectively. The cross-section of the synergy with the mean light and the velocity gradient increased by 38% to 0.69. In general, the tangent double-tube PBR was more beneficial to enhancing the mass transfer and improving the photosynthetic efficiency of algal cells; it will thus have greater potential for large-scale cultivation in a culture experiment. In our follow-up research, we will build an experimental model of a tangential double-tube PBR at laboratory scale and further discuss its performance. The simulation work in this paper provides theoretical justification for future experiments.

4. Conclusions

In this study, a novel tangent double-tube PBR with radial aeration pores along the tube length was proposed based on field synergy theory and simulated using CFD simulation technology. The simulation results are as follows:

The tangential inner tube aeration structure generated symmetrical vertical vortices between the light and dark areas in the PBR, and the novel PBR significantly enhanced the mass transfer, strengthened the flashing-light effect, and reduced the dead zone. Compared to the concentric double-tube PBR, the light/dark cycle frequency and light-time ratio of the tangent double-tube PBR increased by 78.2% and 36.2% to 1.8 Hz and 47.8%, respectively

A downwards aeration direction of 30° and an aeration rate of 0.7 vvm were the most conducive to enhancing the mixing performance of the novel PBR, and the average turbulent kinetic energy (TKE) was enhanced by 48.1%, from 54 to 80 cm²·s⁻²

Field synergy theory can be applied to the design of tubular microalgae PBRs. Compared to the concentric double-tube PBR, the average synergy of the light and velocity gradients across the cross-section increased by 38% to 0.69 in the tangent double-tube PBR. This novel design can provide a more suitable microenvironment for microalgal cultivation and holds promise for bioresource recovery and improving the yield of microalgae

Nomenclature

Abbreviations

L/D: Light and dark cycle period
TKE: Turbulent kinetic energy (cm²·s⁻²)
PBR: Photobioreactor.

Subscripts

k : The turbulence energy item
 q : The q phase
 T : The turbulent term
 ε : Turbulent dissipation item.

Symbols

C : Model constants
 d : The diameter of solid particle (μm)
 \vec{F} : The body force (kg·m⁻²·s⁻²)
 F_p : Pressure gradient force (kg·m⁻²·s⁻²)
 G : The turbulence energy resulted from the average velocity gradient (cm²·s⁻²)
 p : Partial pressure (Pa)
 t : Time (s)
 T : Light/dark cycle time (s)
 \vec{U} : The flow velocity vector (m·s⁻¹)
 \vec{v}_d : The particle velocity vector (m·s⁻¹)
 ρ_q : The density of liquid (kg·m⁻³)
 r : Volume fraction
 μ_t : The turbulence viscosity coefficient (kg·m⁻²·s⁻²)

σ : The turbulent Prandtl numbers
 ρ_d : The density of solid particle (kg·m⁻³)
 V_r : the radial velocity of fluid (m·s⁻¹)
 C_D : A drag coefficient required to compute the drag force
 f : The light/dark cycle frequency (Hz)
 \vec{F}_{lift} : The lift force (kg·m⁻²·s⁻²)
 F_D : Drag force (kg·m⁻²·s⁻²)
 n : Algal cells with a number
 t_l : Light time (s)
 t_d : Dark time (s)
 ∇T : Temperature gradient (K)
 \vec{v}_f : The velocity vector (m·s⁻¹)
 $|\cos\alpha|$: Synergy extent
 φ : The light-time ratio
 ρ : Density (kg·m⁻³)
 II : The impact of dispersed phase on the continuous phase
 α : The angle between the direction of flow velocity and the direction of heat flux.

Data Availability

The analysis data used to support the findings of this study are included within the article.

Conflicts of Interest

The authors declare that they have no competing interests.

Authors' Contributions

Xuyang Cui was responsible for the data curation, original draft preparation, visualization, and reviewing and editing; Junhong Yang was responsible for the conceptualization, methodology, and supervision; Yuanzheng Feng was responsible for the software; and Wenwen Zhang was responsible for the visualization. All authors read and approved the final manuscript.

Acknowledgments

The authors wish to thank the State Key Laboratory of Engines of Tianjin University and Key Laboratory of Efficient Utilization of Low and Medium Grade Energy, MOE, for financial support. This work is supported by the Tianjin Talent Development Special Support Program for High-Level Innovation and Entrepreneurship team. This research was funded by the Natural Science Foundation of Tianjin in China (Grant No. 13JCYBJC19000).

References

- [1] J. Cheng, X. Lai, Q. Ye, W. Guo, and J. Zhou, "Numerical simulation on optimizing flow field and flashing-light effect in jet-aerated tangential swirling-flow plate photobioreactor to improve microalgal growth," *Chemical Engineering Science*, vol. 215, 2020.
- [2] C. Zhu, X. Zhai, J. Jia et al., "Seawater desalination concentrate for cultivation of *Dunaliella salina* with floating

- photobioreactor to produce β -carotene," *Algal Research*, vol. 35, pp. 319–324, 2018.
- [3] C. Zhu, R. Zhang, L. Cheng, and Z. Chi, "A recycling culture of *Neochloris oleoabundans* in a bicarbonate-based integrated carbon capture and algae production system with harvesting by auto-flocculation," *Biotechnology for Biofuels*, vol. 11, no. 1, 2018.
- [4] A. Valente, D. Iribarren, and J. Dufour, "How do methodological choices affect the carbon footprint of microalgal biodiesel? A harmonised life cycle assessment," *Journal of Cleaner Production*, vol. 207, pp. 560–568, 2019.
- [5] G. Sibi, V. Shetty, and K. Mokashi, "Enhanced lipid productivity approaches in microalgae as an alternate for fossil fuels - a review," *Journal of the Energy Institute*, vol. 89, no. 3, pp. 330–334, 2016.
- [6] L. Creswell, *Phytoplankton Culture for Aquaculture Feed*, Southern Regional Aquaculture Center, 2010.
- [7] U. Suparmaniam, M. K. Lam, Y. Uemura, J. W. Lim, K. T. Lee, and S. H. Shuit, "Insights into the microalgal cultivation technology and harvesting process for biofuel production: a review," *Renewable and Sustainable Energy Reviews*, vol. 115, article 109361, 2019.
- [8] Q. Ye, J. Cheng, W. Guo, J. Xu, H. Li, and J. Zhou, "Numerical simulation on promoting light/dark cycle frequency to improve microalgae growth in photobioreactor with serial lantern-shaped draft tube," *Bioresource Technology*, vol. 266, pp. 89–96, 2018.
- [9] Q. Liao, L. Li, R. Chen, and X. Zhu, "A novel photobioreactor generating the light/dark cycle to improve microalgal cultivation," *Bioresource Technology*, vol. 161, pp. 186–191, 2014.
- [10] K. Azizi, M. K. Moraveji, H. Hassanzadeh, and H. A. Najafabadi, "Consideration of inclined mixers embedded inside a photobioreactor for microalgal cultivation using computational fluid dynamic and particle image velocimetry measurement," *Journal of Cleaner Production*, vol. 195, pp. 753–764, 2018.
- [11] C. Qin and J. Wu, "Influence of successive and independent arrangement of Kenics mixer units on light/dark cycle and energy consumption in a tubular microalgal photobioreactor," *Algal Research*, vol. 37, pp. 17–29, 2019.
- [12] C. A. Gómez-Pérez, J. Espinosa, L. C. M. Ruiz, and A. J. B. van Boxtel, "CFD simulation for reduced energy costs in tubular photobioreactors using wall turbulence promoters," *Algal Research*, vol. 12, pp. 1–9, 2015.
- [13] Y. Lei, J. Wang, and J. Wu, "Optimization of Tubular Microalgal Photobioreactors with Spiral Ribs under Single-Sided and Double-Sided Illuminations," *Processes*, vol. 7, no. 9, 2019.
- [14] L. B. Wu, Z. Li, and Y. Z. Song, "Numerical investigation of flow characteristics and irradiance history in a novel photobioreactor," *African Journal of Biotechnology*, vol. 8, no. 18, pp. 4672–4679, 2009.
- [15] I. Perner-Nochta and C. Posten, "Simulations of light intensity variation in photobioreactors," *Journal of Biotechnology*, vol. 131, no. 3, pp. 276–285, 2007.
- [16] C. A. Gómez-Pérez, J. J. E. Oviedo, L. C. M. Ruiz, and A. J. B. van Boxtel, "Twisted tubular photobioreactor fluid dynamics evaluation for energy consumption minimization," *Algal Research*, vol. 27, pp. 65–72, 2017.
- [17] Z. Su, R. Kang, S. Shi, W. Cong, and Z. Cai, "Study on the destabilization mixing in the flat plate photobioreactor by means of CFD," *Biomass and Bioenergy*, vol. 34, no. 12, pp. 1879–1884, 2010.
- [18] J. Pruvost, L. Pottier, and J. Legrand, "Numerical investigation of hydrodynamic and mixing conditions in a torus photobioreactor," *Chemical Engineering Science*, vol. 61, no. 14, pp. 4476–4489, 2006.
- [19] J. Pruvost, J. Legrand, P. Legentilhomme, and A. Muller-Feuga, "Effect of Inlet Type on Shear Stress and Mixing in an Annular Photobioreactor Involving a Swirling Decaying Flow," *The Canadian Journal of Chemical Engineering*, vol. 82, no. 3, pp. 495–503, 2004.
- [20] T. Sato, S. Usui, Y. Tsuchiya, and Y. Kondo, "Invention of outdoor closed type photobioreactor for microalgae," *Energy Conversion and Management*, vol. 47, no. 6, pp. 791–799, 2006.
- [21] Z. Y. Guo, D. Y. Li, and B. X. Wang, "A novel concept for convective heat transfer enhancement," *International Journal of Heat and Mass Transfer*, vol. 41, no. 14, pp. 2221–2225, 1998.
- [22] W. Liu, Z. Liu, and S. Huang, "Physical quantity synergy in the field of turbulent heat transfer and its analysis for heat transfer enhancement," *Chinese Science Bulletin*, vol. 55, no. 23, pp. 2589–2597, 2010.
- [23] L. Wei, L. Zhichun, M. Tingzhen, and G. Zengyuan, "Physical quantity synergy in laminar flow field and its application in heat transfer enhancement," *International Journal of Heat and Mass Transfer*, vol. 52, no. 19-20, pp. 4669–4672, 2009.
- [24] Q. Chen, J. Ren, and Z. Guo, "Field synergy analysis and optimization of decontamination ventilation designs," *International Journal of Heat and Mass Transfer*, vol. 51, no. 3-4, pp. 873–881, 2008.
- [25] J. Yang, X. Cui, Y. Feng, G. Jing, L. Kang, and M. Luo, "Experimental study on microalgal cultivation in novel photobioreactor of concentric double tubes with aeration pores along tube length direction," *International Journal of Green Energy*, vol. 14, no. 15, pp. 1269–1276, 2017.
- [26] F. A. Fernández, F. G. Camacho, J. S. Pérez, J. F. Sevilla, and E. M. Grima, "A model for light distribution and average solar irradiance inside outdoor tubular photobioreactors for the microalgal mass culture," *Biotechnology and Bioengineering*, vol. 55, no. 5, pp. 701–714, 1997.
- [27] M. J. Barbosa, M. Janssen, N. Ham, J. Tramper, and R. H. Wijffels, "Microalgal cultivation in air-lift reactors: modeling biomass yield and growth rate as a function of mixing frequency," *Biotechnology and Bioengineering*, vol. 82, no. 2, pp. 170–179, 2003.
- [28] A. Wileman, A. Ozkan, and H. Berberoglu, "Rheological properties of algae slurries for minimizing harvesting energy requirements in biofuel production," *Bioresource Technology*, vol. 104, pp. 432–439, 2012.
- [29] C. McHardy, G. Luzi, C. Lindenberger, J. R. Agudo, A. Delgado, and C. Rauh, "Numerical analysis of the effects of air on light distribution in a bubble column photobioreactor," *Algal Research*, vol. 31, pp. 311–325, 2018.
- [30] J. Fu, Y. Huang, Q. Liao, A. Xia, Q. Fu, and X. Zhu, "Photobioreactor design for microalgae: a review from the aspect of CO₂ transfer and conversion," *Bioresource Technology*, vol. 292, article 121947, 2019.
- [31] R. K. Saini, P. P. Wangikar, and M. Bose, "CFD analysis of the flow dynamics of microorganisms in dilute cultures in stirred tank photobioreactors," *Bioresource Technology Reports*, vol. 3, pp. 238–246, 2018.

- [32] L. Wang, Y. Tao, and X. Mao, "A novel flat plate algal bioreactor with horizontal baffles: structural optimization and cultivation performance," *Bioresource Technology*, vol. 164, pp. 20–27, 2014.
- [33] H.-P. Luo and M. H. Al-Dahhan, "Verification and validation of CFD simulations for local flow dynamics in a draft tube airlift bioreactor," *Chemical Engineering Science*, vol. 66, no. 5, pp. 907–923, 2011.
- [34] Z. Yang, J. Cheng, Q. Ye, J. Liu, J. Zhou, and K. Cen, "Decrease in light/dark cycle of microalgal cells with computational fluid dynamics simulation to improve microalgal growth in a raceway pond," *Bioresource Technology*, vol. 220, pp. 352–359, 2016.
- [35] J. Huang, Y. Li, M. Wan et al., "Novel flat-plate photobioreactors for microalgal cultivation with special mixers to promote mixing along the light gradient," *Bioresource Technology*, vol. 159, pp. 8–16, 2014.
- [36] B. Haut, H. Ben Amor, L. Coulon, A. Jacquet, and V. Halluin, "Hydrodynamics and mass transfer in a Couette-Taylor bioreactor for the culture of animal cells," *Chemical Engineering Science*, vol. 58, no. 3-6, pp. 777–784, 2003.
- [37] B. Gris, T. Morosinotto, G. M. Giacometti, A. Bertucco, and E. Sforza, "Cultivation of *Scenedesmus obliquus* in photobioreactors: effects of light intensities and light-dark cycles on growth, productivity, and biochemical composition," *Applied Biochemistry and Biotechnology*, vol. 172, no. 5, pp. 2377–2389, 2014.
- [38] L. Xu, R. Liu, F. Wang, and C. Liu, "Development of a draft-tube airlift bioreactor for *Botryococcus braunii* with an optimized inner structure using computational fluid dynamics," *Bioresource Technology*, vol. 119, pp. 300–305, 2012.
- [39] Q. H. Zhang, X. Wu, S. Z. Xue, Z. H. Wang, C. H. Yan, and W. Cong, "Hydrodynamic characteristics and microalgal cultivation in a novel flat-plate photobioreactor," *Biotechnology Progress*, vol. 29, no. 1, pp. 127–134, 2013.

Research Article

Response and Adaptation of Microbial Community in a CANON Reactor Exposed to an Extreme Alkaline Shock

Ruili Yang,^{1,2} Wenlong Mao,^{1,3} Xiaojun Wang ¹, Zhaoji Zhang,¹ Junbin Wu,¹ and Shaohua Chen ¹

¹CAS Key Laboratory of Urban Pollutant Conversion, Institute of Urban Environment, Chinese Academy of Sciences, Xiamen 361021, China

²University of Chinese Academy of Sciences, Beijing 100049, China

³Fujian Agriculture and Forestry University, Fuzhou 350002, China

Correspondence should be addressed to Xiaojun Wang; xjwang@iue.ac.cn and Shaohua Chen; shchen@iue.ac.cn

Received 22 April 2020; Revised 27 May 2020; Accepted 4 June 2020; Published 1 July 2020

Academic Editor: Rong Chen

Copyright © 2020 Ruili Yang et al. This is an open access article distributed under the Creative Commons Attribution License, which permits unrestricted use, distribution, and reproduction in any medium, provided the original work is properly cited.

Responses of a microbial community in the completely autotrophic nitrogen removal over nitrite (CANON) process, which was shocked by a pH of 11.0 for 12 h, were investigated. During the recovery phase, the performance, anaerobic ammonia oxidation (anammox) activity, microbial community, and correlation of bacteria as well as the influencing factors were evaluated synchronously. The performance of the CANON process deteriorated rapidly with a nitrogen removal rate (NRR) of $0.13 \text{ kg} \cdot \text{m}^{-3} \cdot \text{d}^{-1}$, and Firmicutes, spore-forming bacteria, were the dominant phyla after alkaline shock. However, it could self-restore within 107 days after undergoing four stages, at which Planctomycetes became dominant with a relative abundance of 64.62%. Network analysis showed that anammox bacteria (*Candidatus Jettenia*, *Kuenenia*, and *Brocadia*) were positively related to some functional bacteria such as *Nitrosomonas*, *SM1A02*, and *Calorithrix*. Canonical correspondence analysis presented a strong correlation between the microbial community and influencing factors during the recovery phase. With the increase of nitrogen loading rate, the decrease of free nitrous acid and the synergistic effects, heme c content, specific anammox activity (SAA), NRR, and the abundance of dominant genus increased correspondingly. The increase of heme c content regulates the quorum sensing system, promotes the secretion of extracellular polymeric substances, and further improves SAA, NRR, and the relative abundance of the dominant genus. This study highlights some implications for the recovery of the CANON reactor after being exposed to an alkaline shock.

1. Introduction

A completely autotrophic nitrogen removal over nitrite (CANON) process, a combination of partial nitrification and anaerobic ammonia oxidation (anammox), is highly sensitive to key environmental parameters, such as nitrite ($\text{NO}_2^- \text{-N}$), dissolved oxygen (DO), and pH [1–3]. Although these parameters are always automatically controlled in engineering applications [4], a fortuitous occurrence of the CANON process can happen accidentally when the automatic control fails. In particular, pH as a crucial parameter can adversely affect the performance of the CANON process if it is not well controlled. In addition, substrate inhibition, which refers to the toxicity of free ammonia (FA) and free nitrous acid

(FNA) in the CANON process, is pH-dependent [5]. Therefore, pH can have a strong effect on the CANON process [6]. Research on the effect of alkaline shock on the CANON process often uses $\text{pH} < 10.0$ [7–9]. Fux et al. [10] pointed out that specific anammox activity (SAA) of anammox was completely inhibited by pH 9.3. Li et al. [11] observed the disintegration of anammox granule at pH 9.0. When the concentration of FA reaches approximately $32.5 \text{ mg} \cdot \text{L}^{-1}$ at pH 8.5, anammox bacteria and ammonia oxidising bacteria (AOB) activities are severely inhibited, and the performance of the CANON system deteriorates quickly [9]. Apart from pH influence, the microbial community is known as an essential factor affecting the efficiency of the CANON process, and the structure of microbial communities is very

sensitive to an alkaline situation [12]. In spite of this, studies about the CANON system are mainly focused on the nitrogen removal performance and abundances of anammox bacteria, AOB, and nitrite oxidising bacteria (NOB) [13, 14]. Limited studies have considered the interaction of anammox bacteria, AOB, NOB, and denitrifying bacteria (DNB) [15]. Wu et al. [15] observed that the abundance of *Sphingobacteria*, which is closely related to aerobic denitrifying bacteria, in the CANON system was much higher than that in the anammox system when incubated with anaerobic sludge. Moreover, correlation among the microbial communities in the CANON system in response to alkaline shock remains to be studied in depth. In addition, pH is found to inhibit microbial communities in two ways: (1) pH inhibits the microbial activity by changing the characteristics of microbial habitats [16], and (2) pH inhibits microorganisms directly or via changing the concentrations of FA, FNA, and organics to inactivate irreversible enzymes, obstruct metabolic function, and reduce transcriptional activity [12]. Although the mechanisms of pH effects on the microbial community have been well studied, a few studies have focused on the response of microbial communities during the recovery phase in the CANON process when exposed to alkaline shock.

In this study, we hypothesised that synergy effects among the bacteria associated with the nitrogen cycle would improve the performance of the CANON process after applying transient alkaline pH shock. To test this hypothesis, the CANON process was exposed to an alkaline shock of pH 11.0 for 12 h. The nitrogen removal performance, activity indicators (SAA, heme c, extracellular polymeric substances (EPS), and signalling molecule), variation of the microbial community structure, correlation among the microorganisms, and the correlation between the microbial community and the influencing factors in the CANON reactor were investigated during the whole recovery process. This study is aimed at broadening our current knowledge of the underlying mechanisms of the microbial community in response to an alkaline shock and encouraging technical regulations optimising the CANON process for a maximal efficiency during the recovery process.

2. Materials and Methods

2.1. Experimental Setup and Reactor Operation. A pilot-scale upflow anaerobic filter (UAF) reactor (Figure 1) was used in this study. It had a working volume of 100 L and an internal diameter of 30 cm and was filled with polypropylene pall rings as biological carriers. A flexible electrical heating belt was adopted to maintain the temperature at $35 \pm 1^\circ\text{C}$ and protect anammox bacteria against the competition of photosynthetic microorganisms. The hydraulic retention time (HRT) of the UAF reactor was set at 1 day. The pH and DO were controlled by an online controller and maintained at 7.4–7.8 and $0.02\text{--}0.8\text{ mg}\cdot\text{L}^{-1}$, respectively [7]. The inoculation sludge was taken from an anammox reactor, and its concentrations of mixed liquor suspended solid (MLSS) and mixed liquor volatile suspended solid (MLVSS) were approximately 22.87 and $12.49\text{ g}\cdot\text{L}^{-1}$, respectively.

The CANON process was cultivated using synthetic wastewater, and the mineral medium was supplied according to our previous study [17]. After stable operation for 1.5 y, the CANON process showed a good performance with ammonium removal efficiency and nitrogen removal rate (NRR) of 93.74% and $0.80\text{ kg}\cdot\text{m}^{-3}\cdot\text{d}^{-1}$, respectively. Then, it was exposed to a transient alkaline shock of pH 11.0 for 12 h. The recovery phase mainly consisted of four stages: accommodation stage (days 1–37), anammox recovery stage (days 38–68), CANON recovery stage (days 69–100), and steady stage (days 101–107), according to the nitrogen removal performance of the CANON reactor and a previously reported method by Zhang et al. [18]. The operating conditions of the CANON process during the recovery phase are summarised in Table 1. To ensure the recovery of anammox bacteria activity, first, we inhibited aeration and adjusted the pH to 7.8 by washing bioreactor with the synthetic wastewater without $\text{NH}_4^+\text{-N}$ and $\text{NO}_2^-\text{-N}$ for approximately 1 h at a flow rate of $1600\text{ mL}\cdot\text{min}^{-1}$. The influent concentrations of $\text{NH}_4^+\text{-N}$ and $\text{NO}_2^-\text{-N}$ were decreased to $250\text{ mg}\cdot\text{L}^{-1}$ to avoid the substrate inhibition [19]. Next, the operating conditions (Table 1) were implemented according to the performance of the CANON reactor.

2.2. Sample Collection and Analysis. SAA, an important parameter to evaluate the performance of the anammox pathway [8], and heme c, an indispensable part of the key enzymes [20] directly associated with the substance and energy metabolism of anammox bacteria [21, 22], were used to codetermine the activity of anammox bacteria [23]. EPS, as the stress resister and indicator of the stability and settling property of anammox sludge, coupled with the signalling molecule, are secreted as the metabolites of microorganisms and are beneficial for the formation of biofilm [24, 25]. In this study, EPS was beneficial for initiating the CANON system [26]. The settleability and strength of granule sludge or biofilm are usually evaluated by the ratio of protein (PN) to polysaccharides (PS) [27]. All these factors were used to evaluate the recovery of the CANON process.

Sludge and water samples were withdrawn from the CANON process on days 1, 37, 53, 63, 75, 85, and 107, in order to investigate the EPS concentration, SAA, heme c content, and signalling molecule. Sample collection was conducted in triplicate. Concentrations of EPS and heme c were determined based on the previous reports by Ma et al. [28] and Berry and Trumppower [29], respectively. The semi-quantitative estimation of signalling molecule was determined according to the method proposed by Yeon et al. [30]. SAA was conducted according to our previous investigation [31]. Simultaneously, the concentrations of MLSS, MLVSS, ammonia ($\text{NH}_4^+\text{-N}$), nitrite ($\text{NO}_2^-\text{-N}$), nitrate ($\text{NO}_3^-\text{-N}$), and total nitrogen (TN) were analysed based on standard methods [32].

2.3. DNA Extraction and Amplicon Sequencing. To investigate responses of microbial communities in the CANON process to the exposure of an alkaline shock, sludge samples collected from the reactor on days 1, 37, 63, and 107 were subjected to DNA extraction, and quality control was also

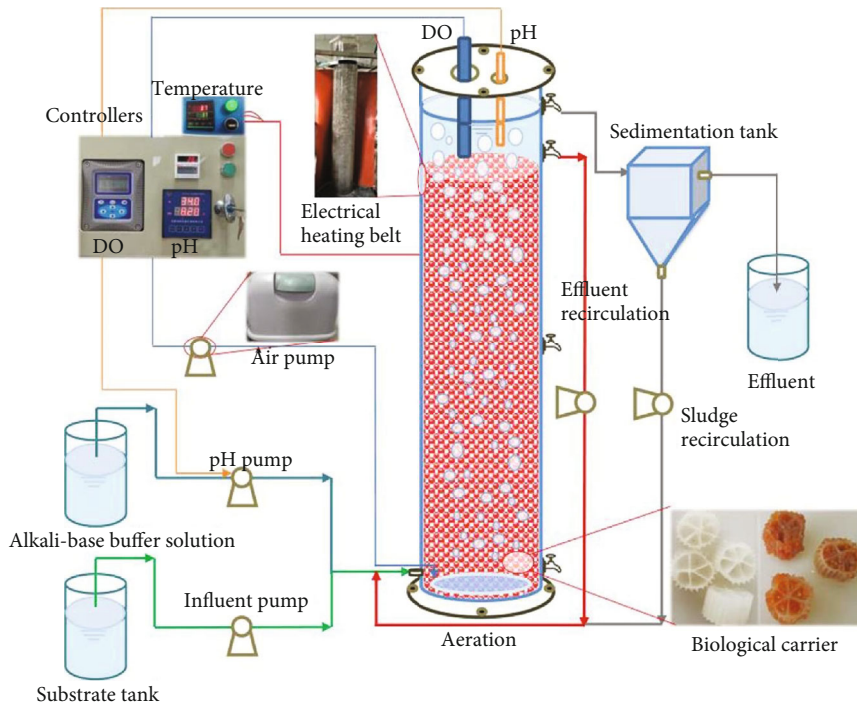


FIGURE 1: Schematic of the experimental device.

TABLE 1: Operational conditions of the CANON process after the alkaline shock.

Stage	Time (d)	$\text{NH}_4^+\text{-N}$ ($\text{mg}\cdot\text{L}^{-1}$)	$\text{NO}_2^-\text{-N}$ ($\text{mg}\cdot\text{L}^{-1}$)	NLR ($\text{kg}\cdot\text{m}^{-3}\cdot\text{d}^{-1}$)	DO ($\text{mg}\cdot\text{L}^{-1}$)
Accommodation stage	1-3	250	250	0.5	
	4-37	100	100	0.2	
	38-61	100	100	0.2	<0.05
Anammox recovery stage	62-64	150	150	0.3	
	65-68	250	250	0.5	
	69-76	450	150	0.6	
CANON recovery stage	77-81	600	0	0.6	
	82-86	800	0	0.8	0.2-0.8
	87-100	1000	0	1	
Steady stage	101-107	1000	0	1	

performed according to our previous study [17]. Next, the V3-V4 hypervariable region of 16S rDNA gene of the qualified DNA samples was selected for polymerase chain reaction (PCR) amplification using the universal primer sets: 341F (5'-CCT ACG GGN GGC WGC AG-3') and 806R (5'-GGA CTA CHV GGG TAT CTA AT-3') [17]. PCR amplifications were conducted in triplicate, and the products were quantified using a Qubit 2.0 fluorometer (Promega Co., Madison, USA). The purified amplicons were pooled together in an equal amount. Then, the sequencing library was constructed and sent for paired end sequencing on a HiSeq2500 PE250 platform (Gene Denovo Biotechnology Co., Ltd., Guangzhou, China). The sequence data were processed using the Quantitative Insights into Microbial Ecology software [33],

and results were assigned to operational taxonomic units (OTUs) with >97% similarity.

2.4. Statistical and Network Analyses. Canonical correspondence analysis (CCA) was conducted to further explore the relationship between microbial communities and influencing factors using the “vegan” package in RStudio environment (<https://www.rstudio.com/>). Pairwise Spearman’s correlation coefficients among 12 genera, which have an average abundance higher than 1%, were calculated by SPSS Statistics 22 (IBM, USA) (<http://www.ibm.com/analytics/us/en/technology/spss/>). Furthermore, network analysis based on Spearman’s correlation coefficient (r) > 0.6 or < -0.6, and the corresponding p value < 0.05 between two genera was performed

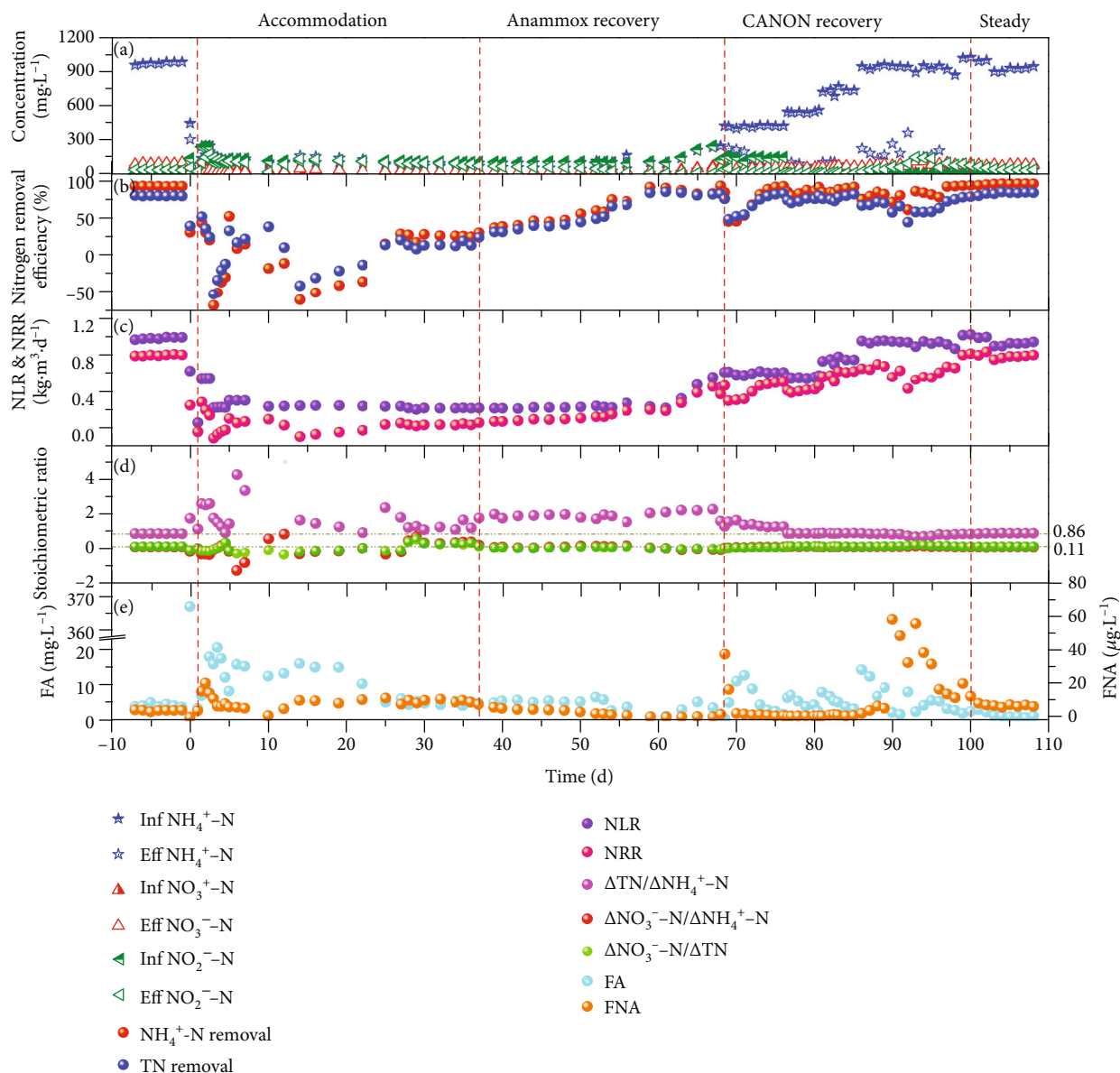


FIGURE 2: Shifts in nitrogen concentration (a), nitrogen removal efficiency (b), nitrogen loading rate and removal rate (c), stoichiometric ratio (d), and free ammonia and free nitrous acid (e) of the CANON process after alkaline shock.

and visualised by Gephi software (version 0.9.2, <https://gephi.org/>) [34].

3. Results and Discussion

3.1. Performance of the CANON Process during the Recovery Phase after Alkaline Shock. Figure 2 shows the nitrogen removal performance of the CANON reactor during the experiment. As depicted by Figure 2, the FA concentration of the CANON reactor sharply increased from 3.81 mg·L⁻¹ to 367.08 mg·L⁻¹, which was much higher than inhibition thresholds of AOB and anammox bacteria after being exposed to alkaline shock of pH 11.0 for 12 h [1, 9]. Thus, the CANON process was severely inhibited by the alkaline shock. As Li et al. [11] reported, the effect of an alkaline pH (9.0) shock on the performance of anammox granular sludge

was much more severe than that of an acidic pH (6.5) shock, and the alkaline condition disintegrated anammox granules. Based on the impact of influent pH of 4 and 10 for 12 h, Yu and Jin [35] also found a loss of anammox performance only in alkaline condition. In addition to the increase of FA, researchers suggested that activity loss could be related on the unavailability of trace elements as caused by extreme alkaline condition [35, 36]. Subsequently, aeration, pH, and influent concentrations of NH₄⁺-N and NO₂⁻-N were adjusted according to Table 1. Despite this, a progressive deterioration of the nitrogen removal performance was still observed, and the concentration of effluent TN was 41.21% higher than that of influent at the early accommodation stage (days 1–14). However, in the late accommodation stage (days 15–37), the CANON system gradually adapted to the changed environment.

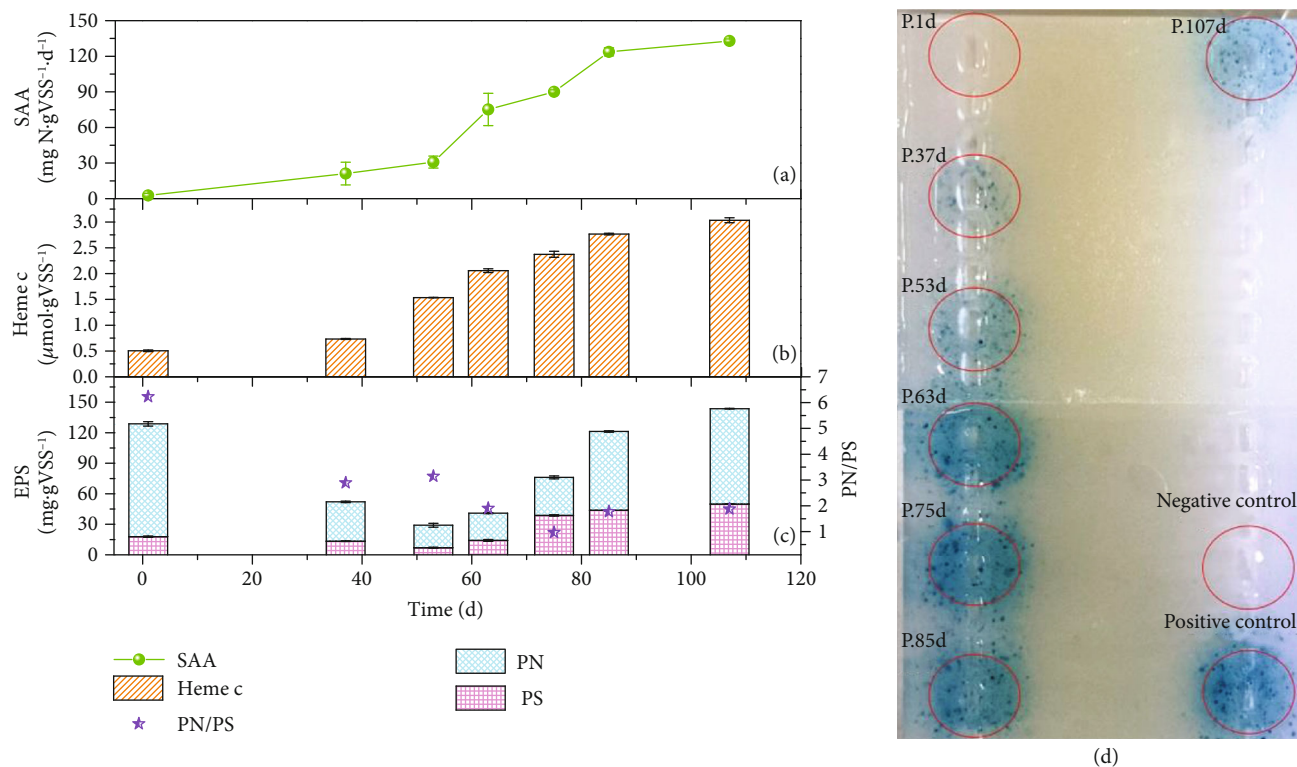


FIGURE 3: Variations of SAA (a), heme c (b), EPS (c), and signalling molecule (d) content in the CANON process after alkaline shock.

On days 38–52, the nitrogen removal performance of the anammox process recovered slowly with an increase of nitrogen removal efficiency (NRE) from 32% to 49.67%. Afterwards, the NRE and NRR increased rapidly to 86.44% and $0.18 \text{ kg}\cdot\text{m}^{-3}\cdot\text{d}^{-1}$, respectively, within 9 days. This phenomenon was similar to the lag stage in the start-up of the anammox process [37]. On days 62–68, the anammox process was enhanced rapidly with NRR increasing from 0.18 to $0.45 \text{ kg}\cdot\text{m}^{-3}\cdot\text{d}^{-1}$. To improve the nitrogen removal performance of the CANON system during the recovery stage (days 69–100), DO was maintained at $0.2\text{--}0.8 \text{ mg}\cdot\text{L}^{-1}$. As expected, the NRR increased to $0.82 \text{ kg}\cdot\text{m}^{-3}\cdot\text{d}^{-1}$ and NRE was at around 72%. Simultaneously, the stoichiometric ratios of $\Delta\text{TN}/\Delta\text{NH}_4^+\text{-N}$, $\Delta\text{NO}_3^-\text{-N}/\Delta\text{NH}_4^+\text{-N}$, and $\Delta\text{NO}_3^-\text{-N}/\Delta\text{TN}$ gradually increased from 1.29, 0.10, and 0.10, respectively, on day 1, to their theoretical value (0.86, 0.11, and 0.127, respectively), as described in the relevant studies [8, 38]. This meant there was significant synergy between AOB and anammox bacteria and there was no excess proliferation of NOB in the CANON reactor. In addition, the effect of the FNA fluctuation ($>15 \text{ }\mu\text{g}\cdot\text{L}^{-1}$) on nitrogen removal performance was more significant ($p < 0.05$) than that of the FA fluctuation on days 62–68. Previous studies report the FNA inhibition of AOB activity to be $100 \text{ }\mu\text{g}\cdot\text{L}^{-1}$ [9], whereas the inhibition on anammox bacteria activity is approximately $15 \text{ }\mu\text{g}\cdot\text{L}^{-1}$ [1]. Deterioration of the CANON performance, which was affected by FNA fluctuation, could be explained by this reason during the recovery phrase of the CANON system. He et al. [1] also pointed out that the anammox pathway, after being exposed to transient pH (9.0) shock, could be recov-

ered rapidly by simultaneously increasing nitrogen loading rate (NLR) and decreasing FNA ($<15 \text{ }\mu\text{g}\cdot\text{L}^{-1}$).

At the steady stage (days 101–107), the water quality of effluent and stoichiometric ratios became stable, and the nitrogen removal performance was even better than the initial level where the averages of NRE and NRR increased to 83.28% and $0.80 \text{ kg}\cdot\text{m}^{-3}\cdot\text{d}^{-1}$, respectively. The sensibility, low biomass yield, and slow growth rate of anammox bacteria were the main challenges for the application of the CANON process [8], though autotrophic bacteria of AOB and anammox bacteria were simultaneously grown in a single reactor [39]. Recovery of anammox bacteria should be focused on after the CANON reactor is exposed to an alkaline shock.

3.2. Changes of SAA, Heme c, EPS, and Signalling Molecule during the Recovery of the CANON Process after Alkaline Shock. Shifts in SAA, heme c, EPS, and signalling molecule content of the CANON process are shown in Figure 3. The SAA and heme c were maintained at low levels of $2.75 \text{ mg N}\cdot\text{g}^{-1} \text{ VSS}\cdot\text{d}^{-1}$ and $0.50 \text{ }\mu\text{mol}\cdot\text{g}^{-1} \text{ VSS}$, respectively, on day 1. It was clear that approximately 98% of anammox activity was lost compared to the activity in the initial phase. In the meantime, signalling molecule content was nearly zero, which was the quickest response to the transient alkaline shock. The signalling molecule was easily affected by the pH and quickly degraded under alkaline conditions [40]. It implied that AOB and anammox bacteria were inactivated, which was also supported by the performance of low NRE and NRR on day 1 in the CANON reactor. However, there was a delayed change in EPS, with a high concentration

of 128.76 mg·g⁻¹ VSS on day 1. This was likely because some microbial members excreted excessive EPS. Subsequently, the signalling molecule-based quorum sensing (QS) system could not regulate EPS production normally after being adversely influenced by the extreme alkaline shock [11, 40]. Previous studies [41, 42] have reported that the signalling molecule-based QS system could regulate EPS secretion under normal conditions. Subsequently, these parameters were gradually recovered during the recovery phase.

Significant increases of SAA, heme c, and the signalling molecule were observed on days 53–63, 37–53, and 53–63, respectively, during which the corresponding NRE were being recovered from 53% to 85%. This meant the anammox bacteria and AOB activities were recovered gradually. Moreover, the recovery time of heme c was shorter than that of the other parameters. Heme c is an important component of hydrazine synthesis, hydroxylamine oxidoreductase, and hydrazine oxidase in purified anammox cells [21]. It is directly associated with the metabolism of substances and energy in anammox bacteria [21, 22], and it also determines the activity of anammox biomass [23]. Chen et al. [43] found a similar result in an anammox-EGSB recovery system which experienced a longer-term starvation. Badalamenti et al. [44] reviewed one of 38 putative multiheme c-type cytochromes containing 69 heme-binding motifs and concluded that a LuxI/LuxR QS cassette can produce an unidentified signalling molecule. A signalling molecule-based QS system could regulate EPS secretion [41, 42]. Zhang et al. [45] confirmed that C8-HSL and C6-HSL, the examples of signalling molecules, favour EPS production and improve the activity of anammox bacteria, AOB, and others. Therefore, the enhancement of heme c was found to accelerate the secretion of a signalling molecule and promote the microbial activity [21, 44]. As a result, an increase in EPS content was found following the changing pattern of the signalling molecule. On day 107, the concentrations of SAA, heme c, and EPS were increased to 132.86 mg N·g⁻¹ VSS·d⁻¹, 3.03 μmol·g⁻¹ VSS, and 143.65 mg·g⁻¹ VSS, respectively. Although these values were similar to the findings in previous studies [45, 46], they were much higher than the values at the initial levels ($p < 0.01$) after the alkaline shock in this study. The NLR, NRR, and NRE reached the maximum values, and the CANON system remained stable.

3.3. Microbial Community Shift in the CANON Process after Alkaline Shock. A shift in the microbial community structure of the CANON process after alkaline shock was investigated by amplicon sequencing. The OTU number and diversity index increased gradually as the CANON process resumed (Table 2). Figure 4(a) shows the bacterial community composition in the CANON process at the phylum level. As shown in Figure 4(a), Firmicutes was the dominant bacterial taxum with a relative abundance of 73.93% after the alkaline shock. A similar phenomenon was also observed by Callejas et al. [47] after a transient pH increase. Wang and Gu [48] reported that the effect of alkaline condition (9.0) on the microbial community structure of the anammox process was stronger than that of acid condition (5.0). Firmicutes are spore-forming bacteria and related to complex organic

TABLE 2: Characteristics of amplicon libraries.

Group	OTUs	Shannon	Simpson	Chao	Ace	Coverage
P1d	758	5.04	0.912	812.0	854.41	0.998
P37d	780	4.81	0.829	842.4	884.32	0.998
P63d	1058	6.90	0.973	1096.8	1149.77	0.997
P107d	1063	5.15	0.843	1099.1	1152.35	0.998

matter degradation, which could explain the resistance to cell lysis in an alkaline environment [47]. The recovery of the CANON process also experienced four stages according to the variations in the microbial community at the phylum's level. Proteobacteria and Bacteroidetes, which are involved in nitrogen removal and organic acid degradation [49], became the two dominant phyla with their relative abundances increasing from 4.33% to 71.63% and from 1.32% to 14.29%, respectively, at the accommodation stage. Proteobacteria, Planctomycetes, and Bacteroidetes were the three dominant phyla at the growth stage, and the relative abundance of Planctomycetes increased from 2.28% to 16.87%. On day 107, Planctomycetes became the dominant phyla with a relative abundance of 64.62%, indicating that the CANON process had recovered to a certain degree. Wang et al. [50] also observed this phenomenon during the recovery of the CANON process when stressed by salt.

At the genus level (Figure 4(b)), *Bacillus*, belonging to Firmicutes, was the dominant genus with a relative abundance of 67.98% after the alkaline shock. *Bacillus* is a robust model organism for biofilm formation [51]. *Bacillus* can not only contribute to O₂ removal [52], nitrate reduction [53], and organic matter degradation [54] but can also secrete EPS, especially EPS-PN, for increasing resistances to adverse environmental stresses [55]. All these factors may explain why the *Bacillus* survived after alkaline shock. The accommodation stage (days 1–37) in this study was analogous to the cell lysis stage in the start-up of the anammox process [56]. *Thermomonas* was capable of utilising the organic products from cell lysis [57]; therefore, it became the dominant genus at the accommodation stage. At the growth stage (days 38–61), the microbial diversity of the CANON process was consistently increasing. The relative abundances of anammox bacteria (*Candidatus Jettenia*, *Kuenenia*, and *Brocadia*) gradually increased from 0.13% to 7.52%. After that, AOB (*Nitrosomonas*) together with anammox bacteria (*Candidatus Jettenia*, *Kuenenia* and *Brocadia*) became the dominant genera as aeration began. The relative abundances of AOB and anammox bacteria (*Candidatus Jettenia* + *Kuenenia* + *Brocadia*) at the enhancement stage increased quickly from 2.57% and 7.52% to 3.05% and 53.30%, respectively. Excess proliferation of NOB was not detected throughout the experiment. The good performance of the CANON process could be explained through microbiological perspectives.

3.4. Correlations of Microbial Communities and the Influencing Factors in the CANON Process after Alkaline Shock. Network analysis is an effective analytical approach

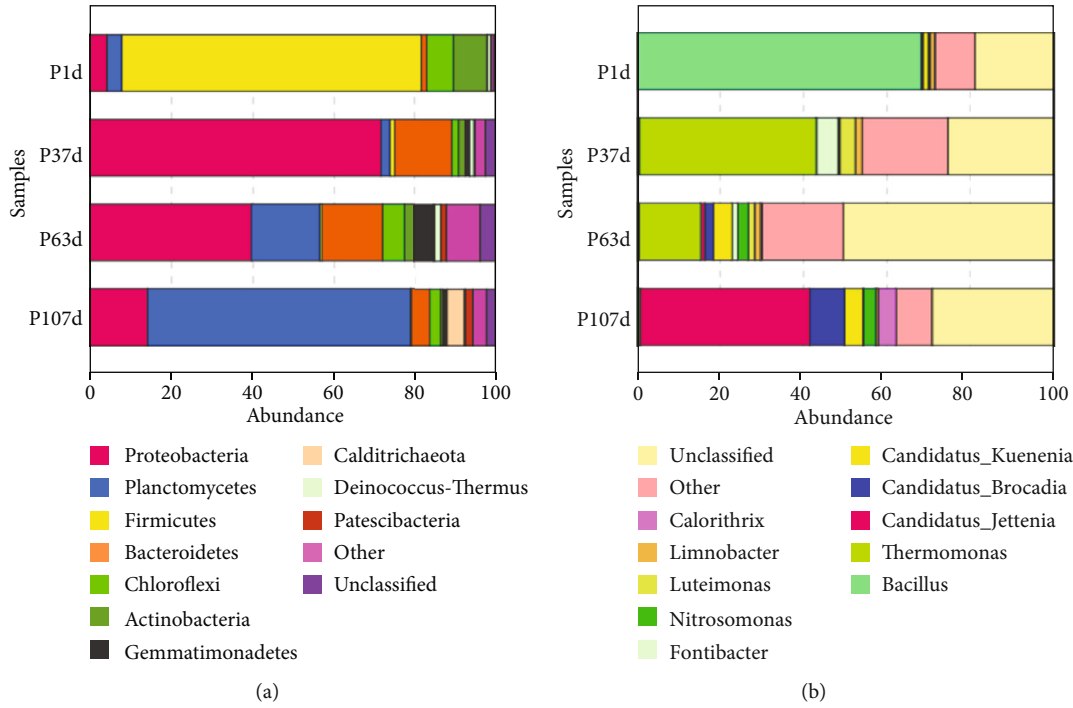


FIGURE 4: Bacterial community composition at the phylum (a) and genus (b) levels in the CANON process after alkaline shock.

for further exploring the correlation among the dominant microbial taxa (Figure 5(a)) in the CANON process exposed to alkaline shock. As shown in Figure 5(a), the dominant flora was divided into three modules based on the Fruchterman-Reingold algorithm. Members in module A, which accounted for 50% of the network, were *Candidatus Jettenia*, *Candidatus Kuenenia*, *Candidatus Brocadia*, *Nitrosomonas*, *SMIA02*, and *Calorithrix*. They were positively related to each other ($p < 0.05$). *Limnobacter*, one genus of module B, showed a significant negative correlation with *Candidatus Jettenia*, *Candidatus Brocadia*, *Nitrosomonas*, and *Calorithrix* ($p < 0.05$). Additionally, *Bacillus* was negatively correlated with all members in module A. CCA was further applied to determine the correlation of microbial communities and the influencing factors (Figure 5(b)) during the recovery phase. As is presented in Figure 5(b), the dominant genera of *Candidatus jettenia*, *Candidatus Kuenenia*, *Candidatus Brocadia*, *SMIA02*, and *Calorithrix*, had a significantly positive correlation ($p < 0.05$) with the influencing factors of SAA, NLR, NRR, heme c, EPS-PS, and FNA. *Nitrosomonas* was positively correlated with EPS, EPS-PN, SAA, NLR, NRR, heme c, EPS-PS, and FNA. However, *Bacillus* was only positively correlated with EPS-PN.

The abovementioned results can be explained by (1) the impact of NLR-led influencing factors, (2) synergistic effects of the dominant genus in the network module A, and (3) antagonistic effect of *Limnobacter*, *Bacillus*, and the dominant genus in network module A. As shown in Figure 5(c), anammox bacteria (*Candidatus Jettenia*, *Brocadia*, and *Kuenenia*) oxidised $\text{NH}_4^+\text{-N}$ to N_2 with $\text{NO}_2^-\text{-N}$ and CO_2 , which

were produced by AOB (*Nitrosomonas*) and DNB (*Calorithrix*), respectively. These served as the electron acceptors and inorganic carbon sources under anaerobic conditions [49, 58]. As reported in previous studies, *SMIA02* has the anammox ability and might be a novel anammox strain; therefore, it has the same synergistic effects with *Nitrosomonas* and *Calorithrix* [59–61]. In addition, *Nitrosomonas* can utilise $\text{NH}_4^+\text{-N}$ and DO and create anaerobic conditions for anammox bacteria such as *SMIA02* and *Calorithrix* [49, 60]. *Calorithrix* provides a substrate of $\text{NH}_4^+\text{-N}$ to anammox bacteria, *SMIA02*, and *Nitrosomonas* by dissimilatory $\text{NO}_3^-\text{-N}$ reduction to $\text{NH}_4^+\text{-N}$ [58]. All members in module A could secrete EPS to protect the members from adverse environmental stresses [58–60]. With the increase of NLR, decrease of FNA, and enhancement of synergistic effects of the dominant genus on network module A, it was observed that heme c content, SAA, NRR, and the relative abundance of dominant genus increased correspondingly [1, 21, 44, 45]. He et al. [1] reported that the anammox reactor recovered rapidly by simultaneously increasing NLR and decreasing FNA after experiencing a transient pH shock. However, *Limnobacter* competed with other functional bacteria for acetate, O_2 , and $\text{NO}_3^-\text{-N}$ [62] and consumed the EPS-PN produced by the members in module A. This explains why *Limnobacter* deteriorated the resistance of the microbial community to adverse influences [62, 63] and was assigned to module B. In addition, *Bacillus* was eliminated in long-term anaerobic conditions with the increase of NLR and therefore was negatively correlated with module A [64]. The synergistic and antagonistic effects of these functional bacteria, coupled with the control of NLR, FA, and FNA,

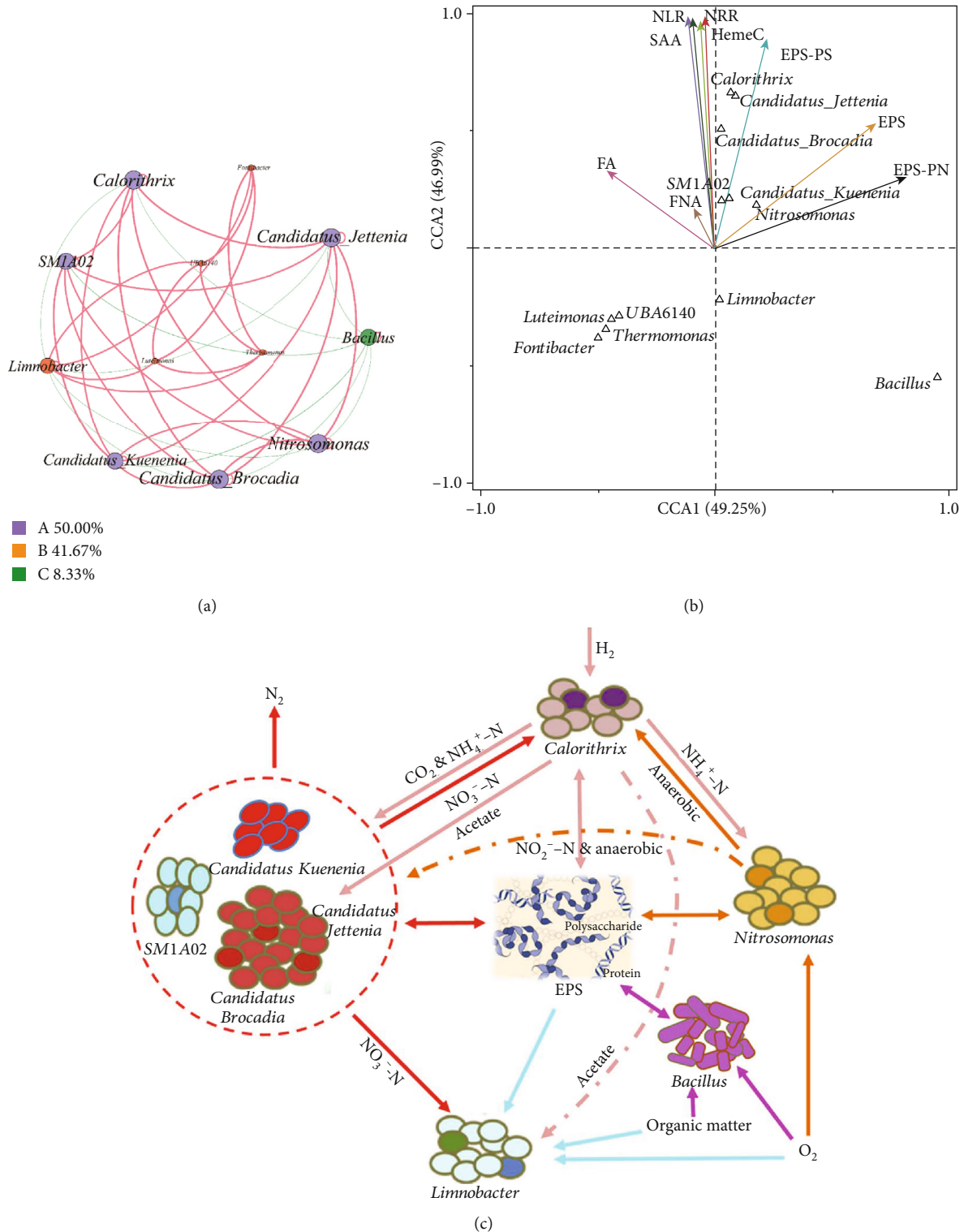


FIGURE 5: (a) Cooccurring network analysis of dominant microflora, (b) CCA of microbial communities and the influencing factors, and (c) correlation among dominant microflora, in the CANON process exposed to alkaline shock. The cooccurring network is coloured by the modularity class. Each node represents a dominant genus. Red and green lines represent positive and negative correlations, respectively. Node sizes are weighted by the node degree (numbers of connections).

codetermined the performance of the CANON process. All these supplied the underlying mechanisms of the microbial community in response to the alkaline shock. Meanwhile,

these could also inform technical regulations optimising the CANON process for maximal efficiency during the recovery process.

4. Conclusions

The CANON process was found to rapidly deteriorate after an alkaline shock of pH 11. However, it could be self-restored with the final NRR of $0.80 \text{ kg}\cdot\text{m}^{-3}\cdot\text{d}^{-1}$ after the system underwent four stages (accommodation, anammox recovery, CANON recovery, and steady stages). During the entire recovery process, heme c content responded the fastest to the transient alkaline shock among all tested parameters and increased gradually, followed by the signalling molecule. Both parameters improved the AOB and anammox activity and regulated the EPS secretion. Firmicutes, a type of spore-forming bacterium, was dominant at the initial stage, and subsequently at the later period, Planctomycetes became the dominant phylum with a relative abundance of 64.62%. Network analysis clearly revealed positive relationships among anammox bacteria (*Candidatus Jettenia*, *Kuenenia*, and *Brocadia*), AOB (*Nitrosomonas*), *SM1A02*, and DNB (*Calorithrix*). Additionally, there was a strong correlation between microbial communities and the influencing factors during the recovery phase. With the increase of NLR, decrease of FNA, and synergistic effects of dominant microbial members, heme c content, SAA, NRR, and the relative abundance of the dominant genus increased correspondingly. The increase of heme c content regulates the quorum sensing system, promotes the secretion of EPS, and further improves SAA, NRR, and the relative abundance of the dominant genus. The response of the microbial community to environmental change gives an insight into the recovery of the CANON process after being exposed to an alkaline shock and provides technical regulations for its engineering application.

Data Availability

The data used to support the findings of this study are included within the article.

Conflicts of Interest

The authors declare that there is no conflict of interest regarding the publication of this article.

Acknowledgments

This research was financially supported by the National Natural Science Foundation of China (grant No. 51708536) and the Science and Technology Program of Fujian Province (grant No. 2019Y01010111).

References

- [1] S. He, Y. Zhang, Q. Niu, H. Ma, and Y. Y. Li, "Operation stability and recovery performance in an Anammox EGSB reactor after pH shock," *Ecological Engineering*, vol. 90, pp. 50–56, 2016.
- [2] X. Yue, G. Yu, Y. Lu et al., "Effect of dissolved oxygen on nitrogen removal and the microbial community of the completely autotrophic nitrogen removal over nitrite process in a submerged aerated biological filter," *Bioresource Technology*, vol. 254, pp. 67–74, 2018.
- [3] A. O. Sliemers, K. A. Third, W. Abma, J. G. Kuenen, and M. S. M. Jetten, "CANON and Anammox in a gas-lift reactor," *FEMS microbiology letters*, vol. 218, no. 2, pp. 339–344, 2003.
- [4] S. Lackner, E. M. Gilbert, S. E. Vlaeminck, A. Joss, H. Horn, and M. C. M. van Loosdrecht, "Full-scale partial nitrification/anammox experiences - An application survey," *Water Research*, vol. 55, pp. 292–303, 2014.
- [5] S. He, Q. Niu, H. Ma, Y. Zhang, and Y. Y. Li, "The treatment performance and the bacteria preservation of anammox: a review," *Water, Air, & Soil Pollution*, vol. 226, no. 5, 2015.
- [6] X. Chang, D. Li, Y. Liang et al., "Performance of a completely autotrophic nitrogen removal over nitrite process for treating wastewater with different substrates at ambient temperature," *Journal of Environmental Sciences*, vol. 25, no. 4, pp. 688–697, 2013.
- [7] X. Yue, G. Yu, Z. Liu, J. Tang, and J. Liu, "Fast start-up of the CANON process with a SABF and the effects of pH and temperature on nitrogen removal and microbial activity," *Biore-source Technology*, vol. 254, pp. 157–165, 2018.
- [8] T. V. Huynh, P. D. Nguyen, T. N. Phan et al., "Application of CANON process for nitrogen removal from anaerobically pre-treated husbandry wastewater," *International Biodeterioration & Biodegradation*, vol. 136, pp. 15–23, 2019.
- [9] S. Li, Y. P. Chen, C. Li, J. S. Guo, F. Fang, and X. Gao, "Influence of free ammonia on completely autotrophic nitrogen removal over nitrite (CANON) process," *Applied Biochemistry and Biotechnology*, vol. 167, no. 4, pp. 694–704, 2012.
- [10] C. Fux, V. Marchesi, I. Brunner, and H. Siegrist, "Anaerobic ammonium oxidation of ammonium-rich waste streams in fixed-bed reactors," *Water Science and Technology*, vol. 49, no. 11–12, pp. 77–82, 2004.
- [11] J. Li, W. Zhu, H. Dong, and D. Wang, "Performance and kinetics of ANAMMOX granular sludge with pH shock in a sequencing batch reactor," *Biodegradation*, vol. 28, no. 4, pp. 245–259, 2017.
- [12] C. Wang, S. Liu, X. Xu, Y. Guo, F. Yang, and D. Wang, "Role of cyclic diguanylate in affecting microbial community shifts at different pH during the operation of simultaneous partial nitrification, anammox and denitrification process," *Science of The Total Environment*, vol. 637–638, pp. 155–162, 2018.
- [13] W. Mi, J. Zhao, X. Ding, G. Ge, and R. Zhao, "Treatment performance, nitrous oxide production and microbial community under low-ammonium wastewater in a CANON process," *Water Science and Technology*, vol. 76, no. 12, pp. 3468–3477, 2017.
- [14] X. Li, J. Zhang, X. Zhang, J. Li, F. Liu, and Y. Chen, "Start-up and nitrogen removal performance of CANON and SNAD processes in a pilot-scale oxidation ditch reactor," *Process Biochemistry*, vol. 84, pp. 134–142, 2019.
- [15] P. Wu, X. Zhang, X. Wang, C. Wang, F. Faustin, and W. Liu, "Characterization of the start-up of single and two-stage Anammox processes with real low-strength wastewater treatment," *Chemosphere*, vol. 245, p. 125572, 2020.
- [16] C. L. Lauber, M. Hamady, R. Knight, and N. Fierer, "Pyrosequencing-based assessment of soil pH as a predictor of soil bacterial community structure at the continental scale," *Applied and Environmental Microbiology*, vol. 75, no. 15, pp. 5111–5120, 2009.

- [17] R. Yang, X. Wang, Y. Guo, Z. Zhang, and S. Chen, "Evaluation of anammox pathway recovery after high COD loading using water quality, molecular biology and isotope labelling analysis," *Bioprocess and Biosystems Engineering*, vol. 43, no. 4, pp. 625–636, 2020.
- [18] Q.-Q. Zhang, G.-F. Yang, H. Wang, K. Wu, R. C. Jin, and P. Zheng, "Estimating the recovery of ANAMMOX performance from inhibition by copper (II) and oxytetracycline (OTC)," *Separation and Purification Technology*, vol. 113, pp. 90–103, 2013.
- [19] K. Isaka, T. Sumino, and S. Tsuneda, "High nitrogen removal performance at moderately low temperature utilizing anaerobic ammonium oxidation reactions," *Journal of Bioscience and Bioengineering*, vol. 103, no. 5, pp. 486–490, 2007.
- [20] M. G. Klotz, M. C. Schmid, M. Strous, H. J. M. op den Camp, M. S. M. Jetten, and A. B. Hooper, "Evolution of an octahaem cytochrome c protein family that is key to aerobic and anaerobic ammonia oxidation by bacteria," *Environmental Microbiology*, vol. 10, no. 11, pp. 3150–3163, 2008.
- [21] M. S. M. Jetten, L. van Niftrik, M. Strous, B. Kartal, J. T. Keltjens, and H. J. M. Op den Camp, "Biochemistry and molecular biology of anammox bacteria," *Critical Reviews in Biochemistry and Molecular Biology*, vol. 44, no. 2-3, pp. 65–84, 2009.
- [22] M. C. Schmid, A. B. Hooper, M. G. Klotz et al., "Environmental detection of octahaem cytochrome c hydroxylamine/hydrazine oxidoreductase genes of aerobic and anaerobic ammonium-oxidizing bacteria," *Environmental Microbiology*, vol. 10, no. 11, pp. 3140–3149, 2008.
- [23] Q. Q. Zhang, Y. H. Zhao, C. J. Wang et al., "Expression of the *nirS*, *hzsA*, and *hdh* genes and antibiotic resistance genes in response to recovery of anammox process inhibited by oxytetracycline," *Science of The Total Environment*, vol. 681, pp. 56–65, 2019.
- [24] A. Alagely, C. J. Krediet, K. B. Ritchie, and M. Teplitski, "Signaling-mediated cross-talk modulates swarming and biofilm formation in a coral pathogen *Serratia marcescens*," *The ISME Journal*, vol. 5, no. 10, pp. 1609–1620, 2011.
- [25] C. Wang, S. Liu, X. Xu, C. Zhao, F. Yang, and D. Wang, "Potential coupling effects of ammonia-oxidizing and anaerobic ammonium-oxidizing bacteria on completely autotrophic nitrogen removal over nitrite biofilm formation induced by the second messenger cyclic diguanylate," *Applied Microbiology & Biotechnology*, vol. 101, no. 9, pp. 3821–3828, 2017.
- [26] Z. Zhang, S. Chen, P. Wu, L. Lin, and H. Luo, "Start-up of the Canon process from activated sludge under salt stress in a sequencing batch biofilm reactor (SBBR)," *Bioresource Technology*, vol. 101, no. 16, pp. 6309–6314, 2010.
- [27] X. Hou, S. Liu, and Z. Zhang, "Role of extracellular polymeric substance in determining the high aggregation ability of anammox sludge," *Water Research*, vol. 75, pp. 51–62, 2015.
- [28] C. Ma, R. C. Jin, G. F. Yang, J. J. Yu, B. S. Xing, and Q. Q. Zhang, "Impacts of transient salinity shock loads on Anammox process performance," *Bioresource Technology*, vol. 112, pp. 124–130, 2012.
- [29] E. A. Berry and B. L. Trumpower, "Simultaneous determination of hemes *a*, *b*, and *c* from pyridine hemochrome spectra," *Analytical Biochemistry*, vol. 161, no. 1, pp. 1–15, 1987.
- [30] K.-M. Yeon, W. S. Cheong, H. S. Oh et al., "Quorum sensing: a new biofouling control paradigm in a membrane bioreactor for advanced wastewater treatment," *Environmental Science & Technology*, vol. 43, no. 2, pp. 380–385, 2009.
- [31] X. Wang, R. Yang, Z. Zhang, J. Wu, and S. Chen, "Mass balance and bacterial characteristics in an in-situ full-scale swine wastewater treatment system occurring anammox process," *Bioresource Technology*, vol. 292, p. 122005, 2019.
- [32] The State Environmental Protection Administration of China (SEPA), *Editorial Committee of "monitoring and analytical methods of water and wastewater"*, China Environmental Science Press, Beijing, 4th edition, 2002.
- [33] Y. H. Yang, Z. L. Lei, L. Huang et al., "Antitumor ability of berberine accompanied by modulation of gut microbiome in sarcoma-180 tumor-bearing mice," *International Journal of Pharmacology*, vol. 14, pp. 460–470, 2018.
- [34] H. He, L. Fu, Q. Liu et al., "Community structure, abundance and potential functions of bacteria and archaea in the Sansha Yongle Blue Hole, Xisha, South China Sea," *Frontiers in microbiology*, vol. 10, 2019.
- [35] J.-J. Yu and R.-C. Jin, "The ANAMMOX reactor under transient-state conditions: process stability with fluctuations of the nitrogen concentration, inflow rate, pH and sodium chloride addition," *Bioresource Technology*, vol. 119, pp. 166–173, 2012.
- [36] G. M. Gadd and A. J. Griffiths, "Microorganisms and heavy metal toxicity," *Microbial Ecology*, vol. 4, no. 4, pp. 303–317, 1977.
- [37] J. Guo, S. Wang, J. Lian et al., "Rapid start-up of the anammox process: effects of five different sludge extracellular polymeric substances on the activity of anammox bacteria," *Bioresource Technology*, vol. 220, pp. 641–646, 2016.
- [38] X. Wang and D. Gao, "In-situ restoration of one-stage partial nitrification-anammox process deteriorated by nitrate build-up via elevated substrate levels," *Scientific reports*, vol. 6, 2016.
- [39] X. Zhang, N. Zhang, H. Fu et al., "Effect of zinc oxide nanoparticles on nitrogen removal, microbial activity and microbial community of CANON process in a membrane bioreactor," *Bioresource Technology*, vol. 243, pp. 93–99, 2017.
- [40] A. W. Decho, P. T. Visscher, J. Ferry et al., "Autoinducers extracted from microbial mats reveal a surprising diversity of N-acylhomoserine lactones (AHLs) and abundance changes that may relate to diel pH," *Environmental Microbiology*, vol. 11, no. 2, pp. 409–420, 2009.
- [41] Y. Ding, H. Feng, W. Huang, D. Shen, and M. Wang, "A sustainable method for effective regulation of anaerobic granular sludge: artificially increasing the concentration of signal molecules by cultivating a secreting strain," *Bioresource Technology*, vol. 196, pp. 273–278, 2015.
- [42] Y. Li, J. Lv, C. Zhong, W. Hao, Y. Wang, and J. Zhu, "Performance and role of N-acyl-homoserine lactone (AHL)-based quorum sensing (QS) in aerobic granules," *Journal of Environmental Sciences*, vol. 26, no. 8, pp. 1615–1621, 2014.
- [43] T. T. Chen, P. Zheng, and L. D. Shen, "Growth and metabolism characteristics of anaerobic ammonium-oxidizing bacteria aggregates," *Applied Microbiology and Biotechnology*, vol. 97, no. 12, pp. 5575–5583, 2013.
- [44] J. P. Badalamenti, Z. M. Summers, C. H. Chan, J. A. Gralnick, and D. R. Bond, "Isolation and genomic characterization of 'desulfuromonas soudanensis WTL', a Metal- and electrode-respiring bacterium from anoxic deep subsurface brine," *Frontiers in microbiology*, vol. 7, 2016.
- [45] J. Zhang, Y.-z. Zhang, B.-h. Zhao et al., "Effects of pH on AHL signal release and properties of ANAMMOX granules with

- different biomass densities,” *Environmental Science: Water Research & Technology*, vol. 5, no. 10, pp. 1723–1735, 2019.
- [46] C. Tan, D. Cui, Y. Liu, and Y. Ji, “Influence of tourmaline on the anaerobic ammonium oxidation process in sequencing batch reactors,” *Journal of Environmental Engineering*, vol. 143, no. 9, 2017.
- [47] C. Callejas, A. Fernández, M. Passeggi et al., “Microbiota adaptation after an alkaline pH perturbation in a full-scale UASB anaerobic reactor treating dairy wastewater,” *Bioprocess and Biosystems Engineering*, vol. 42, no. 12, pp. 2035–2046, 2019.
- [48] Y.-F. Wang and J.-D. Gu, “Effects of allylthiourea, salinity, and pH on ammonia/ammonium-oxidizing prokaryotes in mangrove sediment incubated in laboratory microcosms,” *Applied Microbiology and Biotechnology*, vol. 98, no. 7, pp. 3257–3274, 2014.
- [49] D. R. Speth, S. Guerrero-Cruz, B. E. Dutilh, and M. S. M. Jetten, “Genome-based microbial ecology of anammox granules in a full-scale wastewater treatment system,” *Nature communications*, vol. 7, no. 1, 2016.
- [50] Y. Wang, J. Chen, S. Zhou et al., “16S rRNA gene high-throughput sequencing reveals shift in nitrogen conversion related microorganisms in a CANON system in response to salt stress,” *Chemical Engineering Journal*, vol. 317, pp. 512–521, 2017.
- [51] H. Vlamakis, Y. Chai, P. Beauregard, R. Losick, and R. Kolter, “Sticking together: building a biofilm the *Bacillus subtilis* way,” *Nature Reviews Microbiology*, vol. 11, no. 3, pp. 157–168, 2013.
- [52] Y. Qin, Y. He, Q. She, P. Larese-Casanova, P. Li, and Y. Chai, “Heterogeneity in respiratory electron transfer and adaptive iron utilization in a bacterial biofilm,” *Nature Communications*, vol. 10, no. 1, pp. 3702–3712, 2019.
- [53] V. S. Gawas, M. S. Shivaramu, S. R. Damare, D. Pujitha, R. M. Meena, and B. D. Shenoy, “Diversity and extracellular enzyme activities of heterotrophic bacteria from sediments of the Central Indian Ocean Basin,” *Scientific Reports*, vol. 9, no. 1, pp. 9403–9409, 2019.
- [54] H.-x. Lan, D. Yang, H. Zhang et al., “Effects of temperature on white water treatment by the dominant bacteria,” *Nordic Pulp & Paper Research Journal*, vol. 34, no. 1, pp. 133–137, 2019.
- [55] H.-C. Flemming and J. Wingender, “The biofilm matrix,” *Nature reviews microbiology*, vol. 8, no. 9, pp. 623–633, 2010.
- [56] C.-J. Tang, P. Zheng, L.-Y. Chai, and X. B. Min, “Characterization and quantification of anammox start-up in UASB reactors seeded with conventional activated sludge,” *International Biodeterioration & Biodegradation*, vol. 82, pp. 141–148, 2013.
- [57] A. Kostrytsia, S. Papirio, L. Morrison et al., “Biokinetics of microbial consortia using biogenic sulfur as a novel electron donor for sustainable denitrification,” *Bioresource Technology*, vol. 270, pp. 359–367, 2018.
- [58] E. I. Kompantseva, I. V. Kublanov, A. A. Perevalova et al., “*Calorithrix insularis* gen. nov., sp. nov., a novel representative of the phylum Calditrichaeota,” *International journal of systematic and evolutionary microbiology*, vol. 67, no. 5, pp. 1486–1490, 2017.
- [59] Z.-r. Chu, K. Wang, X.-k. Li, M. T. Zhu, L. Yang, and J. Zhang, “Microbial characterization of aggregates within a one-stage nitrification- anammox system using high-throughput amplicon sequencing,” *Chemical Engineering Journal*, vol. 262, pp. 41–48, 2015.
- [60] S. Tian, Z. Tian, H. Yang, M. Yang, and Y. Zhang, “Detection of viable bacteria during sludge ozonation by the combination of ATP assay with PMA-Miseq sequencing,” *Water*, vol. 9, no. 3, p. 166, 2017.
- [61] Y.-W. Cui, H.-Y. Zhang, P.-F. Lu, and Y. Z. Peng, “Effects of carbon sources on the enrichment of halophilic polyhydroxyalkanoate-storing mixed microbial culture in an aerobic dynamic feeding process,” *Scientific reports*, vol. 6, no. 1, 2016.
- [62] C. Wang, S. Liu, X. Xu, C. Zhang, D. Wang, and F. Yang, “Achieving mainstream nitrogen removal through simultaneous partial nitrification, anammox and denitrification process in an integrated fixed film activated sludge reactor,” *Chemosphere*, vol. 203, pp. 457–466, 2018.
- [63] S. Spring, P. Kämpfer, and K. H. Schleifer, “*Limnobacter thiooxidans* gen. nov., sp. nov., a novel thiosulfate-oxidizing bacterium isolated from freshwater lake sediment,” *International Journal of Systematic and Evolutionary Microbiology*, vol. 51, no. 4, pp. 1463–1470, 2001.
- [64] Q. Liu, M. Li, R. Liu et al., “Removal of trimethoprim and sulfamethoxazole in artificial composite soil treatment systems and diversity of microbial communities,” *Frontiers of Environmental Science & Engineering*, vol. 13, no. 2, 2019.

Research Article

Biosorption Mechanism of Aqueous Pb^{2+} , Cd^{2+} , and Ni^{2+} Ions on Extracellular Polymeric Substances (EPS)

Di Cui ¹, Chong Tan,¹ Hongna Deng,¹ Xunxue Gu,¹ Shanshan Pi,² Ting Chen,² Lu Zhou,² and Ang Li ²

¹Pharmaceutical Engineering Technology Research Center, Harbin University of Commerce, Harbin 150076, China

²State Key Laboratory of Urban Water Resource and Environment, School of Environment, Harbin Institute of Technology, Harbin 150090, China

Correspondence should be addressed to Di Cui; jscz_dd@hotmail.com and Ang Li; ang.li.harbin@gmail.com

Received 21 May 2020; Revised 8 June 2020; Accepted 9 June 2020; Published 24 June 2020

Academic Editor: Jin Li

Copyright © 2020 Di Cui et al. This is an open access article distributed under the Creative Commons Attribution License, which permits unrestricted use, distribution, and reproduction in any medium, provided the original work is properly cited.

Heavy metal pollution has been a focus with increasing attention, especially Pb^{2+} , Cd^{2+} , and Ni^{2+} in an aqueous environment. The adsorption capacity and mechanism of extracellular polymeric substances (EPS) from *Agrobacterium tumefaciens* F2 for three heavy metals were investigated in this study. The adsorption efficiency of 94.67%, 94.41%, and 77.95% were achieved for Pb^{2+} , Cd^{2+} , and Ni^{2+} adsorption on EPS, respectively. The experimental data of adsorption could be well fitted by Langmuir, Freundlich, Dubinin–Radushkevich isotherm models, and pseudo-second-order kinetic model. Model parameters analysis demonstrated the great adsorption efficiency of EPS, especially for Pb^{2+} , and chemisorption was the rate-limiting step during the adsorption process. The functional groups of C=O of carboxyl and C-O-C from sugar derivatives in EPS played the major role in the adsorption process judged by FTIR. In addition, 3D-EEM spectra indicated that tyrosine also assisted EPS adsorption for three heavy metals. But EPS from strain F2 used the almost identical adsorption mechanism for three kinds of divalent ions of heavy metals, so the adsorption efficiency difference of Pb^{2+} , Cd^{2+} , and Ni^{2+} on EPS could be correlated to the inherent characteristics of each heavy metal. This study gave the evidence that EPS has a great application potential as a bioadsorbent in the treatment of heavy metals pollution.

1. Introduction

Heavy metal pollution mainly comes from papermaking, smelting, electroplating, and other industrial wastewater and the overuse of pesticide and fertilizer [1]. Heavy metal pollutants are potentially harmful to the environment and human health, and they are not easily degraded by microorganisms in water. People intake heavy metal-contaminated water or food over an extended period, then they will suffer from various diseases or even cancer, such as anemia, bone pain, and chronic respiratory diseases for a long-term exposure to lead, cadmium, and nickel. In general, contaminated water often contains more than one heavy metal, such as industrial effluents, municipal wastewater, and industrial wastewater [2–4]. Therefore, exploring effective methods for controlling heavy metal pollution and improving the

water environment, especially for lead, cadmium, and nickel, are necessary.

At present, the most commonly used treatment techniques for heavy metal pollution include chemical precipitation, ion exchange, adsorption, membrane separation, oxidation reduction, and electrochemical [5–22]. Among these methods, adsorption is preferred for its simplicity, efficiency, flexibility in design, low waste production, and environmental-friendly characteristics for certain biosorbents [23]. Recently, microbial extracellular polymeric substances (EPS) have become a popular research topic in the effective treatment of heavy metal pollution due to its safety, efficiency, low energy consumption, and simple operation [24–30].

EPS produced by *Agrobacterium tumefaciens* F2 is a complex compound with high molecular weight and used

TABLE 1: Thermodynamic and kinetics models of heavy metals adsorption on EPS.

Models	Formula	Model parameters
Langmuir adsorption isothermal model	$q_e = q_m b C_e / (1 + b C_e)$	C_e —the initial concentration of heavy metals (mg L^{-1}) q_e —the unit adsorption capacity when the initial concentration is C_e (mg g^{-1}) q_m —maximum unit adsorption capacity (mg g^{-1}) b —Langmuir adsorption equilibrium constant (L mg^{-1})
Freundlich adsorption isothermal model	$q_e = K_F C_e^{1/n}$	K_F —adsorption capacity (mg g^{-1}) $1/n$ —Freundlich adsorption capacity
Dubinin–Radushkevich adsorption isothermal model	$q_e = q_m \exp(-k\epsilon^2)$ $\epsilon = RT \ln(1 + (1/C_e))$	q_e —equilibrium adsorption capacity (mg g^{-1}) q_m —maximum unit adsorption capacity (mg g^{-1}) k —constant related to adsorption capacity (mol^2/kJ^2) R —ideal gas constant ($8.314 \text{ J mol}^{-1} \text{ K}^{-1}$) T —thermodynamic temperature C_e —initial concentration of contaminants (mg L^{-1}) Average adsorption energy $E = (2k)^{-0.5}$
Pseudo-first order kinetics model	$\log(q_t - q_e) = \log q_e - (k_1/2.303)t$	t —adsorption time (min); q_t —unit adsorption capacity after t min (mg g^{-1}); q_e —the maximum unit adsorption capacity (mg g^{-1}); k_1 —pseudo-first-order reaction rate constant
Pseudo-second order kinetics model	$t/q_t = (1/k_2 q_e^2) + (1/q_e)t$	k_2 —pseudo-second-order reaction rate constant

to adsorb Pb^{2+} , Cd^{2+} , and Ni^{2+} pollutants in this study. Our previous researches focused on heavy metals or antibiotics adsorbed by bioflocculant MFX, which is one kind of EPS extracted from *Klebsiella* sp. J1 [31–38]. The results showed the great potential of EPS as water treatment materials and guided our subsequent studies. However, the main components of EPS produced by strain F2 are polysaccharide, which is different from the protein as the main component in bioflocculant MFX produced by strain J1. It was still unknown for the application potential of EPS produced by strain F2. Thus, it was used to adsorb heavy metal contaminants, and the adsorption mechanisms were systematically investigated via qualitative and quantitative analyses, thereby providing a new available bioadsorbent in water treatment.

2. Experimental Section

2.1. Strains and Reagents. *Agrobacterium tumefaciens* F2 is isolated by our group and now deposited in the China Common Microbial Culture Collection (CGMCC No. 10131). Lead nitrate, cadmium chloride, and nickel nitrate were purchased from Sigma-Aldrich, St Louis, MO, USA. Medium components were purchased from the Sinopharm Chemical Reagent Co., Ltd., Shanghai, China. Ultrapure water for all experiments was prepared with the Milli-Q system. All chemicals were analytical grade.

2.2. EPS Preparation. Strain F2 was applied to prepare EPS by the fermentation culture. The fermentation medium was composed of the following ingredients (g/L): glucose 10, K_2HPO_4 5, KH_2PO_4 2, NaCl 0.1, $\text{MgSO}_4 \cdot 7\text{H}_2\text{O}$ 0.2, yeast extract 0.5, and urea 0.5 adjusted at pH 7.2–7.5. Strain F2

was precultured in the fermentation medium to obtain the seed liquid, which was then inoculated into the fermentation medium with 5% carried by a sterilized fermentor. The relevant culture parameters were set at 30°C , 150 rpm for 24 h with 2.5 L min^{-1} . Then, the final fermentation liquid was centrifuged to eliminate the bacteria, and the precooling ethanol was added into the residual supernatant to collect white flocs and then dialyzed for 24 h. The flocs were freeze-dried by vacuum to obtain the dry powder of EPS and dissolved into ultrapure water before use.

2.3. Batch Adsorption Experiments. The stock solutions (100 mg L^{-1}) of Pb^{2+} , Cd^{2+} , and Ni^{2+} were prepared by dissolving lead nitrate, cadmium chloride, and nickel nitrate in ultrapure water. Working solutions were obtained by appropriate dilution of the stock solutions with ultrapure water and pH adjustment using 1 mol L^{-1} HNO_3 or NaOH. In each batch adsorption experiment, 0.2, 0.7, and 0.8 g L^{-1} adsorbents were added into 20 mL of Pb^{2+} , Cd^{2+} , and Ni^{2+} aqueous solution (20 mg L^{-1} , pH 6.0) and stirred for 0–70 min at 30°C . After adsorption, the concentrations of initial and residual ions in the aqueous solution were then measured by inductively coupled plasma optical emission spectrometry (ICP-OES; Optima 5300 DV, PE, USA) with the detection limit of $10 \mu\text{g L}^{-1}$. All samples were filtered by $0.45 \mu\text{m}$ cellulose acetate fiber before measurement. The adsorption efficiency (η) and the adsorption capacity (q_e) of Pb^{2+} , Cd^{2+} , and Ni^{2+} on EPS were calculated as follows:

$$q_e = \frac{(C_0 - C_e) V}{M}, \quad (1)$$

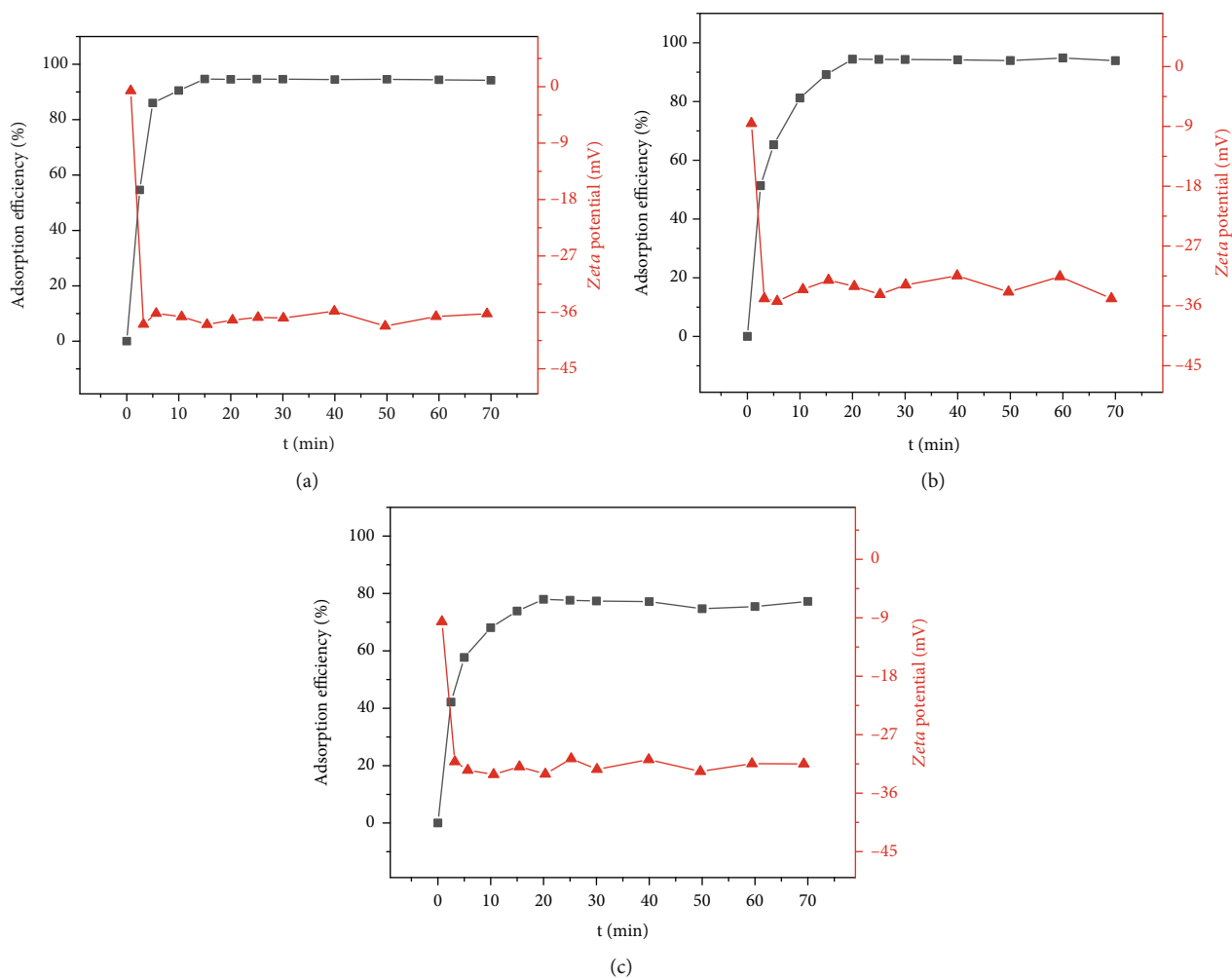


FIGURE 1: Adsorption efficiency and *Zeta* potential of Pb^{2+} (a), Cd^{2+} (b), and Ni^{2+} (c) adsorption on EPS.

$$\eta = \frac{(C_0 - C_e)}{C_0} \times 100\%, \quad (2)$$

where C_0 and C_e are the initial and equilibrium concentrations of heavy metal ion, respectively (mg L^{-1}), V is the solution volume (L), and M is the used amount of EPS (g). The average values were recorded with standard deviations within $\pm 1.3\%$, and some error bars are not shown due to the magnitude being smaller than that of the symbols used to plot the graphs.

2.4. Adsorption Isotherms and Kinetics. Langmuir, Freundlich, and Dubinin–Radushkevich isotherm models were used to determine the sorption equilibrium at 20°C , 30°C , and 40°C , respectively. To investigate the adsorption isotherm, the initial concentration of heavy metal ions was ranged at $5\text{--}50\text{ mg L}^{-1}$, and other conditions were consistent with the abovementioned batch adsorption experiments. For sorption kinetic experiment of heavy metal ions on EPS, the experimental data were analyzed using pseudo-first-order and pseudo-second-order kinetic models. The sorption time was during 2.5–70 min, and other parameters were the same with the abovementioned batch adsorption

experiments. All models and key parameters are shown in Table 1.

2.5. Characterization of Adsorption Mechanism. The adsorption mechanism of heavy metal ions on EPS and characteristics before and after adsorption was analyzed using Fourier-transform infrared spectroscopy (FTIR), *Zeta* potential analysis, and three-dimensional fluorescence spectrophotometry (3D-EEM) to examine the interactions between EPS and Pb^{2+} , Cd^{2+} , and Ni^{2+} , respectively. EPS loading Pb^{2+} , Cd^{2+} , and Ni^{2+} samples under the optimal experimental conditions were collected and then rinsed to remove free heavy metal ions using ultrapure water. EPS (before and after Pb^{2+} , Cd^{2+} , and Ni^{2+} loading) were processed by vacuum freeze-drying. The spectra in the range of $400\text{--}4000\text{ cm}^{-1}$ were recorded via an FTIR spectrometer using the KBr disc technique. The *Zeta* potential of the system in the entire process was measured with zeta meter equipment. 3D-EEM was applied to study the variation of active ingredients before and after adsorption via a three-dimensional fluorescence spectrometer (FP6500, JASCO, Japan). Scanning parameters were set as the emission spectra of $220\text{--}450\text{ nm}$ at 1 nm increment by varying the excitation wavelength of $220\text{--}650\text{ nm}$ at

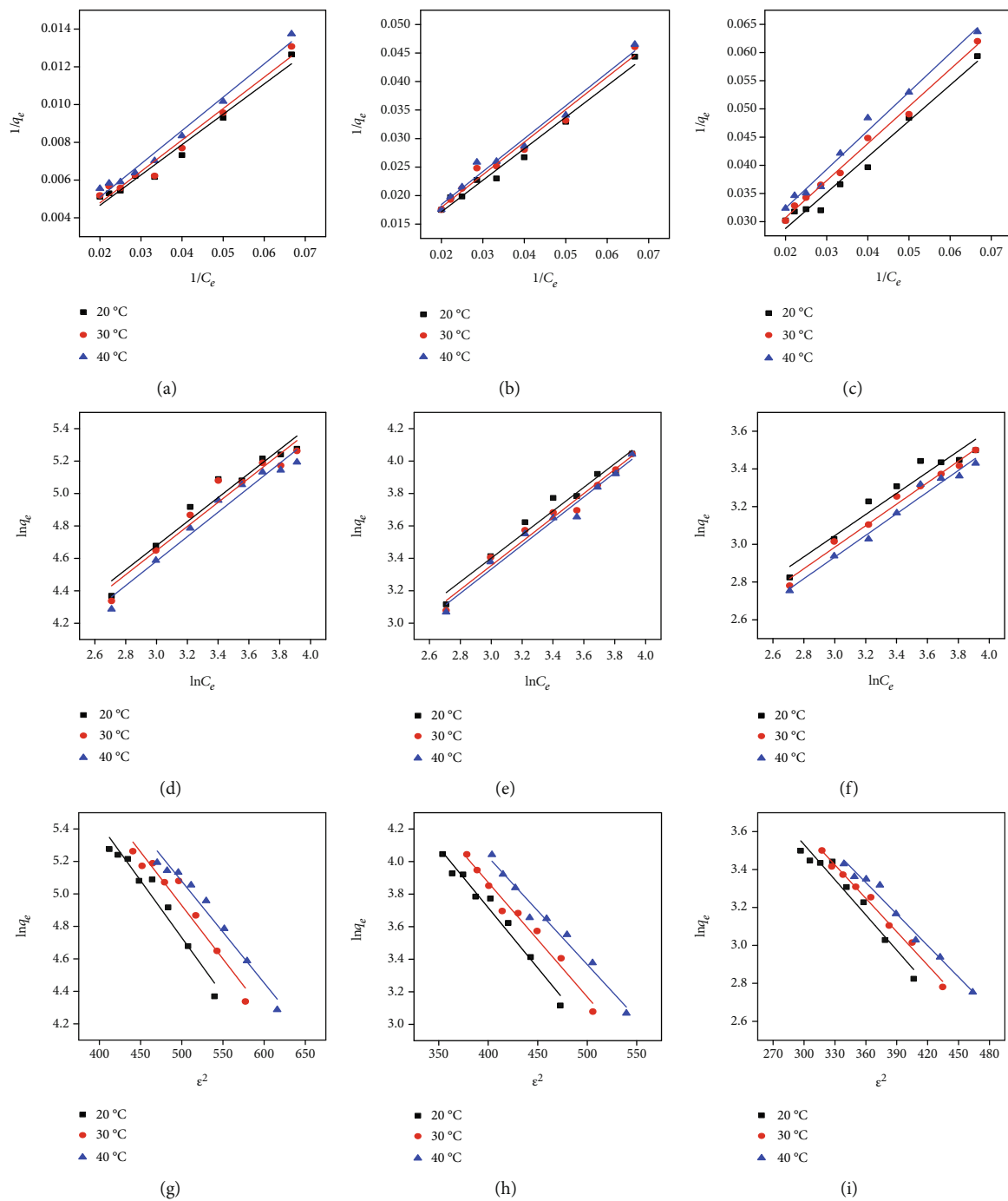


FIGURE 2: Continued.

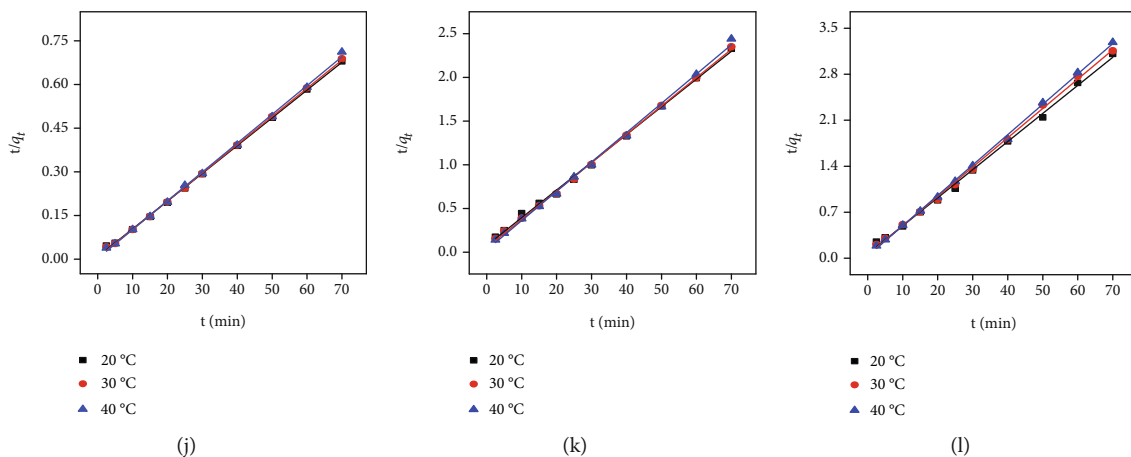


FIGURE 2: Langmuir (a–c), Freundlich (d–f), Dubinin–Radushkevich (g–i) isotherms, and pseudo-second-order kinetics (j–l) model of Pb^{2+} , Cd^{2+} , and Ni^{2+} adsorption on EPS.

5 nm increment. A blank solution (Milli-Q water) was subtracted from the sample.

3. Results and Discussion

3.1. Adsorption Efficiency of Heavy Metals on EPS. Figure 1 shows the adsorption efficiency and *Zeta* potential of metal ions on EPS at different adsorption time. The adsorption efficiency increased rapidly in the initial 5 min and increased gradually until adsorption saturation at almost 20 min with the highest adsorption efficiency of 94.67%, 94.41%, and 77.95% for Pb^{2+} , Cd^{2+} , and Ni^{2+} on EPS. Thus, EPS exhibited superior adsorption efficiency for target pollutants, especially Pb^{2+} and Cd^{2+} . However, the adsorption efficiency for Ni^{2+} on EPS is clearly not as ideal as Pb^{2+} and Cd^{2+} , so the further adsorption mechanism is still needed to explain the adsorption difference. *Zeta* potential analysis was used to analyze the stability of adsorption reaction along with different time before and after Pb^{2+} , Cd^{2+} , and Ni^{2+} adsorption on EPS. As seen in Figure 1(b), the *Zeta* potentials of reaction system rapidly decreased after adding EPS into Pb^{2+} , Cd^{2+} , and Ni^{2+} and reached stable at -37.90 , -34.9 , and -31.2 mV, respectively. Subsequently, the *Zeta* potential remained stable along with the increased adsorption efficiency, thus indicating that the whole adsorption reaction process is stable. Negatively charged EPS was favorable for its adsorption for positively charged heavy metals, so it exhibited the superior adsorption efficiency for Pb^{2+} , Cd^{2+} , and Ni^{2+} .

3.2. Isotherm Models

3.2.1. Langmuir Adsorption Isotherm Model. The fitting results of the Langmuir adsorption isotherms of Pb^{2+} , Cd^{2+} , and Ni^{2+} on EPS at 20°C , 30°C , and 40°C are shown in Figures 2(a)–2(c). The results showed that the R^2 are all greater than 0.90, indicating that Pb^{2+} , Cd^{2+} , and Ni^{2+} adsorption on EPS could be fitted well by Langmuir adsorption isotherm models. The data for the adsorption process of Pb^{2+} , Cd^{2+} , and Ni^{2+} on EPS satisfactorily fitted to the Langmuir model in an aquatic system with $R^2 > 0.90$, indicating

TABLE 2: Parameters of Langmuir adsorption isotherms.

Heavy metals	Temperature ($^\circ\text{C}$)	q_m (mg g^{-1})	b (L mg^{-1}) $\times 10^{-3}$	R^2
Pb^{2+}	20	714.29	8.71	0.97
	30	666.67	9.01	0.97
	40	625.00	9.07	0.98
Cd^{2+}	20	104.17	20.16	0.96
	30	97.09	21.03	0.96
	40	92.59	21.80	0.96
Ni^{2+}	20	51.28	34.20	0.96
	30	48.08	35.48	0.94
	40	45.05	36.53	0.97

TABLE 3: Parameters of Freundlich adsorption isotherms.

Heavy metals	Temperature ($^\circ\text{C}$)	K_F (mg g^{-1})	n	R^2
Pb^{2+}	20	11.63	1.3484	0.95
	30	11.22	1.3452	0.94
	40	10.18	1.3259	0.97
Cd^{2+}	20	5.05	1.6739	0.93
	30	4.68	1.6464	0.94
	40	4.57	1.6447	0.95
Ni^{2+}	20	4.69	2.0080	0.94
	30	4.47	2.0076	0.93
	40	4.25	2.0072	0.97

that monolayer adsorption could exist [31]. The model parameters are shown in Table 2, in which q_m gradually decreases and b increases with the increased temperature, indicating the exothermic nature of the adsorption process.

3.2.2. Freundlich Adsorption Isotherm Model. The fitting results of the Freundlich isotherm model are shown in Figures 2(d)–2(f), and the model parameters are presented in Table 3. The results suggested that adsorption of Pb^{2+} ,

TABLE 4: Parameters of Dubinin–Radushkevich model.

Heavy metals	Temperature (°C)	E (kJ mol ⁻¹)	R^2
Pb ²⁺	20	8.45	0.96
	30	8.70	0.95
	40	8.91	0.97
Cd ²⁺	20	9.05	0.93
	30	9.28	0.95
	40	9.62	0.95
Ni ²⁺	20	9.53	0.95
	30	9.90	0.93
	40	10.21	0.97

Cd²⁺, and Ni²⁺ on EPS is also consistent with the Freundlich isotherm model with $R^2 > 0.90$. With the gradual increase of temperature, the gradually decreased K_F of Pb²⁺, Cd²⁺, and Ni²⁺ adsorption on EPS indicated that the adsorption reaction is exothermic [39]. $n > 1$ indicated the good adsorption capacity of Pb²⁺, Cd²⁺, and Ni²⁺ on EPS [31, 37].

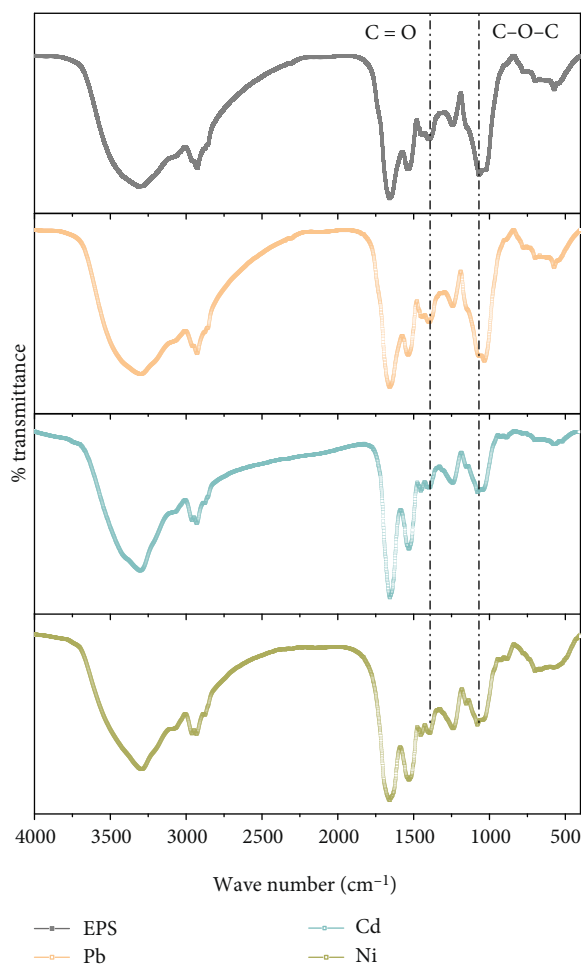
3.2.3. Dubinin–Radushkevich Adsorption Isotherm Model.

The model is used to judge whether the adsorption process is completed by a physical or chemical reaction [40]. The model parameters of Dubinin–Radushkevich can be used to explain the adsorption process with $R^2 > 0.90$. The fitting results of Dubinin–Radushkevich models and parameters at 20°C, 30°C, and 40°C are presented in Figures 2(g)–2(i) and Table 4, respectively. Based on the Dubinin–Radushkevich model, the physical adsorption is resulted from Van der Waals forces judged by that E value was lower than 8 kJ mol⁻¹, whereas the chemical adsorption usually involves ion exchange judged by that the E value was 8–16 kJ mol⁻¹ [41]. E values of Pb²⁺, Cd²⁺, and Ni²⁺ adsorption on EPS are between 8 kJ mol⁻¹ and 16 kJ mol⁻¹, respectively, indicating that the adsorption process is mainly completed by the chemical adsorption. The above analysis showed that the adsorption process of Pb²⁺, Cd²⁺, and Ni²⁺ on EPS could be well fitted by the Langmuir, Freundlich, and Dubinin–Radushkevich isotherm models ($R^2 > 0.90$), indicating the complex adsorption process involved in multiple adsorption mechanism, especially chemical adsorption related to ion exchange.

3.3. Kinetic Models. The pseudo-first- and second-order kinetic models were applied to fit the data for adsorption behavior. However, the pseudo-first-order dynamic model could not effectively fit the adsorption process with $R^2 < 0.80$ (data not shown). The pseudo-second-order kinetic model is usually used to clarify the limiting step during the adsorption process. The model was used to analyze the adsorption process and mechanism via quantitative approaches in this study. The fitting results of the pseudo-second-order kinetics model are shown in Figures 2(j)–2(l), and the model parameters are presented in Table 5. $R^2 > 0.90$ indicated that the adsorption process can be better fitted by the pseudo-second-order kinetic model. The results

TABLE 5: Parameters of pseudo-second-order kinetics model.

Heavy metals	Temperature (°C)	q_m (mg g ⁻¹)	k_2 (min ⁻¹) × 10 ⁻²	R^2
Pb ²⁺	20	105.26	1.04	0.99
	30	103.09	1.57	0.99
	40	101.01	3.77	0.99
Cd ²⁺	20	31.55	1.33	0.99
	30	30.86	2.09	0.99
	40	29.85	4.40	0.99
Ni ²⁺	20	23.42	2.74	0.99
	30	22.42	4.00	0.99
	40	21.65	6.45	0.99

FIGURE 3: Functional group analysis of EPS before and after Pb²⁺, Cd²⁺, and Ni²⁺ adsorption.

showed that the chemical adsorption was the rate-limiting step during the adsorption process [24].

The apparent activation energy (E_a) is calculated from the reaction rate k based on the Arrhenius formula in the pseudo-second-order kinetics. The adsorption process is physical adsorption when the E_a is 5–40 kJ mol⁻¹ and

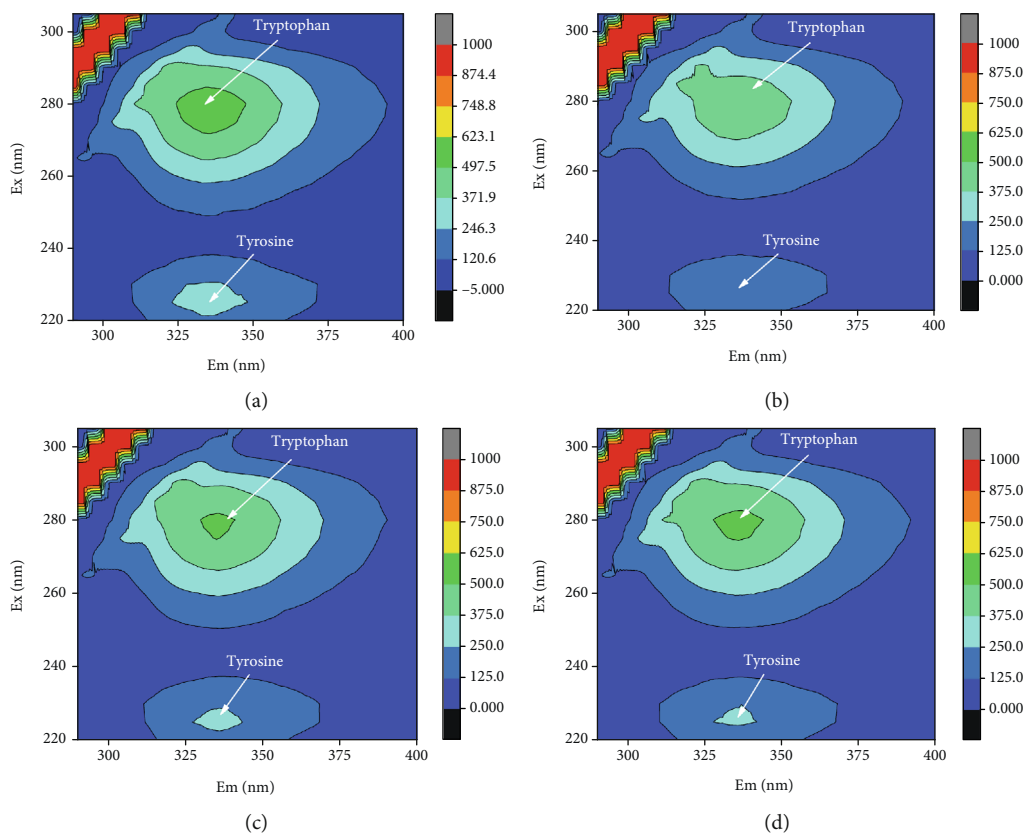


FIGURE 4: 3D-EEM spectrum of EPS (a) before adsorption, and after adsorption of (b) Pb^{2+} , (c) Cd^{2+} , (d) Ni^{2+} .

chemical adsorption when the E_a is 40–800 kJ mol^{-1} [32, 42]. The E_a values of Pb^{2+} , Cd^{2+} , and Ni^{2+} adsorption on EPS were 709.27, 660.44, and 472.23 kJ mol^{-1} , respectively, indicating a chemical adsorption process.

3.4. Adsorption Mechanism. Several studies have shown that the functional group is a key factor for contaminant adsorption on the EPS. The infrared spectra of EPS before and after adsorption of Pb^{2+} , Cd^{2+} , and Ni^{2+} are shown in Figure 3, and several peaks are observed, including O-H, C=O, N-H, C-N, C-O-C, and C-O in EPS [32, 33]. As shown in Figure 3, obvious changes of the peak intensity in C=O of carboxyl and C-O-C bands from sugar derivatives were observed after heavy metal adsorption. This finding might be explained by the polysaccharides as the main constituent in EPS played the key role during the adsorption process.

3D-EEM spectrum exhibited that $\lambda_{\text{ex}}/\lambda_{\text{em}} = (270 - 280) \text{ nm}/(325 - 335) \text{ nm}$ and $\lambda_{\text{ex}}/\lambda_{\text{em}} = (225 - 235) \text{ nm}/(325 - 335) \text{ nm}$ could represent aromatic amino acid tryptophan and tyrosine of protein-like substances [43]. Figure 4 showed that their fluorescence intensity weakened after EPS absorbing Pb^{2+} , Cd^{2+} , and Ni^{2+} , displaying different levels of quenching. The fluorescence intensity of tyrosine proteins in EPS showed relatively more obvious quenching after absorbing Pb^{2+} , Cd^{2+} , and Ni^{2+} . Results showed the tyrosine of protein-like substances in EPS also played a somewhat role in the adsorption for heavy metals. A possible explanation was that polysaccharide is the main component in EPS produced by strain F2 [44], while the low protein content in

EPS resulted in the minor change during the adsorption of heavy metals.

In summary, EPS from strain F2 used the almost identical adsorption mechanism for three kinds of divalent ions of heavy metals. The adsorption efficiency difference of Pb^{2+} , Cd^{2+} , and Ni^{2+} on EPS could be correlated to the inherent characteristics of each heavy metals, which deserve an in-depth investigation via a quantitative structure–activity relationship (QSAR). The obvious changes in C=O of carboxyl and C-O-C bands from sugar derivatives via FTIR could support the viewpoint of that the polysaccharides as the main constituent in EPS played the key role during the adsorption process of Pb^{2+} , Cd^{2+} , and Ni^{2+} ions. In addition, the weak quenching changes in tyrosine of protein-like substances in EPS via 3D-EEM was also observed after absorbing heavy metals, which could indicate protein-like substances in EPS also assisted in heavy metals adsorption. At present, EPS has been reported to be used in the Sb(V) reduction and adsorption, which was enhanced through nZVI coating [45]. Therefore, we would consider applying EPS from strain F2 into the redox-adsorption of other substances, such as perchlorate and vanadate [46, 47], in the future work.

4. Conclusion

EPS from *Agrobacterium tumefaciens* F2 exhibited effective adsorption efficiency for Pb^{2+} , Cd^{2+} , and Ni^{2+} , especially for Pb^{2+} . But EPS from strain F2 used the almost identical adsorption mechanism for three kinds of divalent ions of

heavy metals, so the adsorption efficiency difference of Pb^{2+} , Cd^{2+} , and Ni^{2+} on EPS could be correlated to the inherent characteristics of each heavy metals. Thermodynamics and kinetics analysis displayed the exothermic nature of the adsorption process, the good adsorption capacity of adsorbents, and the key role of chemical adsorption. The adsorption mechanism demonstrated Pb^{2+} , Cd^{2+} , and Ni^{2+} adsorption on EPS was mainly attributed to the functional groups of the C=O of carboxyl and C-O-C from sugar derivatives. To some extent, amino acid protein-like substances in EPS also assisted in heavy metals adsorption. EPS from strain F2 as a bioadsorbent has great application potential in the treatment of heavy metal ions from contaminated aquatic systems.

Data Availability

Data can be available by contacting the corresponding author.

Conflicts of Interest

The authors declare no actual or potential competing financial interests.

Acknowledgments

This work was financially supported by the National Natural Science Foundation of China (51608154), the Foundation for Distinguished Young Talents in Higher Education of Heilongjiang, China (UNPYSCT-2017211), the Foundation for Distinguished Young Talents of Harbin University of Commerce, China (18XN026), and the PhD early development program of Harbin University of Commerce, China (2016BS15).




References

- [1] A. Azimi, A. Azari, M. Rezakazemi, and M. Ansarpour, "Removal of heavy metals from industrial wastewaters: a review," *ChemBioEng Reviews*, vol. 4, no. 1, pp. 37–59, 2017.
- [2] C. Wang, X. Hu, M. Chen, and Y. Wu, "Total concentrations and fractions of Cd, Cr, Pb, Cu, Ni and Zn in sewage sludge from municipal and industrial wastewater treatment plants," *Journal of Hazardous Materials*, vol. 119, no. 1-3, pp. 245–249, 2005.
- [3] A. Demirbas, E. Pehlivan, F. Gode, T. Altun, and G. Arslan, "Adsorption of Cu(II), Zn(II), Ni(II), Pb(II), and Cd(II) from aqueous solution on Amberlite IR-120 synthetic resin," *Journal of Colloid and Interface Science*, vol. 282, no. 1, pp. 20–25, 2005.
- [4] H. A. Aziz, M. N. Adlan, and K. S. Ariffin, "Heavy metals (Cd, Pb, Zn, Ni, Cu and Cr(III)) removal from water in Malaysia: post treatment by high quality limestone," *Bioresource Technology*, vol. 99, no. 6, pp. 1578–1583, 2008.
- [5] M. Q. Jiang, X. Y. Jin, X. Q. Lu, and Z. L. Chen, "Adsorption of Pb(II), Cd(II), Ni(II) and Cu(II) onto natural kaolinite clay," *Desalination*, vol. 252, no. 1-3, pp. 33–39, 2010.
- [6] S. Chatterjee and S. De, "Adsorptive removal of arsenic from groundwater using chemically treated iron ore slime incorporated mixed matrix hollow fiber membrane," *Separation and Purification Technology*, vol. 179, pp. 357–368, 2017.
- [7] E. Padilla-Ortega, R. Leyva-Ramos, and J. V. Flores-Cano, "Binary adsorption of heavy metals from aqueous solution onto natural clays," *Chemical Engineering Journal*, vol. 225, pp. 535–546, 2013.
- [8] A. Kongsuwan, P. Patnukao, and P. Pavasant, "Binary component sorption of Cu(II) and Pb(II) with activated carbon from Eucalyptus camaldulensis Dehn bark," *Journal of Industrial and Engineering Chemistry*, vol. 15, no. 4, pp. 465–470, 2009.
- [9] Y. Chen, X. Wu, L. Lv et al., "Enhancing reducing ability of α -zein by fibrillation for synthesis of Au nanocrystals with continuous flow catalysis," *Journal of Colloid and Interface Science*, vol. 491, pp. 37–43, 2017.
- [10] R. Mukherjee, P. Bhunia, and S. De, "Impact of graphene oxide on removal of heavy metals using mixed matrix membrane," *Chemical Engineering Journal*, vol. 292, pp. 284–297, 2016.
- [11] K. Athanasiadis and B. Helmreich, "Influence of chemical conditioning on the ion exchange capacity and on kinetic of zinc uptake by clinoptilolite," *Water Research*, vol. 39, no. 8, pp. 1527–1532, 2005.
- [12] B. Alyuz and S. Veli, "Kinetics and equilibrium studies for the removal of nickel and zinc from aqueous solutions by ion exchange resins," *Journal of Hazardous Materials*, vol. 167, no. 1-3, pp. 482–488, 2009.
- [13] M. Kumar, R. Shevate, R. Hilke, and K. V. Peinemann, "Novel adsorptive ultrafiltration membranes derived from polyvinyltetrazole-co-polyacrylonitrile for Cu(II) ions removal," *Chemical Engineering Journal*, vol. 301, pp. 306–314, 2016.
- [14] M. Mondal, M. Dutta, and S. De, "A novel ultrafiltration grade nickel iron oxide doped hollow fiber mixed matrix membrane: spinning, characterization and application in heavy metal removal," *Separation and Purification Technology*, vol. 188, pp. 155–166, 2017.
- [15] B. A. Marinho, R. O. Cristóvão, R. Djellabi, J. M. Loureiro, R. A. R. Boaventura, and V. J. P. Vilar, "Photocatalytic reduction of Cr(VI) over TiO_2 -coated cellulose acetate monolithic structures using solar light," *Applied Catalysis B: Environmental*, vol. 203, pp. 18–30, 2017.
- [16] N. Abdullah, R. J. Gohari, N. Yusof et al., "Polysulfone/hydroxide ferric oxide ultrafiltration mixed matrix membrane: preparation, characterization and its adsorptive removal of lead (II) from aqueous solution," *Chemical Engineering Journal*, vol. 289, pp. 28–37, 2016.
- [17] Q. Chen, Z. Luo, C. Hills, G. Xue, and M. Tyrer, "Precipitation of heavy metals from wastewater using simulated flue gas: sequent additions of fly ash, lime and carbon dioxide," *Water Research*, vol. 43, no. 10, pp. 2605–2614, 2009.
- [18] M. T. Alvarez, C. Crespo, and B. Mattiasson, "Precipitation of Zn(II), Cu(II) and Pb(II) at bench-scale using biogenic hydrogen sulfide from the utilization of volatile fatty acids," *Chemosphere*, vol. 66, no. 9, pp. 1677–1683, 2007.
- [19] X. Li, H. Li, X. Xu, N. Guo, L. Yuan, and H. Yu, "Preparation of a reduced Graphene oxide @ stainless steel net electrode and its application of electrochemical removal Pb(II)," *Journal of the Electrochemical Society*, vol. 164, no. 4, pp. E71–E77, 2017.
- [20] Q. Chang, M. Zhang, and J. Wang, "Removal of Cu^{2+} and turbidity from wastewater by mercaptoacetyl chitosan," *Journal of Hazardous Materials*, vol. 169, no. 1-3, pp. 621–625, 2009.

- [21] W. Peng, H. Li, Y. Liu, and S. Song, "A review on heavy metal ions adsorption from water by graphene oxide and its composites," *Journal of Molecular Liquids*, vol. 230, pp. 496–504, 2017.
- [22] S. Deng, P. Wang, G. Zhang, and Y. Dou, "Polyacrylonitrile-based fiber modified with thiosemicarbazide by microwave irradiation and its adsorption behavior for Cd(II) and Pb(II)," *Journal of Hazardous Materials*, vol. 307, pp. 64–72, 2016.
- [23] D. P. Sounthararajah, P. Loganathan, J. Kandasamy, and S. Vigneswaran, "Adsorptive removal of heavy metals from water using sodium titanate nanofibres loaded onto GAC in fixed-bed columns," *Journal of Hazardous Materials*, vol. 287, pp. 306–316, 2015.
- [24] J. Feng, Z. Yang, G. Zeng et al., "The adsorption behavior and mechanism investigation of Pb(II) removal by flocculation using microbial flocculant GA1," *Bioresource Technology*, vol. 148, pp. 414–421, 2013.
- [25] L. Wei, Y. Li, D. R. Noguera et al., "Adsorption of Cu²⁺ and Zn²⁺ by extracellular polymeric substances (EPS) in different sludges: effect of EPS fractional polarity on binding mechanism," *Journal of Hazardous Materials*, vol. 321, pp. 473–483, 2017.
- [26] M. Shahadat, T. T. Teng, M. Rafatullah, Z. A. Shaikh, T. R. Sreekrishnan, and S. W. Ali, "Bacterial biofloculants: a review of recent advances and perspectives," *Chemical Engineering Journal*, vol. 328, pp. 1139–1152, 2017.
- [27] N. Li, D. Wei, S. Wang et al., "Comparative study of the role of extracellular polymeric substances in biosorption of Ni(II) onto aerobic/anaerobic granular sludge," *Journal of Colloid and Interface Science*, vol. 490, pp. 754–761, 2017.
- [28] J. Wang, Q. Li, M. M. Li, T. H. Chen, Y. F. Zhou, and Z. B. Yue, "Competitive adsorption of heavy metal by extracellular polymeric substances (EPS) extracted from sulfate reducing bacteria," *Bioresource Technology*, vol. 163, pp. 374–376, 2014.
- [29] J. Guo and J. Yu, "Sorption characteristics and mechanisms of Pb(II) from aqueous solution by using biofloculant MBFR10543," *Applied Microbiology and Biotechnology*, vol. 98, no. 14, pp. 6431–6441, 2014.
- [30] P. Yan, J. S. Xia, Y. P. Chen et al., "Thermodynamics of binding interactions between extracellular polymeric substances and heavy metals by isothermal titration microcalorimetry," *Bioresource Technology*, vol. 232, pp. 354–363, 2017.
- [31] A. Li, S. Pi, W. Wei, T. Chen, J. Yang, and F. Ma, "Adsorption behavior of tetracycline by extracellular polymeric substrates extracted from *Klebsiella sp. J1*," *Environmental Science and Pollution Research*, vol. 23, no. 24, pp. 25084–25092, 2016.
- [32] W. Wei, Q. Wang, A. Li et al., "Biosorption of Pb (II) from aqueous solution by extracellular polymeric substances extracted from *Klebsiella sp. J1*: Adsorption behavior and mechanism assessment," *Scientific Reports*, vol. 6, no. 1, p. 31575, 2016.
- [33] J. Yang, W. Wei, S. Pi et al., "Competitive adsorption of heavy metals by extracellular polymeric substances extracted from *Klebsiella sp. J1*," *Bioresource Technology*, vol. 196, pp. 533–539, 2015.
- [34] A. Li, C. Zhou, Z. Liu et al., "Direct solid-state evidence of H₂-induced partial U(VI) reduction concomitant with adsorption by extracellular polymeric substances (EPS)," *Biotechnology and Bioengineering*, vol. 115, no. 7, pp. 1685–1693, 2018.
- [35] W. Wei, A. Li, F. Ma et al., "Simultaneous sorption and reduction of Cr(VI) in aquatic system by microbial extracellular polymeric substances from *Klebsiella sp. J1*," *Journal of Chemical Technology & Biotechnology*, vol. 93, no. 11, pp. 3152–3159, 2018.
- [36] W. Wei, A. Li, J. Yang et al., "Synergetic effects and flocculation behavior of anionic polyacrylamide and extracellular polymeric substrates extracted from *Klebsiella sp. J1* on improving soluble cadmium removal," *Bioresource Technology*, vol. 175, pp. 34–41, 2015.
- [37] S. Pi, A. Li, W. Wei et al., "Synthesis of a novel magnetic nano-scale biosorbent using extracellular polymeric substances from *Klebsiella sp. J1* for tetracycline adsorption," *Bioresource Technology*, vol. 245, no. Part A, pp. 471–476, 2017.
- [38] W. Wei, A. Li, S. Pi et al., "Synthesis of core-shell magnetic nanocomposite Fe₃O₄@ microbial extracellular polymeric substances for simultaneous redox sorption and recovery of silver ions as silver nanoparticles," *ACS Sustainable Chemistry & Engineering*, vol. 6, no. 1, pp. 749–756, 2017.
- [39] S. Ghorai, A. Sinhamahapatra, A. Sarkar, A. B. Panda, and S. Pal, "Novel biodegradable nanocomposite based on XG-g-PAM/SiO₂: application of an efficient adsorbent for Pb²⁺ ions from aqueous solution," *Bioresource Technology*, vol. 119, pp. 181–190, 2012.
- [40] A. Çabuk, T. Akar, S. Tunali, and S. Gedikli, "Biosorption of Pb(II) by industrial strain of *Saccharomyces cerevisiae* immobilized on the biomatrix of cone biomass of *Pinus nigra*: equilibrium and mechanism analysis," *Chemical Engineering Journal*, vol. 131, no. 1-3, pp. 293–300, 2007.
- [41] Y. A. Aydın and N. D. Aksoy, "Adsorption of chromium on chitosan: optimization, kinetics and thermodynamics," *Chemical Engineering Journal*, vol. 151, no. 1-3, pp. 188–194, 2009.
- [42] S. Chakravarty, A. Mohanty, T. N. Sudha et al., "Removal of Pb(II) ions from aqueous solution by adsorption using bael leaves (*Aegle marmelos*)," *Journal of Hazardous Materials*, vol. 173, no. 1-3, pp. 502–509, 2010.
- [43] S. Pi, A. Li, D. Cui et al., "Biosorption behavior and mechanism of sulfonamide antibiotics in aqueous solution on extracellular polymeric substances extracted from *Klebsiella sp. J1*," *Bioresource Technology*, vol. 272, pp. 346–350, 2019.
- [44] J. Yang, D. Wu, A. Li et al., "The addition of N-hexanoyl-homoserine lactone to improve the microbial flocculant production of *Agrobacterium tumefaciens* strain F2, an exopolysaccharide biofloculant-producing bacterium," *Applied Biochemistry and Biotechnology*, vol. 179, no. 5, pp. 728–739, 2016.
- [45] L. Zhou, A. Li, F. Ma et al., "Combining high electron transfer efficiency and oxidation resistance in nZVI with coatings of microbial extracellular polymeric substances to enhance Sb(V) reduction and adsorption," *Chemical Engineering Journal*, vol. 395, p. 125168, 2020.
- [46] C. Y. Lai, Q. Y. Dong, J. X. Chen et al., "Role of extracellular polymeric substances in a methane based membrane biofilm reactor reducing vanadate," *Environmental Science & Technology*, vol. 52, no. 18, pp. 10680–10688, 2018.
- [47] P. L. Lv, L. D. Shi, Q. Y. Dong, B. Rittmann, and H. P. Zhao, "How nitrate affects perchlorate reduction in a methane-based biofilm batch reactor," *Water Research*, vol. 171, p. 115397, 2020.

Research Article

Integration of Marine Macroalgae (*Chaetomorpha maxima*) with a Moving Bed Bioreactor for Nutrient Removal from Maricultural Wastewater

Xian Li ^{1,2,3}, Yale Deng,⁴ Xueying Li,^{1,2,3} Xiaona Ma ^{1,2,3}, Jinxia Wang ^{1,2,3}, and Jun Li^{1,2,3}

¹Key Laboratory of Experimental Marine Biology, Institute of Oceanology, Chinese Academy of Sciences, Qingdao 266071, China

²Laboratory for Marine Biology and Biotechnology, Qingdao National Laboratory for Marine Science and Technology, Qingdao 266071, China

³Center for Ocean Mega-Science, Chinese Academy of Sciences, Qingdao 266071, China

⁴Aquaculture and Fisheries Group, Department of Animal Sciences, Wageningen University, Wageningen 6708, Netherlands

Correspondence should be addressed to Xiaona Ma; marianna_iocas@163.com and Jinxia Wang; jxwang@qdio.as.cn

Received 16 April 2020; Revised 18 May 2020; Accepted 26 May 2020; Published 23 June 2020

Academic Editor: Jin Li

Copyright © 2020 Xian Li et al. This is an open access article distributed under the Creative Commons Attribution License, which permits unrestricted use, distribution, and reproduction in any medium, provided the original work is properly cited.

Rather than direct nutrient removal from wastewaters, an alternative approach aimed at nutrient recovery from aquacultural wastewaters could enable sustainable management for aquaculture production. This study demonstrated the feasibility of cultivating marine macroalgae (*Chaetomorpha maxima*) with a moving bed bioreactor (MBBR-MA), to remove nitrogen and phosphorus in aquaculture wastewater as well as to produce macroalgae biomass. MBBR-MA significantly increased the simultaneous removal of nitrate and phosphate in comparison with only MBBR, resulting in an average total nitrogen (TN) and total phosphorus (TP) removal efficiency of $42.8 \pm 5.5\%$ and $83.7 \pm 7.7\%$, respectively, in MBBR-MA while MBBR had no capacity for TN and TP removal. No chemical oxygen demand (COD) removal was detected in both reactors. Phosphorus could be a limiting factor for nitrogen uptake when N:P ratio increased. The recovered nitrogen and phosphorus resulted in a specific growth rate of 3.86%–10.35%/day for *C. maxima* with an uptake N:P ratio of 6. The presence of macroalgae changed the microbial community in both the biofilter and water by decreasing the relative abundance of Proteobacteria and Nitrospirae and increasing the abundance of Bacteroidetes. These findings indicate that the integration of the macroalgae *C. maxima* with MBBR could represent an effective wastewater treatment option, especially for marine recirculating aquaculture systems.

1. Introduction

Nitrogen and phosphorus removal from wastewater in aquaculture production systems is crucial to reduce the eutrophication of receiving water and to ensure the sustainable development of the industry. The limited availability of land and water resources is restricting the further expansion of aquaculture. There has been growing interest in the development of intensive land-based marine aquaculture, especially recirculating aquaculture systems (RASs), in which water can be reused after a series of treatment processes [1]. A biofilter is the core water treatment unit in an RAS, in which

ammonia, as the most toxic form of nitrogen, is converted to nitrite by ammonia-oxidizing bacteria (AOB) and then further converted by nitrite-oxidizing bacteria (NOB) to nitrate [2]. A moving bed biological filter (MBBR) is widely used in RASs due to its advantageous properties, including sufficient mixing, effective mass transfer, high removal rate of pollutants, and relatively small spatial requirements [3]. However, the nitrate and phosphorus concentration tends to accumulate to a high value in an MBBR system, and nitrate even could reach hundreds of mg/L [4–6]. It has been shown that high nitrate concentrations can also pose a potential

hazard to the cultured species [7–9]. Without proper treatment, the nitrate and phosphorus discharged in the saline wastewater can lead to eutrophication of the adjacent ecosystems [10].

Biological denitrification that converts nitrate and nitrite to nitrogen gas has been applied in RASs [11]; however, this process faces operational challenges, such as the requirement for a large carbon input, technical management, and nitrous oxide emissions [12, 13]. Moreover, eliminating nitrate from the system through nitrogen gas reduces the nutrient recovery efficiency from wastewater. Phosphorus is considered a growth-limiting nutrient in many water systems, which could be removed by plants, microorganism, and chemicals, while no effective approaches have been developed in RAS for phosphorus, especially dissolved phosphorus elimination. Yogeve et al. [14] combined denitrification with anaerobic digestion to recover phosphorus by its sustainable reuse as a fertilizer for plants in fresh RAS. Macroalgae have been used for water purification due to their high nitrogen and phosphate removal efficiencies, which make them suitable for biomass production and as a resource for biofuel feedstocks [15, 16]. The use of macroalgae could significantly reduce the harvesting and dewatering costs compared with microalgae due to their larger size and tendency to grow as dense floating mats or substrate-attached turfs [17]. Macroalgae are usually used in integrated multitrophic aquaculture (IMTA) systems to maintain water quality and to serve as food for cultured species [18]. Bambaranda et al. [19] tried to use *Caulerpa lentillifera* as a bioremediatory species instead of MBBR for nutrient removal in a RAS where a huge volume of macroalgae was needed to achieve the required high efficacy. However, no studies have investigated the feasibility of incorporating macroalgae with an MBBR within marine wastewater treatment.

Nambiar and Bokil [20] proposed the concept of a microalgae-bacteria consortia to study the uptake of nitrogen, and several researches were carried to study the interactions of microalgae and bacteria [21]. Both macroalgae and microalgae have numerous effects on microbial community structure and aquatic organisms by directly altering water nutrients, moderating hydrological conductivity, transporting oxygen through their bodies, and secreting chemicals as catalysts [22, 23]. Some bacteria and algae in the system have a mutually beneficial relationship, through which bacteria can convert ammonia into nitrite or nitrate, which can be utilized by algae, while the algae produce oxygen and organic matter for the growth of bacteria. Compared with the traditional single-step treatment, the nitrogen removal efficiency in aquaculture water can be improved by exploiting the synergistic effect that occurs among multiple species [24].

Chaetomorpha maxima, which is known for its blooming nature as well as its tolerance to fluctuating aquarium conditions, is a suitable marine macroalgae (MA) species for aquaculture wastewater nutrient recovery and biomass production [25]. And in our preliminary study, *Chaetomorpha maxima* is a good feed candidate for sea cucumber. In this study, integrated MBBR-MA (*Chaetomorpha maxima*) circulating systems were built to evaluate the nitrogen and phosphorus removal performance as well as macroalgae bio-

mass production by comparing them with MBBRs with no macroalgae culture. How the inclusion of macroalgae influenced the microbial community composition in both water bodies and the packed biofilters was also analyzed. This study provides the basis for the application of the MBBR-MA system, which could reduce nutrient accumulations in aquaculture wastewater and improve the sustainability of aquaculture production system.

2. Materials and Methods

2.1. Experimental Setup and Operational Procedure. A schematic of the integrated recirculating MBBR-MA system is shown in Figure 1. The MBBR-MA system included a 20 L water storage tank, two 3.5 L MBBRs, and a 150 L upflow algae reactor. The laboratory-scale MBBR was packed with ring plastic suspension filler (64 holes) to a filling rate of 30%. The MBBR was covered by the blackout cloth to avoid light. The water in the storage tank was lifted by a submerged pump to the MBBR and then to the algae reactor and finally flowed back to the storage tank. An underwater light at 15000 lx light intensity was set in the algae reactor, and the ratio of red to white light was 1 : 3.

Three replicates of two treatments, MBBR-MA and MBBR, were used to test the nutrient removal performance. At the start of the experiment, 50 g of MA (*Chaetomorpha maxima*) was stocked in each of the three algal reactors in the MBBR-MA treatment, while no MA was stocked in the MBBR treatment. The systems were fed with simulated maricultural wastewater prepared using fermented Atlantic salmon residual excrement [26]. The residual excrement was dried at 105°C for 48 h and then broken into a powder and mixed with seawater. A solution of the mixture was anaerobically fermented in a sealed container for 5 d before use. The influent wastewater quality was adjusted as follows: $\text{NH}_4^+\text{-N}$, 2.0 ± 0.5 mg/L; $\text{NO}_2^-\text{-N}$, 0.1 ± 0.05 mg/L; $\text{NO}_3^-\text{-N}$, 2.0 ± 0.5 mg/L; $\text{PO}_4^{3-}\text{-P}$, 0.2 ± 0.5 mg/L; total P, 0.3 ± 0.05 mg/L; chemical oxygen demand (COD), 3.00 ± 0.5 mg/L, and Salinity, 31‰. Both systems were operated in recirculating mode at a rate of 7.5 mL/min to achieve a hydraulic retention time (HRT) of 24 h. The experiment lasted for 75 d, consisting of 15 cycles, with each cycle operating for 4 d, with an interval of 1 d to change the wastewater. The whole experimental period was divided into two stages, with stage I lasting for 10 cycles and stage II lasting for 5 cycles. Stage I was designed to evaluate nutrient removal efficiencies between MBBR-MA and MBBR. The fresh algae in the MBBR-MA systems were weighed after each cycle. Stage II was designed to verify whether the MBBR could recover after the removal of the algae reactor. After stage I, the algae in the MBBR-MA systems were removed. All the algae bioreactors were cleaned, and all the underwater lights were removed.

2.2. Water and Biofilm Collection. Water samples (250 mL) were taken from the water sample tape from the outlet of the algae bioreactor of all the six systems every 12 h for the analysis of total ammonia nitrogen (TAN), nitrite nitrogen ($\text{NO}_2^-\text{-N}$), nitrate nitrogen ($\text{NO}_3^-\text{-N}$), total nitrogen (TN), total phosphorus (TP), and chemical oxygen demand

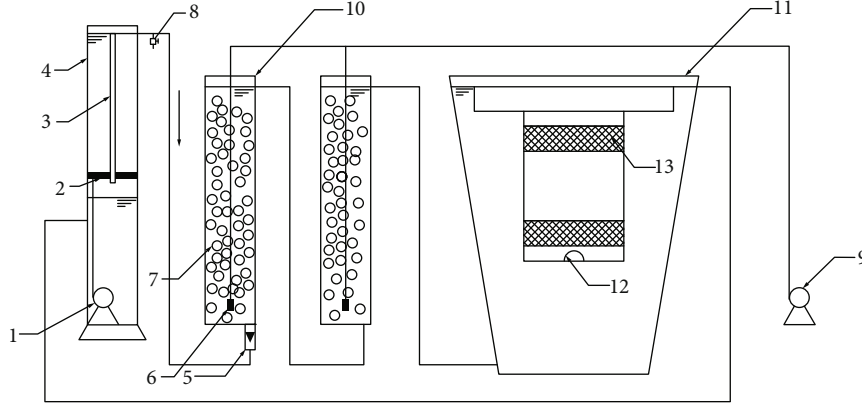


FIGURE 1: Schematic of the recirculating marine macroalgae with a moving bed bioreactor (MBBR-MA) system. 1, submerged pump; 2, baffle plate; 3, overflow pipe; 4, water storage tank; 5, flowmeter; 6, air stone; 7, biofilm carrier; 8, water sample tap; 9, aeration pump; 10, moving bed biofilm reactor; 11, algae bioreactor; 12, underwater light; 13, sieve.

(COD) according to standard methods [27]. All the water samples were stored at 4°C immediately after the collection and were analyzed for 12 hours. Microbial samples in both the biofilter and water were taken at the end of stage I (10 cycles) from the six systems. In detail, 15 plastic suspension fillers were randomly selected from each MBBR system. The biofilms attached to the fillers were collected by shaking in 30 mL of sterile seawater with 100 μ L of stabilizer (Tween 80 detergent solution) using a vortex mixer for 10 min. Then, the solution was filtered through a 0.22 μ m polycarbonate filter (Millipore, Burlington, MA, USA) to collect the microorganisms. Similarly, 500 mL of water sampled from each system was filtered through a 0.22 μ m polycarbonate filter (Millipore, MA, USA) to collect the microorganisms in the water. All the processed samples were stored at -80°C prior to DNA extraction.

2.3. DNA Extraction and High-Throughput Sequencing. The total DNA on the filter was extracted with an E.Z.N.A.® Water DNA Kit (Omega Bio-Tek, Norcross, GA, USA) according to the manufacturer's protocol. The DNA from the 12 microbial samples (six biofilm microbial samples and six water microbial samples) were profiled by polymerase chain reaction (PCR) amplification using 515F and 806R primers. The PCR products were separated by electrophoresis on 2% agarose gel, purified using a SanPrep DNA Gel Extraction Kit, and then quantified with NanoDrop. The purified mixtures were finally deep sequenced on the HiSeq2500 sequencing platform (Illumina, San Diego, CA, USA).

2.4. Processing of Sequencing Data. Raw data from the HiSeq2500 sequencing platform was processed with Cutadapt and the UCHIME algorithm to obtain clean reads [28, 29]. The clean reads without chimeras were clustered into operational taxonomic units (OTUs) at 97% similarity with UPARSE [30]. Representative sequences processed with QIIME 1.9.1 were used for taxonomic assignments based on the SILVA [31] and SSUrRNA databases [32]. Alpha diversity index values (Chao1 richness estimator, Shannon index, and Simpson index) were obtained using the QIIME

1.9.1 package. A hierarchical cluster heat map was generated, and a principal coordinate analysis (PCoA) was performed based on weighted UniFrac distances of the detected OTUs, with the R package *vegan*.

2.5. Statistical Analyses. The specific growth rates (SGR, %/d) of macroalgae were determined using the following formula:

$$\text{SGR} = \left[\left(\frac{W_t}{W_0} \right)^{1/t} - 1 \right] \times 100\%, \quad (1)$$

where W_0 (g) is the initial fresh weight, W_t (g) is the fresh weight at time t , and t (d) is the time interval.

The nitrogen, phosphorus, and COD removal efficiency (RE) was calculated using the following equation:

$$\text{RE} = \frac{C_0 - C_t}{C_0} \times 100\%, \quad (2)$$

where C_0 (mg/L) and C_t (mg/L) are the nitrogen, phosphorus, or COD concentrations in the water at the start and after that each cycle, respectively.

Statistical analyses were performed using SPSS 20.0 software and included a Student t -test and one-way analysis of variance (ANOVA). Data was reported as the mean \pm standard deviation (SD). The data were subjected to a Student t -test. A p value of <0.05 was considered statistically significant.

3. Results and Discussion

3.1. Long-Term Nitrogen and Phosphorus Removal Performance. The variation in the TAN, NO_2^- -N, NO_3^- -N, and TP dynamics in both the MBBR-MA and MBBR systems is shown in Figure 2. The TAN concentrations at the start of each cycle were 2.02 ± 0.10 mg/L and were reduced to 0.23 ± 0.07 (MBBR-MA) and 0.24 ± 0.08 (MBBR) mg/L at the end of each cycle (Figure 2(a)). In stage I, TAN removal followed zero-order elimination kinetics in

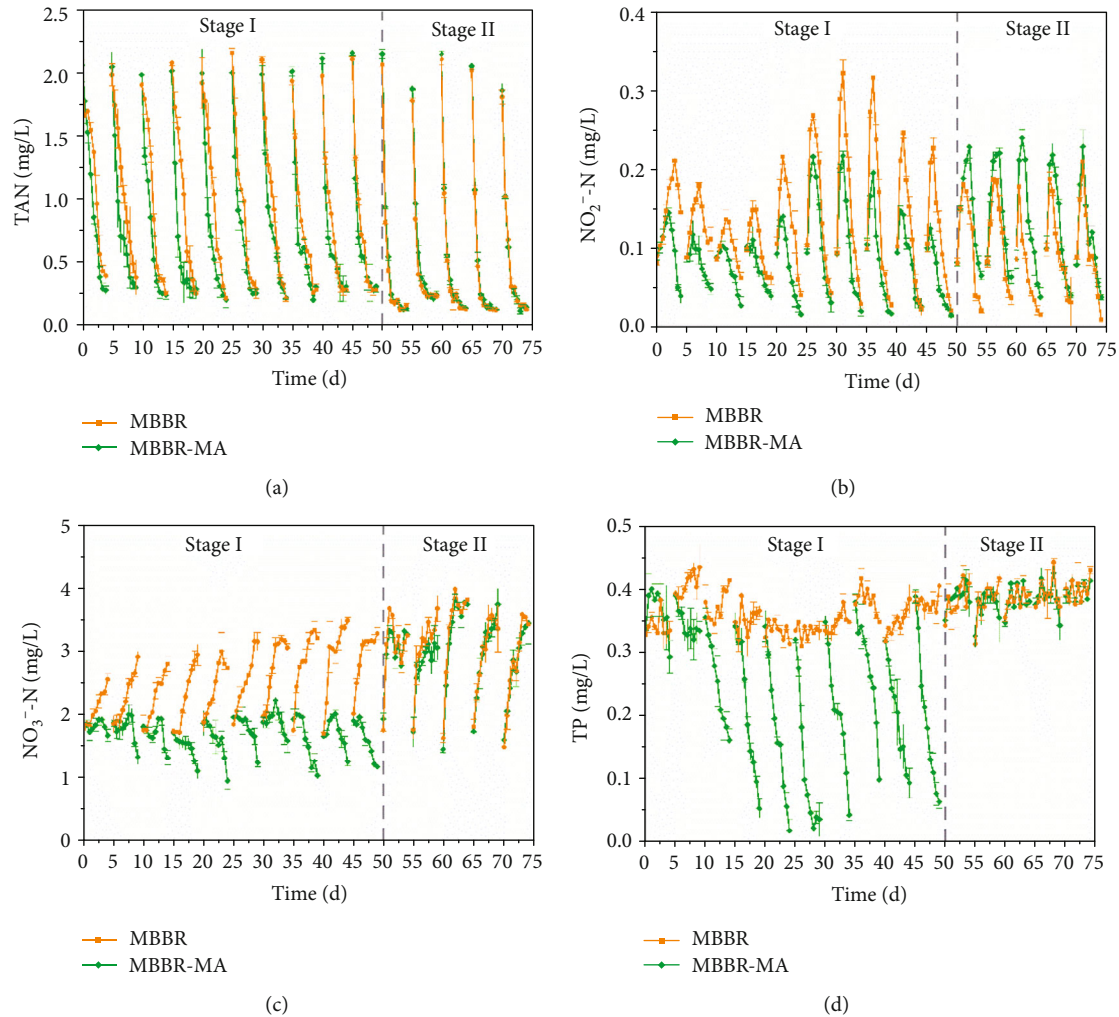


FIGURE 2: The concentrations of TAN (a), NO₂⁻-N (b), NO₃⁻-N (c), and TP (d) dynamics in both MBBR and MBBR-MA.

the MBBR system during the first four days of a cycle, while the MBBR-MA system had a higher TAN removal rate, indicating that MA contributed to TAN absorption, with the microorganisms in the MBBR playing the main role in TAN transformation. This result was in line with that of stage II, when MA was removed from the algae reactor in the MBBR-MA system, with no difference detected in TAN elimination in both systems.

Nitrite, as an intermediate product of nitrification, accumulated to a peak of 0.22 ± 0.06 mg/L during the first two days and was further oxidized to nitrate in the MBBR system (Figure 2(b)). During stage I, the nitrite accumulation in the MBBR system was significantly ($p < 0.05$) higher than that in the MBBR-MA system, which could be attributed to the nitrite and ammonia assimilation by MA and relatively lower ammonia concentration utilized by bacteria in the MBBR-MA system. Therefore, when the algae were removed from the MBBR-MA in stage II, the sudden increase in the TAN loading caused a slightly higher nitrite accumulation in the MBBR-MA than in the MBBR. The nitrification process resulted in a constant nitrate accumulation of an average of 3.25 ± 0.37 mg/L in

the MBBR (Figure 2(c)). On the other hand, the nitrate concentration decreased to 1.00 ± 0.10 mg/L at the end of stage I in the MBBR-MA system (Figure 2(c)), which could be explained by the absorption of MA. Direct nitrate adsorption by MA played a significant role in the nitrate reduction, which was confirmed by Ge and Champagne [17]. When MA was removed from the algae reactor in the MBBR-MA system at stage II, nitrate accumulation reoccurred.

As expected, MBBR had no contribution to phosphorus removal (Figure 2(d)). The biological removal of phosphorus is based on the phosphate-accumulating organisms (PAOs) under anaerobic and aerobic or anoxic conditions through sludge recycling [33]. The aerobic process of MBBR cannot enrich PAOs in the biofilm, which causes phosphorus accumulation in the system. On the hand, TP was eliminated from 0.35 mg/L in the influent to 0.06 mg/L in effluent of the MBBR-MA system after the acclimation of marine macroalgae for three cycles. The high capacity of TP removal in MBBR-MA was attributed to the uptake of phosphorus compounds for photosynthesis of marine macroalgae [34]. In our study, the average initial influent N:P ratio in

MBBR-MA was 12.4 while the average uptake N:P ratio of MA was 6.0 at day 4 during cycle 4 to cycle 10 in stage I. A previous study showed that N:P ratios greater than 15 in a temperate region indicated phosphate limitation for several species of MA [35]. The higher N:P ratio in wastewater influent than that in macroalgae uptake implied that phosphorus availability was a limiting factor for *C. maxima* growth, inhibiting the further uptake of nitrogen from aquaculture wastewater.

3.2. Nutrient Removal Efficiency within a Cycle. The nutrient removal efficiency over the four days within a cycle is shown in Figure 3. The TAN removal efficiency increased gradually from day one to day four in each cycle (Figure 3(a)). In stage I, the average accumulating TAN removal efficiency was 54.9% (MBBR-MA) and 33.2% (MBBR) on the first day, 70.8% (MBBR-MA) and 53.8% (MBBR) on the second day, 84.1% (MBBR-MA) and 77.4% (MBBR) on the third day, and 86.9% (MBBR-MA) and 86.0% (MBBR) on the fourth day. It was reported by the fact that *C. maxima* prefers to absorb ammonia as nitrogen source than nitrate when ammonia concentration is higher than 1.5 mg/L and prefers to absorb nitrite and nitrate when ammonia dropped below 1.5 mg/L [25]. Those results indicated that MA only contributed to TAN removal in MBBR-MA mainly on the first day when the TAN concentration was higher than 1.0 mg/L (Figure 2(a)). However, the difference between the two groups became insignificant on d4, indicating that microorganisms attached to MBBR played a significant role in TAN transformation. This assumption can be verified in stage II that there was no significant ($p < 0.05$) difference between the two treatments in TAN removal efficiency when macroalgae was removed.

In an MBBR, nitrification is a major ammonia transformation process, by which ammonia is oxidized to nitrite and further oxidized to nitrate. In stage I, the accumulation of NO_3^- -N was consistent with the degradation of TAN caused by the nitrification process in the MBBR which explained the zero removal of TN in MBBR (Figure 3(b)). The decrease of nitrate mainly started from d2 in MBBR-MA (Figure 2(c)), implying that *C. maxima* first utilize ammonia as nitrogen source then switched to nitrate when ammonia was lower than approximate 1.0 mg/L. Overall, the direct absorption of nitrogen by *C. maxima* contributed to the TN removal in the MBBR-MA, with an average removal efficiency of 42.8% for TN, ranging from 34.4% to 54.3% at day 4 (Figure 3(b)). *C. maxima* exhibited higher removal efficiency in TP removal (average, 80.0%) when compared with TN removal (Figure 3(c)). This indicated that the relatively low phosphorus availability in aquaculture wastewater limited the nitrogen uptake by MA. Nevertheless, since autotrophic macroalgae uptake no carbon from the wastewater (Figure 3(d)), the lower nitrate level in the MBBR-MA system may elevate the C:N ratio that could facilitate the denitrification process, which could benefit the zero-exchange operation of RAS.

3.3. Characteristics of MA Growth. The algal growth was described as the weight gain and SGR of MA on a fresh

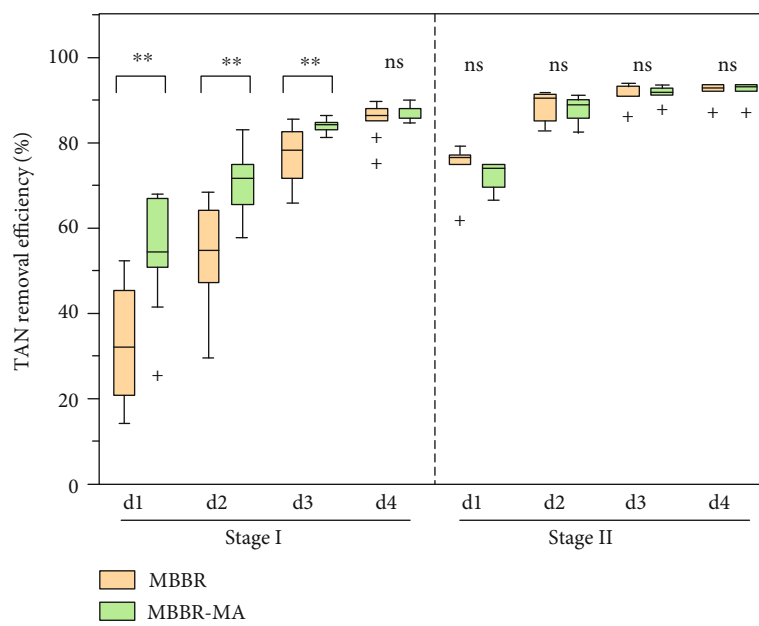
weight basis (Table 1). The fresh weight increased and the rate of growth gradually accelerated over the course of the study. At the end of the tenth period, the fresh weight of MA was 564.03 g, i.e., 11 times the original algae weight. These results confirmed that MA can use inorganic nitrogen for their growth, contributing to aquaculture water purification [36–38]. However, the growth performance of the macroalgae varied according to the species used for cultivation. For example, *Ulva lactuca* grown in a mixture of seawater and sewage effluent (40%:60%) had an SGR of 0.5%/day [37]. In Brazil, a study of the growth and biofiltration capacity of the macroalgae *Gracilaria birdiae* in tank cultivation had an SGR of 3.6%/day [38]. Our study revealed a significant growth performance, with the SGR varying from 3.86 to 10.35%/day, indicating that the application of *C. maxima* could be an optimal algae alternative when treating maricultural wastewater.

3.4. Characteristics of Microbial Diversity in Water and Biofilter

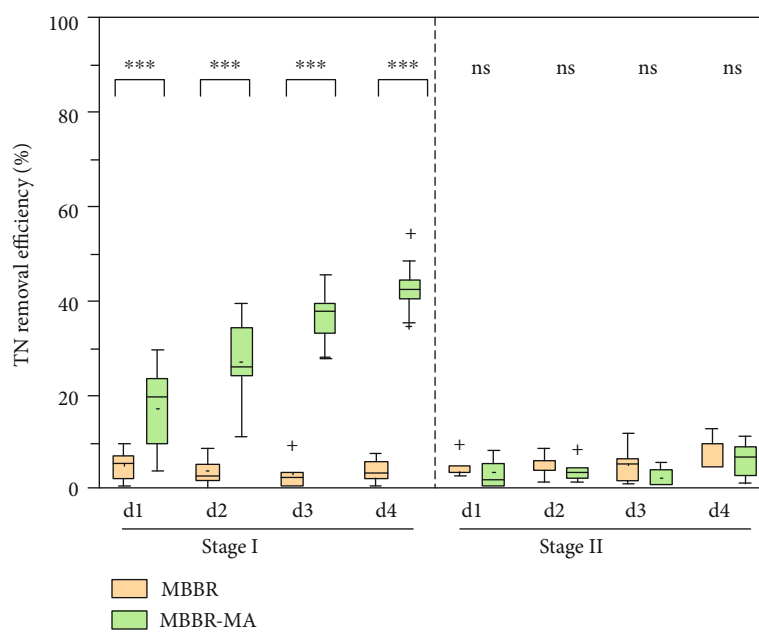
3.4.1. Alpha-Diversity Analysis. A total of 855,846 high-quality 16S rRNA gene sequence reads were obtained from the 12 biofilter and water samples. Each library contained 56,298–87,910 reads that were normalized to 56,298 reads for the comparison of microbial community diversity between the MBBR-MA and MBBR systems (Table 2). Water samples had a significantly ($p < 0.05$) higher microbial richness than biofilter samples according to the OTU number and Chao1 index values, while the addition of macroalgae did not significantly ($p < 0.05$) change the microbial richness in biofilters. Moreover, the Shannon and Simpson indices indicated that MA did not significantly change the evenness of the microbial community in biofilter samples. The Simpson index was significantly higher in the water samples with algae than in those without algae. The results of the alpha diversity analysis showed that the microbial community richness and diversity were lower in the biofilm than in the water samples, particularly for the Shannon and Simpson index results ($p < 0.05$), which was in line with previous studies [39, 40].

3.4.2. Beta Diversity Analysis. The difference in microbial composition between systems was analyzed by the weighted UniFrac distance and presented as a PCoA plot (Figure 4). A clear separation between the biofilter and water samples was observed along PC1 axes, which accounted for 75.97% of the total changes in the bacterial community composition. Many aquatic microorganisms are capable of colonizing surfaces, leading to the formation of biofilms with specialized properties [39, 40]. Thus, in terms of diversity (Table 2) and composition, the bacterial community in the water and biofilters was clearly different, which reflected the different microbiota compositions attached to RAS biofilters compared to the free-living community in the water phase of aquaculture systems [41].

The samples could be separated between MBBR-MA and MBBR along PC2, which explained 14.81% of the total variation in the bacterial community composition. This result



(a)



(b)

FIGURE 3: Continued.

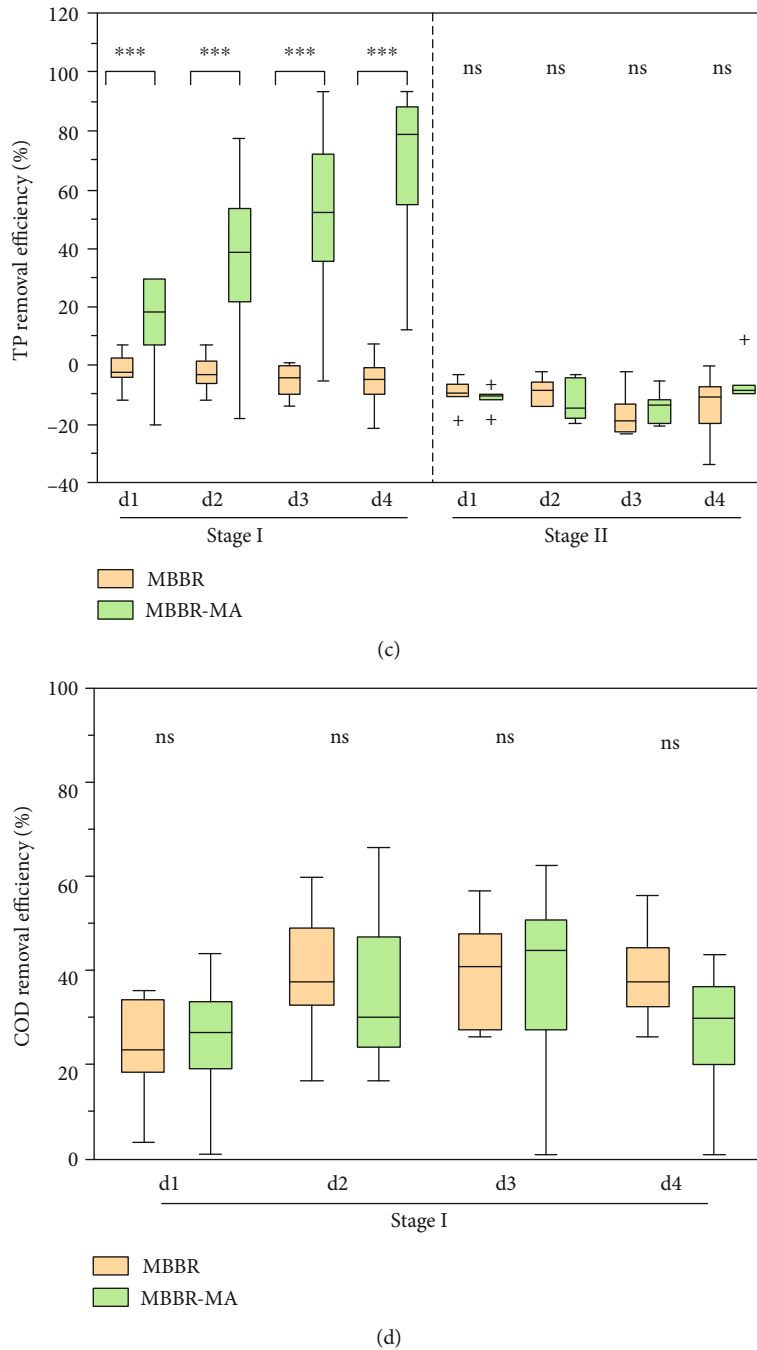


FIGURE 3: The TAN (a), TN (b), TP (c), and COD (d) removal efficiency over the four days in stage I and stage II of both MBBR and MBBR-MA.

demonstrated that the microbial communities in both the biofilm and water samples were influenced by the presence of macroalgae. The MA induced a bigger shift in the microbial community in the water than in the biofilters. One reason for this was that the utilization of CO_2 and release of oxygen during photosynthesis might change the pH in the water and further influence the microbial community composition [42, 43]. Another possible reason could be that the reduction in the nitrogen concentration by algae could also affect the microbial communities in MBBR, as suggested by previous studies [7, 44].

3.5. Microbial Community Composition. The microbial community composition of the biofilm and water samples was analyzed at phylum, class, and genus taxon levels (Figure 5). At the phylum level, the top 10 phyla were selected, and the remaining phyla were assigned to a cluster named “the others” (Figure 5(a)). The results showed that Proteobacteria (average relative abundance (RA), 63.4%) was the most abundant phylum across all the samples, followed by Bacteroidetes (average RA, 22.4%), which was also found with a high abundance in other marine MBBRs [45–47]. The integration of MA with MBBR significantly

TABLE 1: The growth performance of marine macroalgae (MA) in each cycle in stage I.

Cycle	0	1	2	3	4	5	6	7	8	9	10
Fresh weight (g)	50.86 ± 0.31	75.42 ± 13.17	94.68 ± 8.88	113.90 ± 11.07	143.54 ± 6.18	182.44 ± 15.46	212.31 ± 7.11	278.28 ± 9.79	329.72 ± 8.02	424.38 ± 15.16	564.03 ± 30.35
Fresh weight gain (g)	—	24.56 ± 9.02	19.26 ± 5.73	19.22 ± 5.76	29.64 ± 6.95	38.90 ± 8.57	29.87 ± 7.03	65.97 ± 10.29	51.44 ± 6.09	94.66 ± 11.33	139.65 ± 14.94
SGR (%/d)	—	10.35	5.85	4.73	5.95	6.19	3.86	7.05	4.28	6.51	7.37

TABLE 2: Alpha-diversity indices of the biofilter and water samples from both MBBR and MBBR-MA.

Sample name ($n = 3$)		ACE	Chao1	Shannon	Simpson	PD whole tree
Biofilter	MBBR-MA	900 ^a	901 ^a	6.10 ^a	0.96 ^a	76.73 ^a
	MBBR	844 ^a	840 ^a	6.25 ^a	0.97 ^a	77.63 ^a
Water	MBBR-MA	1094 ^b	1096 ^b	6.67 ^b	0.96 ^a	101.84 ^b
	MBBR	1194 ^b	1183 ^b	6.70 ^b	0.94 ^b	112.17 ^b

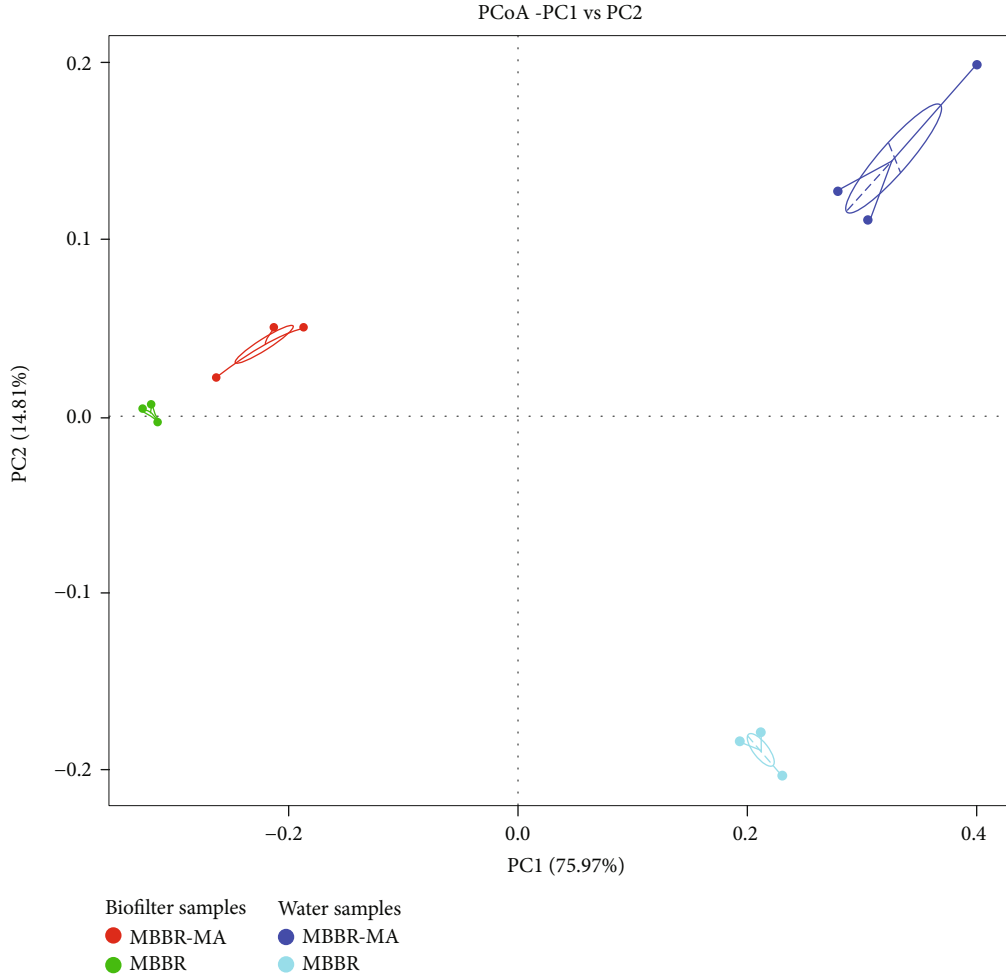


FIGURE 4: The microbial community distribution in both biofilter and water samples according to a principal coordinate analysis (PCoA) plot of MBBR and MBBR-MA.

decreased the RA of Proteobacteria and Nitrospirae and significantly increased the RA of Bacteroidetes in both biofilter and water samples. Nitrospirae is the dominant NOB in wastewater treatment systems [48], and many Bacteroidetes species have been reported to have the capacity for organic carbon degradation [49]. The relatively lower abundance of Nitrospirae in MBBR-MA biofilter samples could be explained by the relatively lower nitrite concentration detected in the MBBR-MA system (Figure 2(b)), because macroalgae also contribute to ammonia and nitrite removal. On the other hand, macroalgae may also enhance the growth of heterotrophic bacteria by producing organic compounds.

A heat map of the 35 most abundant genus-level taxa is shown in Figure 5(b). A clear separation between biofilter and water samples was observed. In the biofilter samples, *Halomonas*, *Leisingera*, *Pseudoalteromonas*, *unidentified_Gracilibacteria*, *Alteromonas*, *Vibrio*, and *Kordia* were the most abundant genera in both treatments. Among them, macroalgae significantly ($p < 0.05$) increased the RA of *unidentified_Gracilibacteria* and *Kordia* in the MBBR-MA compared with the MBBR. According to Chen et al. [50], genera belonging to *Gracilibacteria* can participate in the denitrification process and have nitrate removal abilities. According to Paul and Pohnert [51], *Kordia*, as algicidal

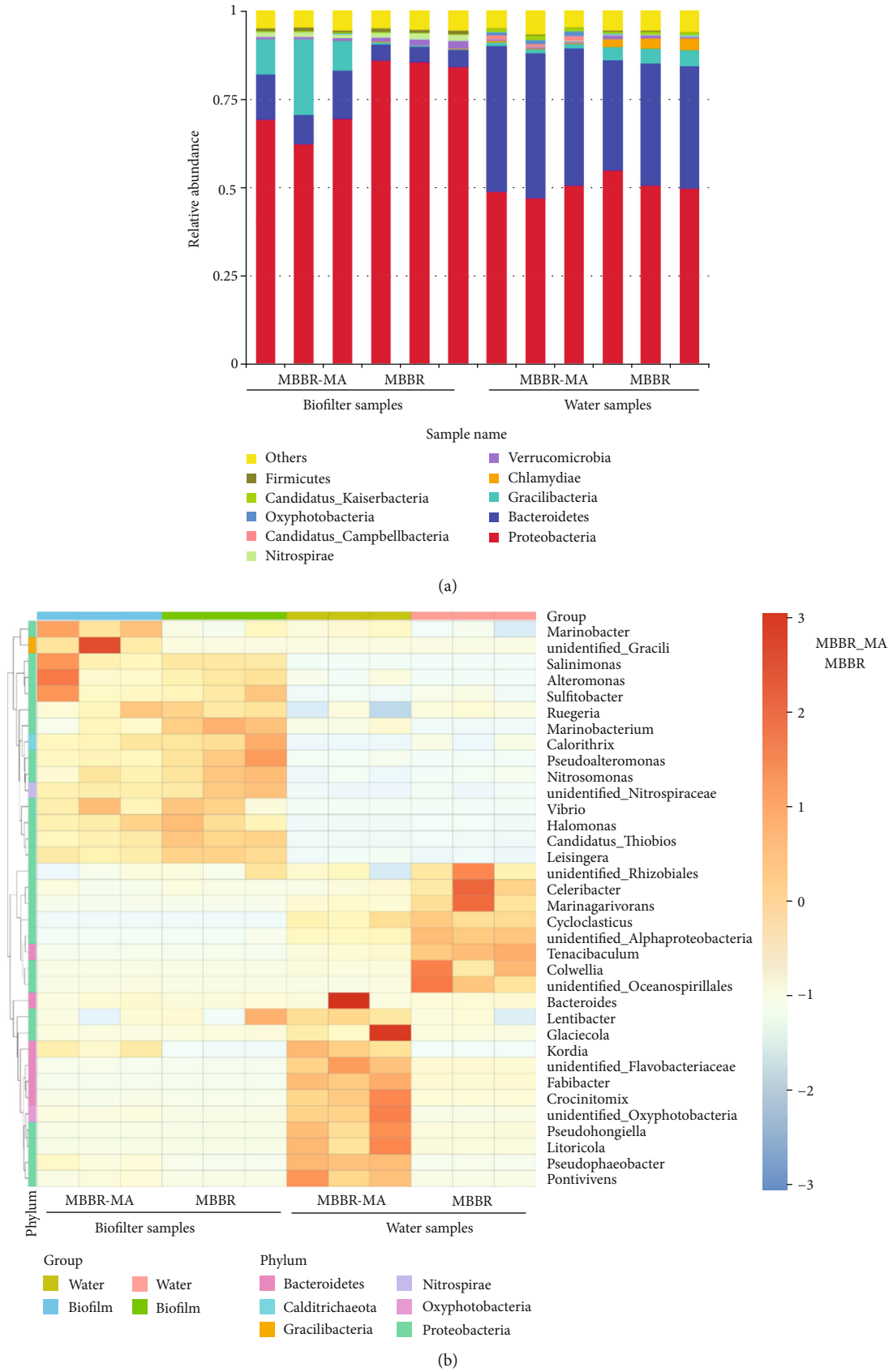


FIGURE 5: The microbial community composition of biofilm and water samples of MBBR and MBBR-MA at the (a) phylum taxon level and (b) genus taxon level.

bacterium, can release protease as an algicidal protein when they receive signals from algae indicating cellular senescence. On the other hand, macroalgae significantly reduced the RA of *Pseudoalteromonas* and *Alteromonas* in the MBBR-MA system compared to the MBBR system. It has been documented that members of the genus *Pseudoalteromonas* are involved in the formation of biofilms [52]. Bacteria belonging to the genera *Pseudoalteromonas* and *Alteromonas* produce depolymerizing enzymes and are associated with macroalgal degradation processes or algicidal activities [53, 54]. The lower abundance of those genera may be beneficial for the growth of macroalgae. Moreover, macroalgae reduced the RA of nitrifying bacteria, including *Nitrosomonas* (0.49% for MBBR-MA, 0.80% for MBBR) and *Nitrospiraceae* (1.22% for MBBR-MA, 1.76% for MBBR), in biofilters. The numerical dominance of NOB (i.e., *Nitrospiraceae*) over AOB (i.e., *Nitrosomonas*) might be a general characteristic of ammonium limited systems [55], which was in agreement with other studies in which the ammonia concentration was relatively low (around 2 mg/L). Most of the dominant microorganisms in the biofilm were present at very low levels in the water samples, which reinforced the above findings of differences in microbiota between water and biofilms.

Intensive interactions were identified between bacteria and macroalgae, including stimulatory and inhibitory effects on each other by modifying the chemical microenvironment of the other group through metabolic activities [55, 56]. Our study revealed that an MA culture integrated with an MBBR changed the microbial community in biofilters, decreasing the abundance of nitrifying bacteria and increasing the abundance of heterotrophic bacteria through the absorption of inorganic nitrogen and release of organic matter. Further research is required to determine how the integration of macroalgae influences the microbial functionality and nitrogen removal efficiency of an MBBR biofilter and to investigate the potential interactions between macroalgae and bacteria.

4. Summary and Conclusions

An integrated MBBR-MA circulating system was performed for both nutrient removal and macroalgae biomass production. The MA improved the TN removal efficiency of MBBR from 3.9% to 42.8%, mainly by nitrate absorption, and contributed to 66.8% TP removal which enabled the sustainable operation of a marine RAS. *Chaetomorpha maxima* achieved a specific growth rate of 3.86–10.35%/day through nutrient recovery, and the uptake N:P ratio by MA was 6. Phosphorus could be a limiting factor for *Chaetomorpha maxima* to uptake nitrogen when the influent N:P ratio increased. The high-throughput sequencing results revealed a shift in the microbial composition of both water and biofilter samples in the systems with and without macroalgae.

Data Availability

The data used to support the findings of this study are included within the article.

Conflicts of Interest

The authors declare that they have no known competing financial interests or personal relationships that could have appeared to influence the work reported in this paper.

Authors' Contributions

Xian Li and Yale Deng contributed equally to this work and should be considered co-first authors.

Acknowledgments

This work was supported by the National Key R&D Program of China (2017YFD0701700), Key R&D Program of Guangdong Province (2019B020215001), the Agricultural Application Technology Innovation Project of Shandong Province in 2018 and China Agriculture Research System (CARS-47).

References

- [1] C. I. M. Martins, E. H. Eding, M. C. J. Verdegem et al., "New developments in recirculating aquaculture systems in Europe: a perspective on environmental sustainability," *Aquacultural Engineering*, vol. 43, no. 3, pp. 83–93, 2010.
- [2] W. Jiang, X. Tian, L. Li et al., "Temporal bacterial community succession during the start-up process of biofilters in a cold-freshwater recirculating aquaculture system," *Bioresource Technology*, vol. 287, p. 121441, 2019.
- [3] R. K. Sonwani, G. Swain, B. S. Giri, R. S. Singh, and B. N. Rai, "A novel comparative study of modified carriers in moving bed biofilm reactor for the treatment of wastewater: process optimization and kinetic study," *Bioresource Technology*, vol. 281, pp. 335–342, 2019.
- [4] T. M. Samocha, J. S. Wilkenfeld, T. C. Morris, E. S. Correia, and T. Hanson, "Intensive raceways without water exchange analyzed for white shrimp culture," *Global Aquaculture Advocate*, vol. 13, pp. 22–24, 2010.
- [5] J. Van Rijn and J. M. Ebeling, "Denitrification," in *Recirculating Aquaculture*, pp. 387–424, Cayuga Aqua Ventures, Ithaca, New York, 2010.
- [6] W. Liu, H. Tan, W. Chen et al., "Pilot study on water quality regulation in a recirculating aquaculture system with suspended growth bioreactors," *Aquaculture*, vol. 504, pp. 396–403, 2019.
- [7] C. I. M. Martins, M. G. Pistrin, S. S. W. Ende, E. H. Eding, and J. A. J. Verreth, "The accumulation of substances in Recirculating Aquaculture Systems (RAS) affects embryonic and larval development in common carp *Cyprinus carpio*," *Aquaculture*, vol. 291, no. 1–2, pp. 65–73, 2009.
- [8] J. Davidson, C. Good, C. Williams, and S. T. Summerfelt, "Evaluating the chronic effects of nitrate on the health and performance of post-smolt Atlantic salmon *Salmo salar* in freshwater recirculation aquaculture systems," *Aquacultural Engineering*, vol. 79, pp. 1–8, 2017.
- [9] X. Yang, X. Song, L. Peng, E. Hallerman, and Z. Huang, "Effects of nitrate on aquaculture production, blood and histological markers and liver transcriptome of *Oplegnathus punctatus*," *Aquaculture*, vol. 501, pp. 387–396, 2019.
- [10] A. K. Buhmann, U. Waller, B. Wecker, and J. Papenbrock, "Optimization of culturing conditions and selection of species

- for the use of halophytes as biofilter for nutrient-rich saline water," *Agricultural Water Management*, vol. 149, pp. 102–114, 2015.
- [11] J. Van Rijn, Y. Tal, and H. J. Schreier, "Denitrification in recirculating systems: theory and applications," *Aquacultural Engineering*, vol. 34, no. 3, pp. 364–376, 2006.
- [12] Y. J. Ruan, Y. L. Deng, X. S. Guo et al., "Simultaneous ammonia and nitrate removal in an airlift reactor using poly (butylene succinate) as carbon source and biofilm carrier," *Bioresource Technology*, vol. 216, pp. 1004–1013, 2016.
- [13] S. M. Zhu, Y. L. Deng, Y. J. Ruan, X. S. Guo, M. M. Shi, and J. Z. Shen, "Biological denitrification using poly (butylene succinate) as carbon source and biofilm carrier for recirculating aquaculture system effluent treatment," *Bioresource Technology*, vol. 192, pp. 603–610, 2015.
- [14] U. Yogev, M. Vogler, O. Nir, J. Londong, and A. Gross, "Phosphorous recovery from a novel recirculating aquaculture system followed by its sustainable reuse as a fertilizer," *The Science of the total environment*, vol. 722, p. 137949, 2020.
- [15] E. B. Taboada, "Simultaneous ammonium and phosphate uptake capacity of macroalga *Ulva* species in effluent seawater," *Journal of Bioscience and Bioengineering*, vol. 108, pp. S77–S78, 2009.
- [16] D. Kerrigan and C. C. Suckling, "A meta-analysis of integrated multitrophic aquaculture: extractive species growth is most successful within close proximity to open-water fish farms," *Reviews in Aquaculture*, vol. 10, no. 3, pp. 560–572, 2018.
- [17] S. Ge and P. Champagne, "Cultivation of the marine macroalgae *Chaetomorpha linum* in municipal wastewater for nutrient recovery and biomass production," *Environmental Science & Technology*, vol. 51, no. 6, pp. 3558–3566, 2017.
- [18] S. Laramore, R. Baptiste, P. S. Wills, and M. D. Hanisak, "Utilization of IMTA-produced *Ulva lactuca* to supplement or partially replace pelleted diets in shrimp (*Litopenaeus vannamei*) reared in a clear water production system," *Journal of Applied Phycology*, vol. 30, no. 6, pp. 3603–3610, 2018.
- [19] B. V. A. S. M. Bambaranda, T. W. Tsusaka, A. Chirapart, K. R. Salin, and N. Sasaki, "Capacity of caulerpa *lentillifera* in the removal of fish culture effluent in a recirculating aquaculture system," *Processes*, vol. 7, no. 7, p. 440, 2019.
- [20] K. R. Nambiar and S. D. Bokil, "Luxury uptake of nitrogen in flocculating algal-bacterial system," *Water Research*, vol. 15, no. 6, pp. 667–669, 1981.
- [21] J. Liu, Y. Wu, C. Wu et al., "Advanced nutrient removal from surface water by a consortium of attached microalgae and bacteria: a review," *Bioresource Technology*, vol. 241, pp. 1127–1137, 2017.
- [22] X. Ma, W. Zhou, Z. Fu et al., "Effect of wastewater-borne bacteria on algal growth and nutrients removal in wastewater-based algae cultivation system," *Bioresource Technology*, vol. 167, pp. 8–13, 2014.
- [23] S.-J. Chun, Y. Cui, C.-Y. Ahn, and H.-M. Oh, "Improving water quality using settleable microalga *Ettlia* sp. and the bacterial community in freshwater recirculating aquaculture system of *Danio rerio*," *Water Research*, vol. 135, pp. 112–121, 2018.
- [24] K. Brenner, L. You, and F. H. Arnold, "Engineering microbial consortia: a new frontier in synthetic biology," *Trends in Biotechnology*, vol. 26, no. 9, pp. 483–489, 2008.
- [25] X. Li, X. Li, J. Wang et al., "Removal efficiency of nitrogen salts by *Chaetomorpha maxima* in aquacultural wastewater," *Trans. CSAE*, vol. 35, no. 24, 2019.
- [26] Y. Zhang, J. Chen, J. Shen, S. Hou, Y. Liu, and Y. Liu, "A study on transformation of main pollutants along the wastewater flow in biological aerated filter," *China Environmental Science*, vol. 31, no. 11, pp. 1808–1814, 2011.
- [27] M. Li, Z. Liang, M. D. Callier et al., "Nutrients removal and substrate enzyme activities in vertical subsurface flow constructed wetlands for mariculture wastewater treatment: effects of ammonia nitrogen loading rates and salinity levels," *Marine Pollution Bulletin*, vol. 131, pp. 142–150, 2018.
- [28] M. Martin, "Cutadapt removes adapter sequences from high-throughput sequencing reads," *EMBnet.journal*, vol. 17, no. 1, pp. 10–12, 2011.
- [29] R. C. Edgar, B. J. Haas, J. C. Clemente, C. Quince, and R. Knight, "UCHIME improves sensitivity and speed of chimera detection," *Bioinformatics*, vol. 27, no. 16, pp. 2194–2200, 2011.
- [30] R. C. Edgar, "UPARSE: highly accurate OTU sequences from microbial amplicon reads," *Nature Methods*, vol. 10, no. 10, pp. 996–998, 2013.
- [31] Q. Wang, G. M. Garrity, J. M. Tiedje, and J. R. Cole, "Naïve Bayesian classifier for rapid assignment of rRNA sequences into the new bacterial taxonomy," *Applied and Environmental Microbiology*, vol. 73, no. 16, pp. 5261–5267, 2007.
- [32] C. Quast, E. Pruesse, P. Yilmaz et al., "The SILVA ribosomal RNA gene database project: improved data processing and web-based tools," *Nucleic Acids Research*, vol. 41, no. D1, pp. D590–D596, 2012.
- [33] Z. Chen, S. Shao, Y. He et al., "Nutrients removal from piggery wastewater coupled to lipid production by a newly isolated self-flocculating microalga *Desmodesmus* sp. PW1," *Bioresource Technology*, vol. 302, p. 122806, 2020.
- [34] N. Arumugam, S. Chelliapan, H. Kamyab, S. Thirugnana, N. Othman, and N. Nasri, "Treatment of wastewater using seaweed: a review," *International Journal of Environmental Research and Public Health*, vol. 15, no. 12, p. 2851, 2018.
- [35] S. T. Larned, "Nitrogen- versus phosphorus-limited growth and sources of nutrients for coral reef macroalgae," *Marine Biology*, vol. 132, no. 3, pp. 409–421, 1998.
- [36] S. A. Lavania-Baloo, M. I. M. Said, F. Ahmad, and M. Mohamad, "Biofiltration potential of macroalgae for ammonium removal in outdoor tank shrimp wastewater recirculation system," *Biomass & Bioenergy*, vol. 66, no. 7, pp. 103–109, 2014.
- [37] P. Tsagakimilis, D. Danielidis, M. J. Dring, and C. Katsaros, "Removal of phosphate by the green seaweed *Ulva lactuca* in a small-scale sewage treatment plant (Ios Island, Aegean Sea, Greece)," *Journal of Applied Phycology*, vol. 22, no. 3, pp. 331–339, 2010.
- [38] E. Marinho-Soriano, R. A. Panucci, M. A. A. Carneiro, and D. C. Pereira, "Evaluation of *Gracilaria caudata* J. Agardh for bioremediation of nutrients from shrimp farming wastewater," *Bioresource Technology*, vol. 100, no. 24, pp. 6192–6198, 2009.
- [39] J. W. Costerton, Z. Lewandowski, D. E. Caldwell, D. R. Korber, and H. M. Lappin-Scott, "Microbial biofilms," *Annual Review of Microbiology*, vol. 49, no. 1, pp. 711–745, 1995.

- [40] O. E. Petrova and K. Sauer, "Sticky situations: key components that control bacterial surface attachment," *Journal of Bacteriology*, vol. 194, no. 10, pp. 2413–2425, 2012.
- [41] J. P. Blancheton, K. J. K. Attramadal, L. Michaud, E. R. d'Orbcastel, and O. Vadstein, "Insight into bacterial population in aquaculture systems and its implication," *Aquacultural Engineering*, vol. 53, pp. 30–39, 2013.
- [42] H. Hirata, S. Yamasaki, H. Maenosono, T. Nakazono, T. Yamauchi, and M. Matsuda, "Relative budgets of $p\text{O}_2$ and $p\text{CO}_2$ in cage polycultured Red Sea bream, *Pagrus major* and sterile *Ulva* sp.," *Suisanzoshoku*, vol. 42, pp. 377–381, 1994.
- [43] L. C. Rai, H. D. Kumar, F. H. Mohn, and C. J. Soeder, "Services of algae to the environment," *Journal of Microbiology and Biotechnology*, vol. 10, pp. 119–136, 2000.
- [44] X. Y. Shen, L. M. Zhang, J. P. Shen, L. H. Li, C. L. Yuan, and J. Z. He, "Nitrogen loading levels affect abundance and composition of soil ammonia oxidizing prokaryotes in semiarid temperate grassland," *Journal of Soils and Sediments*, vol. 11, no. 7, pp. 1243–1252, 2011.
- [45] D.-E. Lee, J. Lee, Y.-M. Kim, J.-I. Myeong, and K.-H. Kim, "Uncultured bacterial diversity in a seawater recirculating aquaculture system revealed by 16S rRNA gene amplicon sequencing," *Journal of Microbiology*, vol. 54, no. 4, pp. 296–304, 2016.
- [46] D. Woebken, B. M. Fuchs, M. M. M. Kuypers, and R. Amann, "Potential interactions of particle-associated anammox bacteria with bacterial and archaeal partners in the Namibian upwelling system," *Applied and Environmental Microbiology*, vol. 73, no. 14, pp. 4648–4657, 2007.
- [47] K. Kersters, P. D. Vos, M. Gillis, J. Swings, and E. Stackebrandt, *Introduction to the Proteobacteria*, The Prokaryotes, New York, America, 2006.
- [48] M. K. H. Winkler, Q. H. Le, and E. I. P. Volcke, "Influence of partial denitrification and mixotrophic growth of NOB on microbial distribution in aerobic granular sludge," *Environmental Science & Technology*, vol. 49, no. 18, pp. 11003–11010, 2015.
- [49] M. Bauer, M. Kube, H. Teeling et al., "Whole genome analysis of the marine Bacteroidetes '*Gramella forsetii*' reveals adaptations to degradation of polymeric organic matter," *Environmental Microbiology*, vol. 8, no. 12, pp. 2201–2213, 2006.
- [50] D. Chen, H. Wang, K. Yang, and F. Ma, "Performance and microbial communities in a combined bioelectrochemical and sulfur autotrophic denitrification system at low temperature," *Chemosphere*, vol. 193, pp. 337–342, 2018.
- [51] C. Paul and G. Pohnert, "Interactions of the algicidal bacterium *Kordia algicida* with diatoms: regulated protease excretion for specific algal lysis," *Plos One*, vol. 6, no. 6, article e21032, 2011.
- [52] J. Bowman, "Bioactive compound synthetic capacity and ecological significance of marine bacterial genus *Pseudoalteromonas*," *Marine Drugs*, vol. 5, no. 4, pp. 220–241, 2007.
- [53] S. Egan, N. D. Fernandes, V. Kumar, M. Gardiner, and T. Thomas, "Bacterial pathogens, virulence mechanism and host defence in marine macroalgae," *Environmental Microbiology*, vol. 16, no. 4, pp. 925–938, 2014.
- [54] F. Goecke, A. Labes, J. Wiese, and J. F. Imhoff, "Chemical interactions between marine macroalgae and bacteria," *Marine Ecology Progress Series*, vol. 409, pp. 267–299, 2010.
- [55] B. U. Foesel, A. Gieseke, C. Schwermer et al., "Nitrosomonas Nm143-like ammonia oxidizers and *Nitrospira marina*-like nitrite oxidizers dominate the nitrifier community in a marine aquaculture biofilm," *Fems Microbiology Ecology*, vol. 63, no. 2, pp. 192–204, 2008.
- [56] J. A. Hargreaves, "Photosynthetic suspended-growth systems in aquaculture," *Aquacultural Engineering*, vol. 34, no. 3, pp. 344–363, 2006.

Research Article

Characteristics of Biohydrogen Production and Performance of Hydrogen-Producing Acetogen by Increasing Normal Molasses Wastewater Proportion in Anaerobic Baffled Reactor

Xuejia Gu,^{1,2} Yufeng Wang,^{1,2} Huaibo Li,³ Ji Li,^{3,4} and Shuo Wang^{3,4,5} 

¹Institute of Soil Fertilizer and Environment Resources, Heilongjiang Academy of Agricultural Sciences, Harbin 150086, China

²Key Laboratory of Agricultural Environment of Northeast Plain, Ministry of Agriculture and Rural Affairs, Harbin 150086, China

³Jiangsu Key Laboratory of Anaerobic Biotechnology, School of Environment and Civil Engineering, Jiangnan University, Wuxi 214122, China

⁴Jiangsu College of Water Treatment Technology and Material Collaborative Innovation Center, Suzhou 215009, China

⁵Department of Civil Engineering, Schulich School of Engineering, University of Calgary, Calgary, Canada T2N 1N4

Correspondence should be addressed to Shuo Wang; shuowang@jiangnan.edu.cn

Received 9 April 2020; Revised 16 May 2020; Accepted 25 May 2020; Published 5 June 2020

Academic Editor: Yu Tao

Copyright © 2020 Xuejia Gu et al. This is an open access article distributed under the Creative Commons Attribution License, which permits unrestricted use, distribution, and reproduction in any medium, provided the original work is properly cited.

The biohydrogen production efficiency and performance of hydrogen-producing acetogen in a four-compartment anaerobic baffled reactor (ABR) were studied by gradually increasing the influent normal molasses wastewater (NMWW) proportion. When the influent NMWW proportion increased to 55%, ABR could develop microbial community with methanogenic function in 63 days and reach a stable operation. When the influent NMWW proportion increased to 80% and reached a stable state, ethanol fermentation was established from butyric acid fermentation in the first three compartments, whereas butyric acid fermentation in the fourth compartment was strengthened. The average biohydrogen production yield and biohydrogen production capacity by COD removal increased to as high as 12.85 L/day and 360.22 L/kg COD when the influent NMWW proportion increased from 55% to 80%, respectively. Although the biogas yield and the specific biogas production rate reached 61.54 L/day and 232 L/kg MLVSS-day, the biohydrogen production yield and specific biohydrogen production rate were only 12.85 L/day and 48 L/kg MLVSS-day, which results in hydrogen consumption by homoacetogenesis and methanogenesis.

1. Introduction

A considerable amount of high-strength organic wastewater has been discharged into aquatic systems with poor treatment performance, which causes serious water pollution and destroys the ecological environment and poses a threat to the environment and human health [1]. Given the increasing demand for eliminating organic wastewater pollution, the ultimate goal is to achieve waste minimization and clean manufacturing [2]. Biohydrogen production by fermentation can utilize hydrogen-producing microorganisms to metabolize organic matters to produce hydrogen in anaerobic conditions and acidic circumstance [3]. At present, the basic principle of biohydrogen production is mainly based on the acidogenic fermentation of hydrogen-producing bacteria

[4]. The terminal liquid products of fermentation are ethanol, acetic acid, propionic acid, and butyric acid [5]. Given the limited degradation of soluble products, most hydrogen is not released in the form of H₂, which considerably limits the hydrogen conversion rate and becomes a technical bottleneck restricting the development and application of the biological hydrogen production technology through fermentation [6–8].

Normal molasses wastewater (NMWW) is an important byproduct in beet sugar and sugar cane factories [9], in which a large amount of molasses wastewater containing high-strength chemical oxygen demand (COD) in the range of 80000–130000 mg/L is produced and gradually becomes one of the most polluted wastewater in the food industry. However, NMWW is an excellent substrate for

fermentative biohydrogen production because it contains a considerable amount of sucrose, glucose, fructose, nitrogen, and vitamins [10]. Upflow anaerobic sludge blanket reactor [11], which can recover energy in the form of methane through the NMWW treatment process, has been utilized for NMWW treatment. Nevertheless, with high organic-loading wastewater, high biogas flux often leads to biomass loss [12].

The principle of anaerobic baffled reactor (ABR) is to set up a series of vertical baffles in the reactor; thus, the wastewater can be introduced up and down along the baffle in ABR and then pass through the sludge bed of each compartment [13]. The operation flow path of ABR is similar to the plug flow process, which presents the provision of upper and lower baffles to form a compartment [14]. Such process can connect and effectively separate microorganisms from methanogenic and acidogenic phases [15]; therefore, two-phase fermentation can be established in a single reactor. Suaisom et al. [16] found that the increase in organic-loading rate eliminates methanogens and subsequently decreases methane production. Nachaiyasit and Stuckey [17] studied the effect of low temperature on the performance of ABR and discovered that the temperature had no significant effect on COD removal under medium organic-loading conditions. However, when the temperature was further reduced to 15°C, the performance of ABR decreased significantly; the possible reason could be due to the inhibition of bioactivity and the remarkable increase of half saturation degradation constant of volatile fatty acids (VFAs).

The present study aims at enhancing the treatment efficiency of NMWW from a macroscopic perspective by utilizing the characteristics of biological phase separation in enhancing the microbial activity of hydrogen-producing acetogen. Based on the good separation of the microbial community in ABR, this study intends to explore the combination of the fermentation bacteria and hydrogen-producing acetogen through the start-up of ABR. The biohydrogen production method on the basis of increasing the NMWW proportion (increasing COD) was performed to provide substantial biohydrogen production from NMWW.

2. Materials and Methods

2.1. NMWW and Inoculation Sludge. The NMWW, with an initial pH ranging from 5.3 to 5.8, was obtained from a sugar beet factory, and small amounts of urea and K_2HPO_4 were added to regulate the COD/N/P ratio to 200–500:5:1. The inoculated aerobic activated sludge was obtained from the local Wastewater Treatment Plant (Harbin, China), and anaerobic activated sludge (AnAS) was collected in a beer brewhouse. The AnAS was initially filtered and washed to remove inorganic particles. The first and fourth compartments were inoculated with aerobic and anaerobic sludge, respectively. Compartments 2 and 3 were inoculated with mixed aerobic activated sludge and AnAS in the proportions of 2.5:1 and 1:2.5 (v/v), respectively, and the initial mixed liquor volatile suspended solids (MLVSS) in each compartment were 6.9, 14.8, 23.1, and 22.7 g/L.

2.2. ABR Set-Up. A four-compartment ABR with a total volume of 28.75 L was adopted in the experiment (Figure 1). Each compartment had equal size, with downflow and upflow chambers of 2.5 cm and 11.5 cm in width, respectively. NMWW was introduced to the bottom of the upflow chamber and finally drained through a guide plate with an inclination of 45° at the downflow chamber. The sampling ports were arranged at different heights of each compartment, and an effluent pipe was set at the top to connect with the water seal. The sealed water bottle and wet gas flowmeter were filled with HCl (pH of 3) to prevent gas dissolution, and the ABR temperature was maintained at $35 \pm 1^\circ\text{C}$. The hydraulic retention time was 24 h in the ABR, and the initial influent NMWW proportion was 30%. Table 1 lists the start-up stages of the ABR and the main operational parameters.

2.3. Analytical Methods. COD, pH, alkalinity (ALK, in terms of CaCO_3), and mixed liquor volatile suspended solids (MLVSS) were regularly determined by the standard method (APHA [18]). The morphology of AnAS was observed by a scanning electrical microscope (JSM-5610). Biogas production in each compartment was measured by a wet gas flow meter, and the fermentation biogas, VFA, and ethanol compositions and contents were measured by gas chromatography (GC-122 and 4890G) [8].

3. Results

3.1. AnAS Biomass and Morphology. The biomass in each compartment presented a downward trend and reached the lowest values on day 62, which were the MLVSS values of 9.5, 12.9, 17.0, and 14.8 g/L, respectively (Figure 2). Then, the biomass gradually increased and remained stable along with the operation of ABR. In Stage II, the ABR system reached a steady state on day 101, and the respective biomass in each compartment stabilized at 13.5, 11.0, 12.5, and 10.4 g/L. With the increase in the NMWW proportion to 80% in Stage III, the operation of ABR achieved a stable state on day 127, and the MLVSS decreased to 8.0, 8.5, 12.1, and 9.9 g/L, respectively.

With the increase in the NMWW proportion in Stage I, the apparent characteristics of AnAS in each compartment did not change. However, the internal morphology changed significantly in each compartment.

As shown in Figure 3, the AnAS in compartment 1 was attached to the filament, and the microorganisms were mainly composed of *bacilli* and *cocci*. The dominant species in compartment 2 were mainly *bacilli*, and large numbers of filamentous bacteria were observed. *Bacilli* in compartment 3 were prevalent, and a large number of *Brevibacterium* and few *cocci* were observed in compartment 4.

As shown in Figure 4, the morphology of microorganisms in the four compartments changed in Stage II, the *cocci* in compartment 1 gradually disappeared, and long *bacilli* become prevalent. In comparison with Stage I, the *Brevibacterium* in compartment 2 decreased. The dominant bacteria in compartment 3 was still *bacilli*, and the quantity of long *bacilli* increased. The AnAS in compartment 4 consisted of *bacilli*, and the number of *cocci* remarkably increased.

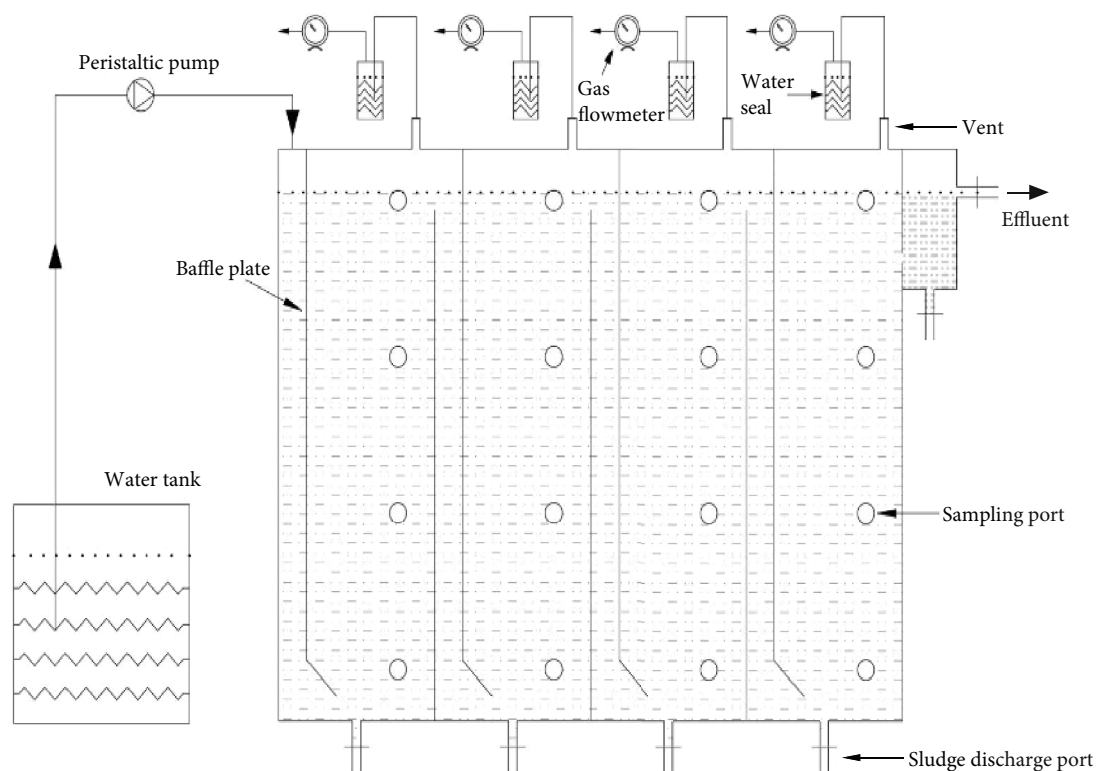


FIGURE 1: Schematic of ABR.

TABLE 1: Start-up parameters of ABR.

Operation phase	HRT (h)	T ($^{\circ}\text{C}$)	Influent pH	Influent COD (mg/L)	NMWW proportion	Organic load rate (kg COD/m ³ ·day)
Stage I (days 1–73)	24	35 ± 1	6.8–7.0	6131–6338	30%	0.54–6.11
Stage II (days 74–118)	24	35 ± 1	4.3–4.5	6868–7107	55%	6.56–7.66
Stage III (days 119–139)	24	35 ± 1	4.1–4.3	7718–8466	80%	7.73–8.49

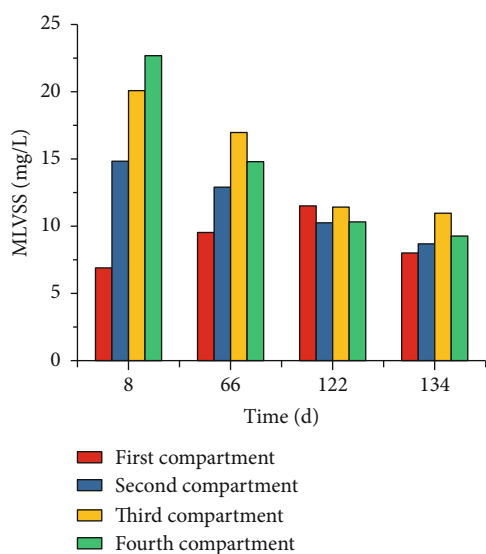


FIGURE 2: Biomass in each ABR compartment.

As depicted in Figure 5, the morphology of the microorganisms in the four compartments significantly changed with the increase in the NMWW proportion to 80%. The main microbial community in compartment I was *bacilli*, and the species became abundant. In comparison with Stages I and II, *cocci* began to appear in compartment 2. The short *bacilli* in compartment 3 gradually disappeared, whereas the *cocci* increased with the ABR operation. Additional *cocci* were observed in compartment 4, and the number of plump cells significantly decreased. This result could be due to the depletion of organic substances in compartments 1–3. The lack of substances finally led to a decline in microbial activity. The discrepancy of pH and alkalinity in each compartment also provided the foundation for the formation of the stable microbial community.

3.2. Biogas Production. With the start-up and operation of ABR, the biogas fluctuation was discovered in each compartment in the first 40 days. After 50 days of operation, the biogas production rate showed a steady upward trend and remained stable from days 64 to 73. Given the influence NMWW proportion of 55% and 80%, the biogas production

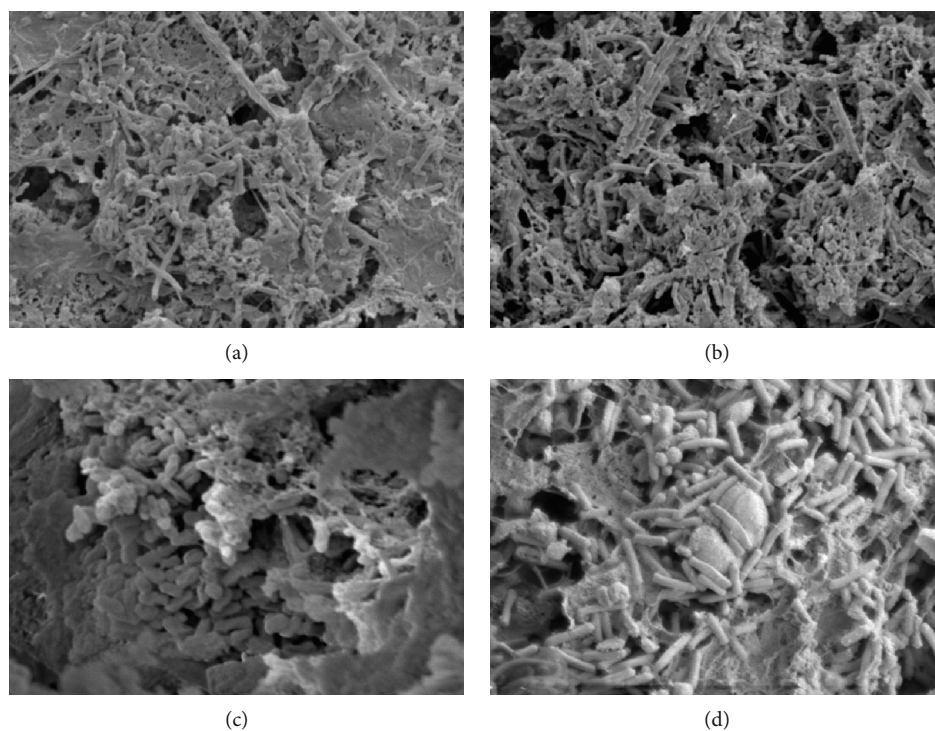


FIGURE 3: AnAS morphology in Stage I ((a) compartment 1, 5 k; (b) compartment 2, 5 k; (c) compartment 3, 8 k; and (d) compartment 4, 10 k).

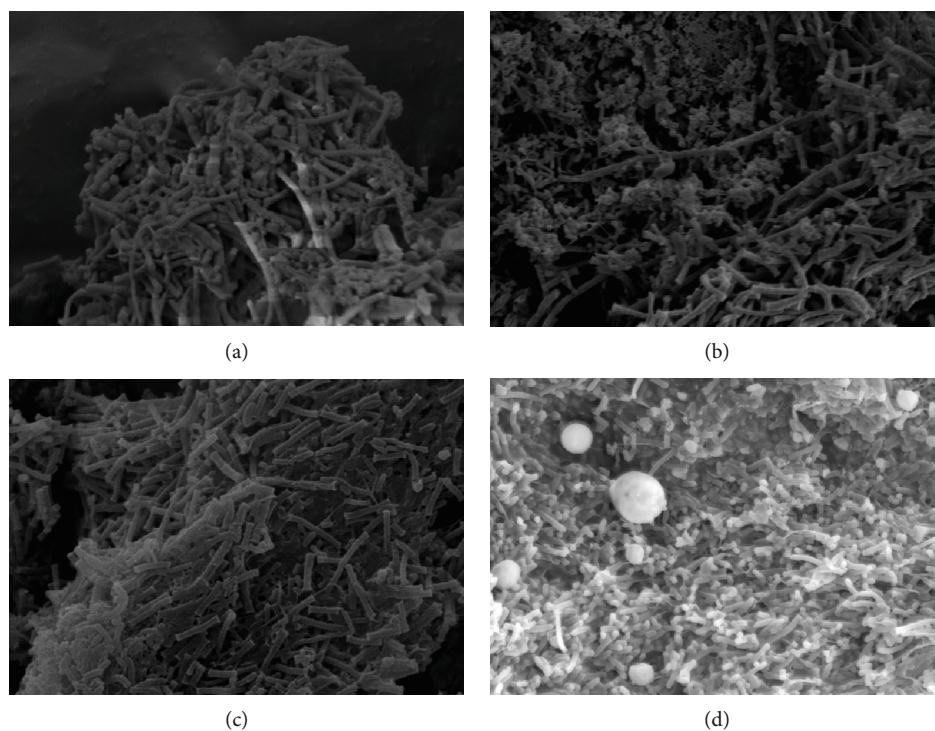


FIGURE 4: AnAS morphology in Stage II ((a) compartment 1, 5 k; (b) compartment 2, 5 k; (c) compartment 3, 5 k; (d) compartment 4, 5 k).

rate fluctuated at the initial period of Stages II and III, and the stable state of operation was restored on days 108–117 (Stage II) and days 130–139 (Stage III). During the stabilization period of the three stages, the biogas production rates

in compartment 1 were 19.32, 35.43, and 31.16 L/day (Figure 6), and the hydrogen contents were maintained at 13.6%, 27.1%, and 31.9%, respectively (Figure 7). The maximum biogas production rate in compartment 1 occurred in

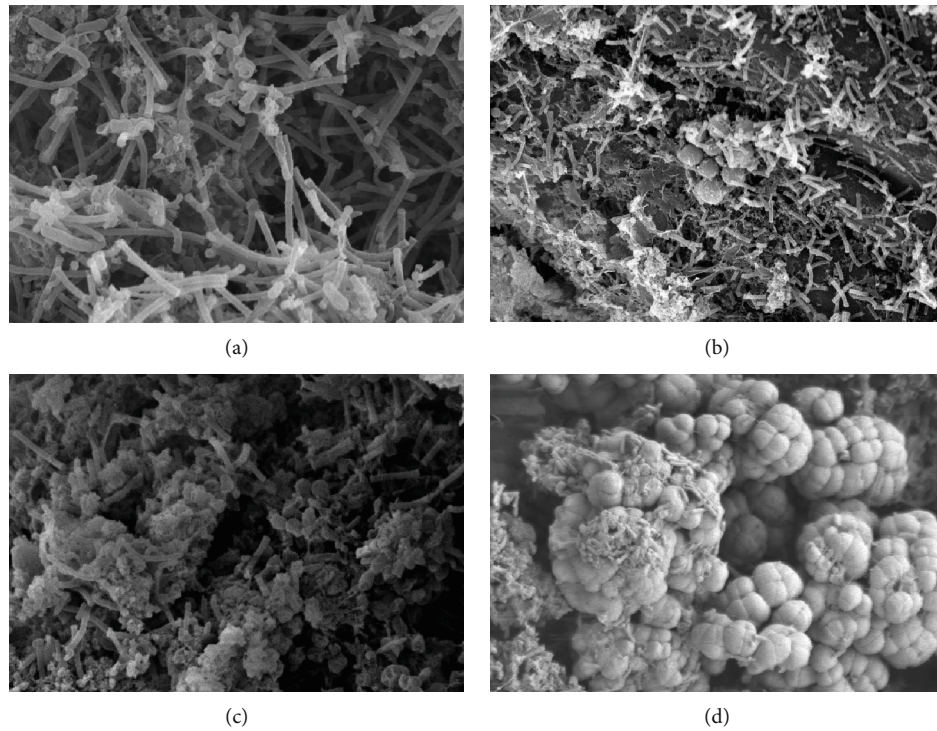


FIGURE 5: AnAS morphology in Stage III ((a) compartment 1, 6 k; (b) compartment 2, 3 k; (c) compartment 3, 5 k; (d) compartment 4, 4 k).

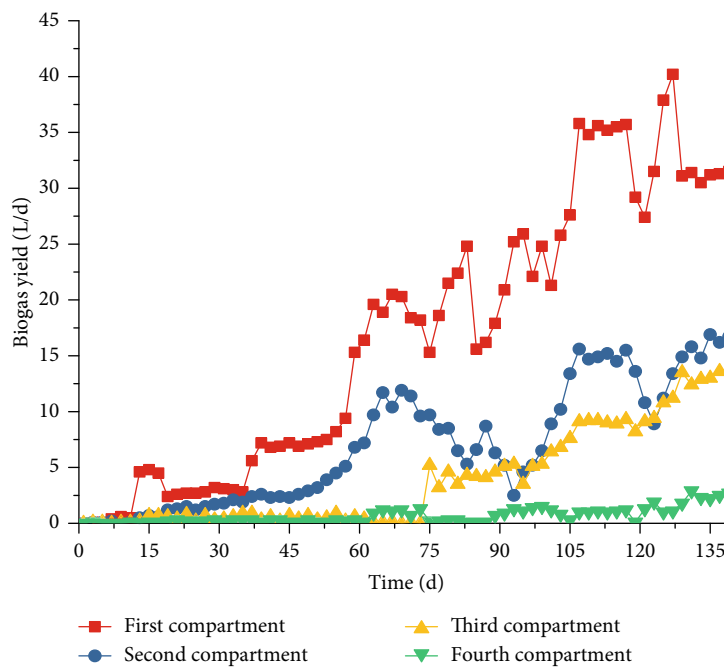
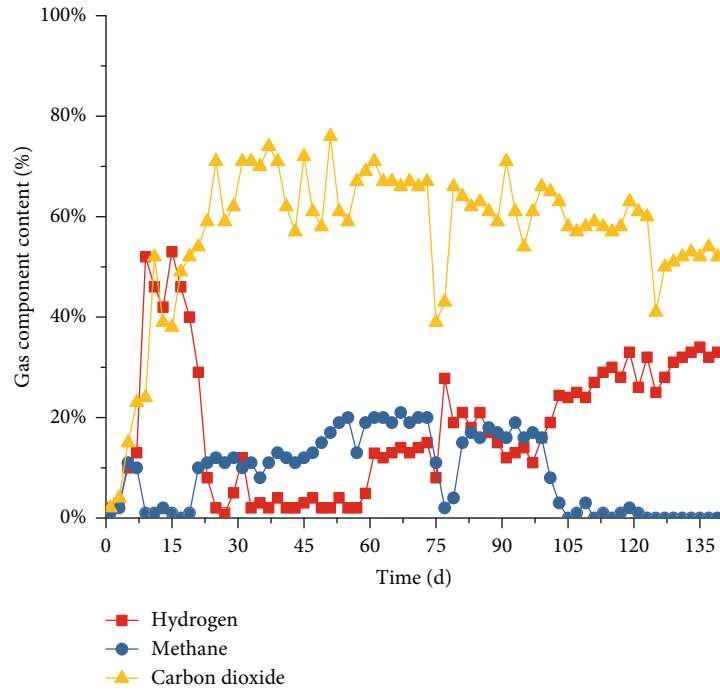


FIGURE 6: Biogas production in each compartment.

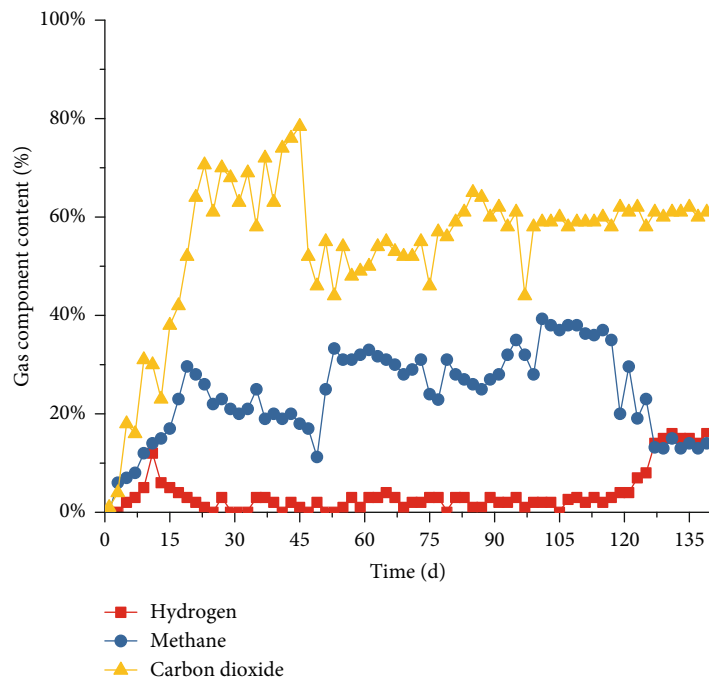
Stage II but decreased in Stage III, and the biogas production rates in compartments 2–4 showed a gradual increase as the NMWW proportion increased. From Stages I to III, the biogas production rates in compartment 2 were 10.79, 15.07, and 15.88 L/day, and the hydrogen contents were 2.5%, 2.6%, and 15%, respectively. The biogas production rates in

compartment 3 were 0.08, 9.12, and 13.18 L/day, and the hydrogen contents were 1.4%, 0.9%, and 0.7% in compartment 4, respectively.

In Stage I, the average CH₄ contents in each compartment were 9.9%, 30.1%, 33.2%, and 38.2% (Figure 7), which showed an increasing trend along the process, whereas the

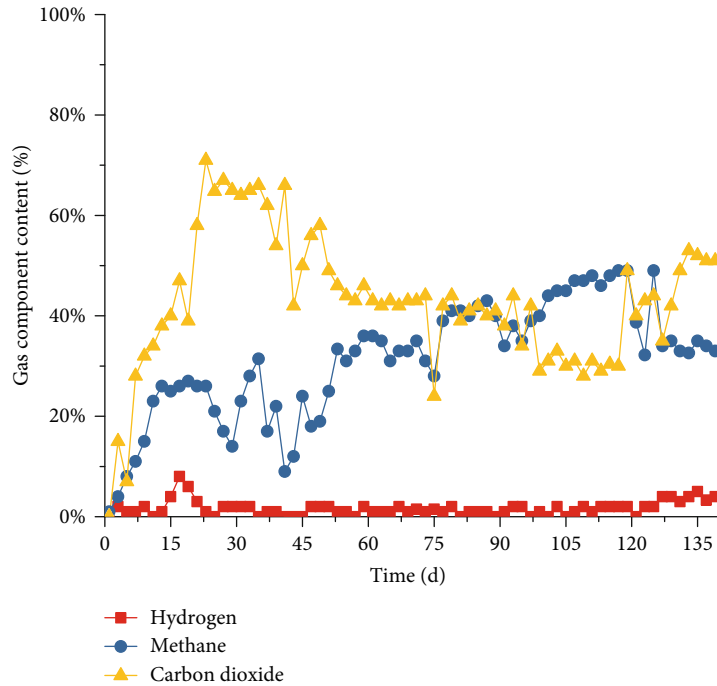


(a)

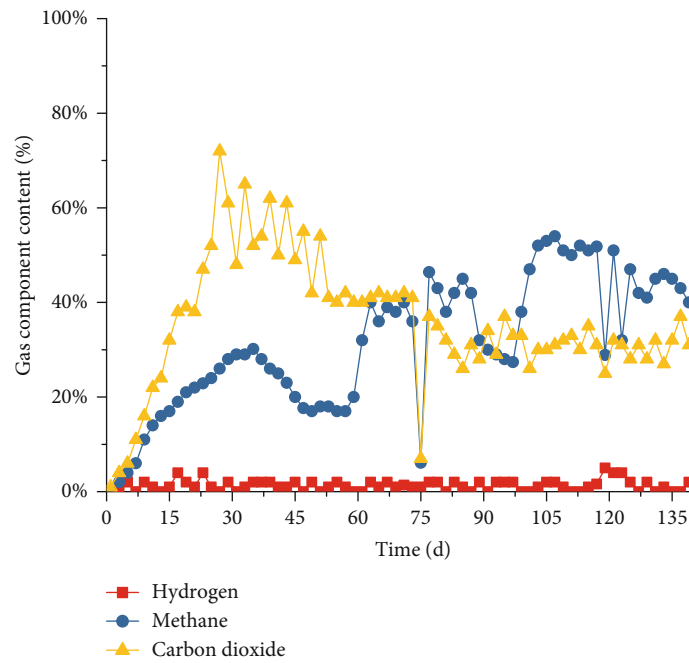


(b)

FIGURE 7: Continued.



(c)



(d)

FIGURE 7: Variation in biogas concentration ((a) compartment 1; (b) compartment 2; (c) compartment 3; and (d) compartment 4).

corresponding CO₂ content showed a decreasing trend. However, with the increase in the NMWW proportion, the variations in CH₄ and CO₂ contents in compartment 1 showed different properties to other compartments. During Stage II, the CH₄ content in compartment 1 significantly reduced to 0.9%, and a small amount of CH₄ was detected in Stage III. Thus, the methanogenic activity of AnAS was completely inhibited. The methanogenic activity of AnAS in compartments 2–4 was enhanced in Stage II. The CH₄

content in compartments 2–4 increased to 36.7%, 47.5%, and 51.7%, with CO₂ contents of 58.8%, 29.9%, and 32.0%, respectively (Figure 7). In Stage III (COD of 8000 mg/L), the methanogenic activity of AnAS in compartments 2–4 was inhibited with different degrees. The methane proportion in compartments 2–4 decreased to 13.6%, 33.8%, and 43.1%, respectively, which may be due to the increase in terminal acidic products that inhibited the bioactivity of methanogens at a relatively low pH condition. The average

biohydrogen production capacity increased with the NMWW proportion. The biohydrogen production rates in compartments 2–4 were 2.92, 10.17, and 12.85 L/day, respectively. The biohydrogen production in compartment 1 was significantly high, which was the most important fermentative biohydrogen production compartment in the ABR.

3.3. Soluble Fermentation Products. The variation in the soluble fermentation products showed a similar trend as the biogas production. At the initial period of each stage, the total VFAs and component oscillatory changed and then gradually stabilized. At the first stable state (days 64–73), the main soluble fermentation products in each compartment were acetic and butyric acid (Figure 8). The total acetic and butyric acid contents reached 62%, 72.8%, 73.6%, and 73.5% and presented butyric acid fermentation.

At the stable period of Stage II (days 108–117), the soluble fermentation products in compartment 1 were converted to ethanol and acetic acid, which accounted for 77.2% of the total VFAs and showed ethanol-type fermentation. The ethanol–acetic acid proportion in compartment 2 was 72.9% (Figure 8(b)), and the fermentation characteristic of AnAS exhibited ethanol-type fermentation. The acetic acid content in compartment 3 accounted for 59.5% of the total VFAs, and the ethanol, propionic acid, and butyric acid contents were 8.5%, 10.9%, and 18.2% (Figure 8(c)), respectively. This result indicated the establishment of mixed fermentation characteristics. The butyric acid content in compartment 4 was significantly higher than that of propionic acid, and the acetic and butyric acid contents accounted for 82.8% (Figure 8(d)) of the total VFAs, showing butyric acid-type fermentation.

Ethanol-type fermentation in compartment 1 was strengthened at the stable period of Stage III (days 130–139), and the ethanol–acetic acid proportion increased to 85.3%. Methane was not detected in the process. Thus, the methanogen activity in compartment 1 was effectively inhibited. Although compartment 2 was maintained in ethanol-type fermentation, the acetic acid content decreased from 44.7% to 31.3% (Figure 8(b)). This result suggests that methane production through acetic acid was enhanced. The ethanol content in compartment 3 increased to 33.2%, whereas the acetic and butyric acid contents decreased to 42.5% and 16%, respectively. The ethanol and acetic acid contents accounted for 75.7%, showing the ethanol-type fermentation property. In compartment 4, although the ethanol content increased significantly from 3.5% to 10.1% in Stage II, it was significantly lower than that of butyric acid. Therefore, the fermentation characteristic was still butyric acid-type fermentation.

With the increase in the NMWW proportion, the total VFAs of ABR showed an increasing trend. During the three stabilization stages, the average influent CODs were 5967, 6872, and 8084 mg/L, and the total effluent VFAs were 4264, 4578, and 4948 mg/L. The accumulation of the terminal acidic products decreased the pH in the ABR, which further inhibited the microbial activity of methanogens. The production and accumulation of ethanol and VFAs indicated that organic matter degradation in NMWW was incomplete,

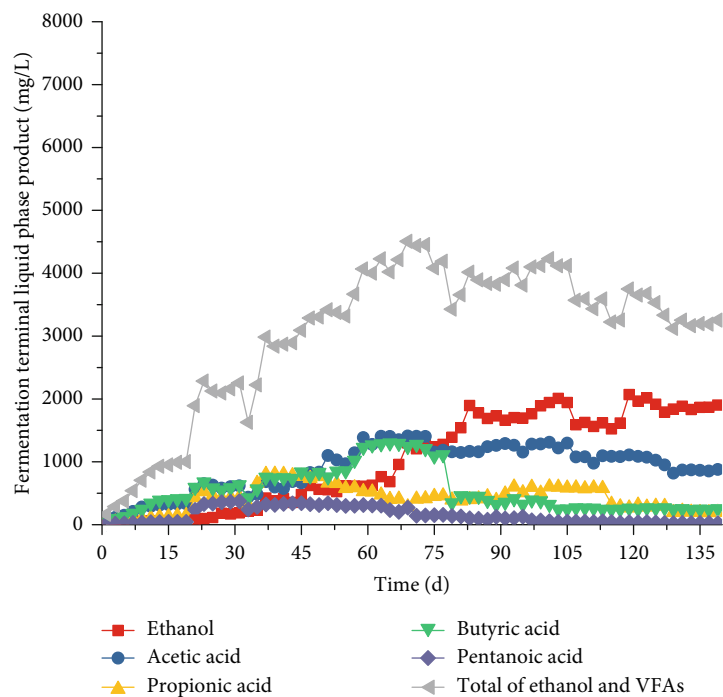
which may directly influence the removal efficiency of COD in the ABR.

3.4. ABR Operation Characteristics

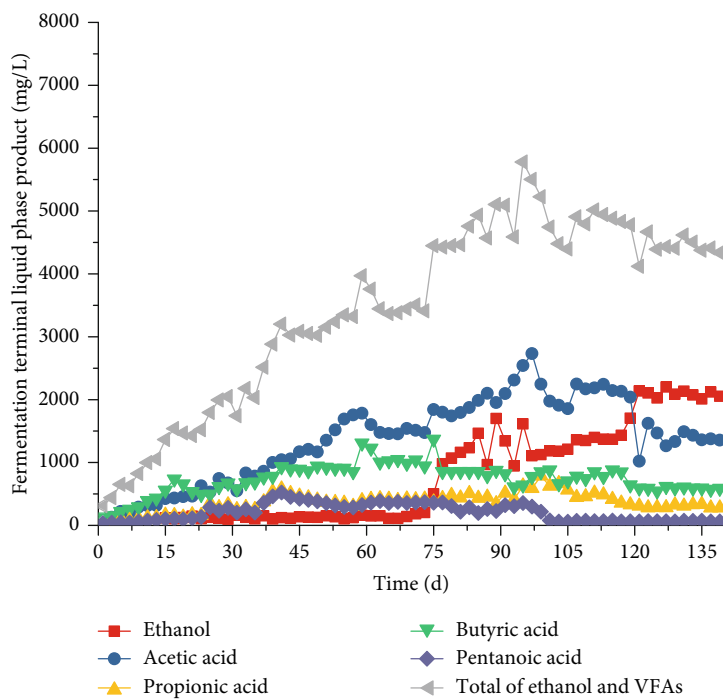
3.4.1. pH and Alkalinity. A considerable amount of VFA was produced due to AnAS fermentation, which resulted in relatively low pH values in the four compartments of ABR. The average pH and alkalinity were 5.2 and 1348 mg/L, respectively (Figure 9), and the pH value in compartment 1 was the highest. The alkalinity of each compartment also increased with the NMWW proportion. In Stage II (days 74–88), the pH value in compartment 2 increased, whereas the alkalinity in compartment 1 continuously decreased. From day 101 to 117, the pH value in compartment 2 was the highest, the pH variations in compartments 1 and 2 were similar, and the pH values in compartments 3 and 4 were stable (Figure 9(a)). With the increase in the NMWW proportion, the pH value in compartment 1 decreased rapidly to 4.6, and the pH value in compartment 2 was still the highest. From day 129, the pH value in each compartment began to increase, and the pH value in compartment 3 was close to that in compartment 2. In Stage III, the influent alkalinity gradually increased, and the alkalinity in compartments 1 and 2 decreased (Figure 9(b)).

The pH value in the ABR mainly depended on VFAs and alkalinity contents, and the variation in alkalinity was essentially based on the relative balance of CO_3^{2-} and HCO_3^- concentrations. When the pH value of the ABR was <5.0 , the alkalinity was principally formed by HCO_3^- . The consumption of HCO_3^- could decrease the alkalinity and pH when the residual VFAs increased. The HCO_3^- content was highly correlated with the CO_2 production in the ABR, and the produced CO_2 concentration was small at the beginning of Stage I. Therefore, the relatively low HCO_3^- decreased pH and alkalinity (Figure 9). However, the biogas production and VFA concentrations in each compartment increased rapidly after day 17, indicating that AnAS adapted to new circumstances; thus, additional CO_2 was produced. With the increase in alkalinity, the buffering capacity of ABR was improved, and the pH values became increasingly stable. The pH value in compartment 1 was the lowest during the start-up process of ABR (days 0–27) due to the high VFA production and consumption of influent alkalinity. With the increase in the NMWW proportion, the alkalinity was accumulated; however, additional VFAs were produced, and the pH value in compartments 2–4 remained stable at 5.1.

3.4.2. COD Removal. During the ABR operation in Stage I, the effluent COD in each compartment presented fluctuation property. Although effluent COD showed a decreasing trend, the discrepancy of COD in each compartment was small. On day 24, the influent COD was 4047 mg/L, and the effluent CODs in compartments 1–4 were 3780, 3586, 3388, and 3218 mg/L (Figure 10), respectively. The average COD removal rate was 15.1%. COD removal gradually increased and reached a stable level after day 43, and the average effluents in the four compartments were 5056, 4872, 4353, and 4192 mg/L, respectively. COD removal



(a)



(b)

FIGURE 8: Continued.

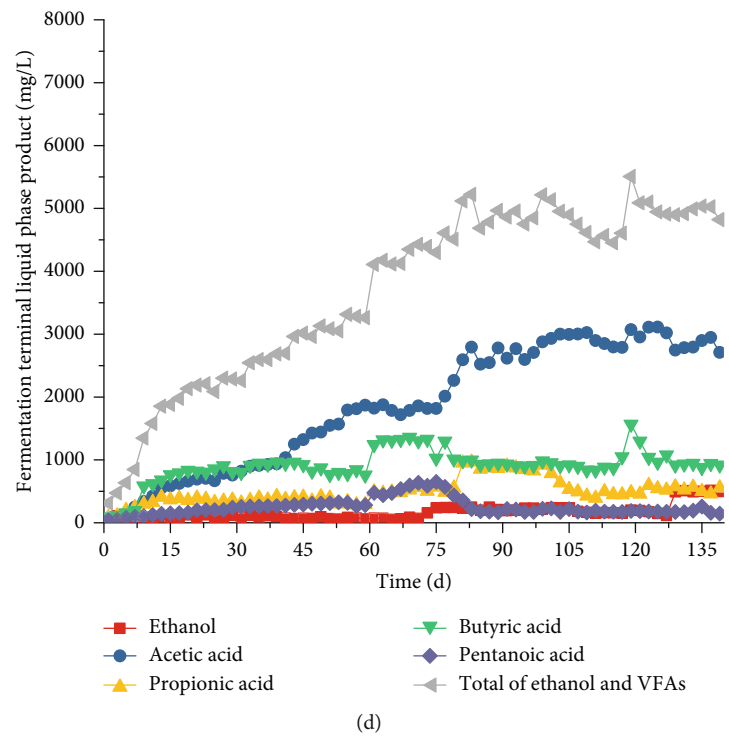
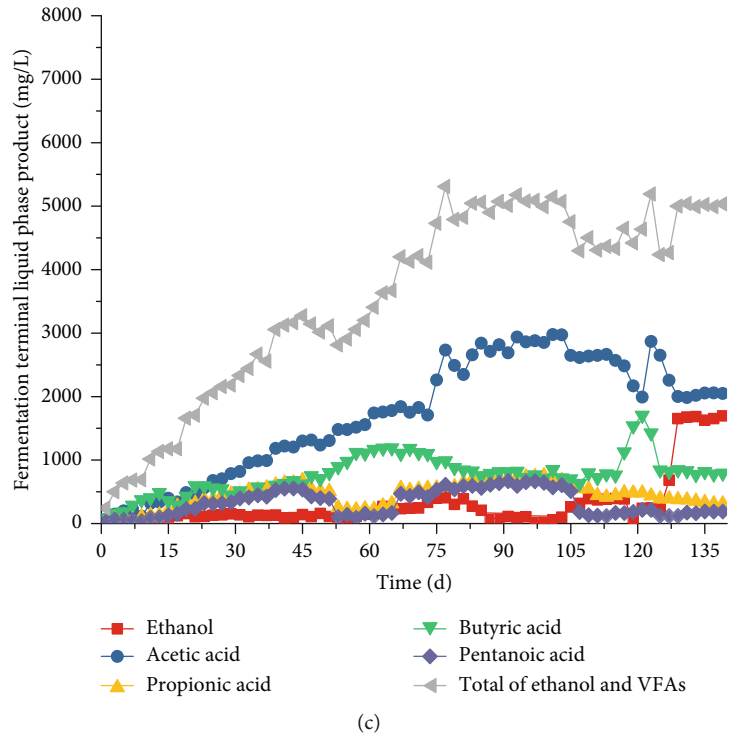


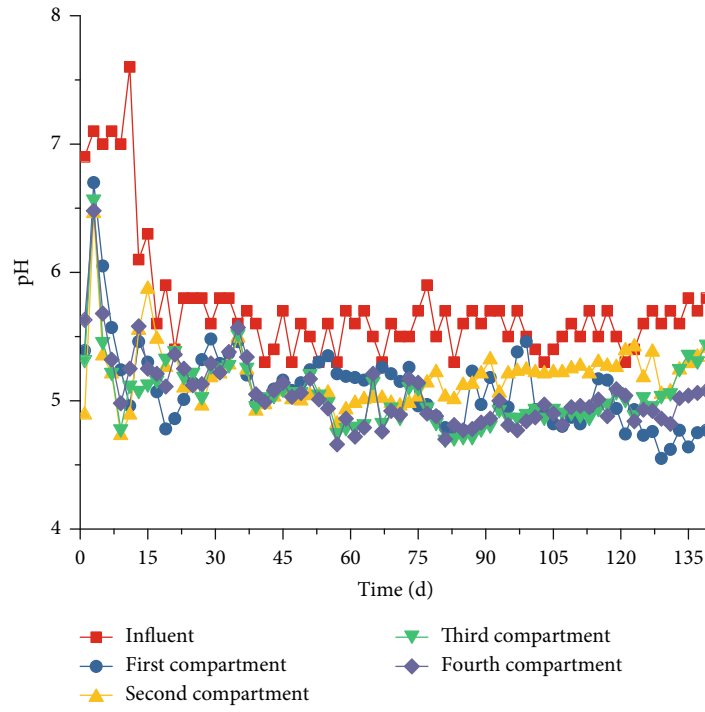
FIGURE 8: Variations in ethanol and VFAs ((a) compartment 1, (b) compartment 2, (c) compartment 3, and (d) compartment 4).

mainly occurred in compartments 1–3, and the least in compartment 4. In Stage II, the influent COD increased to approximately 7000 mg/L, and the COD removal rate rapidly decreased to 14.7%. With the ABR operation, the COD removal gradually increased to 24.0%. The influent COD increased to approximately 8000 mg/L in Stage III, and the COD removal rapidly decreased to 15.0%, whereas

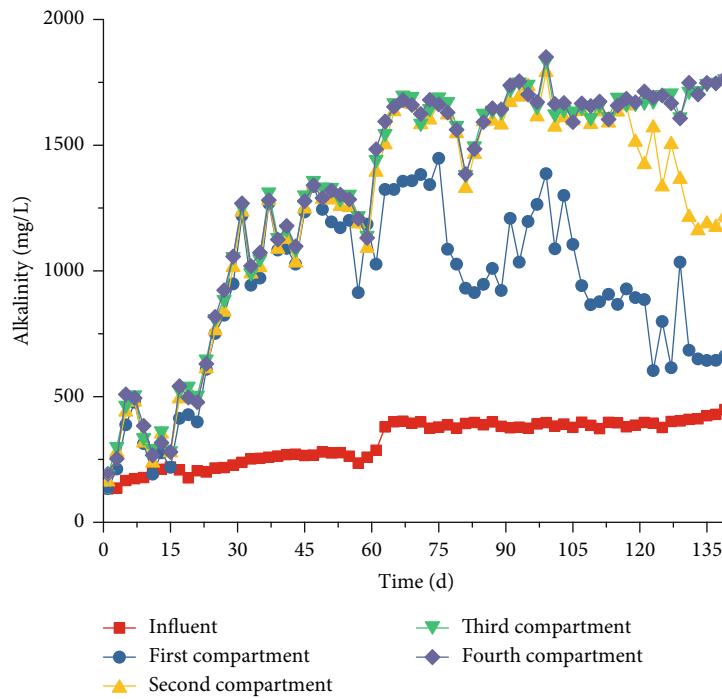
the COD removal rate gradually increased to 17.2% and remained stable after 123 days.

4. Discussions

4.1. Biohydrogen Production Activity and Fermentation Types. pH is an important ecological factor that affects the



(a)



(b)

FIGURE 9: Effluent pH and alkalinity in each compartment ((a) pH; (b) alkalinity).

type of acid production, and the variation in pH values not only influences biohydrogen production but also leads to the variation in microbial community structure [19]. In the ABR biohydrogen production system, a large number of VFAs were produced due to the acidification and fermentation of microorganisms, which resulted in the low pH in each compartment, and the pH values changed in the range of

4.5–5.4. During the stable period of Stage I, the average pH and alkalinity values in compartment 1 were 5.2 and 1348 mg/L (Figure 9), respectively, and the metabolic characteristic of AnAS was butyric acid fermentation. The respective pH and alkalinity decreased to below 5.0 and 875 mg/L during the stabilization period of Stages II and III, and the fermentation type converted from butyric acid fermentation

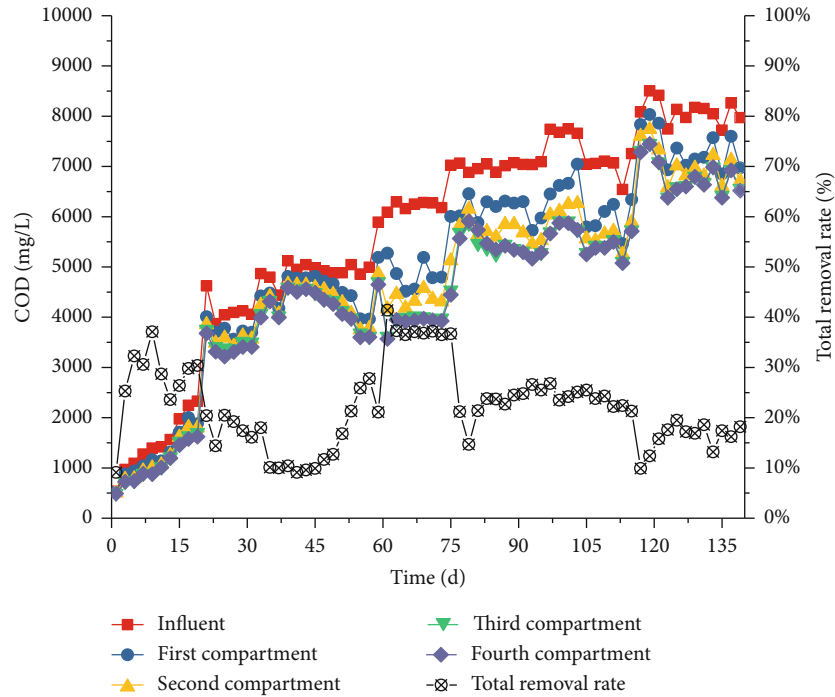


FIGURE 10: Variation and removal of COD in each compartment.

to ethanol-type fermentation. The pH and alkalinity in compartment 2 were significantly different. However, the fermentation type slightly changed because a large number of byproducts were introduced from compartment 1. The variation in metabolic characteristics in compartment 3 was overtly typical. With the increase in the NMWW proportion, the pH and alkalinity gradually increased from 5.0 and 1493 mg/L to 5.3 and 1785 mg/L (Figure 9). The metabolic characteristic transformed from butyric acid fermentation to mixed fermentation and finally formed ethanol fermentation. In compartment 4, given the positive influence of buffer effect in compartments 1–3, the variations in pH and alkalinity were slightly small (5.0 and 1514–1784 mg/L), and the metabolic characteristic maintained butyric acid fermentation.

COD removal was mainly through the methanogenesis of the methanogenic flora [20]. However, the ABR system was characterized by acidogenic fermentation flora and showed relatively low COD removal performance due to the bioactivity of methanogens [8]. COD could also be effectively removed by microbial synthesis and the release of CO_2 and H_2 . Thus, additional VFAs remained and presented low COD removal efficiency. As shown in Figure 10, effluent COD decreased through each compartment; however, the total COD removal rates were only 37.6%, 21.4%, and 15.4% in the stable periods of Stages I–III, with corresponding biohydrogen production capacities by COD removal of 45.29, 241.04, and 360.22 L/kg COD, respectively. With the increase in the NMWW proportion (up to 80%), the biohydrogen production rate significantly improved (Figures 6 and 7). The soluble terminal products in the four compartments were dominated by acetic and butyric acid, and the average COD removal rate was 37.6%. The average biohydro-

gen production was 3.2 L/day, and the specific biohydrogen production by COD removal rate was 45.29 L/kg COD. When the influent NMWW proportion increased to 80% (COD of 8000 mg/L), the first three compartments showed ethanol-type fermentation, whereas butyric acid fermentation was strengthened in compartment 4. The average COD removal rate reduced to 15.4%, and the average biohydrogen and biohydrogen production capacity by COD removal increased to 12.85 L/day and 360.22 L/kg COD, respectively.

The initial biomasses (MLVSS) in compartments 1–4 were 6.9, 14.8, 23.1, and 22.7 g/L (Figure 2), respectively. With the ABR operation, the biomass in compartment 1 increased to 9.5 g/L at the first stable state in Stage I (day 66), whereas the biomass in compartments 2–4 decreased significantly to 12.9, 17.0, and 14.8 g/L, respectively. The biomass in compartment 1 increased to 11.5 g/L at the stable period of Stage II (day 112), whereas the biomass in compartments 2–4 continuously decreased. In Stage III, the biomass in compartments 2–4 were 8.0, 8.7, 11.0, and 9.3 g/L, respectively. The bioactivity of AnAS was further enhanced with high influent COD, and the biogas production significantly increased, which caused uplift and loss of AnAS in each compartment. The microbial activity of the AnAS in each compartment continuously improved with the increase in the NMWW proportion, and the specific biohydrogen production rates were 41.52, 123.55, and 217.5 L/kg MLVSS in Stages I–III, respectively.

4.2. Biohydrogen Production Efficiency in ABR. Although the biomass in compartments 2–4 gradually decreased, the biogas and biohydrogen production rates showed an upward trend. During the stable period of Stages I–III, the specific biogas production rates in compartment 2 were 116, 205,

and 254 L/kg MLVSS-day, whereas those in compartment 3 were 101, 111, and 167 L/kg MLVSS-day and those in compartment 4 were 80, 194, and 232 L/kg MLVSS-day, respectively. The metabolic activity of AnAS in each compartment enhanced biohydrogen production efficiency. During the stabilization period of Stages I–III, the biohydrogen production rates in compartment 2 were 0.27, 0.39, and 2.38 L/day; those in compartment 3 were 0, 0.16, and 0.52 L/day; and the biohydrogen production rates for compartment 4 were 0.01, 0.01, and 0.02 L/day, respectively.

The variation in the biogas production rate in compartment 1 was significantly different from those in the subsequent three compartments. The biogas production rate reached the highest in the stable period of Stage II, which increased from 19.3 L/day to 35.4 L/day. However, the biogas production rate reduced to 31.2 L/day in Stage III. Although the biomass decreased, the specific biogas production rate increased, which were 282, 428, and 541 L/kg MLVSS-day, and the final biohydrogen production rates were 2.6, 9.6, and 10.0 L/day. Compartment 1 produced the most biohydrogen in the stable period of Stages I and II, and the contribution rate reached above 90%. However, in Stage III, the contribution rate decreased to 77.4% because the biohydrogen production efficiency in compartment II was significantly enhanced. Although a certain amount of hydrogen-producing acetogens was enriched in other compartments, their contribution to the total biohydrogen production of ABR was relatively low due to the limitation of fermentation substrates (carbohydrates) and hydrogen consumption of methanogens and homoacetogen [21]. Compartment 2 showed the highest contribution rate of 18.5% in Stage III, whereas compartment 4 presented little contribution rate for biohydrogen production.

4.3. Performance of Hydrogen-Producing Acetogen and Biohydrogen Production Efficiency. The methanogens were gradually eliminated by increasing influent COD and VFAs and reducing pH values to enrich the hydrogen-producing acetogens in the ABR. As shown in Figure 8, the acetic acid concentration increased with the decrease in ethanol and butyric acid. Thus, the performance of biohydrogen and acetogenic production was evident, and the hydrogen-producing acetogens were enriched well [22]. However, the average biohydrogen production rate was only 12.85 L/day under the optimum operation conditions, which was significantly lower than the result in the research conducted by van Ginkel [23].

When the influent COD gradually increased, the pH value reduced to lower than 5.2; however, the methanogenic activity was not completely inhibited in the ABR. The H₂ and CO₂ contents decreased with the increase in methane content in fermentation biogas (Figure 7). The amount of biohydrogen production was considerably affected due to the hydrogen consumption property of methanogens [24]. A relatively low hydrogen partial pressure was beneficial to the performance of hydrogen-producing acetogens, and the hydrogen-consuming homoacetogen and methanogens were generally the symbiotic bacteria with hydrogen-producing acetogens [25, 26]. Therefore, the existence of homoacetogen

and methanogens was not conducive to the enrichment of hydrogen-producing acetogens and subsequently limited the biohydrogen production capacity in the ABR.

5. Conclusions

The biogas and biohydrogen production rates of ABR increased from 31.27 and 2.92 L/day to 61.54 and 12.85 L/day, respectively, when the influent COD increased to 8000 mg/L. Compartment 1 contributes most biohydrogen production, which accounted for >77.4%. When the influent COD was increased to 8000 mg/L, the pH of each compartment decreased continuously, and the fermentation metabolism characteristics significantly changed. The first three compartments eventually formed ethanol-type fermentation, whereas the butyric acid fermentation in compartment 4 was further enhanced. Although the biohydrogen production and acetogenic was improved in the ABR, the hydrogen-consuming bacteria methanogens and homoacetogen were effectively inhibited, which considerably affected the biohydrogen production efficiency. When the specific biogas production rate reached 232 L/kg MLVSS-day, the specific biohydrogen production rate was only 48 L/kg MLVSS-day.

Data Availability

The data used to support the findings of this study are included within the article.

Conflicts of Interest

The authors declare that there is no conflict of interest regarding the publication of this paper.

Acknowledgments

Special thanks to Prof. Tay Joo Hwa for the contribution to this work, may you rest in peace. This research was supported by the National Natural Science Foundation of China (grant no. 51478141), the Major Science and Technology Program for Water Pollution Control and Treatment (2017ZX07201-001), and National Key Research and Development Program of China (2018YFD0800900).

References

- [1] T. Xia, X. Zhang, H. Wang et al., “Power generation and microbial community analysis in microbial fuel cells: a promising system to treat organic acid fermentation wastewater,” *Bioresource Technology*, vol. 284, pp. 72–79, 2009.
- [2] W. Zhang, X. Ren, J. He, Q. Zhang, C. Qiu, and B. Fan, “Application of natural mixed bacteria immobilized carriers to different kinds of organic wastewater treatment and microbial community comparison,” *Journal of Hazardous Materials*, vol. 377, pp. 113–123, 2019.
- [3] R. Wang, H. Wen, and C. Cui, “Bio-hydrogen production by a new isolated strain *Rhodospseudomonas* sp. WR-17 using main metabolites of three typical dark fermentation type,” *International Journal of Hydrogen Energy*, vol. 44, no. 46, pp. 25145–25150, 2019.

- [4] Y. Wang, D. Wang, F. Chen et al., "Nitrate addition improves hydrogen production from acidic fermentation of waste activated sludge," *Chemosphere*, vol. 235, pp. 814–824, 2019.
- [5] Y. Pu, J. Tang, X. Wang et al., "Hydrogen production from acidogenic food waste fermentation using untreated inoculum: effect of substrate concentrations," *International Journal of Hydrogen Energy*, vol. 44, no. 50, pp. 27272–27284, 2019.
- [6] Z. Zhang, Y. Li, H. Zhang, C. He, and Q. Zhang, "Potential use and the energy conversion efficiency analysis of fermentation effluents from photo and dark fermentative bio-hydrogen production," *Bioresource Technology*, vol. 245, pp. 884–889, 2017.
- [7] W. Wei, Y. Zhang, Q. Huang, and B. Ni, "Polyethylene terephthalate microplastics affect hydrogen production from alkaline anaerobic fermentation of waste activated sludge through altering viability and activity of anaerobic microorganisms," *Water Research*, vol. 163, p. 114881, 2019.
- [8] J. Li, G. Zheng, J. He, S. Chang, and Z. Qin, "Hydrogen-producing capability of anaerobic activated sludge in three types of fermentations in a continuous stirred-tank reactor," *Biotechnology Advances*, vol. 27, no. 5, pp. 573–577, 2009.
- [9] M. Salari, M. S. Khiabani, R. R. Mokarram, B. Ghanbarzadeh, and H. S. Kafil, "Preparation and characterization of cellulose nanocrystals from bacterial cellulose produced in sugar beet molasses and cheese whey media," *International Journal of Biological Macromolecules*, vol. 122, pp. 280–288, 2019.
- [10] H.-Y. Ren, F. Kong, J. Ma et al., "Continuous energy recovery and nutrients removal from molasses wastewater by synergistic system of dark fermentation and algal culture under various fermentation types," *Bioresource Technology*, vol. 252, pp. 110–117, 2018.
- [11] K. Kuroda, T. Chosei, N. Nakahara et al., "High organic loading treatment for industrial molasses wastewater and microbial community shifts corresponding to system development," *Bioresource Technology*, vol. 196, pp. 225–234, 2015.
- [12] W. Han, B. Wang, Y. Zhou et al., "Fermentative hydrogen production from molasses wastewater in a continuous mixed immobilized sludge reactor," *Bioresource Technology*, vol. 110, pp. 219–223, 2012.
- [13] J. Yu, H. Chen, Q. Guo, Z. Zhang, L. Guo, and R. Jin, "Response of performance of an anammox anaerobic baffled reactor (ABR) to changes in feeding regime," *Ecological Engineering*, vol. 83, pp. 19–27, 2015.
- [14] M. J. Hahn and L. A. Figueroa, "Pilot scale application of anaerobic baffled reactor for biologically enhanced primary treatment of raw municipal wastewater," *Water Research*, vol. 87, pp. 494–502, 2015.
- [15] G. A. Vuitik, L. T. Fuess, V. Del Nery, R. Bañares-Alcántara, and E. C. Pires, "Effects of recirculation in anaerobic baffled reactors," *Journal of Water Process Engineering*, vol. 28, pp. 36–44, 2019.
- [16] P. Suaisom, P. Pholchan, and P. Aggarangsi, "Holistic determination of suitable conditions for biogas production from *Pennisetum purpureum* x *Pennisetum americanum* liquor in anaerobic baffled reactor," *Journal of Environmental Management*, vol. 247, pp. 730–737, 2019.
- [17] S. Nachaiyasit and D. C. Stuckey, "Effect of low temperatures on the performance of an anaerobic baffled reactor (ABR)," *Journal of Chemical Technology and Biotechnology*, vol. 69, no. 2, pp. 276–284, 1997.
- [18] APHA, *Standard Methods for the Examination of Water and Wastewater*, American Public Health Association, American Water Works Association, Water Environmental Federation, Washington, DC, USA, 21st edition, 2005.
- [19] Y. Yuan, X. Hu, H. Chen, Y. Zhou, Y. Zhou, and D. Wang, "Advances in enhanced volatile fatty acid production from anaerobic fermentation of waste activated sludge," *Science of the Total Environment*, vol. 694, p. 133741, 2019.
- [20] A. Aziz, F. Basheer, A. Sengar, Irfanullah, S. U. Khan, and I. H. Farooqi, "Biological wastewater treatment (anaerobic-aerobic) technologies for safe discharge of treated slaughterhouse and meat processing wastewater," *Science of The Total Environment*, vol. 686, pp. 681–708, 2019.
- [21] S. Wang, J. Li, G. Zheng, G. Du, and J. Li, "Bioaugmentation with mixed hydrogen-producing acetogen cultures enhances methane production in molasses wastewater treatment," *Archaea*, vol. 2018, Article ID 4634898, 10 pages, 2018.
- [22] G. Zheng, J. Li, F. Zhao et al., "Effect of illumination on the hydrogen-production capability of anaerobic activated sludge," *Frontiers of Environmental Science Engineering*, vol. 6, no. 1, pp. 125–130, 2012.
- [23] S. W. van Ginkel and B. Logan, "Increased biological hydrogen production with reduced organic loading," *Water Research*, vol. 39, no. 16, pp. 3819–3826, 2005.
- [24] C. Liu, J. Li, S. Wang, and L. Nies, "A syntrophic propionate-oxidizing microflora and its bioaugmentation on anaerobic wastewater treatment for enhancing methane production and COD removal," *Frontiers of Environmental Science Engineering*, vol. 10, no. 4, p. 13, 2016.
- [25] M. Aslam, R. Ahmad, M. Yasin et al., "Anaerobic membrane bioreactors for biohydrogen production: recent developments, challenges and perspectives," *Bioresource Technology*, vol. 269, pp. 452–464, 2018.
- [26] F. Jiang, Z. Peng, H. Li, J. Li, and S. Wang, "Effect of hydraulic retention time on anaerobic baffled reactor operation: enhanced biohydrogen production and enrichment of hydrogen-producing acetogens," *Processes*, vol. 8, no. 3, p. 339, 2020.